The University Of Sheffield.

Advanced Fault Detection Methods for Permanent Magnets Synchronous Machines

By

Fernando Alvarez Gonzalez

A thesis submitted for the degree of Doctor of Philosophy

Department of Electronic and Electrical Engineering

Faculty of Engineering

The University of Sheffield

December 2018

ABSTRACT

The trend in recent years of transport electrification has significantly increased the demand for reliability and availability of electric drives, particularly in those employing Permanent Magnet Synchronous Machines (PMSM), often selected due to their high efficiency and energy density. Fault detection has been identified as one of the key aspects to cover such demand. Stator winding faults are known to be the second most common type of fault, after bearing fault.

An extensive literature review has shown that, although a number of methods has been proposed to address this type of fault, no tool of general application, capable of dealing effectively with fault detection under transient conditions unrelated to the fault, has been proposed up to date.

This thesis has made contributions to modelling, real-time emulation and stator winding fault detection of PMSM. Fault detection has been carried out through model-based and signal-based methods with a specific aim at operation during transient conditions. Furthermore, fault classification methods already available have been implemented with features computed by proposed signal-based fault detection methods.

The main conclusion drawn from this thesis is that model-based fault detection methods, particularly those based on residuals, appear to be better suited for transient conditions analysis, as opposed to signal-based fault detection methods. However, it is expected that a combination of the two (model/signal) would yield the best results, something mostly left out of the scope of this thesis due to lack of time and available material.

ACKNOWLEDGMENTS

I would like to thank my supervisor Dr. Antonio Griffo for his infinite patience and unparalleled dedication to his students, and especially for the opportunity that he gave me and led to the completion of this thesis. I would like to thank as well my second supervisor Prof. Jiabin Wang for his constructive criticism that motivated the search for continuous improvement. Thanks are due as well to my colleagues, in particular Dr. Rongguang Hu, Dr. Bo Wang and Dr. Igor Tsyokhla, all of them instrumental in the validation of my proposed methodology.

I would like to thank as well the Engineering and Physical Sciences Research Council, The University of Sheffield Electronic and Electrical Engineering department and its staff, for the funding, resources and help that have made this work possible.

Finally, this thesis and the work it entails wouldn’t have been possible without the support of my family and friends, but most of all, my partner, Marta. It is to her that I dedicate this thesis.

TABLE OF CONTENTS

INTRODUCTION

Permanent Magnet Synchronous Machines (PMSM) have found numerous applications where higher power density and higher efficiency are key requirements, such as in traction applications in the automotive and aerospace industries or in wind energy generation. However, most of these applications have stringent requirements in terms of reliability and availability of the drive systems. Any faults will be considered unacceptable in safety critical applications like those in the aerospace sector, or cause undesirable downtime with consequent loss of revenue in e.g. wind generation systems. The most common type of fault affecting PMSM are bearing faults, which account for 40-50% of the total. The second most common faults, accounting for roughly 21% of the total, are those affecting the stator winding [1], [2]. Interturn faults at the stator winding tend to appear first due to insulation degradation and may quickly develop into major short circuit faults and catastrophic failure without effective fault detection methods which facilitates the use of remedial actions. The work presented in this thesis addresses interturn faults, from modelling to real-time detection and diagnosis.

It could be argued perhaps, given the relatively long history of design and manufacturing of electric motors, that winding reliability does not constitute a problem of modern electric powertrain systems anymore. However, it has been precisely in recent years, that machine designed has undergone a dramatic explosion of new topologies, partially thanks to the widespread application of finite element software tools. This myriad of new topologies are finding new applications, of increasing reliability demand, and the stator winding they display are being subject to new aggravating conditions. Working in conjunction with the newest power electronics technology, such as SiC, constitutes on its own a significant enough challenge to provoke a revaluation of past and present fault detection and diagnosis techniques.

Given the wide range of machine technologies, this thesis has deliberately avoided Induction Machines (IM) as subject of analysis, and has focused instead on synchronous machines, particularly those employing permanent magnets, since they constitute better candidates for new applications, such as aerospace ones, due to their higher power density.

With an aim in this type of machines and from the author's point of view, at least five research questions related to PMSM stator winding fault provide cause for the development of this thesis and the work it entails:

1) What is the degree to which the lowest severity stator winding fault, e.g. single turn fault, can be reliably detected?
2) How do transient conditions, unrelated to the fault, such as load or speed variations, affect fault detection?
3) Between advanced signal-based fault detection methods, conventionally more common, and model-based methods, which is better suited to detect the fault under those transient conditions?
4) Again, for the lowest severity of stator winding fault, is it feasible to improve on the signal-based method side by approaching a known method in a different manner?
5) Finally, and building on the previous question, is it possible to extract from this a meaningful fault indicator to work in conjunction with classification methods?

The objectives of the work being presented have been designed to address these research questions. Whilst progress and redefinition of the objectives was not always linear, chronologically speaking, the main aim and focus has always been clear. This thesis is divided into seven chapters, constituting an attempt to answer each of these research questions. First, and foremost, a literature review explores the state-of-the-art of PMSM modelling, simulation, Hardware-in-the-loop (HIL) emulation, and fault detection of stator winding faults, more specifically, interturn faults. The objective of this is to identify gaps in literature which constitute the source for the research questions summarized before. Chapter 2 provides a brief complementary chapter on analytical modelling and the effects of stator winding faults. It provides, to some extent, an answer to the first research question, outlining the relation between fault severity and the rise of harmonic components in stator currents, shown for *abc*, $\alpha\beta$ and *dq* reference frames.

Chapter 3 deals with both healthy and faulty modelling of PMSM and HIL implementation. This chapter is instrumental in facilitating the use of simulation tools as well as providing a platform for real-time testing of fault detection techniques. The work carried out in this chapter was identified as a requirement early on into the PhD and provided the first contribution of this thesis, a methodology to emulate any PMSMs under

healthy/faulty operation in real time. Chapters 4 and 5 present the major contribution of this thesis to fault detection in the form of model-based and signal-based fault detection. These two chapters deal with questions 2) to 4). These research questions are not novel, however, a definitive answer cannot be found in literature. Chapter 4 makes extensive use of HIL work presented in Chapter 3, whilst Chapter 5 explores a new approach to the Hilbert Huang transform and provides a feature extraction method used on machine learning classification work presented in Chapter 6. The new approach proposed in Chapter 5 explores the influence of stator winding faults on stator currents after the different components, known as Intrinsic Mode Functions (IMF), have been extracted by means of Empirical Mode Decomposition (EMD). Chapter 6 is clearly linked with research question 5), and provides promising results with regards to indicator use for Support Vector Machine (SVM) classification. Finally, Chapter 7 accounts for a summary and discussion of results, as well as details on the issues and challenges that could be found should the work in this thesis continue.

PUBLICATIONS

Submitted for publication

- F. Alvarez-Gonzalez, A. Griffo, B. Wang, R. Hu and J. Wang, "Model-Based Residual Analysis for the Detection of Inter-Turn Short Circuit Faults in Permanent Magnet Synchronous Machines," submitted to *IEEE Trans. Ind. Electron.*
- F. Alvarez-Gonzalez, A. Griffo, "Real-Time PMSM Stator Winding Fault Detection by Hilbert-Huang Transform Generated Instantaneous Features," submitted to *IEEE Trans. Ind. Electron.*, undergoing second review at the time of completion of this thesis.

Published

- F. Alvarez-Gonzalez, A. Griffo and B. Wang, "Permanent Magnet Synchronous Machine Stator Windings Fault Detection by Hilbert-Huang Transform," *The Journal of Engineering*, no. 17, pp. 3505-3509, 2019.
- F. Alvarez-Gonzalez, A. Griffo and B. Wang, "Permanent Magnet Synchronous Machines Inter-Turn Short Circuit Fault Detection by Means of Model-Based Residual Analysis," *IECON 2018 - 44rd Annual Conference of the IEEE Industrial Electronics Society*, Washington D.C., Oct., 2018.
- F. Alvarez-Gonzalez, A. Griffo and B. Wang, "Permanent Magnet Synchronous Machine Stator Windings Fault Detection by Hilbert-Huang Transform," In *Proc. 9th IET Conf. PEMD*, Liverpool, Apr., 2018.
- F. Alvarez-Gonzalez, A. Griffo, B. Sen, and J. Wang, "Real-time hardware-in-the-loop simulation of permanent-magnet synchronous motor drives under stator faults*," IEEE Trans. Ind. Electron*., vol. 64, no. 9, pp. 6960–6969, Mar., 2017.
- F. Alvarez-Gonzalez, A. Griffo. "High-Fidelity Modelling of Permanent Magnet Synchronous Motors for Real-Time Hardware-in-the-Loop Simulation". In *Proc. 8th IET Conf. PEMD*, Glasgow, Apr., 2016.

CHAPTER 1

LITERATURE REVIEW

1.1. Overview

The choice in recent years of Permanent Magnet Synchronous Machines (PMSMs) as favoured option for transportation electrification is generating an increasing demand for fast, reliable and efficient fault detection methods. With the already significant presence of electric and hybrid-electric vehicles, the efforts on more electric aircraft and the predicted advent of hybrid-electric and full electric aircraft propulsion, fault detection is undergoing a paradigm shift from operational cost avoidance to safety critical implications.

Among the most common faults occurring in electric machines are stator winding short circuits, representing between 21% and 37% of all faults [1], [2] mainly due to insulation degradation. These faults usually start as interturn short circuits which, if not quickly detected, may develop into catastrophic failure. To facilitate developing and testing novel fault detection methods, modelling and simulation are identified early on as necessary tools. This literature review provides an insight into modelling methods and simulation tools for the analysis of machines under stator fault conditions. Methods for real-time simulations suitable for Hardware-in-the-Loop implementations are reviewed.

An extensive review of stator winding fault detection methods is also presented, together with an overview of fault classification methods, suitable for automated detection and diagnosis of faults. Whilst other types of faults such as demagnetization or bearing fault are briefly cited, this literature review, the research questions it has generated, and the objectives designed to address them, focus on low severity stator winding faults.

The main gap in literature this review focuses on, is the degree to which developed fault detection methods can cope with constantly changing transient conditions unrelated to the fault, and whether if a model-based approach is superior to a signal-based one. However, the gap in literature this review tries to address involves not only fault detection itself, but the means to implement it and automatize it as well. This is an idea that structures this thesis. Research often ignores implementation of its findings, causing to

some extent a loss of valuable developments. For this reason, modelling and real-time Hardware-in-the-loop (HIL) implementation are key topics of this review. The main gaps identified in this area are: a high fidelity non-linear modelling approach of general application and ease of implementation, and the ability to run this model in hardware, fast enough to take advantage of the reliability of the modelling approach, and working at the top of off-the-shelf electronics development. Answers to this last gaps, shown in later chapters, are a non-linear model based on current maps obtained from finite element, and an FPGA HIL implementation.

Finally, and to complete the fault detection and diagnosis cycle, the means to automatize them are studied in search for an additional gap. This area has been studied in detail, however, the contributions of this thesis to the topic are limited since it is a vast area, more related to computer science than electrical and electronic engineering, and demanding, as such, advanced specific knowledge. The main conclusion in this aspect is that it appears that the use of machine-learning methods to the PMSM fault detection is only starting to gain visibility and hasn't yet found its niche of application.

1.2. Healthy PMSM Modelling

Simulation of electrical motor drives for accurate real-time applications requires application of high-fidelity machine modelling. The aim is to capture all involved phenomena which is most times neglected in less complex models. Examples of this are higher order harmonics in machine currents and output torque or saturation effects. In fact, simplified models will only provide relatively accurate results if the parasitic effects represent a small percentage when compared to the magnitude of the fundamental component [3].

Traditionally, modelling has been carried out by use of a conventional *abc* three phase system which accounts for the inductance in the form of a three by three matrix with self-inductances on the main diagonal and mutual inductances relating the phases with each other as may be seen in (1)-(4).

$$\left[V_{s,abc}\right] = [R_{sh}]\left[i_{s,abc}\right] + \frac{d}{dt}\left[\Psi_{s,abc}\right] \quad (1)$$

$$\left[\Psi_{s,abc}\right] = [L_{sh}]\left[i_{s,abc}\right] + \left[\Psi_{PM,abc}\right] \quad (2)$$

$$\text{Where } [R_{sh}] = \begin{bmatrix} R_s & 0 & 0 \\ 0 & R_s & 0 \\ 0 & 0 & R_s \end{bmatrix} \text{ and } [L_{sh}] = \begin{bmatrix} L & M & M \\ M & L & M \\ M & M & L \end{bmatrix} \quad (3)$$

$$\left[V_{s,abc}\right] = [R_{sh}]\left[i_{s,abc}\right] + [L_{sh}]\frac{d}{dt}\left[i_{s,abc}\right] + \frac{d}{dt}\left[\Psi_{PM,abc}\right] \quad (4)$$

Making use of Park's transformation, it is possible to rewrite (1)-(4) as direct and quadrature (*dq)*-axes expressions, into the synchronous reference frame [4], as seen in (5)-(8).

$$V_{qs} = R_q i_{qs} + \frac{d\Psi_{qs}}{dt} + \omega\psi_d \quad (5)$$

$$V_{ds} = R_d i_{ds} + \frac{d\Psi_{ds}}{dt} - \omega\psi_q \quad (6)$$

$$\Psi_{qs} = L_{qq} i_{qs} + L_{qd} i_{ds} \quad (7)$$

$$\Psi_{ds} = L_{dq} i_{qs} + L_{dd} i_{ds} \quad (8)$$

The resulting *dq*-axes model is nonetheless based on simplifying assumptions that neglect saturation and higher order spatial harmonics caused by non-sinusoidal winding distributions, slotting effect, and rotor magnet field, resulting in a difficult prediction of non-sinusoidal back electromotive force (back-EMF), the aforementioned higher order harmonics or torque ripple. An extension of the previous direct and quadrature axis model is required to approach the problem of saturation and cross-saturation. This extension usually comes in the form of a variation in the inductances dependant on current.

In order to work properly, control algorithms, often based on inductances values, require that machine modelling is done accurately, matching as close as possible the real machine. The physics-based phase variable model proposed in [5], provides a circuit description of the machine, capable of achieving the accuracy of the field model and eliminating its computational inefficiency drawback.

For physics-based models based on the traditional approach, the key aspect is the description of the inductances, which vary nonlinearly with the position of rotor and armature currents. In fact, *dq*-models often ignore the effects resulting from the geometrical structure such as slotting, rotor shape or magnet surface as well as those effects related to the nonlinear magnetization properties of iron core materials e.g.

saturation or differences on mutual inductances due to asymmetric magnetization [6]. An example of a model which identifies the parameters needed to accurately represent the behaviour of a non-linear model is presented in [7]. Furthermore, this model is able to obtain the most relevant parameters from the point of view of control (permanent magnet flux, stator resistance, *dq*-inductances) during online operation. This ability is useful since the key in developing diagnostic techniques to detect machine faults as well as to design fault tolerant control strategies, lies in the ability to model accurately the faulty machine together with the effects of the control system.

Other approaches to the development of an accurate model which accounts for magnetic saturation, spatial harmonics and iron losses are based on pre-calculated flux or inductances by means of Finite Element (FE) analysis which are represented in the model by large Look-Up-Tables (LUTs). Given that FE analysis is done prior to the implementation of the model, the only characteristic slowing down the simulation is the actual processing of the tables themselves. Some examples of these are provided in [5]-[8]. The method proposed in [8] was later extended to account for temperature variation as well [9].

1.3. Faulty PMSM Modelling

The ability to model accurately the machine operating under fault is crucial when developing diagnostic techniques, as it is when designing fault tolerant control strategies [10]. Several models have been presented on this topic applied to fault modelling of PMSM [10]–[25] . Fault modelling is usually performed by dividing the affected phase into healthy and fault parts. A graphical example of the model of a faulty machine is seen in Fig. 1.1, where a resistor R_f is used to model the short-circuit between one or more turns in a phase windings.

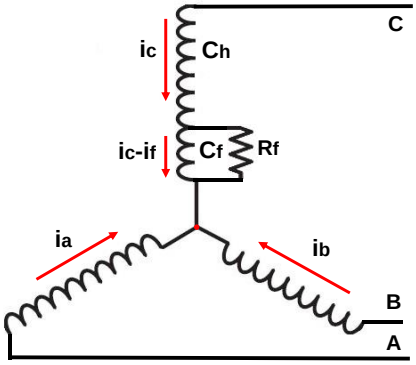

Fig. 1.1. Electrical model of a faulty 3-phase machine.

A relatively extensive model of PMSM accounting for non linearities due to spatial harmonics was presented in [11]. It is based on the traditional voltage equations as shown in (9), (10), depending on resistance and inductance matrices as previously shown in (3). However, an extra term is included to account for the fault as seen in (11), (12). The entire model will be discussed in detail in Chapter 2 and employed to demonstrate the effects of an interturn short circuit.

$$\left[V_{sf\,,abc}\right] = \left[R_{sf}\right]\left[i_{sf\,,abc}\right] + \left[L_{sf}\right]\frac{d}{dt}\left[i_{sf\,,abc}\right] + \frac{d}{dt}\left[\Psi_{PMf\,,abc}\right] \tag{9}$$

Where $\left[V_{sf\,,abc}\right] = [V_a\ V_b\ V_c\ 0]^t$, $\left[i_{sf\,,abc}\right] = \left[i_a\ i_b\ i_c\ i_f\right]^t$ (10)

$$\left[R_{sf}\right] = \begin{bmatrix} R_s & 0 & 0 & -\mu R_s \\ 0 & R_s & 0 & 0 \\ 0 & 0 & R_s & 0 \\ \mu R_s & 0 & 0 & -\mu R_s - R_f \end{bmatrix} \tag{11}$$

$$\left[L_{sf}\right] = \begin{bmatrix} L & M & M & -\mu L \\ M & L & M & -\mu M \\ M & M & L & -\mu M \\ \mu L & \mu M & \mu M & -\mu^2 L \end{bmatrix} \tag{12}$$

The model can then be converted to the direct and quadrature (*dq*) reference frame to simplify simulation [12]. In [10] a dynamic mesh reluctance model (DMRM) shown in Fig. 1.2 is employed to incorporate saturation and slotting effects. The use of a DMRM is potentially very accurate but requires a special discretisation of the machine and therefore detailed knowledge of machine topology which makes it unsuitable for general purpose modelling

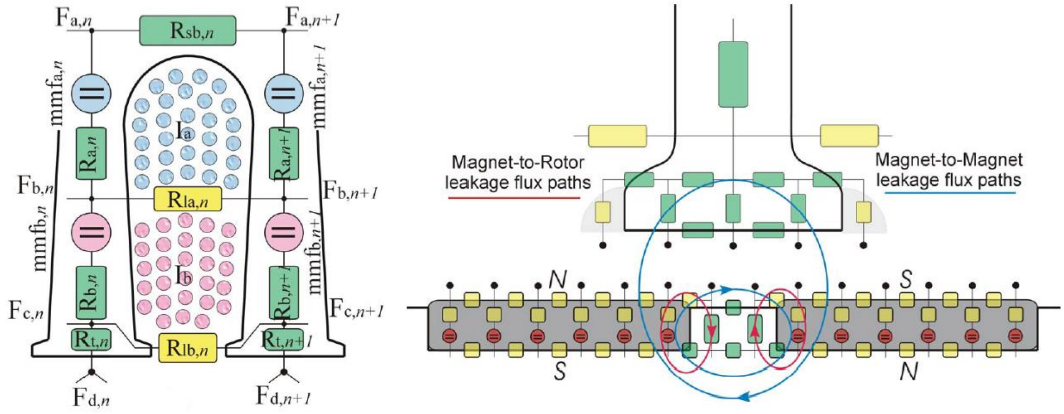

Fig. 1.2. Dynamic Mesh Reluctance Model from literature [10].

Similarly to what it was shown for healthy modelling in [7], a PMSM under inter-turn fault parameter estimation model is presented in [21] for different winding distributions based on energy calculation. A model based on the use of permeance network (PN) shown in Fig. 1.3, similar to the aforementioned DMRM, together with parameter identification, was presented in [22]. The PN model is employed to obtain four-dimensional flux/inductance lookup tables needed to formulate the transient model. However, experimental validation was not carried out and further derivation of a PN model is often relatively tedious and compromises accuracy, particularly for complex rotor geometries [18]. Both models focus on obtaining relatively accurate representations of the inductance, considering in the second case even leakage inductances, as well as self, and cross saturations.

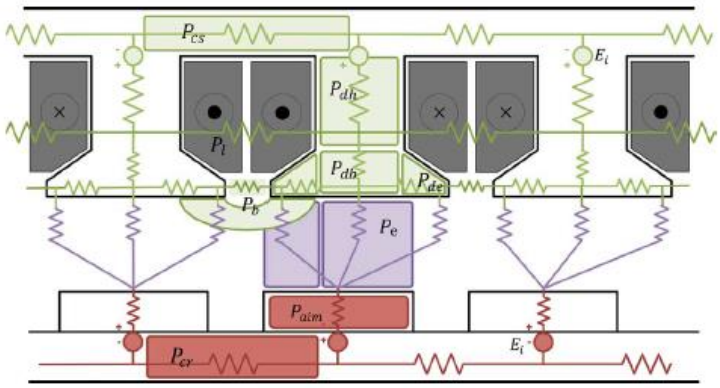

Fig. 1.3. Global Permeance Network of a PMSM from literature [22].

Models which study in detail the relation between series and parallel winding connections during inter-turn shorts have also been proposed [24], where the effect of the faulted turns is analysed with respect to, not only the other phases, but to the remaining

turns of the faulted phase as well. The model is validated through finite-element simulation as is common practice.

An extensive analytical model approach is presented in [15], [17] to extract key machine parameters such as inductances. Common assumptions are taken such as infinite permeability of laminations, coil turns uniformly distributed along slot and slotting effect neglected, which in turn compromise the ability of the model to account for non-linearity as shown by a difference in accuracy of around 7% when validating against FEA inductances and fault current calculations. In [16] however, the same author couples the analytical model with *dq*-axes flux linkage maps obtained from FE simulations. The semi-analytical model provides a closer approach to the non-linear behaviour accounting as well for saturation in IPM motors under stator turn fault been able to detect the asymmetry in flux linkage. The model has been further improved by the same author in [18] achieving a great accuracy in validation against FEA and experimental study. This last model is based on the modelling approach presented in [8], but includes a fourth term to account for the fault, resulting in *dqf* in synchronous reference frame, been *f* the faulted part of the phase where the fault appears. Furthermore, the model presented in [18] takes into account rotor skewing. Extensive details on this modelling approach, will be presented in Chapter 3.

An analytical model of a fault tolerant machine is presented in [17]. Fault tolerance is achieved by dividing the stator winding in five independent phases allowing to shut down a single phase affected by a fault and continue operation. This model is employed for residual-based fault detection. It is shown this fault detection approach is resilient to load disturbances and speed variations for traction applications, which partially motivated its adoption, as shown in Chapter 4.

A. Finite Element Analysis based Fault Modelling

FE analysis is capable of considering physical and geometrical details when modelling different types of faults. As illustrated in Fig. 1.4 and Fig. 1.5, FE modelling can also be coupled with circuit elements in order to model different connections between windings e.g. under short-circuit faults. FEA is usually the most accurate modelling tools for electrical machines as it takes into account the non-linearity of the system, contrary to what most analytical systems consider. Therefore, the use of finite-element applied to the task of fault detection and diagnosis has been proposed and employed to some extent in

the last decade for PMSMs [6], [13], [26], [27] and for IM [28]–[31]. According to O.A. Mohammed et al., FE based models can be classified into five major categories; full FE models [27], data-based models [6], FE-based phase variable models [13], field reconstruction method (FRM) and reluctance network-based models [10]. Usually, FE in a coupled field-circuit analysis domain, shown in Fig. 1.4, Fig. 1.5, offers the most accurate modelling methodology but remains computationally heavy for real-time applications.

In some cases FE analysis is combined with a conventional or phase model, or a signal-based analysis method [8], [9], [13]. It is also possible to apply a pure FE analysis as seen in [26], [27], where it is employed to study the conditions developed during stator faults in detail. After measuring or estimating a fault signal, the two major decision-making techniques include threshold-based techniques and knowledge-based techniques. Measured fault signals may be employed in these methods directly or indirectly after signal processing or feature extraction. Knowledge-based systems are usually more accurate while threshold-based systems are computationally more desirable [25], [32].

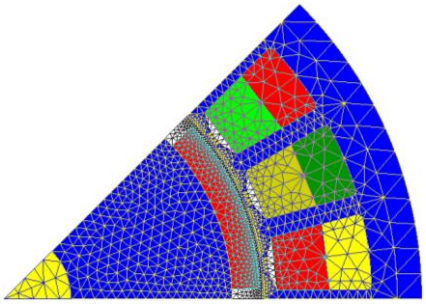

Fig. 1.4. FE machine periodicity representation of a PMSM.

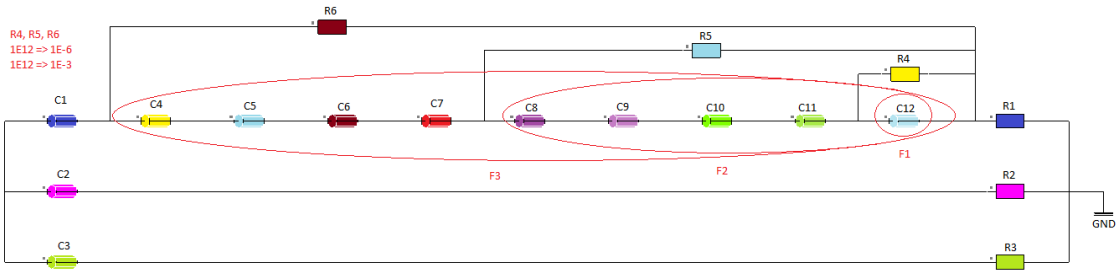

Fig. 1.5. FE circuit representation allowing to simulate different fault severity.

In [27], a time-stepping 2-D FE model is performed for surface PMSM inter-turn fault caused by insulation degradation. Finite element analysis is used to obtain machine parameters such as inductances and back-EMF, where the effect of the turn fault is

presented with relation to the number of faulted turns and its location. Negative current sequence is used as indicator for fault diagnosis purposes.

It is often accepted that FE is time consuming and hence, not suitable for extensive evaluation of different fault scenarios associated with the variation of the number of partially short-circuited turns and their location in the slot [33]. However, as shown in [13], inductance and back-EMF profiles under one short circuit fault can be derived from the corresponding profiles under any other short circuit condition, in other words, the FE computation for parameter determination needs to be performed for one fault case only.

1.4. Real-Time Hardware-in-the-Loop Simulation

Hardware-in-the-Loop (HIL) methodologies whereby a piece of hardware is substituted by an accurate real-time emulation, have gained widespread acceptance as a tool for rapid testing and development of data acquisition systems, electronics and control strategies in a large number of industrial applications including automotive, energy or aerospace sectors where safety implications, cost and complexity of full scale prototyping might be significant. HIL methods can be used as tools to develop control strategies for components and systems in all operating conditions including extreme conditions such as those resulting from faults in a safe, non-destructive environment. Due to the increasing use of PMSM drives in safety critical applications such as automotive traction and aerospace actuation, HIL methods capable of accurately emulating motor drives in all operating modes including faulty conditions, can provide drive systems integrators with a useful and relatively inexpensive tool for the development and testing of fault-detection, diagnostic techniques as well as post-fault control actions.

Although many motor drive emulators for HIL testing have recently been proposed in academic research and by commercial vendors, so far no validated method capable of accurately emulating in real-time the dynamics of a machine under faulty conditions has been demonstrated. The main contribution of this thesis to this topic, developed in Chapter 3, is demonstrating a novel real-time emulation of PMSM drives suitable for HIL testing of both healthy and faulty conditions considering in particular inter-turn stator short-circuit faults which have been identified as a major cause of electrical failure in a machine [34]. Short-circuit faults typically starts with inter-turn faults [35] which can eventually result in demagnetization or further catastrophic failure due to large circulating currents [25].

The degree of fidelity by which HIL systems emulate the physical behaviour of the device under testing in realistic operating conditions, depends on the availability of an accurate representation of the physical system under investigation. Although detailed models such as those based on time-domain co-simulation of Finite Elements (FE) provide a high degree of fidelity, their computational complexity prevents their applicability to the real-time computation required for HIL simulation. Real-time simulation of electric motor drives is particularly challenging due to the fast nature of the dynamics involved. Commutation of PWM signals at tens of kHz requires sampling rates in the order of several MHz in order to obtain reasonable accuracy. The use of digital signal processors (DSP) as hardware platform for real-time simulation was proposed in the past but Field Programmable Gate Arrays (FPGAs) are emerging as the platform of choice for complex real-time simulations due to their ability to process data in parallel allowing for sampling rates and execution up to the MHz range.

HIL emulation of electric machines and drives has been proposed for Induction Motors (IM) [36]–[41] and PMSM [42], [43], [52], [44]–[51]. Due to the requirements for computational efficiency, most of the published methods for real-time emulation of electric machines rely on analytical models with various degrees of simplifications. A HIL model for IM based on permeance network (PN) is presented in [36]. A similar approach based on non-linear Magnetic Equivalent Circuit (MEC) is employed to model IM in [38]. A unified framework for FPGA-based emulation of electrical machines based on state-space representation with constant inductances is presented in [41]. A real-time model based on the analytical solution of field equations to account for space harmonics in the air-gap flux density distribution of PMSM has been developed in [43] under the assumption of linear superposition.

While analytical models based on PN, MEC or analytical field solutions can achieve the computational efficiency required for real-time implementation, they might lack generality, requiring significant effort to adapt models to different topologies. Furthermore, analytical models are often based on simplifying assumptions of linearity/superposition which might not be generally applicable. Models based on pre-calculated FE solutions and stored in look-up tables for real-time implementation have been proposed as an easier to implement and more general solution to take into account non-linearities in machine behaviour [36], [44], [46], [47], [51]. A real-time PMSM model taking into account angular variation of phase inductances due to space harmonics

and slotting effects has been proposed [44]. However, the use of constant inductance-based model lacks the ability to account for non-linearities due to saturation of the magnetic circuit. Even if current dependent inductances are used, the separation of flux linkages in armature reaction and permanent magnet induced fluxes is only valid under linear conditions. Similar models based on pre-tabulated inductances and flux maps accounting for saturation and spatial harmonics have been proposed in [45]–[47]. However, these require proprietary tools and are based on variable inductances which pose problems in real-time simulation in voltage-driven models as the nonlinear relation between flux linkages and currents may not be easily inverted in real-time calculations. The use of differential inductances and pre-calculated inversion of current-flux relationship is proposed in [52].

The use of an inductance-based model lacks the ability to account for non-linearity due to saturation of the magnetic circuit. Even if current dependent inductances are used, the separation of flux linkages in armature reaction and permanent magnet induced fluxes is only valid under linear conditions. By mean of a visible example, a simple block diagram for HIL emulation of electric motors is seen in Fig. 1.6.

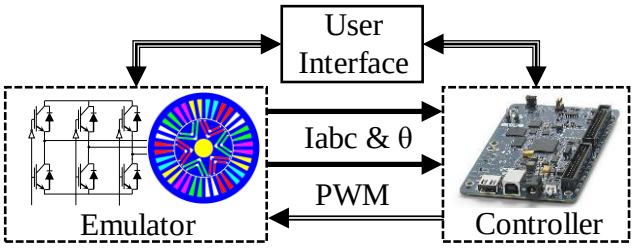

Fig. 1.6. Simplified Hardware-in-the-Loop block diagram.

Although many of the solutions proposed in literature successfully address the issues of accuracy and computational efficiency for real-time emulation of a drive system in healthy conditions, no general method capable of accurately emulating the dynamics of a machine under faulty conditions has been presented. Models of stator winding inter-turn short-circuits for PMSM have been proposed based on a number of analytical modelling techniques including the use of Dynamic Mesh Reluctances Model (DMRM) [10], PN [22] and constant inductances [11], [13]. Besides the relative complexity in the derivation of the model and the inevitable simplifying assumptions required in most analytical models, the difficulty in accounting for the angular variation of flux linkages due to high-order harmonics in the back-EMF or slotting effects in these models has led to the

development of machine models based on the extraction of flux linkage maps from FE magnetostatic computations as function of stator currents and rotor position [8], [51].

1.5. Fault Detection Methods

Machine fault detection has evolved significantly since the time where only simple techniques such as overcurrent or overvoltage detection where employed. Traditionally, once the detection was successfully performed, it was necessary to stop machine operation to carry out needed maintenance and repairs. Nowadays, with the well-established, broad application of electric motors and generators it is not always possible to shut down the machine, especially for transport applications. This demands a continuous improvement on fault-detection techniques to work together with remedial actions. To perform an effective fault detection, speed is key, allowing remedial actions to be taken before catastrophic damage to the machine [53]. This process is crucial for interturn faults, given these quickly develop into major faults, making any fault compensation impossible thereafter.

A number of techniques for fault-detection in electrical machines have been proposed. These can be classified in model-based and signal-based detection techniques. Sometimes a third class is identified in the form of data-based methods as shown in Fig. 1.7. An example of model-based fault detection is the use of residual indicator comparison where the outputs of a model running in real-time are compared with the measured outputs of the real system when same inputs are fed to both the emulator and the real system as shown in Fig. 1.8.

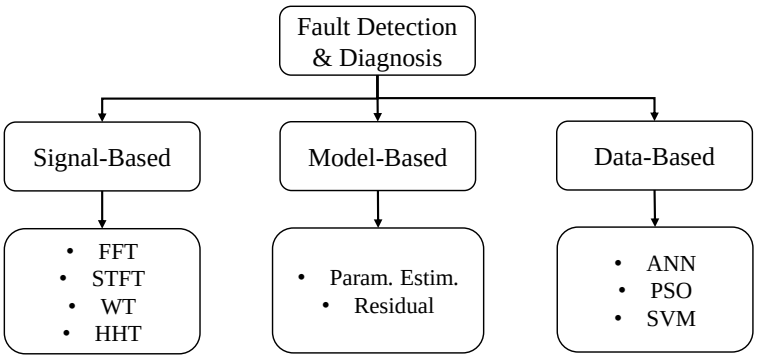

Fig. 1.7. Diagram summarising fault detection methods.

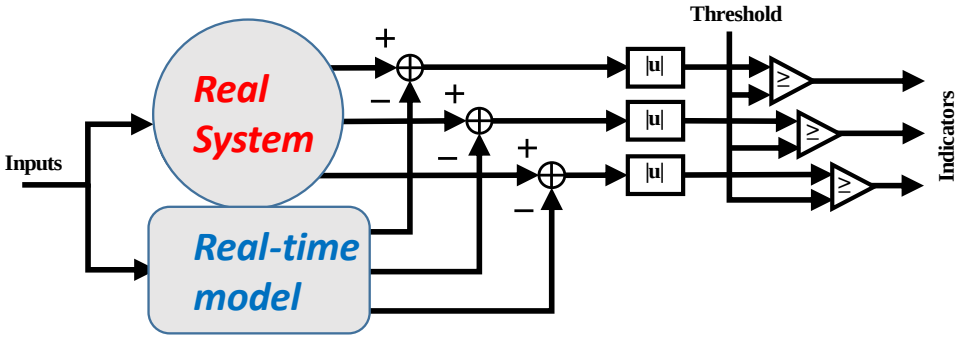

Fig. 1.8. Simplified model-based residual indicator comparison.

Signal-based techniques usually employ motor current signature analysis (MCSA) which is a class of techniques that analyse directly the machine outputs employing a range of filtering, transformations and other signal processing tools to identify the appearance of a fault. The division between signal-based and model-based methods might be in some cases not clear-cut. While some cases are easily classified as model-based, signal/data-based or even hybrid-based as [23], some others remain uncertain and are generally considered as data-based methods, like the use of artificial intelligence (AI) or more specifically machine learning, such as Artificial Neural Networks (ANN), Support Vector Machines (SVM) or Particle Swarm Optimization (PSO), to identify and diagnose faults.

A. Signal-based Fault Detection

It is well known that interturn short circuit faults in PMSMs may generate an increase of the third harmonic in the stator currents [10], [11], [54], [55]. This third harmonic is generated by the effect of the fault current on the main air-gap flux linkage and the interaction of the PM flux with the asymmetry created by such a fault. However, under motoring conditions, the amplitude of any additional harmonics in stator currents caused by a fault may be significantly reduced by the compensating action of the current controller which perceives these effects as a perturbation [56], making fault detection based on the estimation of these harmonics harder. The third harmonic depends greatly on machine and permanent magnet geometry [11], [57] and plays a crucial role in fault detection [58], [59]. Additional details and demonstration of the origin of increased harmonics due to fault conditions are provided in Chapter 2.

Some examples of the application of this method include techniques studying sequence components of stator currents in IM [54], [60] and permanent magnet motors [55], [58], [60]–[62], the use of fast Fourier transform (FFT) [63], Fourier series [64],

current envelopes [65] or different types of wavelet transforms [59], [66]–[68]. In [63], the authors show the use of FFT for fault diagnosis in an inverter fed induction motor applied to the task of broken rotor bars detection in cage induction motors. In [64] Fourier series has been used to monitor the second order harmonic component of the q-axis current in a PMSM under interturn fault. In [65], an envelope of the stator current has been extracted and used for fault diagnosis in an induction machine. The method is based on the analysis of the three-phase stator current envelopes of IMs using reconstructed phase space transforms. The envelope was obtained by constructing a smooth signal using sampled positive peaks of the stator current. Fault signature from the envelope was extracted by means of Gaussian Mixture Statistical Models and fed later to a Bayesian Statistical classifier for purposes of diagnosis.

Traditionally, Motor Current Signature Analysis (MCSA) methods were employed in the past to detect this type of fault, mostly based on frequency analysis techniques such as Fast Fourier transform (FFT) [25], [63], [69], [70]. The use of FFT is however generally constrained to stationary conditions [25]. Speed and load transient conditions, common in many PMSM drives, e.g. in traction applications, often result in deceptive fault detection causing false alarms which may result in unnecessary interruption, as shown by the moving window FFT example seen in Fig. 1.9. In Fig. 1.9 a) the magnitude of an indicator (bottom part) is used to detect a stator interturn short-circuit fault by analysis of one of the phase currents (top part). However, the same indicator level easily falls into false alarm under speed ramp, as shown in Fig. 1.9 b). This is due to the inability of FFT to dynamically adapt without frequency tracking feedback. Short-time Fourier transform (STFT) has been proposed as a means to avoid the limitations due to transient conditions caused by non-stationary signals, but no general method exists for the selection of windowing functions and size [70], [71]. Wavelet transform (WT) has been proposed [66], [67], [71]–[73] as well, for time-frequency analysis, allowing for the localization of a fault in both frequency and time. Even though WTs behave well for non-stationary conditions, they require previous knowledge of the signal and a suitable selection of a mother wavelet. Furthermore, the computational complexity of WT analysis makes its use challenging in real-time conditions. A less computationally intensive and more flexible method with similar capabilities is the Hilbert-Huang transform (HHT).

HHT was first proposed by Huang et al. in the late 90's [74]. It is a signal analysis method which makes use of the empirical mode decomposition (EMD) to decompose the

original signal into components called intrinsic mode functions (IMF), as shown in Fig. 1.10. IMFs have on itself physical meaning and represent the simplest oscillatory modes contained by the original signal. The Hilbert transform and Hilbert spectral analysis (HSA) is subsequently applied to the IMFs to obtain instantaneous frequency (IF) and instantaneous magnitude (IM) data. Its application and results are comparable to that of wavelet transforms, however, HHT is based on an empirical and adaptive algorithm, therefore no prior knowledge of the signal is required. Bearing fault detection has already been studied through the use of HHT [75]–[78] by analysing vibrations signals. Furthermore, HHT has been employed for demagnetization fault detection [79], [80], and detection of other mechanical faults by analysing stator currents [81].

Combination of HHT with machine learning techniques such as a support vector machine (SVM) has also been presented [82], demonstrating the validity of this tool for AI feature extraction. Its use for incipient stator insulation fault detection [83], is of special interest given that short circuits in stator windings are second only to bearing faults. The work presented in [83] relies however purely on cosimulation and lacks experimental validation.

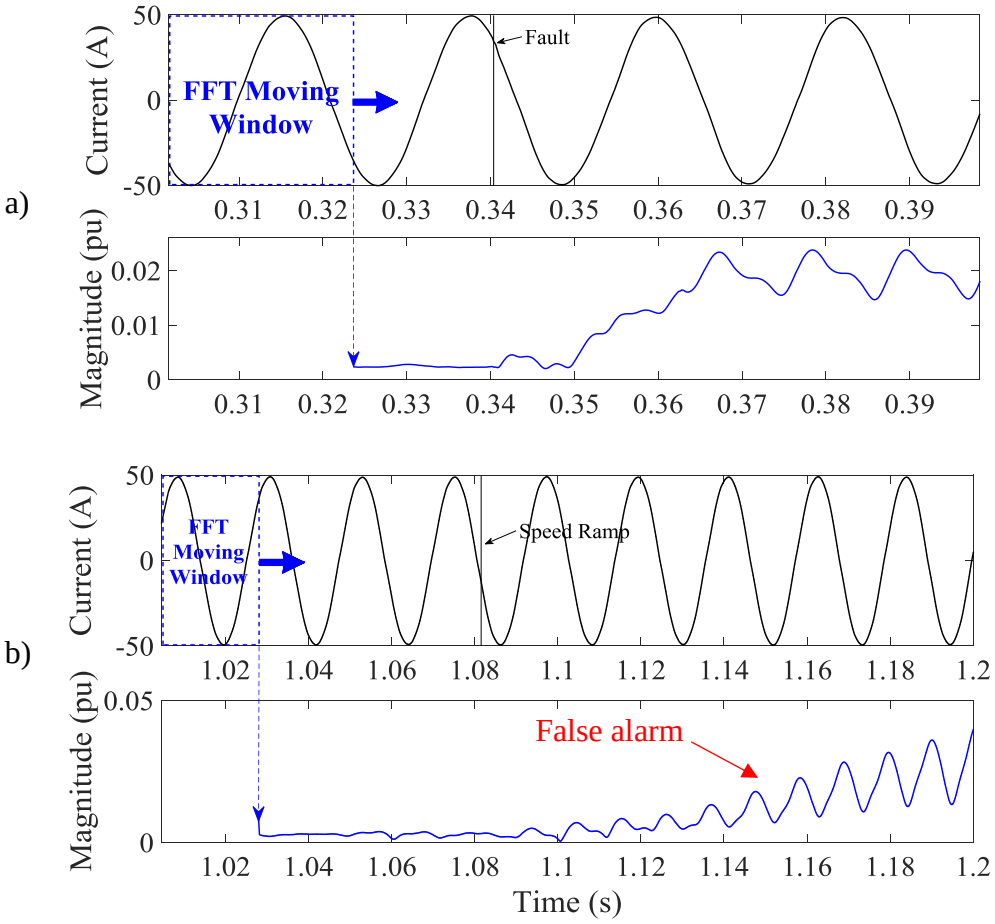

Fig. 1.9. FFT moving window third harmonic under fault a), and healthy transient conditions b).

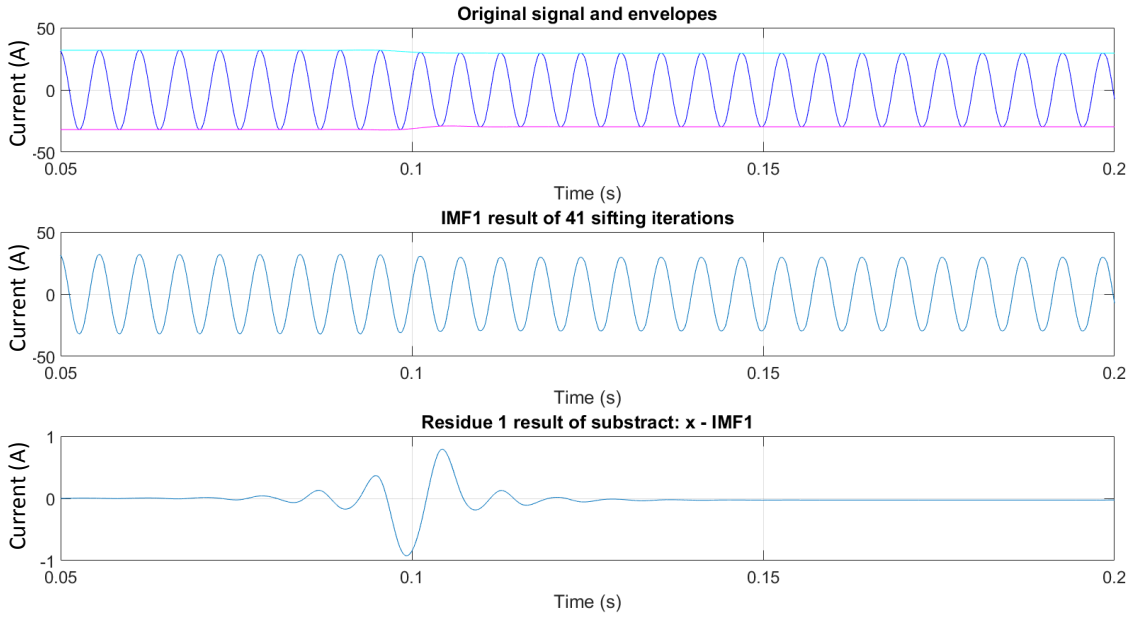

Fig. 1.10. Example of EMD of phase current under interturn stator fault.

The main aim and novelty of the signal-based fault detection work presented in Chapter 5 of this thesis, is to further test the ability of the HHT to identify an interturn

stator winding fault, to explore its limitations, and to propose ways to overcome them. The possibility for a real-time online implementation of the HHT will be investigated, something that has not been presented in previous literature due in part to the relative computational complexity of the algorithm. The method and results shown in Chapter 5 were partially presented in [84].

B. Model-based Fault Detection

In order to overcome the limitations of signal-based analysis, model-based interturn fault detection has been proposed [20], [23], [85]–[91]. Model-based fault diagnosis systems could overcome the limitations of spectrum-based fault diagnosis systems in variable-speed drives. An example is shown in MCSA for PMSM when stator current harmonic components due to interturn faults are superimposed with those that appear in a healthy one decreasing the sensibility of this method in practice [62]. In model-based fault systems inputs to the machine are fed to the model resulting in signals from both the real machine and the model being acquired simultaneously and sent to the fault decision-making process [89].

Most of these methods are based on computing a residual signal from comparison between measured and model output reference features. Any deviation found would in principle indicate the presence of a fault. Since the back electromotive force (back-EMF) is directly related to the fault current magnitude, several models have been presented for fault detection employing an estimation of this quantity [20], [29], [32], [89], [90]. A current residual analysis based on back-EMF and inductance-based modelling is presented in [20]. However, the use of an inductance-based model often lacks the ability to fully account for non-linearities due to saturation of the magnetic circuit.

In [29] the fault detection is carried out based on the difference between the estimated back-EMF and a reference back-EMF. A PMSM is studied both numerically and experimentally under different inter-turn fault and operational conditions. The numerical modelling is accomplished by a FE-based model coupled with a thermal network deliberately affected by inter-turn faults.

In [89] back-EMF estimation is combined with a finite element (FE) model coupled with a thermal network. The method is based on voltage residuals, which are usually considered to behave worse than current ones due to increased noise sensitivity. Nonetheless, the use of FE modelling provides an accurate description of the machine

under study and when combined with back-EMF estimation is shown to provide good results. More recently, a PMSM model-based interturn fault diagnosis has been proposed [86], based on a residual computed through comparison between measured and state observer generated currents. The model builds on several aspects from previous literature, nevertheless, it assumes a linear relationship between flux linkages and currents, i.e. constant inductances, and parameter variations need to be compensated. A motor current signature analysis (MCSA) of current residual was presented in [87]. The use of residual might not be sufficient on its own, however it can amplify the frequency components caused by the fault [87]. Since the same inputs are used both for the physical machine and the model, the fault indicator is in principle insensitive to the effects of transient conditions such as speed or load variations that could otherwise cause false alarms. Aiming at fault detection even at low speeds, a hybrid model-based/data-based method has also been proposed [23]. The benefits of a model-based current residual are discussed in Chapter 4.

Some techniques have been proposed to not only detect the fault but also to diagnose its severity, demonstrating how it affects described indicators. An example of this may be seen in [91] where a mathematical model of a PMSM with inter-turn fault is established. It bases its detection and diagnosis on the study of the zero-sequence voltage component and zero-sequence current component. Fault indicators are defined to remove the influence of the variation of the rotor speed and an effective frequency tracking algorithm is also presented.

C. Data-based Fault Detection (AI)

In the last decade, the relatively fast development of computer, sensor, and signal processing technologies, together with AI techniques, has made it possible to implement condition monitoring, fault diagnosis and even prognosis. Contrary to what is seen for fault detection methods, diagnosis provides further information on the severity or the type of fault, subject to limitations of the method employed. The last step in the study of faults is prognosis, which allows estimating when the fault will happen based on a particular model or tracking of specific characteristics such as insulation degradation monitoring based on stator leakage currents.

The main manner in which data-based fault detection and diagnosis is achieved is through classification. Artificial neural networks have been especially proposed as a valid

alternative to traditional linear techniques in parameter identification of complex systems. An ANN is a model inspired by biological neural networks such as the brain which are used to estimate or approximate functions that can depend on a large number of inputs and are generally unknown. They are divided into several layers, classified as input, hidden or output, of interconnected simple node elements or neurons as seen in Fig. 1.11. The connections have numeric weights that can be adjusted based one experience, giving the system the capability of "learning".

System identification involves the experimental determination of the dynamics of a system from an examination of the input/output relationships. For the application of these techniques a model structure is usually first selected, then, parameters are identified, and finally, the model is simulated for verification and validation against the real system.

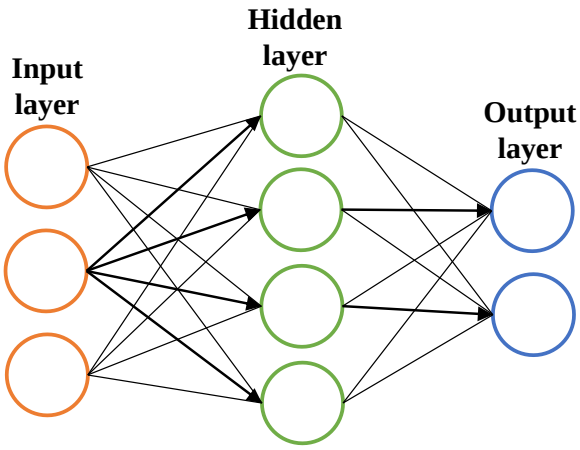

Fig. 1.11. Example neural network block diagram.

Other techniques include particle swarm optimization (PSO) which is an optimization technique that employs the behaviour of animal groups such as flocking birds or swarming locusts to stochastically approach the global optimum of a function. Proposed in the mid 90's, this technique has found application in several areas due to its ease of implementation and its reliability to avoid local optimum variables different than the global. Since it was first introduced, it has undergone several modifications aimed at obtaining a good balance between the rate of execution and the reliability of the solution so that the algorithm is able to avoid local optimal locations while rapidly search for the global best location [92].

The increasing need for reliability, availability and survivability of PMSM has led to the implementation of AI based fault detection to this field [92]–[97]. In [92] an ANN is

presented containing a multilayer recurrent structure with global feedback and trained using PSO for parameter optimization. PSO is employed itself for fault diagnosis as presented in [94], where diagnosis is achieved through parameter identification taking advantage of the ability to avoid local solutions. A generalized lumped parameter is also employed to simulate machine performance, and two parameters are used to identify the location and magnitude of the fault. In [95] a neural network based method is employed for detecting unbalanced voltage faults in three-phase traction motors. Contrary to [92] where the NN is trained by using PSO, this model separates the problem into two parts employing two different NN, one which is trained for classifying the load conditions and a second one for approximating the unbalanced voltage fault percentage. Even though the use of two NNs greatly increases computation time needed, it is still reasonable to carry out this approach given that the most common problem comes from the difficulty of separating the change registered when a fault occurs and the one happening due to a change in the load conditions. NNs present great flexibility in coupling with other analysis methods, such as negative sequence analysis, as presented in [93].

Through parameter identification and feature extraction, classification problems, like the ones solved by NNs or PSO, can often be simplified to linear classification tasks. Linear classification methods have already been applied to fault detection and diagnosis of electric machines [98]–[101]. Linear discriminants can be applied directly for fault classification [98], or for dimensionality reduction and feature extraction of bearing fault [99] and multifault cases [100]. They have been applied as well to induction generator wind turbines for automatic detection of rotor electrical asymmetry fault [101]. While linear classification is often enough to discriminate between healthy and faulty steady state conditions, for cases involving transient conditions, such as for real-time fault classification, a nonlinear discrimination method such as a Support Vector Machine (SVM) might be required [102].

A SVM is an statistical learning algorithm developed to find the optimal solution for a classification problem [103]. On its most simple form (one-class machine) it allows detection of a fault in an electric drive by analysing the deviation from the healthy training data without the need for faulty data training. A slightly more complex system is presented in a two-class SVM which allows accurately separation of data into healthy or faulty classes given previous healthy and faulty training [104]. This is achieved by a transformation of the original data into a feature space where it is possible to compute an

optimal discriminant solution in the form of a hyperplane, as shown in Fig. 1.12. Additional details on SVM are provided in Chapter 6.

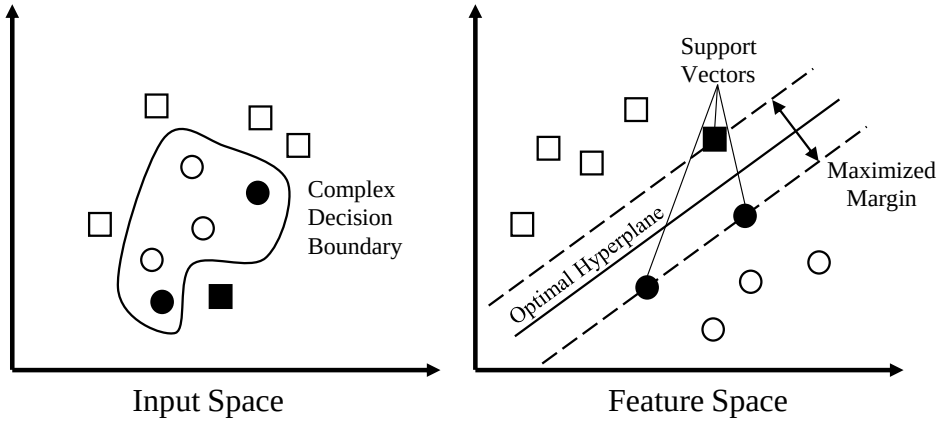

Fig. 1.12. SVM classification diagram.

There is virtually no limit for the number of classes a SVM may have, allowing the algorithm to detect all type of faults, severity and location if enough training data is provided and correct features are selected. A multi-class machine could be handled like a two-class machine in which each of the classes is analysed in opposition to all remaining, which act as one, in a technique known as "one against all" [105]. The only limitation comes thus from the faulty data availability which is difficult to obtain in reality.

A SVM allows to employ successfully a combination of numerous indicators which are selected as features, comparable to what is achieved through sensor fusion. Examples of this are the use of signal analysis methods such as Wavelet Transform (WT), features extracted from Fast Fourier Transform (FFT) other than simply the harmonic amplitude, current analysis features such as rms value, statistical parameters such as median, skewness or kurtosis and others.

Time analysis of three phase currents was employed in [105], [106]. A relatively complex 3D study based on a modified three-phase current analysis is employed in [105] using as features a set of eigenvalues and angles between the eigenvectors of the covariance matrix and the vectors of the 3D landmark of the Cartesian coordinate system in which the analysis is based. The system itself is based on setting a coordinate on a 3D ellipse for each a, b, c current sample. On the other hand, the work presented on [105] employs a simpler approach to construct the feature vector based on the analysis of *dq*-axes currents after Park's vector transformation.

Frequency analysis by means of FFT was shown in [58], [107]. An analysis by means of FFT is performed in [107] based on the study of harmonic curve area, harmonic crest angle and harmonic amplitude extracted from power spectral density. It is shown that a combination of the first two has a better behaviour to detect faults than the common method of monitoring harmonic amplitude. The qualities of the SVM prove crucial to combine several features. The SVM is employed for fault diagnosis in [58] where it is shown the ability to describe stator short-circuit fault severity by means of spectral analysis. In this case feature selection is performed by means of expert models such as autoregressive model or principal-component analysis and then k-nearest neighbour is used as a classifier to demonstrate the capability of these indices for fault estimation.

Time-frequency analysis was used in [104] and [8]-[11]. Different variations of Wavelet transforms were employed in [104], [108] and [109]. Wavelet Packet Transform (WPT) was employed in [104] to obtain features for one and two-class SVMs. A Continuous Wavelet Transform (CWT) is employed in [108] to perform current signal processing after performing Park's and Concordia transformations. Currents I_α and I_β may be employed for fault detection by measuring the pattern deviation from its otherwise circular behaviour under healthy motor conditions. Discrete Wavelet Transform (DWT) and Discrete Cosine Transform (DCT) are employed in [109] to obtain the higher order statistical parameters mentioned previously (skewness and kurtosis).

Park's Vector Modulus (PVM) described as

$$PVM = \sqrt{I_d^2 + I_q^2}$$

is employed after averaging for Time Domain analysis in [110] as a fault indicator making use of the DC characteristic of *dq*-axes currents. Together with statistical features extracted from three phase currents such as skewness, kurtosis, median, standard deviation or mode value. Frequency analysis is also performed in [110] by means of FFT, focusing in peak values, frequency values, signal power and combinations of different values. Finally, a combination of 25 time domain and frequency domain statistical features resulting from phase current analysis are employed in [111] .

In this thesis, contributions to this field are made in the form of Fisher's Linear Discriminant and a two class SVM, as shown in Chapter 6, employing features extracted through HHT, presented in Chapter 5.

1.6. Summary

This chapter has presented a comprehensive literature review of the state of the art of machine modelling for offline and real-time HIL applications, as well as fault detection and diagnosis techniques, with emphasis on stator winding interturn faults. Modeling has been presented for both healthy and faulty operation. The main conclusion driven from this review is that, while modelling has been subject to significant work, there is still some space for improvement. With regards to real-time implementation of these models, the gap for innovation is vast, and this thesis has made a significant effort to contribute to the field, particularly working on real-time HIL modelling under faulty conditions.

Fault detection has been described in depth and divided into signal, model and data based methods. Contributions made in later chapters to each topic have been briefly commented as well. Whilst there are over a hundred references in this review, it has been found that there is still ample room for improvement, particularly regarding accurate fault detection under transient conditions, such as a constant load and speed variations.

CHAPTER 2

ANALYSIS OF WINDING FAULT EFFECTS ON CURRENT HARMONICS

2.1. Overview

This chapter presents an analytical model for the description of PMSMs under inter-turn faults. The model is adapted from [112] and accounts for both healthy and faulty operation, and includes spatial harmonics. The aim here is to use the model to demonstrate the origin of additional harmonic components in PMSM phase currents under stator winding faults. This chapter is intended to provide context regarding the analysed type of fault, low severity stator-winding short circuit fault.

The theory is supported by simulations and experimental validations. In order to simplify the analysis, only the stator of a machine is employed in this chapter.

An additional outcome of this experimental analysis, is to quantify what fault level is detectable using stator currents analysis methods. It is reasonable to assume that degradation due to thermal effects, gradually weakens the interturn insulation. This results in a decrease of insulation resistance. The experiments presented here use an external variable resistor to emulate different levels of insulation degradation between two turns of the machine windings. It is demonstrated that fault detection through current signature analysis is only realistically feasible when the fault is incipient, i.e. when the interturn resistance is already significantly weakened.

2.2. Modelling

The analytical model presented here is adapted from [112] and describes the equivalent circuit shown in Fig. 2.1 modelled as a set of four mutually-coupled RL circuits. One of the three-phase windings has a faulty component made of N_f turns. $\mu = \frac{N_f}{N}$ indicates the fraction of faulted turns relative to the total number of turns per phase N.

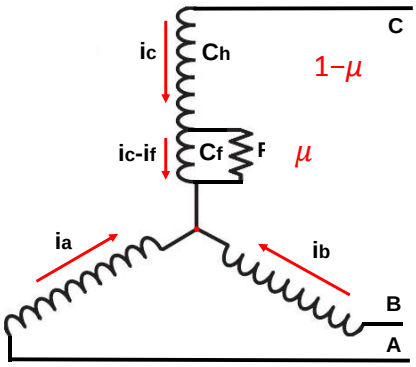

Fig. 2.1. Three-phase windings diagram including faulted turns.

The four coils are modelled in the *abc* reference frame, as

$$[V_{s,abc}] = [R_{sh}][i_{s,abc}] + \frac{d}{dt}[\Psi_{s,abc}] \tag{13}$$

$$[\Psi_{s,abc}] = [L_{sh}][i_{s,abc}] + [\Psi_{PM,abc}] \tag{14}$$

$$[V_{s,abc}] = [R_{sh}][i_{s,abc}] + [L_{sh}\frac{d}{dt}[i_{s,abc}] + \frac{d}{dt}[\Psi_{PM,abc}] \tag{15}$$

$$[V_{sf,abc}] = [R_{sf}][i_{sf,abc}] + [L_{sf}]\frac{d}{dt}[i_{sf,abc}] + \frac{d}{dt}[\Psi_{PMf,abc}] \tag{16}$$

$$[\Psi_{PMf,abc}] = \Psi_{PM}\left[\cos\theta \quad \cos\left(\theta - \frac{2\pi}{3}\right) \quad \cos\left(\theta + \frac{2\pi}{3}\right)\right]^t \tag{17}$$

$$[V_{s,abc}] = [R_{sh}][i_{s,abc}] + [L_{sh}]\frac{d}{dt}[i_{s,abc}] + \frac{d}{dt}[\Psi_{PM,abc}] - \mu[R_{sh}][A_1]i_f - \mu[L_f]\frac{d}{dt}i_f \tag{18}$$

$$V_f = i_f R_f = \mu R_s(i_a - i_f) + \mu[L_f]^t\frac{d}{dt}[i_{s,abc}] - \mu^2 L\frac{d}{dt}i_f + \mu\frac{d}{dt}(\Psi_{PM}\cos\theta) \tag{19}$$

The voltage equation is transformed to the synchronous reference frame through Park's transformation, with an extra term to account for the fault, as shown in (20) and (21).

$$T = T_{dq0} = \frac{2}{3}\begin{bmatrix} cos\theta & \cos(\theta - 2\pi/3) & \cos(\theta + 2\pi/3) & cos\theta \\ -sin\theta & -\sin(\theta - 2\pi/3) & -\sin(\theta + 2\pi/3) & -sin\theta \\ 1/2 & 1/2 & 1/2 & 0 \\ 0 & 0 & 0 & 1 \end{bmatrix} \quad (20)$$

$$\begin{aligned}\left[V_{sf,dq0}\right] = T[R_{sf}]T^{-1}\left[i_{sf,dq0}\right] + T[L_{sf}]\frac{d}{dt}T^{-1}\left[i_{sf,dq0}\right] + T[L_{sf}]T^{-1}\frac{d}{dt}\left[i_{sf,dq0}\right] \\ + T\frac{d}{dt}T^{-1}\left[\Psi_{PMf,dq0}\right] + T\,T^{-1}\frac{d}{dt}\left[\Psi_{PMf,dq0}\right]\end{aligned} \quad (21)$$

dq-axes voltage is then separated into its healthy and positive parts in (22)-(26)

$$\begin{cases} V_d = V_{d,h} + V_{d,f} \\ V_q = V_{q,h} + V_{q,f} \\ V_0 = -\frac{1}{3}\mu R_s i_f - \frac{1}{3}\mu(L + 2M)\frac{d}{dt}i_f \end{cases} \quad (22)$$

$$V_{d,h} = R_s i_d + \omega L_s i_q + L_s \frac{d}{dt} i_d \quad (23)$$

$$\begin{aligned} V_{d,f} = \frac{2}{3}\mu\cos\theta\left[R_s\left(i_d\cos\theta - i_q\sin\theta\right) - \left(2R_s + \frac{R_f}{\mu}\right)i_f\right] \\ -\frac{2}{3}\mu\cos\theta\left[\omega L_s\left(i_d\sin\theta + i_q\cos\theta\right)\right] \\ +\frac{2}{3}\mu\cos\theta\left[L_s\left(\cos\theta\frac{d}{dt}i_d - \sin\theta\frac{d}{dt}i_q\right) - (L_s + \mu L)\frac{d}{dt}i_f\right] \end{aligned} \quad (24)$$

$$V_{q,h} = R_s i_q - \omega L_s i_d + L_s \frac{d}{dt} i_q + \omega\Psi_{PM} \quad (25)$$

$$\begin{aligned} V_{q,f} = \frac{2}{3}\mu\sin\theta\left[-R_s\left(i_d\cos\theta + i_q\sin\theta\right) + \left(2R_s + \frac{R_f}{\mu}\right)i_f\right] \\ +\frac{2}{3}\mu\sin\theta\left[\omega L_s\left(i_d\sin\theta + i_q\cos\theta\right)\right] \\ +\frac{2}{3}\mu\sin\theta\left[-L_s\left(\cos\theta\frac{d}{dt}i_d + \sin\theta\frac{d}{dt}i_q\right) + (L_s + \mu L)\frac{d}{dt}i_f\right] \end{aligned} \quad (26)$$

$$\begin{aligned} V_f' = V_f - i_f R_f = \frac{2}{3}\mu\left[R_s\left(i_d\cos\theta - i_q\sin\theta\right) - \left(R_s + \frac{R_f}{\mu}\right)i_f\right] \\ +\frac{2}{3}\mu\left[L_s\left(\cos\theta\frac{d}{dt}i_d - \sin\theta\frac{d}{dt}i_q\right)\right. \\ \left. -\omega L_s\left(i_d\sin\theta + i_q\cos\theta\right)\right] + \frac{2}{3}\mu^2 L\frac{d}{dt}i_f - \mu\,\omega\,\Psi_{PM}\sin\theta = 0 \end{aligned} \quad (27)$$

Furthermore, spatial harmonics in the flux distribution due to permanent magnets located in the rotor can be defined in the *dq0* reference frame as seen in (28), (29). Expressions (23)-(27) can be then rewritten as (30)-(34).

$$\Psi_{PM_d} = \Psi_{PM_1} + \sum_{\nu=2k+1} \Psi_{PM_\nu} \cos[(\nu \pm 1)\theta - \phi_\nu] \tag{28}$$

$$\Psi_{PM_q} = \sum_{\nu=2k+1} \Psi_{PM_\nu} \sin[(\nu \pm 1)\theta - \phi_\nu] \tag{29}$$

$$V_{d,h} = R_s i_d + \omega L_s i_q + L_s \frac{d}{dt} i_d - \omega \Psi_{PM_q} + \frac{d\Psi_{PM_d}}{dt} \tag{30}$$

$$\begin{aligned} V_{d,f} = {} & \frac{2}{3}\mu \cos\theta \left[R_s\left(i_d \cos\theta - i_q \sin\theta\right) - \left(2R_s + \frac{R_f}{\mu}\right) i_f\right] \\ & - \frac{2}{3}\mu \cos\theta\left[\omega L_s\left(i_d \sin\theta + i_q \cos\theta\right)\right] \\ & + \frac{2}{3}\mu \cos\theta \left[L_s\left(\cos\theta \frac{d}{dt} i_d - \sin\theta \frac{d}{dt} i_q\right) - (2L_s + \mu L)\frac{d}{dt} i_f\right] \end{aligned} \tag{31}$$

$$V_{q,h} = R_s i_q - \omega L_s i_d + L_s \frac{d}{dt} i_q + \omega \Psi_{PM_d} + \frac{d\Psi_{PM_q}}{dt} \tag{32}$$

$$\begin{aligned} V_{q,f} = {} & \frac{2}{3}\mu \sin\theta \left[-R_s\left(i_d \cos\theta + i_q \sin\theta\right) + \left(2R_s + \frac{R_f}{\mu}\right) i_f\right] \\ & + \frac{2}{3}\mu \sin\theta\left[\omega L_s\left(i_d \sin\theta + i_q \cos\theta\right)\right] \\ & + \frac{2}{3}\mu \sin\theta \left[-L_s\left(\cos\theta \frac{d}{dt} i_d + \sin\theta \frac{d}{dt} i_q\right)\right. \\ & \left. + (2L_s + \mu L)\frac{d}{dt} i_f\right] \end{aligned} \tag{33}$$

$$\begin{aligned} V_f' = {} & \frac{2}{3}\mu \left[R_s\left(i_d \cos\theta - i_q \sin\theta\right) - \left(R_s + \frac{R_f}{\mu}\right) i_f\right] \\ & + \frac{2}{3}\mu \left[L_s\left(\cos\theta \frac{d}{dt} i_d - \sin\theta \frac{d}{dt} i_q\right)\right. \\ & \left. - \omega L_s\left(i_d \sin\theta + i_q \cos\theta\right)\right] - \mu^2 \left(Ls + \frac{2}{3}L\right)\frac{d}{dt} i_f \end{aligned} \tag{34}$$

The effects of an interturn fault on machine current depend on the interaction between stator winding and permanent magnet flux linkages. These effects could be verified with simulations of the model (1)-(22). Detailed simulations and experimental results will be presented in the next chapter. Here, the model (1)-(22) is simplified for the case of a rotorless machine.

Assuming the stator current aligned with *d*-axis and the flux linkage due to permanent magnets is equal to zero, the model can be reformulated as

$$V_{d,h} = R_s i_d + L_s \frac{d}{dt} i_d \tag{35}$$

$$V_{d,f} = \frac{2}{3}\mu \cos\theta \left[R_s(i_d \cos\theta) - \left(2R_s + \frac{R_f}{\mu}\right) i_f\right] - \frac{2}{3}\mu \cos\theta[\omega L_s(i_d \sin\theta)] + \frac{2}{3}\mu \cos\theta \left[L_s\left(\cos\theta \frac{d}{dt} i_d\right) - (2L_s + \mu L)\frac{d}{dt} i_f\right] \tag{36}$$

$$V_{q,h} = -\omega L_s i_d \tag{37}$$

$$V_{q,f} = \frac{2}{3}\mu \sin\theta \left[-R_s(i_d \cos\theta) + \left(2R_s + \frac{R_f}{\mu}\right) i_f\right] + \frac{2}{3}\mu \sin\theta[\omega L_s(i_d \sin\theta)] + \frac{2}{3}\mu \sin\theta \left[-L_s\left(\cos\theta \frac{d}{dt} i_d\right) + (2L_s + \mu L)\frac{d}{dt} i_f\right] \tag{38}$$

$$V_f' = \frac{2}{3}\mu \left[R_s(i_d \cos\theta) - \left(R_s + \frac{R_f}{\mu}\right) i_f\right] + \frac{2}{3}\mu \left[L_s\left(\cos\theta \frac{d}{dt} i_d\right) - \omega L_s(i_d \sin\theta)\right] - \mu^2 \left(Ls + \frac{2}{3}L\right)\frac{d}{dt} i_f = 0 \tag{39}$$

Since $V_d = V_{d,h} + V_{d,f}$

$$V_d = R_s i_d + L_s \frac{d}{dt} i_d + \frac{2}{3}\mu \cos\theta \left[R_s(i_d \cos\theta) - \left(2R_s + \frac{R_f}{\mu}\right) i_f\right] - \frac{2}{3}\mu \cos\theta[\omega L_s(i_d \sin\theta)] + \frac{2}{3}\mu \cos\theta \left[L_s\left(\cos\theta \frac{d}{dt} i_d\right) - (2L_s + \mu L)\frac{d}{dt} i_f\right] \tag{40}$$

And $V_q = V_{q,h} + V_{q,f}$

$$V_d = R_s i_d + L_s \frac{d}{dt} i_d + \frac{2}{3}\mu \cos\theta \left[R_s(i_d \cos\theta) - \left(2R_s + \frac{R_f}{\mu}\right) i_f\right] - \frac{2}{3}\mu \cos\theta[\omega L_s(i_d \sin\theta)] + \frac{2}{3}\mu \cos\theta \left[L_s\left(\cos\theta \frac{d}{dt} i_d\right) - (2L_s + \mu L)\frac{d}{dt} i_f\right] \tag{41}$$

Rearranging and solving for $\frac{di_d}{dt}$

$$\frac{di_d}{dt} = \left[V_d - \frac{2}{3}\mu\, i_d[R_s\,(\cos^2(\theta)+1) - \sin(\theta)\cos(\theta)\omega L_s] + \frac{2}{3}\mu\, If\cos(\theta)(2R_s + R_f\mu) + \frac{2}{3}\mu\frac{d}{dt}i_f\cos(\theta)(2Ls + L\mu)\right] / L_s\left(1 + \frac{2}{3}\mu\cos^2(\theta)\right) \quad (42)$$

Finally, employing (39) it is possible to solve for $\frac{di_f}{dt}$ as

$$\frac{di_f}{dt} = \frac{\frac{2}{3}\left(R_s i_d\cos(\theta) - \left(R_s + \frac{R_f}{\mu}\right)i_f + L_s\frac{d}{dt}i_d\cos(\theta) + \omega L_s i_d\sin(\theta)\right)}{\mu\left(Ls + \frac{2}{3}L\right)} \quad (43)$$

Expressions (40)-(43) are enough to describe the behaviour of a rotorless machine operating under both healthy and faulty conditions. Additionally, equation (35) is employed to represent the healthy part of *d*-axis voltage and thus allow to obtain the faulty part by subtracting from the total *d*-axis voltage.

As shown by the formulation, the absence of a rotor eliminates spatial harmonics due to the lack of permanent magnets. As a result, the harmonic components of current in the machine that are normally affected by such a fault no longer see an increase and, in practice, there is only a change in current magnitude due to the short circuiting of part of the winding. Further analysis is made by means of software simulation and experimental results.

2.3. Simulation Results

The model employs expressions (35) and (40)-(43) to demonstrate the behaviour under both healthy and faulty conditions. Machine characteristics employed have been obtained from a commercial stator sample of a 3kW industrial servo motor. The stator winding modelled is excited to a fixed fundamental frequency of 200Hz, equivalent to 4000rpm for a three pole pair machine. The machine is operating under open loop control with fixed *dq*-axes voltages.

The model allows for different levels of fault severity simulation by changing either the fault resistor value or the number of shorted turns. By mean of example, three different fault resistor values have been employed in Fig. 2.2-Fig. 2.6 and two turns have been

short circuited, representing the lowest severity of stator winding fault. Fig. 2.2 represents fault resistance (top) versus fault current (bottom). The fault is generated by modifying the fault resistor from 100Ω to 1.1Ω (blue), 2.2Ω (red) and 5Ω (green). The same colour code is maintained for Fig. 2.2-Fig. 2.4. The effect of the fault resistor is easily observed in Fig. 2.2, were the fault current decreases as the resistance value increases.

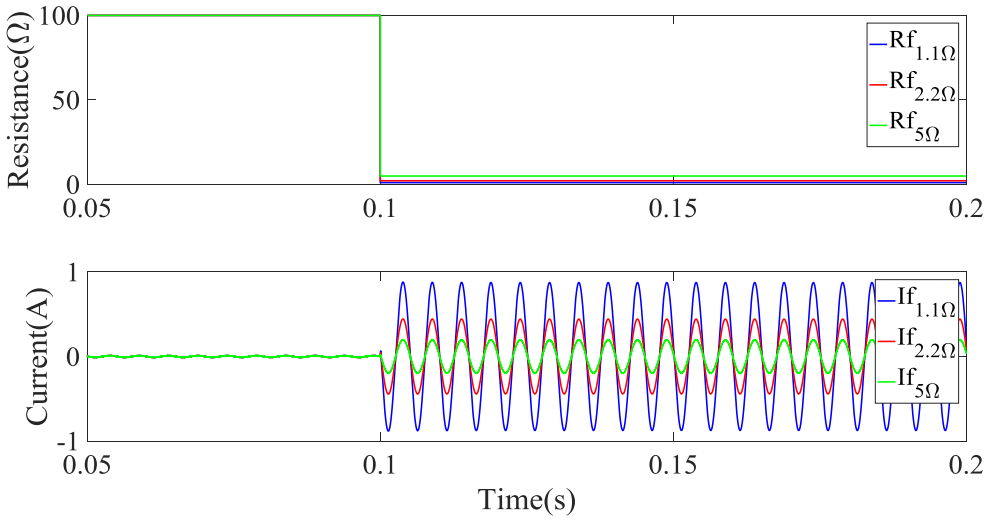

Fig. 2.2. Fault resistance versus fault current for interturn fault under different fault resistor values.

dq-axes currents can be seen in Fig. 2.3. Since *q*-axis current is forced to be zero, the effect of the fault is only visible in *d*-axis current, which average value decreases and ripple increases more the lower the fault resistor magnitude becomes. Although for fixed voltage and decreasing impedance one would expect an increase in current, the fact that healthy voltage decreases means this is not exactly the case. Fig. 2.4 shows the distribution of *d*-axis voltage in healthy (top) and faulty (bottom) parts under the same three conditions analysed in Fig. 2.2 and Fig. 2.3. As expected, the lower the value of the fault resistor, the bigger the reduction in healthy *d*-axis voltage and the complementary increase in faulty part.

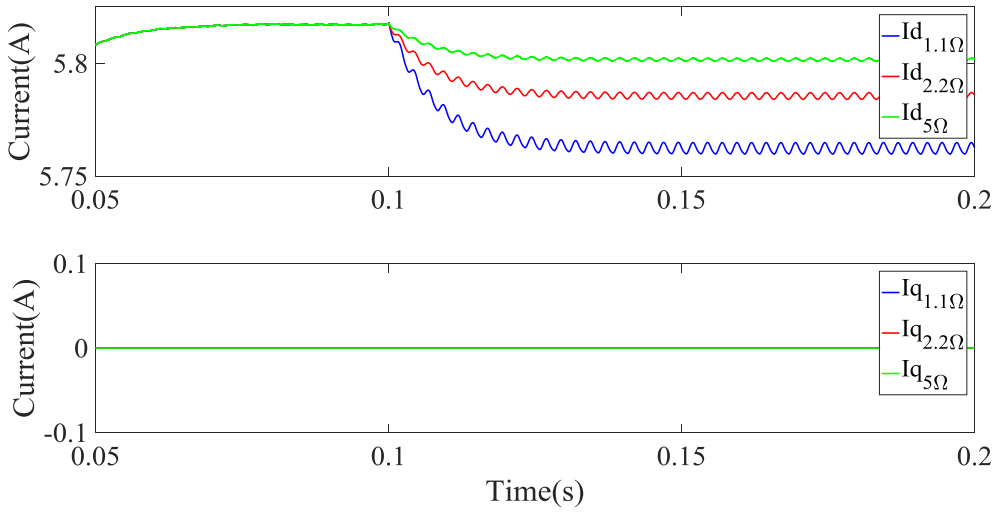

Fig. 2.3. ***dq***-axes currents for interturn fault under different fault resistor values.

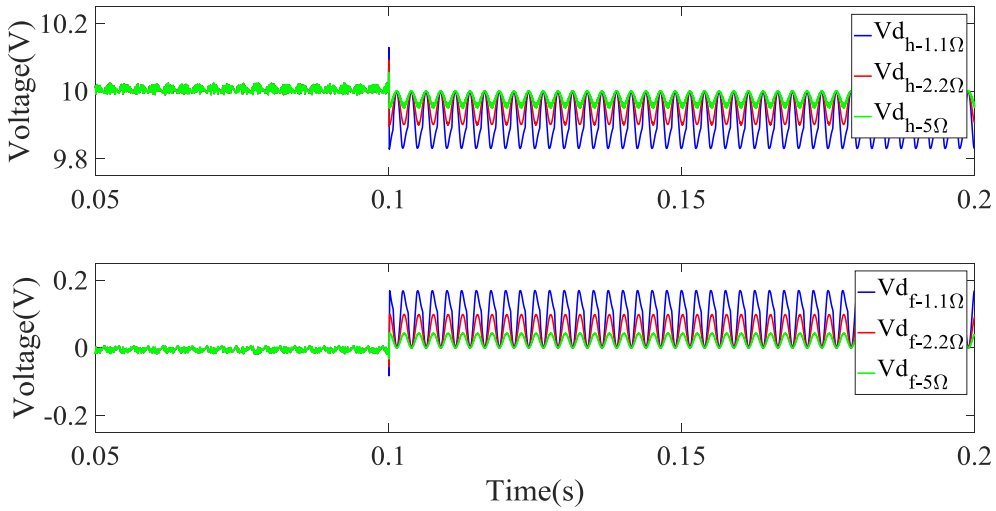

Fig. 2.4. Healthy versus faulty *d*-axis voltage for interturn fault under different fault resistor values.

In Fig. 2.5 and Fig. 2.6 only the case with lower fault resistor (1.1Ω) is studied. Fig. 2.5 represents phase current third harmonics (top) versus *dq*-axes current second harmonics (bottom). As shown, third harmonics do not change significantly with the fault, except for a short transient. In theory, this is caused by the lack of interaction between permanent magnet and stator induced flux normally found in the airgap flux linkage. Again, since *q*-axis current is zero to represent motor current injection without rotation, no second harmonic is measured in this axis. On the other hand, the second harmonic of d-axis current is shown to increase significantly as a result of the change in current magnitude and particularly due to the unbalance that appears between phase currents,

shown in the bottom part of Fig. 2.6. Fig. 2.6 represents three phase currents (top) with a zoom into magnitude change (bottom). Phase currents, entirely dependent on *d*-axis current in this case (and thus the similitude with Fig. 2.2) see their magnitude reduced according to the severity of the fault. The fault is generated by short circuiting 2 turns out of 198 turns per phase in the case under study, representing 1.0101%. The magnitude of the three phase currents is shown to decrease on average a similar amount from 5.818 to 5.76.

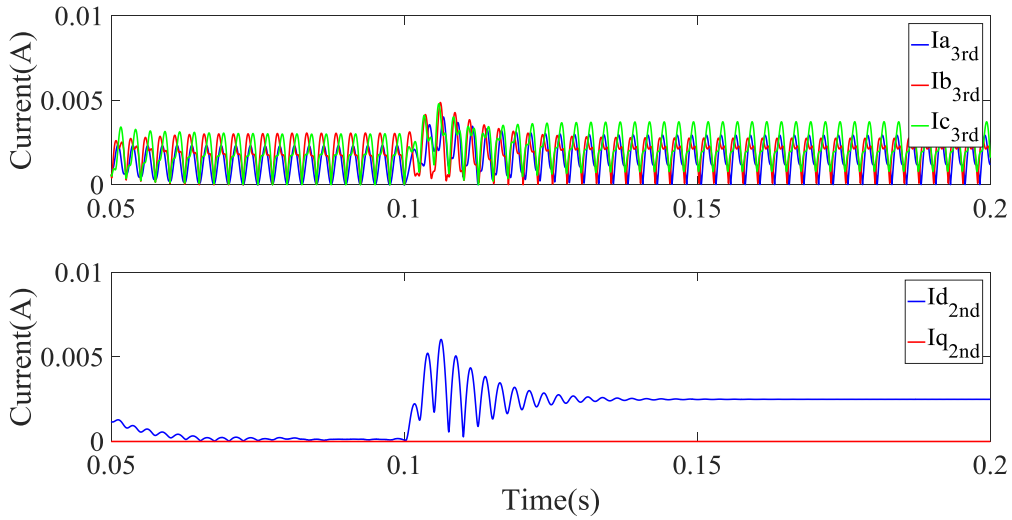

Fig. 2.5. Phase currents third harmonics and *dq*-axes current second harmonics for interturn fault.

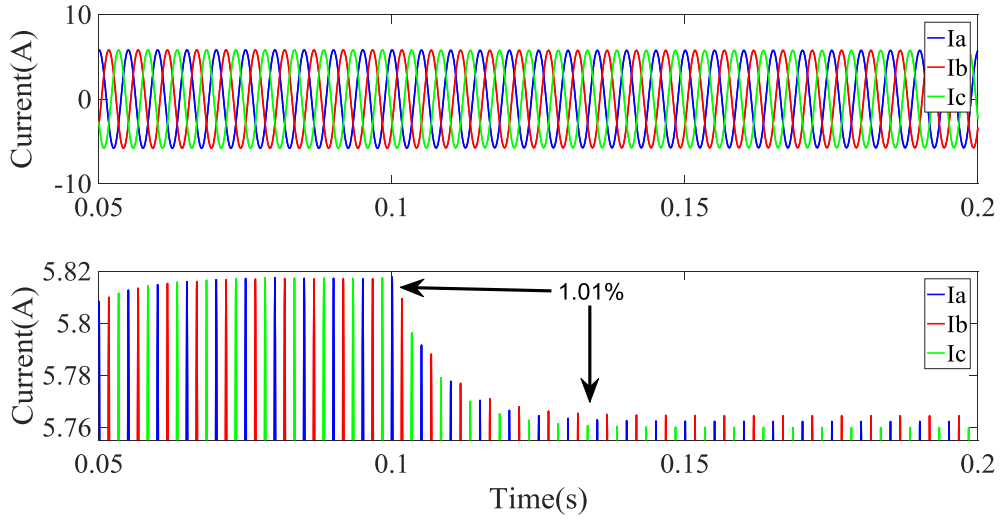

Fig. 2.6 Phase currents for interturn fault.

For all cases it is possible to affirm that given the low severity of the fault and the relatively small difference in fault resistance, the effect on current/voltage magnitude is not significant.

2.4. Experimental setup

Further to the theoretical background provided by the analytical model and supported with software simulations, experimental measurements were performed on the stator of a 3kW servo motor. The experiment is arranged as shown in Fig. 2.7, and consists on a stator located inside an environmental chamber, together with current sensors for each phase and shorted turn, and terminal boxes, as shown in Fig. 2.9. The stator is driven by a variable speed drive (VSD) which is itself commanded from a control and processing rig seen in Fig. 2.8 [113] While current sensors are located inside the chamber, voltage measuring is achieved by use of differential voltage probes located outside the chamber. The experiment is driven in open loop by the commercial VSD operating with a 6kHz PWM frequency. The fault is generated by a Red Pitaya commanding a set of relays which allows switching between different fault resistor values. The fault resistor short circuits two turns out of the 198 available per phase.

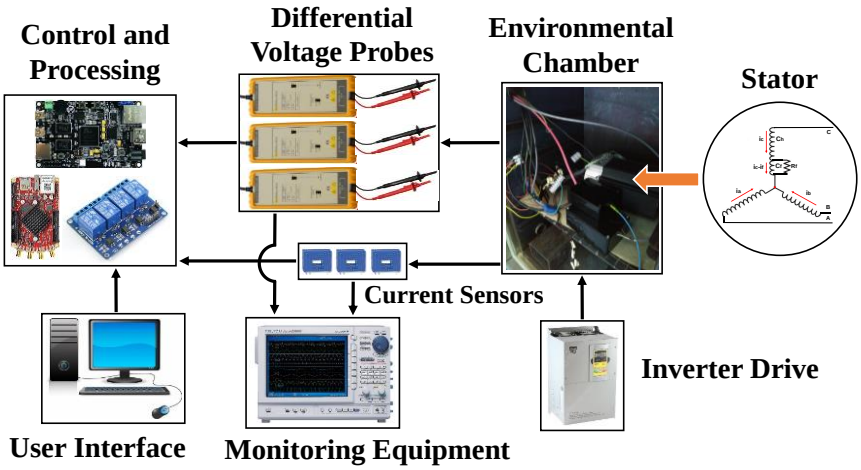

Fig. 2.7. Experiment arrangement diagram including control and measurement equipment.

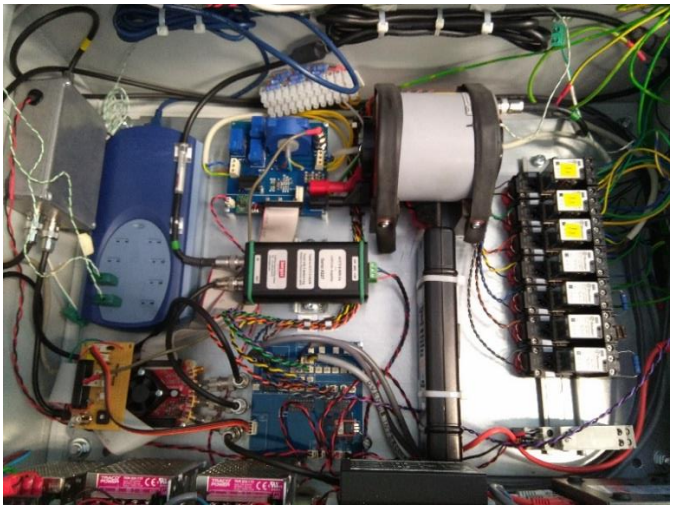

Fig. 2.8. Control and processing rig of experiment.

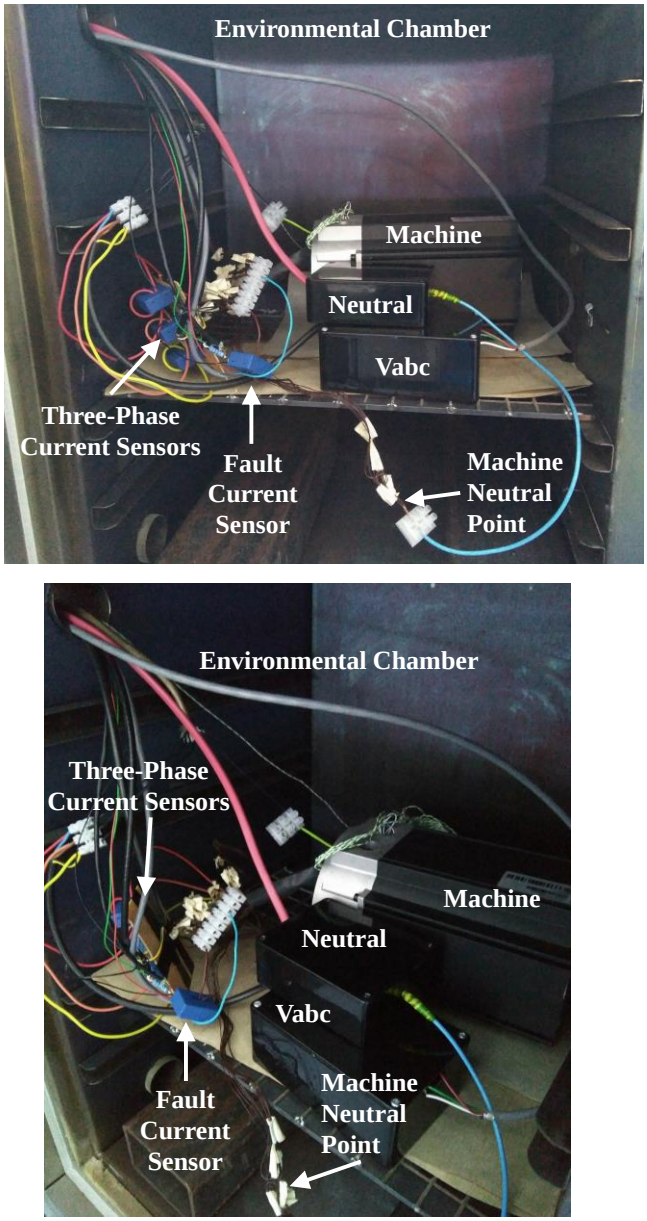

Fig. 2.9. Commercial stator, connections and sensors located inside environmental chamber.

2.5. Experimental Results

A brief experimental validation is described in detail in this section. Six different interturn fault cases are compared in this section, corresponding to six different fault resistor values: 1.1, 2.2, 5, 10, 22 and 56Ω, as shown in Fig. 2.10-Fig. 2.15. The fault is generated in phase A. All cases have the same duration (1 second) and sampling (200kS/s). The fundamental frequency is fixed at 200Hz and the switching frequency at 6kHz. As the value of the fault resistor increases, the fault current becomes significantly smaller. In addition to validating previous assumptions, the availability of results allows studying the relation between fault severity and detection.

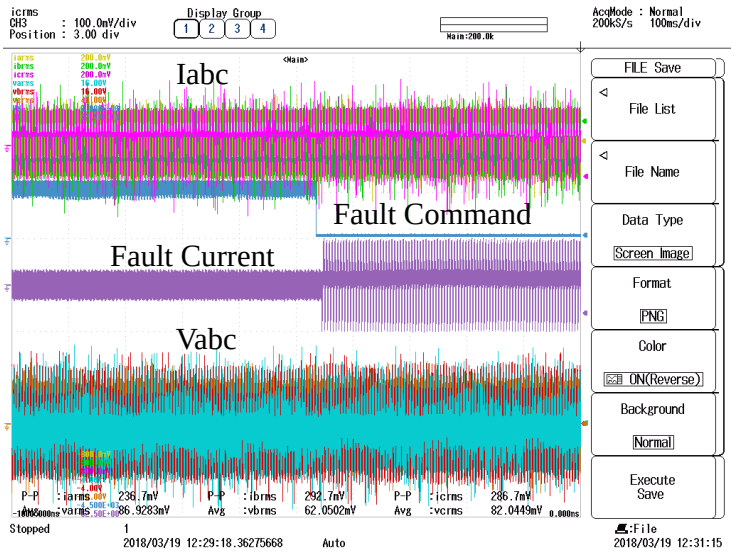

Fig. 2.10. Interturn short circuit with 1.1Ω resistor.

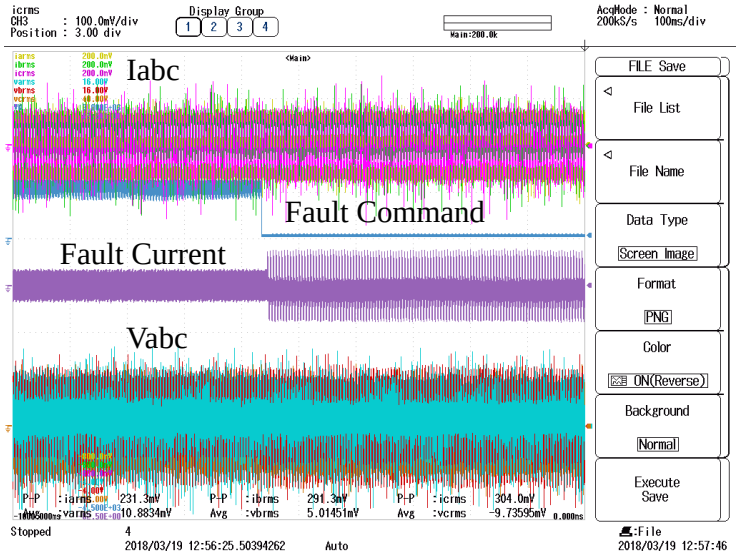

Fig. 2.11. Interturn short circuit with 2.2Ω resistor.

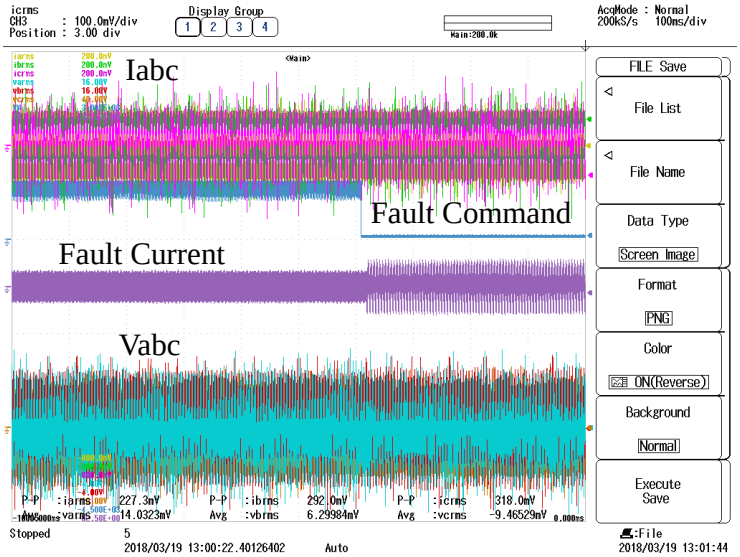

Fig. 2.12. Interturn short circuit with 5Ω resistor.

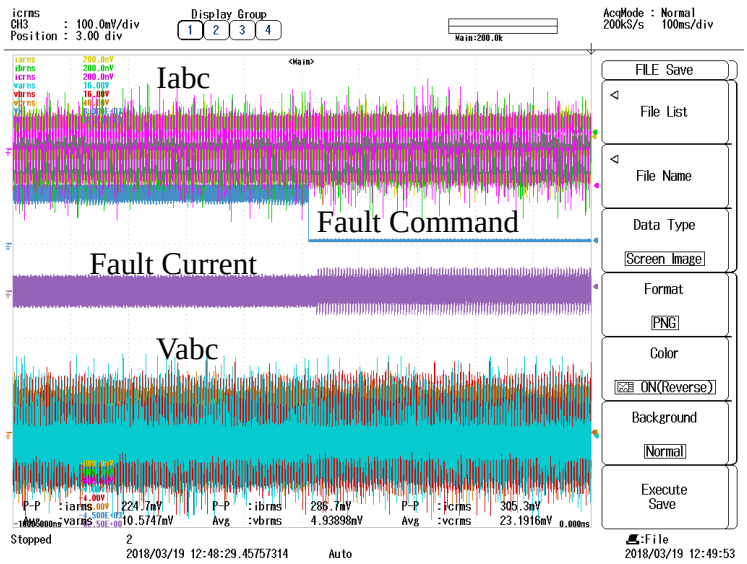

Fig. 2.13. Interturn short circuit with 10Ω resistor.

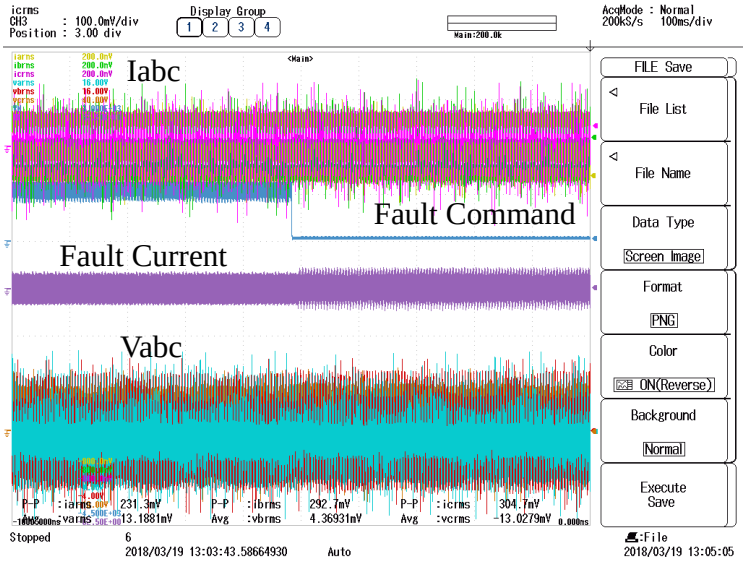

Fig. 2.14. Interturn short circuit with 22Ω resistor.

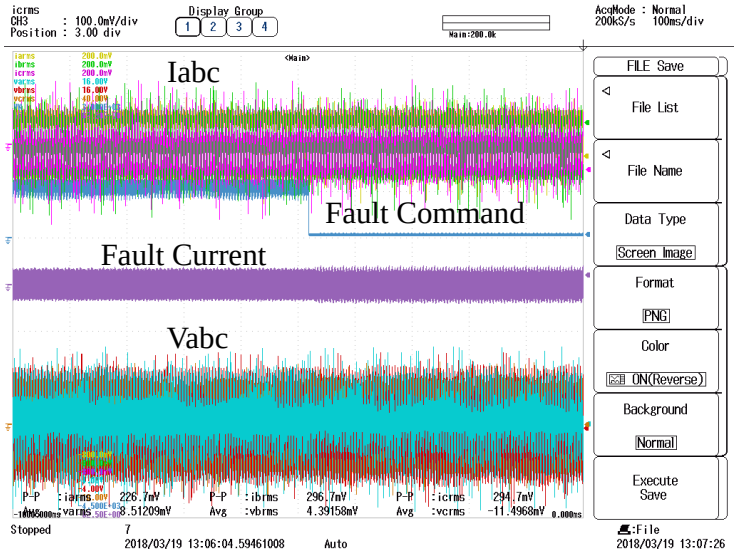

Fig. 2.15. Interturn short circuit with 56Ω resistor.

A zoomed-in representation of the fault transient of Fig. 2.10 is provided in Fig. 2.16 allowing a better visualization of the fault process. Phase currents are shown at the top, followed by phase voltages in the middle and fault current at the bottom. The change is not noticeable in three phase components. However fault current is clearly affected, even by such a low severity fault. Ignoring the ripple, fault current climbs from 0 to around 8A.

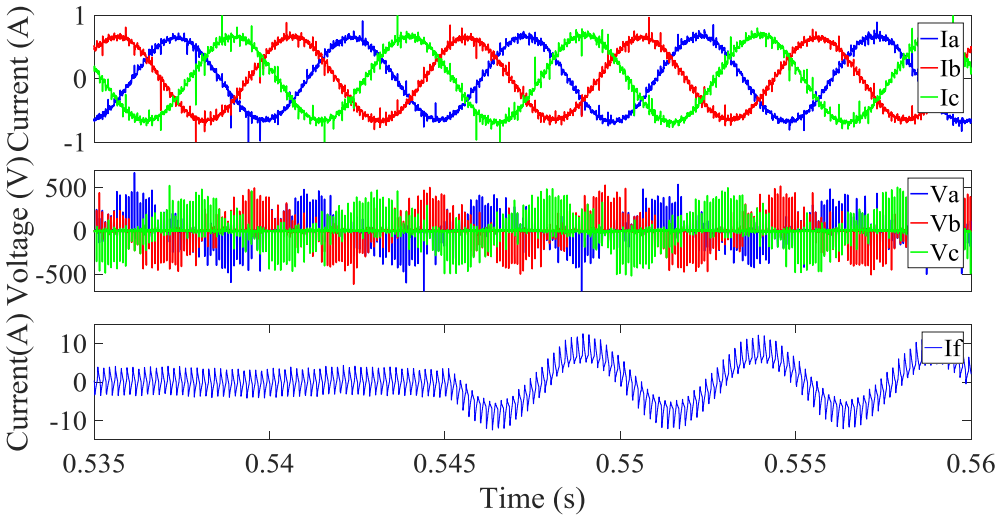

Fig. 2.16. Interturn short circuit with 1.1Ω resistor zoom in.

Finally, an analysis of current harmonic components usually associated with this type of fault is provided in Fig. 2.17-Fig. 2.22. In principle, the effect recorded in the second harmonic is a result of a current unbalance without a significant increase of harmonics in the individual phase currents. A temporary increase in third harmonics is however present due to the fault transient, which disappears in steady-state. Given the fault is generated in phase A, only the third harmonic of current alpha presents a significant transient. The behaviour of this transient is in practice identical to the response under load/current step, and thus, impossible to discriminate from an interturn fault. On the other hand, both *d* and *q* axes reflect an increase due to the imbalance created. Particularly for the first case, seen in Fig. 2.10 and Fig. 2.16, fault severity is easily detected from the second harmonic magnitude. This indicator gradually decreases with the increase in fault resistor, until the effect is no longer perceived between 5 and 10Ω. However, the fault current is visibly affected until at least 22Ω.

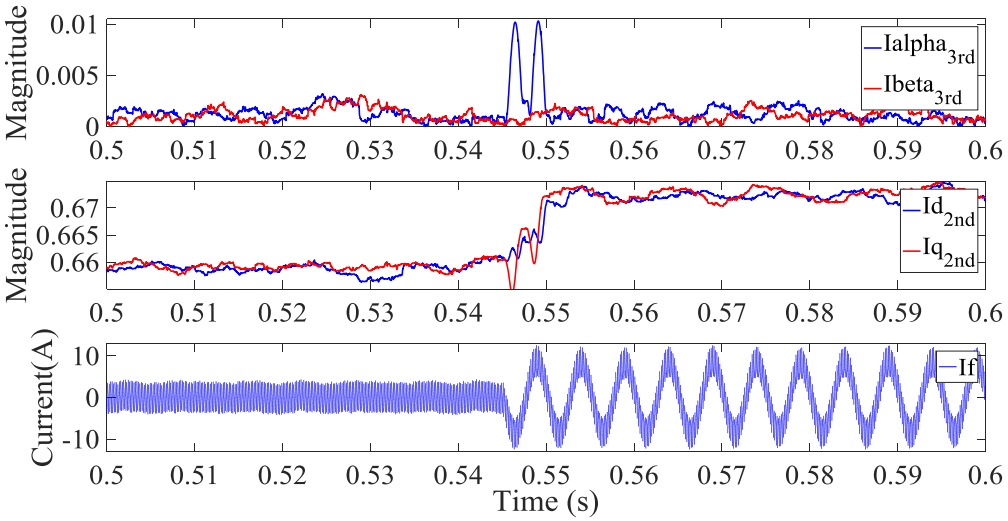

Fig. 2.17. Interturn short circuit with 1.1Ω resistor, phase third versus *dq*-axes second harmonics.

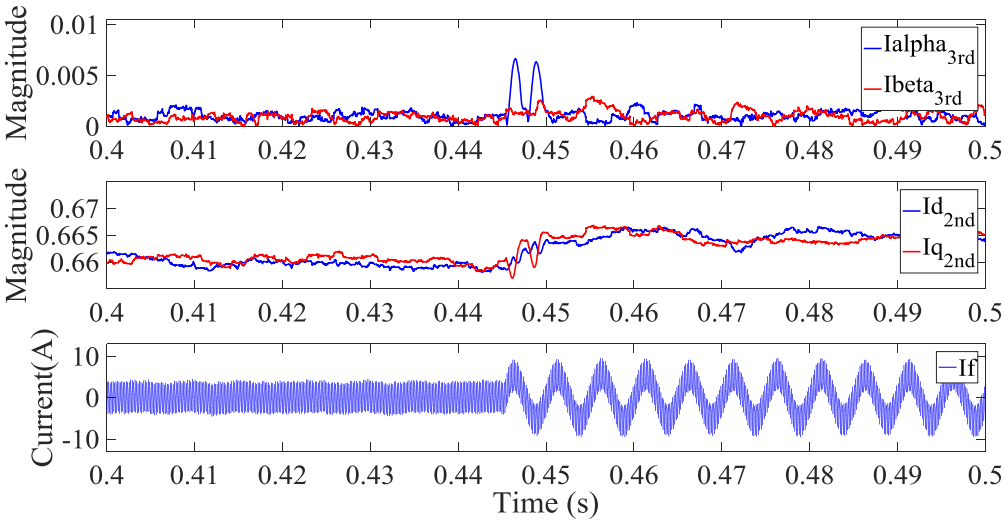

Fig. 2.18. Interturn short circuit with 2.2Ω resistor, phase third versus *dq*-axes second harmonics.

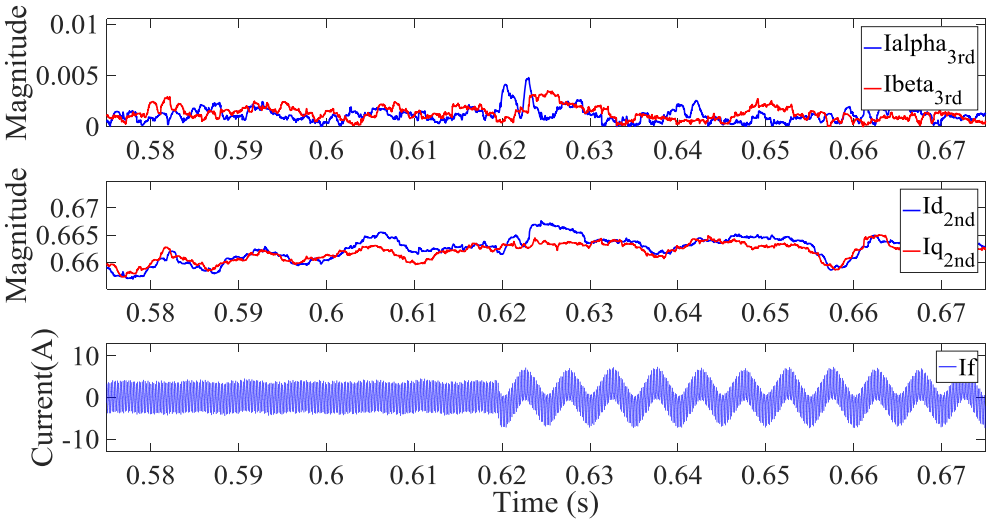

Fig. 2.19. Interturn short circuit with 5Ω resistor, phase third versus *dq*-axes second harmonics.

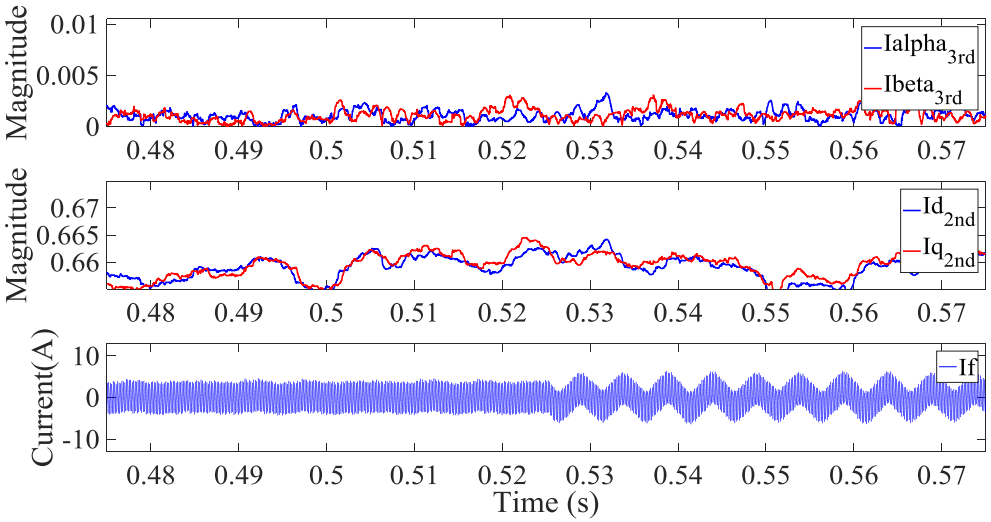

Fig. 2.20. Interturn short circuit with 10Ω resistor, phase third versus *dq*-axes second harmonics.

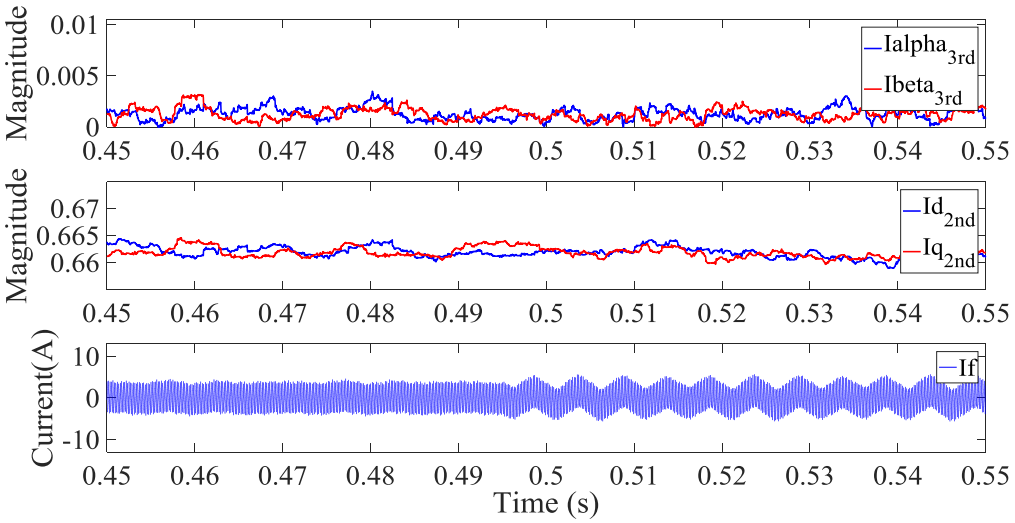

Fig. 2.21. Interturn short circuit with 22Ω resistor, phase third versus *dq*-axes second harmonics.

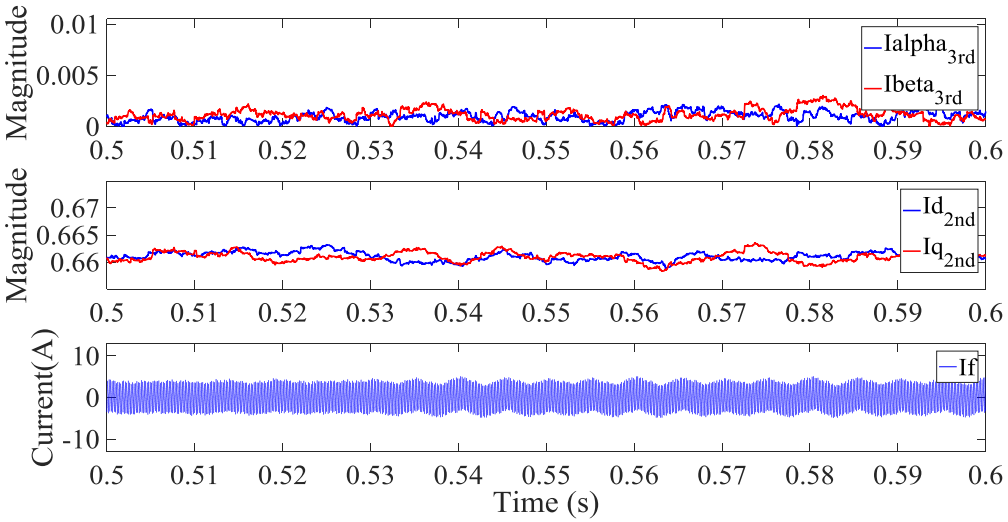

Fig. 2.22. Interturn short circuit with 56Ω resistor, phase third versus *dq*-axes second harmonics.

These tests were also performed with the aim of quantifying what fault level is detectable using stator currents analysis methods. Variable fault resistors provide and emulation of different levels of insulation degradation. In healthy conditions, the interturn resistance has values in the order of Mega Ohms. The results provided here show that fault detection from terminal currents measurements is possible when interturn resistance decreases to values of a few Ohms. This means that fault detection could be possible when insulation is significantly degraded, but still not completely failed.

2.6. Summary

This chapter has demonstrated the origin of the effects associated with a stator winding fault by use of an analytical model, software simulations and experimental results. One of the main assumptions made throughout this thesis is that a short circuit fault in the stator winding of a PMSM should not generate new harmonic components but would modify those already present, dramatically increasing the magnitude of three phase currents third harmonic and *q*-axes current second harmonic in particular. As shown, this is due to a disturbance on the main air-gap flux linkage. If there is no rotor, the main effect of an interturn short circuit is the creation of a current unbalance, rather than the increase of current harmonics. This unbalance can be detected using e.g. second harmonics in the synchronous reference frame.

Modelling and experimental results have been presented to illustrate these effects and to evaluate the sensitivity of current signature analysis methods to the severity of the fault.

CHAPTER 3

MODELLING AND REAL-TIME IMPLEMENTATION

3.1. Overview

This chapter describes the work carried out on machine modelling and its real-time Hardware-in-the-Loop (HIL) implementation. Whilst the main contribution of this thesis is on methodologies for fault detection and diagnosis, accurate Permanent Magnet Synchronous Machine (PMSM) models are required not only for simulation and validation of the proposed strategies, but also for real-time implementation of model-based fault-detection methods. In order to evaluate fault detection techniques, the model should not only account for operation under healthy conditions, but also accurately describe the behaviour of machines under stator winding faults. As discussed in the literature review, a number of techniques suitable for real-time modelling of PMSM under both healthy and faulty conditions exist. Computationally efficient models are required to guarantee execution in real-time. Analytical models based on fluxes or inductances maps pre-calculated using finite element (FE) simulations are discussed in this chapter demonstrating fidelity of emulation whilst retaining relatively high computational efficiency.

Since the final aim is to implement all fault detection work in real-time, HIL tools have been used extensively in this work to test fault-detection methods prior to potentially dangerous and/or expensive tests on hardware prototypes. HIL testing methods can facilitate the development of control strategies in a safe and inexpensive environment particularly when extreme operating conditions such as faults are considered. HIL methods rely on accurate real-time emulation of the equipment under investigation. However, at the beginning of the PhD work for this thesis, no validated tools for real-time emulation of electrical drives under fault conditions were available. This chapter describes the implementation of the selected high-fidelity real-time emulator of a PMSM drive in a platform suitable for HIL tests. The emulator is capable of representing the drive operation under both healthy conditions and during inter-turn stator winding faults. Nonlinearities due to saturation, higher order harmonics, slotting effects, etc. are accounted for using four-dimensional look-up tables (LUTs) obtained by finite element

analysis (FEA). The employed model is computationally efficient and capable of running in real-time in a Field Programmable Gate Arrays (FPGA) platform and is validated against simulations and experimental results in a wide range of operating conditions. Potential applications of the proposed emulation environment to the development of drive control, fault detection and diagnostic algorithms are also proposed.

Two different machines have been modelled in this chapter. While both of them are Interior Permanent Magnet (IPM) machines with the same number of slots (36) and pole pairs (3), there are significant differences in topology, dimensions and rated conditions. However, the same equations and modelling process can be applied to both without differences. The first machine's topology, employed for sections 3.2 and 3.3, is shown in Fig. 3.1 by its finite element model, while its characteristics are summarised in Table I.

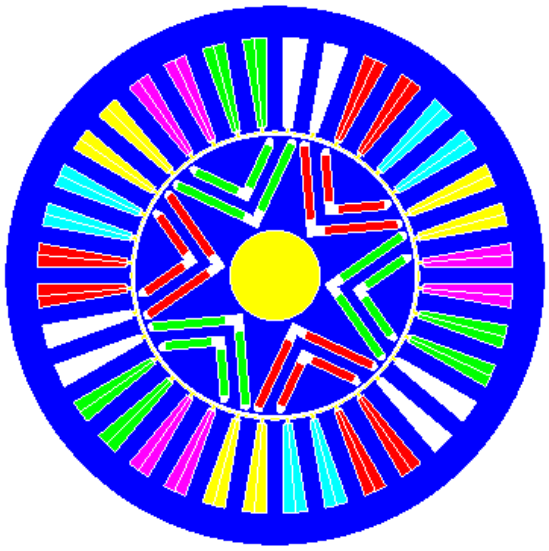

Fig. 3.1. FE model depicting topology of first machine under consideration.

TABLE I

1ST MACHINE CARACTHERISTICS

Characteristic	Value	Unit
Peak Torque	70	Nm
Rated Torque	35.5	Nm
Base Speed	1350	rpm
Max Speed	4500	rpm
Peak Power	9.9	kW
Rated Power	5	kW
DC link Voltage	120	V

Peak Current	125	A
Number of pole-pairs	3	-
Number of slots	36	-
Turns per slot	9	-
Active stack length	118	mm
Stator outer diameter	150	mm
Rotor outer diameter	80	mm

The second machine, presented in [18], was employed in sections 3.5 to 3.7. Its topology is show in Fig. 3.2 while its characteristics are listed in Table II.

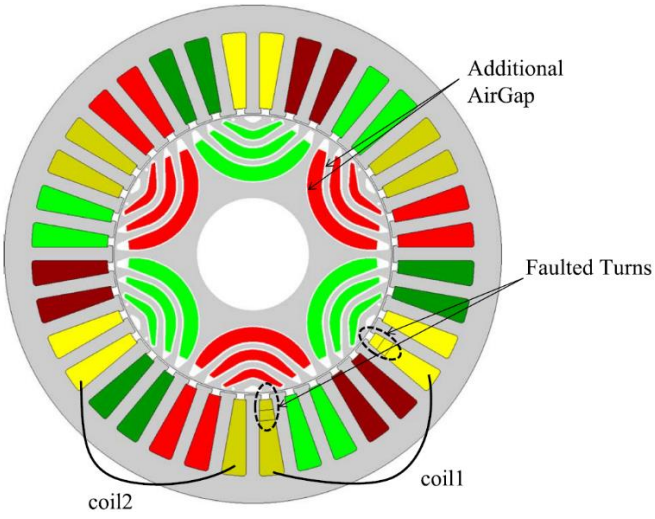

Fig. 3.2. FE model depicting topology of second machine under consideration, including location of the fault [18].

TABLE II

2ND MACHINE CARACTHERISTICS

Characteristic	Value	Unit
Peak Torque	30	Nm
Rated Torque	17	Nm
Base Speed	2100	rpm
Max Speed	8200	rpm
Peak Power	6.6	kW
Rated Power	3.75	kW
Peak Current	85	A
Number of pole-pairs	3	-
Number of slots	36	-
Active stack length	105	mm
Stator outer diameter	120	mm
Rotor outer diameter	67	mm
Airgap	0.35	mm

3.2. PMSM drive modelling in Healthy Conditions

A. Inductance-based model

Standard analytical models of PMSM machines are typically developed in the synchronous reference frame, or *dq*-frame, rotating synchronously with the rotor. If nonlinear effects due to saturation and higher order harmonics, due to e.g. slotting effects, are neglected, the *dq*-frame model of a PMSM is given by:

$$\frac{d\Psi_d^s}{dt} = v_d - R\, i_d + \omega\Psi_q^s \tag{44}$$

$$\frac{d\Psi_q^s}{dt} = v_q - R\, i_q - \omega(\Psi_d^s) \tag{45}$$

Where Ψ^s is flux linkage, v is voltage, R is stator winding resistance, i is current, ω is electrical speed and sub-indexes *d* and *q* correspond to direct and quadratic axes.

Under the assumption of linearity, the relationship between stator flux linkages and phase currents can be represented using inductances. Phase inductances have an even harmonic dependency with rotor position. If only the second harmonic is considered, when transformed into the synchronous reference frame, the inductances become constant, i.e. do not have any dependency on rotor angle and the stator flux linkages-currents relationship can be described by:

$$\begin{bmatrix}\Psi_d^s \\ \Psi_q^s\end{bmatrix} = \begin{bmatrix}L_d & L_{dq} \\ L_{dq} & L_q\end{bmatrix}\begin{bmatrix}i_d \\ i_q\end{bmatrix} \tag{46}$$

A more accurate model that takes saturation and higher order harmonics into account is summarized here. It is assumed that angular dependency of inductances can be represented by a number of even harmonics while the rotor magnetic flux contains an odd harmonic periodicity with rotor position θ. As an example, the model reported here [44] includes up to the eight harmonic for inductances and up to the seventh for rotor flux, as shown in (47)-(52). This model was replicated but simulation found it less accurate than that reported in next subsection. Additionally, issues were found when reconstructing from curve fitted values.

$$\frac{d\Psi_d^s}{dt} = v_d - R\, i_d + \omega\Psi_q^s + \omega(7P_5^m + 5P_7^m)\sin 6\theta \tag{47}$$

$$\frac{d\Psi_q^s}{dt} = v_q - R\, i_q - \omega(\Psi_d^s + P_1^m) - \omega(7P_5^m + 5P_7^m)\cos 6\theta \tag{48}$$

$$\begin{bmatrix}\Psi_d^s \\ \Psi_q^s\end{bmatrix} = \begin{bmatrix}L_d & L_{dq} \\ L_{dq} & L_q\end{bmatrix}\begin{bmatrix}i_d \\ i_q\end{bmatrix} \tag{49}$$

where the inductances are rotor angle dependent and given by,

$$L_d = L_{s0} - L_{m0} + \frac{1}{2}L_{s2} + L_{m2} + \left(\frac{1}{2}L_{s4} + L_{m4} + L_{s6} - L_{m6} + \frac{1}{2}L_{s8} + L_{m8}\right)\cos 6\theta \tag{50}$$

$$L_q = L_{s0} - L_{m0} - \frac{1}{2}L_{s2} - L_{m2} + \left(-\frac{1}{2}L_{s4} - L_{m4} + L_{s6} - L_{m6} + \frac{1}{2}L_{s8} - L_{m8}\right)\cos 6\theta \tag{51}$$

$$L_{dq} = \frac{1}{2}(L_{s4} - 2L_{m4} - L_{s8} - 2L_{m8})\sin 6\theta \tag{52}$$

Parameters can be extracted from FEA computation using least square error minimization applied to three phase flux linkages as shown in (53).

$$\min \left|\left|\Psi_{abc}^{FEA} - (\Psi_{abc}^s(i_{abc}) + \Psi_{abc}^m)\right|\right|^2 \tag{53}$$

Curve fitting, as shown by Fig. 3., can be used to fit polynomial interpolation to the results as function of rotor position and stator currents. The resulting model is computationally efficient and has relatively low memory requirements as only a limited number of coefficients are required to be stored. Higher accuracy can be obtained by increasing the number of harmonics and/or the order of polynomial interpolation.

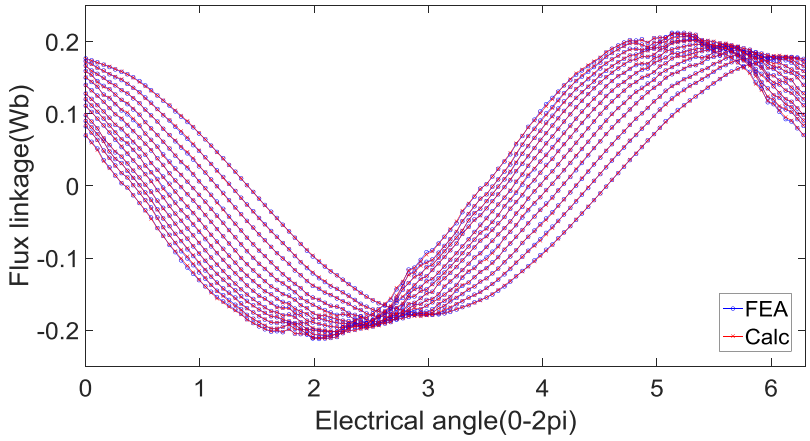

Fig. 3.3. Square error minimization curve fitting of phase flux linkage.

B. Flux-based model

A potentially more accurate but still computationally efficient machine model accounting for non-linearities is based on three-dimensional look-up tables of the currents as function of the stator flux linkages extracted via offline FE simulations. This model accurately captures all nonlinear effects without approximations including higher order harmonics, slotting effects or saturation, as opposed to a smooth, or even flat flux map typically obtained by means fixed inductance. Furthermore, a flux-based approach has the advance of allowing for easy inversion of the equations into current maps by means of integration, as opposed to the need for derivatives in the case of inductances, and thus additional computational requirements. A trade-off between accuracy and memory requirements for the look-up tables has to be considered. This method will be used throughout the rest of this work for model-based fault detection and diagnosis.

The stator flux linkage equations in the synchronous reference frame are:

$$V_d = \frac{d\Psi_d}{dt} + R_S i_d - \omega_e \Psi_q$$
$$V_q = \frac{d\Psi_q}{dt} + R_S i_q + \omega_e \Psi_d \quad (54)$$

where $V_{d,q}$, $i_{d,q}$, $\Psi_{d,q}$, stand for d and q axes voltages, currents and flux linkages, respectively, ω_e refers to the electrical speed, θ is the rotor position and R_s the stator resistance. The flux linkages are in general nonlinear function of the currents and rotor position, and can then be represented by three-dimensional relationships:

$$\Psi_d = f(i_d, i_q, \theta)$$
$$\Psi_q = g(i_d, i_q, \theta) \quad (55)$$

which can be calculated from a set of magnetostatic FE simulations for all combinations of *dq*-axes currents and rotor position for one electric revolution. An example for a 6-pole PMSM developed for traction application is shown in Fig. 3. for rotor position 0°. *d*-axis flux is typically associated with main saturation and *q*-axis flux with cross saturation. The model (54)-(55) is not in a form suitable for real-time HIL applications where voltage is assumed as input to the motor model and current are calculated as resulting output. Integration of (54) provides flux linkages but current output can only be obtained by inversion of (55) which is not an easy task in real-time given the nonlinearity of (55). In order to generate a computationally efficient and causal input-output model of the motor, the inverse solution of the flux linkage/stator currents relationship (56) is pre-calculated offline by inversion of (55) using iterative algorithms and stored in three-dimensional lookup-tables

$$\begin{aligned} i_d &= f^{-1}(\Psi_d, \Psi_q, \theta) \\ i_q &= g^{-1}(\Psi_d, \Psi_q, \theta) \end{aligned} \tag{56}$$

The method, originally proposed in [8], is later adapted and extended in a formulation suitable for real-time HIL simulation.

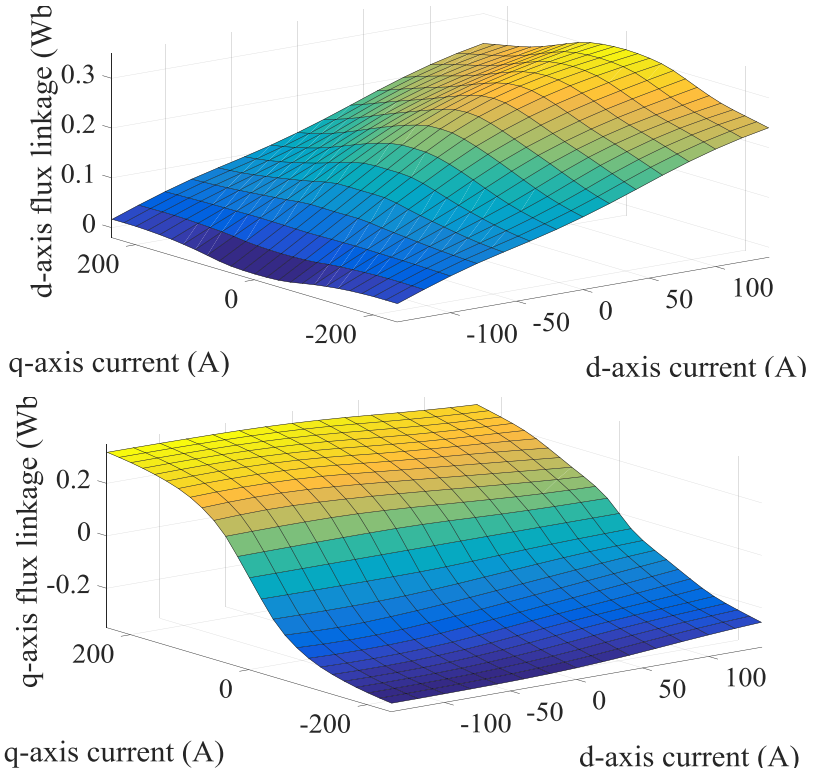

Fig. 3.4. *d*-axis (top) and *q*-axis (bottom) lux linkage maps versus *dq*-axes currents at rotor position 0°.

An example of the *dq*-axes current maps obtained as a function of stator flux linkages are shown in Fig. 3.5. They represent the key element on the model and they account for all information needed to represent the electromagnetic behaviour of a PMSM model.

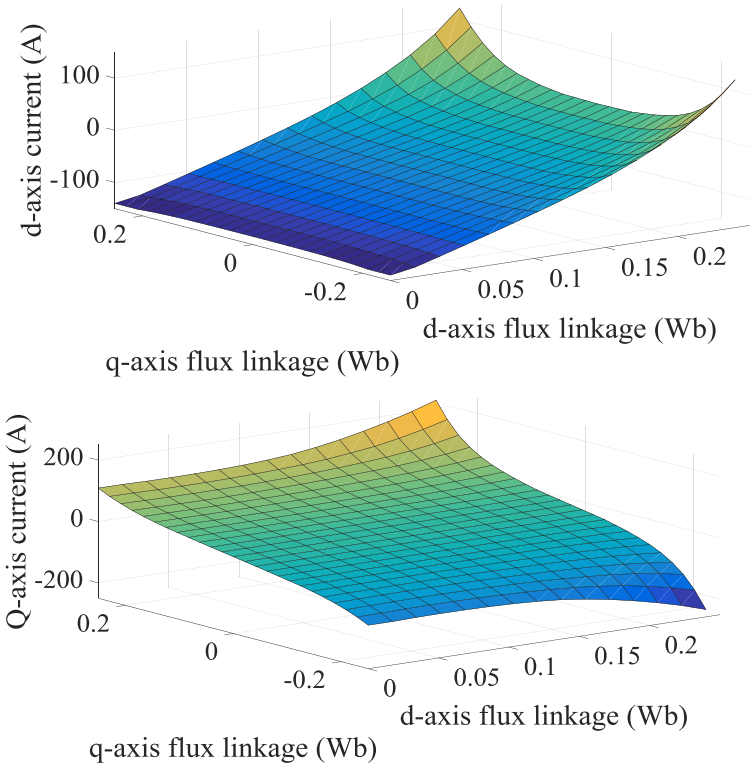

Fig. 3.5. *d*-axis (top) and *q*-axis (bottom) current maps versus flux linkages at rotor position 0°.

The output torque of the motor is:

$$T_{em} = \frac{m}{2} p\left(\Psi_d i_d - \Psi_q i_d\right) + T_{cog}(\theta) \tag{57}$$

where m is the number of phases and p is the number of pole pairs, T_{cog} is the cogging torque which does not depend on currents. An example of the calculated torque for the same condition in Fig. 3., Fig. 3.5 is illustrated in Fig. 3.6. T_{cog} can also be obtained from FEA and implemented in look-up table as function of rotor position.

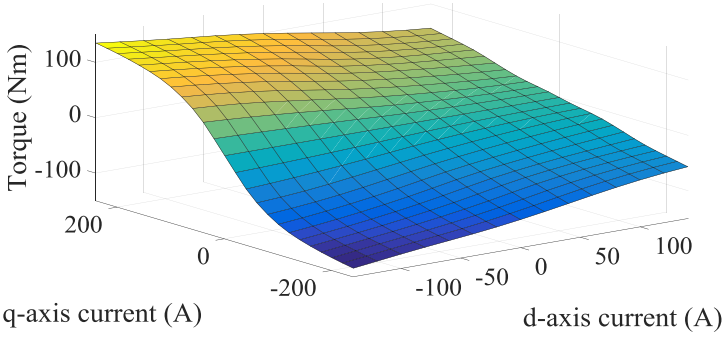

Fig. 3.6. Torque map at rotor position 0°.

A reduction of the number of FE calculations can be achieved by recognising periodicity, 20 mechanical degrees for this case, as illustrated in Fig. 3.7, where three different combinations of *d* and *q* axes currents are presented. By way of example, the model in this section has been generated using 7875 FE magnetostatic simulations resulting from 25, 15 and 21 steps in i_q, i_d, θ, respectively.

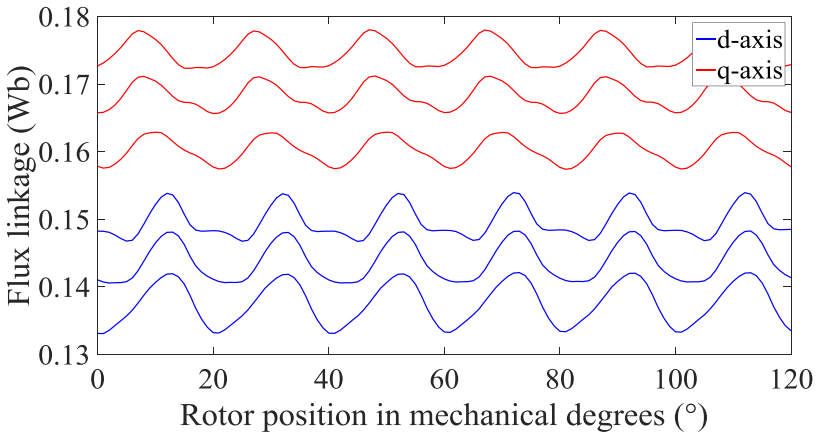

Fig. 3.7 *dq*-axes flux linkages vs rotor position angle.

3.3. FE Modelling of Fault Transient

Further to the use of magnetostatic FEA as a mean to generate LUTs for modelling, FE simulations under both healthy and faulty conditions have been performed on a modified version of the same model, shown in Fig. 3.8.

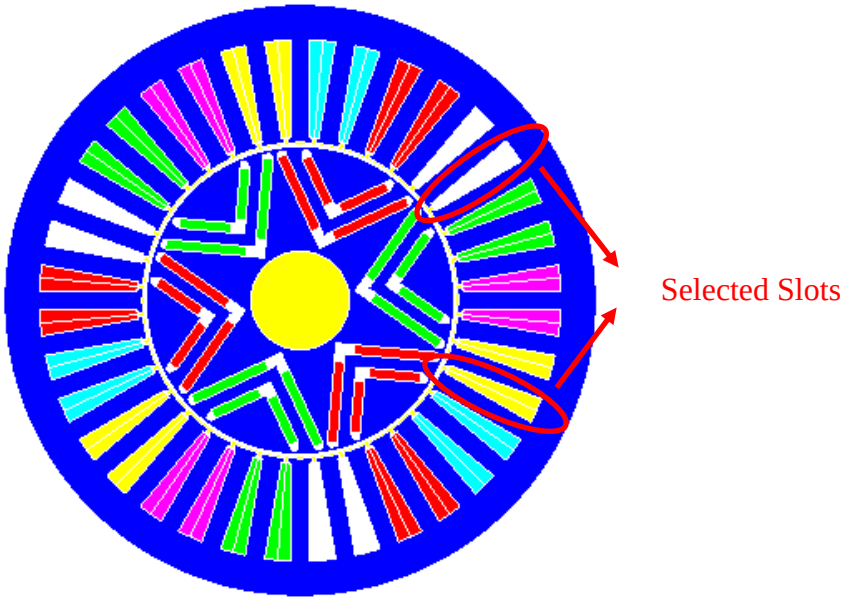

Fig. 3.8. FE transient model of 36 slot-6 slot PMSM machine with fault capability.

This was intended to provide a more practical mean of studding faults, a tool for verifying future assumptions and quantifying the necessary accuracy for fault detection implementation. In both models, each one of the three phases is divided into twelve slots, six for positive sequence and six for negative sequence. In the modified model, seen in Fig. 3.8, two slots (positive and negative sequences) have been divided into nine different regions with equal area to represent the division of each slot into its turns. Employing the circuit shown in Fig. 3.9 it is possible then, to create an interturn fault and study the behaviour of the model under such a fault.

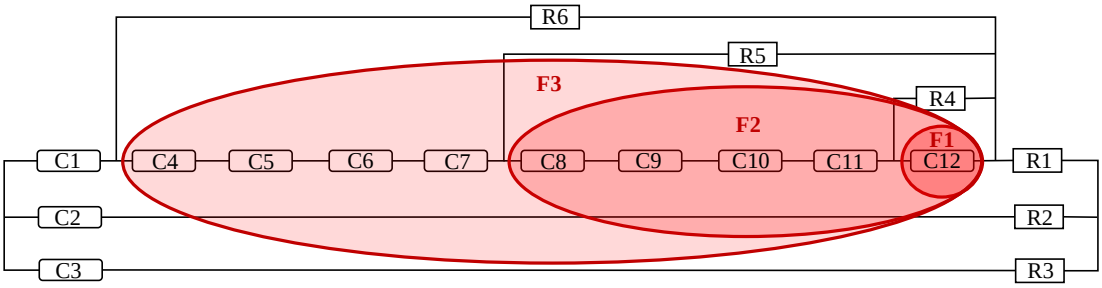

Fig. 3.9. FEA circuit.

Each of the coils shown in the circuit, from C4 to C12, represent a single turn. Without loss of generality the fault has been created in phase A. The circuit allows for the short circuiting of 11.11%, 55.55% or 100% of the slot, corresponding to 1 turn, 5 turns or a maximum of 9 turns (the entire slot), respectively. The values represent the minimum, intermediate and maximum level of short circuiting within one slot. Since the goal of this thesis is to study early stage faults, these combinations are considered representative enough. The resistors employed for short circuiting each combination of turns present an initial value of 10^{12} Ω and, depending on the case, each one will change abruptly to a value of 1μΩ. This creates an immediate short-circuit which allows representing the change on its output variables. For the first case, where only one turn is short-circuited it is possible to observe in Fig.30-31 the three phase currents together with the fault current circulating through the resistor creating the fault and also the current circulating through the faulted turn in opposite direction, and thus, compensating the huge current peak.

It is possible to see the phase current reduction, particularly on the affected phase. This change accounts for 5.66% on phase A where the fault occurs, the variation in phase B, adjacent to the fault, is 4.64%, and the variation in C corresponds to 1.56%. Indicating clearly that the fault has been created in phase A on a slot closer to phase B than phase C.

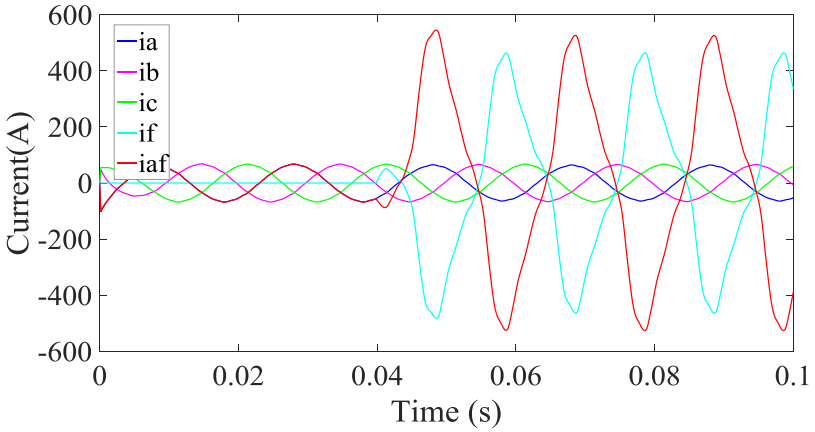

Fig. 3.10. Three phase and fault currents.

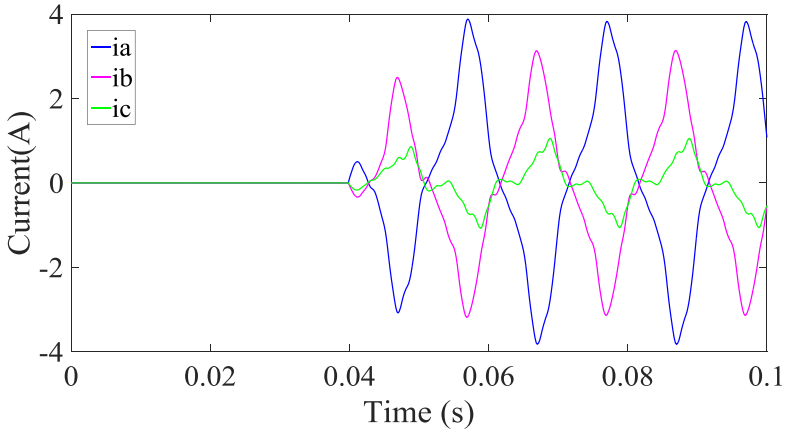

Fig. 3.11. Three phase current variation under fault.

Although only one turn has been short-circuited for the case under study the variation in phase A accounts for a considerable percentage, this is due to the fact that the machine considered contains only 9 turns per slot, therefore 1 turn constitute 11.11% of the total.

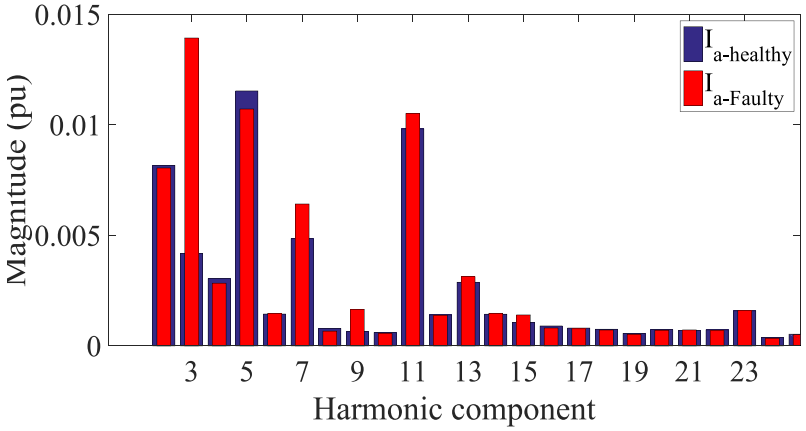

Fig. 3.12. FFT Harmonic components of faulted phase.

The effect of the shorted fault is also studied by means of FFT as seen in Fig. 3.12, where there is a drastic increase on the current's third harmonic component. This effect was expected due to the unbalance created by such a fault [11], [54], [55], [114]. A large third harmonic component in the fault current i_{sf} seen for phase A (i_{af}) in Fig. 3.13 is greatly influenced by the geometry of the permanent magnets [11].

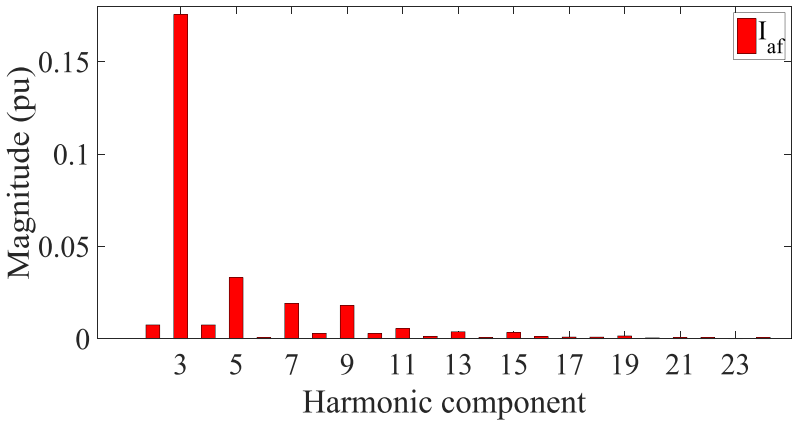

Fig. 3.13. FFT Harmonic components of current fault.

According to voltage equation including fault conditions (58), presented in [55], there is a connection between i_{sf} and the stator currents i_a, i_b, and i_c. For this reason the stator currents spectrum must present a third harmonic component originated by the shorted turns [11], [55].

$$[V_{sf,abc}] = [R_{sf}][i_{sf,abc}] + [L_{sf}]\left[\frac{di_{sf,abc}}{dt}\right] + [e] + [V_0] \tag{58}$$

where V is voltage, R is stator winding resistance, i is current, L is phase inductance, e is back electromotive force and V_0 is voltage of the faulted part.

Additionally, the behaviour of the faulted phase flux linkages is compared to that of the healthy ones, depicted in Fig. 3.14 Fig. 3.15. Furthermore, FEA allows for a decomposition of flux linkage flux into its healthy and faulty parts, as shown in Fig. 3.16.

Similarly to what is shown for currents, the variation registered in the faulted phase accounts for 3.89%, the variation in phase B, adjacent to the fault, is 2.27% and finally, the magnitude variation in phase C corresponds to 1.2%.

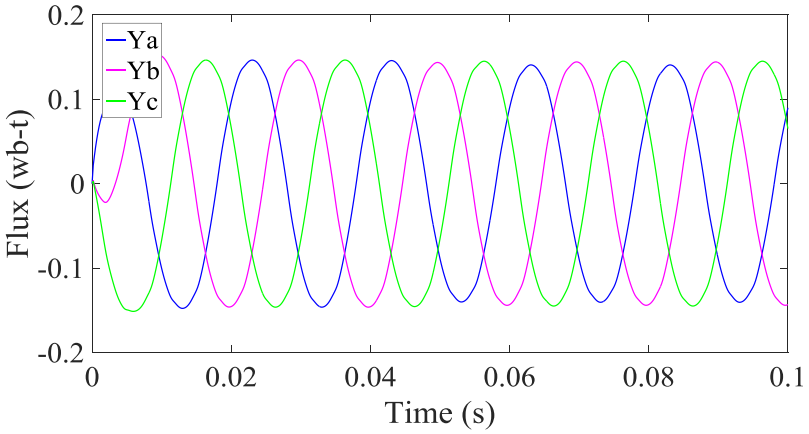

Fig. 3.14. Three phase flux linkages.

Fig. 3.16 depicts flux linkage of the entire faulted phase, as well as that coming from the healthy part minus the slot where the fault appears, the flux of the slot itself, and the flux from the faulted turn.

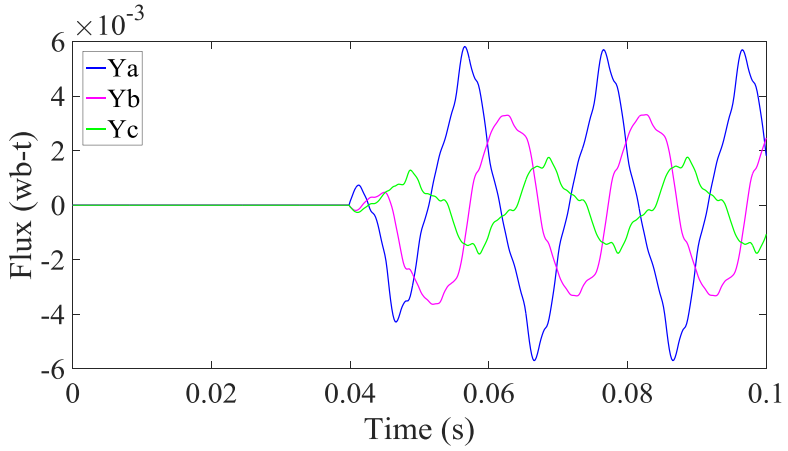

Fig. 3.15. Three phase flux linkages variation under fault.

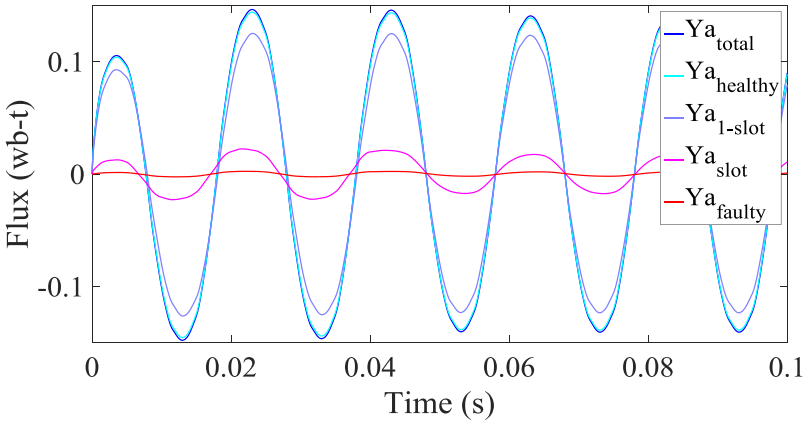

Fig. 3.16. Flux linkage distribution. Phase flux linkage (total), flux of the phase's healthy part (healthy), phase flux minus affected slot (1-slot), the flux of one slot and of the faulted turn.

Finally, the effect of different fault severities on torque is tested, corresponding to the three cases made possible by the circuit shown in Fig. 3.9. The variation in torque recorded when short-circuiting the entire slot, this is 9 turns, is far greater than the registered for the previous cases as seen on Fig. 3.17.

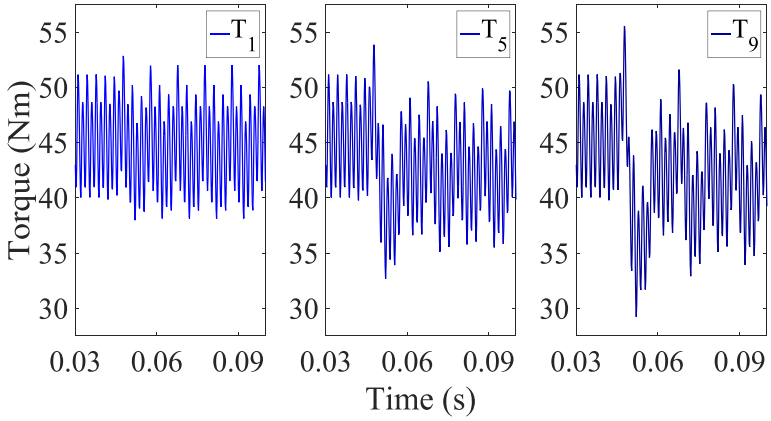

Fig. 3.17. Torque variation for three fault cases.

3.4. Real-time PMSM model in Faulty Conditions

The proposed modelling framework for PMSM under inter-turn short-circuit fault is adapted from [18] and illustrated with reference to Fig. 3.18. Without loss of generality, the turn fault is assumed to be in phase C divided into a healthy and a faulty coils denoted as C_h and C_f respectively. The fault is modelled by a fault resistance R_f, and the fault current is denoted by i_f. The ratio of short-circuited turns to the total number of turns in the phase winding is indicated with μ.

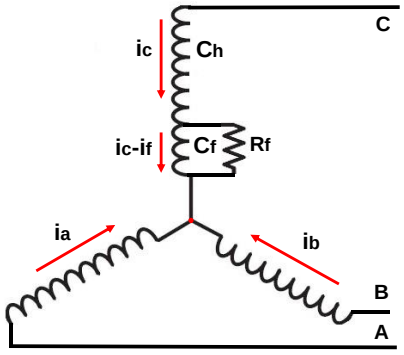

Fig. 3.18. Three phase stator winding with interturn short-circuit fault.

In the synchronous dq reference frame the voltage equations describing the stator flux linkages dynamics can be demonstrated to be [18]:

$$v_d = R_s i_d + \frac{d\psi_d}{dt} - \omega_e \psi_q - \frac{2}{3}\mu R_s \sin\left(\theta_e + \frac{2}{3}\pi\right) i_f \tag{59}$$

$$v_q = R_s i_q + \frac{d\psi_q}{dt} + \omega_e \psi_d - \frac{2}{3}\mu R_s \cos\left(\theta_e + \frac{2}{3}\pi\right) i_f \tag{60}$$

while the voltage across the shorted turns is given by:

$$v_f = R_f i_f = \mu R_s\left(i_d \sin(\theta_e + 2\pi/3) + i_q \cos(\theta_e + 2\pi/3) - i_f\right) + \frac{d\Psi_f}{dt} \tag{61}$$

The relationships between stator flux linkages, stator currents and rotor mechanical angular position θ_m is given by the non-linear four-dimensional maps:

$$\begin{aligned} \Psi_d &= f_d(i_d, i_q, i_f, \theta_m) \\ \Psi_q &= f_q(i_d, i_q, i_f, \theta_m) \\ \Psi_f &= f_f(i_d, i_q, i_f, \theta_m) \end{aligned} \tag{62}$$

which can be extracted from a set of magnetostatic FE computations and stored in lookup tables. Saturation, spatial saliency and harmonics are accounted for. Although neglected here, iron losses and thermal effects can also be included in the same modelling framework [9]. Integration of (59)-(61) requires the inversion of the flux maps (62) to give:

$$\begin{aligned} i_d &= f_d^{-1}(\Psi_d, \Psi_q, \Psi_f, \theta_m) \\ i_q &= f_q^{-1}(\Psi_d, \Psi_q, \Psi_f, \theta_m) \\ i_f &= f_f^{-1}(\Psi_d, \Psi_q, \Psi_f, \theta_m) \end{aligned} \tag{63}$$

While this inversion could in principle be achieved in dynamic simulations using e.g. iterative algorithms, given the non-linearity of (62), it would result in computationally intensive calculations which could be very challenging for real-time implementation. Instead, the current maps (63) are pre-calculated offline and stored in four-dimensional lookup-tables.

3.5. Real-Time Hardware-in-the-Loop Implementation

A. Fault Model Implementation

Given the aim of this thesis is to develop new methods and techniques for PMSMs fault detection and diagnosis, particularly model-based methods, real-time implementation of PMSM models in the form of Hardware-in-the-Loop (HIL) simulation, was identified early on as a logical and necessary step. The ability to accurately represent the machine under study by emulation, including its attached controller, constitutes a powerful tool, saving up the time and cost of acquiring or building machines which may be subjected to faults that compromise its integrity. The degree of fidelity by which HIL systems emulate the physical behaviour of the device under testing in realistic operating conditions, depends on the availability of an accurate representation of the physical system under investigation. Although detailed models such as those based on time-domain co-simulation of Finite Elements (FE) provide a high degree of fidelity, their computational complexity prevents their applicability to the real-time computation required for HIL simulation. Real-time simulation of electric motor drives is particularly challenging due to the fast nature of the dynamics involved. Commutation of PWM signals at tens of kHz requires sampling rates in the order of several MHz in order to obtain reasonable accuracy. FPGAs are emerging as the platform of choice for complex real-time simulations due to their ability to process data in parallel allowing for sampling rates and execution up to the MHz range.

Real-time implementation requires discretization of eqs. (59)-(61). The chosen algorithm could have implications on accuracy and stability of the numerical simulation depending on the discretization time step [115]. The computational efficiency of the model allows the choice of relatively small time step (~1μs) compared to the electrical time constants guaranteeing stability and accuracy. For simplicity in implementation the forward Euler discretization is used resulting in:

$$\psi_d(k+1) = \psi_d(k) + \Delta t \left[v_d(k) - R_s i_d(k) + \omega_e(k)\psi_q(k) + \frac{2}{3}\mu R_s \sin(\theta_e(k) + 2/3\pi) i_f(k) \right] \quad (64)$$

$$\psi_q(k+1) = \psi_q(k) + \Delta t \left[v_q(k) - R_s i_q(k) - \omega_e(k)\psi_d(k) + \frac{2}{3}\mu R_s \cos(\theta_e(k) + 2/3\pi) i_f(k) \right] \quad (65)$$

$$\begin{aligned} \psi_f(k+1) = \psi_f(k) \\ + \Delta t \Big[v_f(k) \\ - \mu R_s \Big(i_d(k) \sin(\theta_e(k) + 2\pi/3) \\ + i_q(k) \cos(\theta_e(k) + 2/3\pi) - i_f(k) \Big) \Big] \end{aligned} \quad (66)$$

The developed model is implemented on a commercially available data acquisition and control platform NI cRIO-9082. The code is implemented on the Spartan-6 LX150 FPGA-based chassis and programmed through LabVIEW FPGA. The FPGA is clocked at 40MHz. Six PWM gate drives digital inputs are sampled at 5MHz. Output currents are generated with a digital-to-analog conversion at 115 kHz rate. A schematic of the proposed arrangement in a typical Controller-in-the-loop testing is shown in Fig. 3.19.

A 32-bit fixed-point representation is used for the internal variables. A schematic diagram illustrating the emulation step is shown in Fig. 3.20.

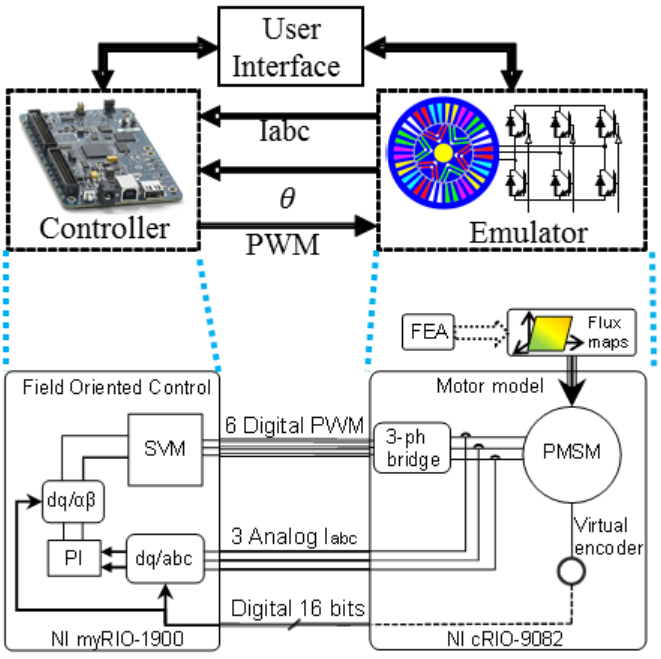

Fig. 3.19. Block diagram illustrating HIL arrangement.

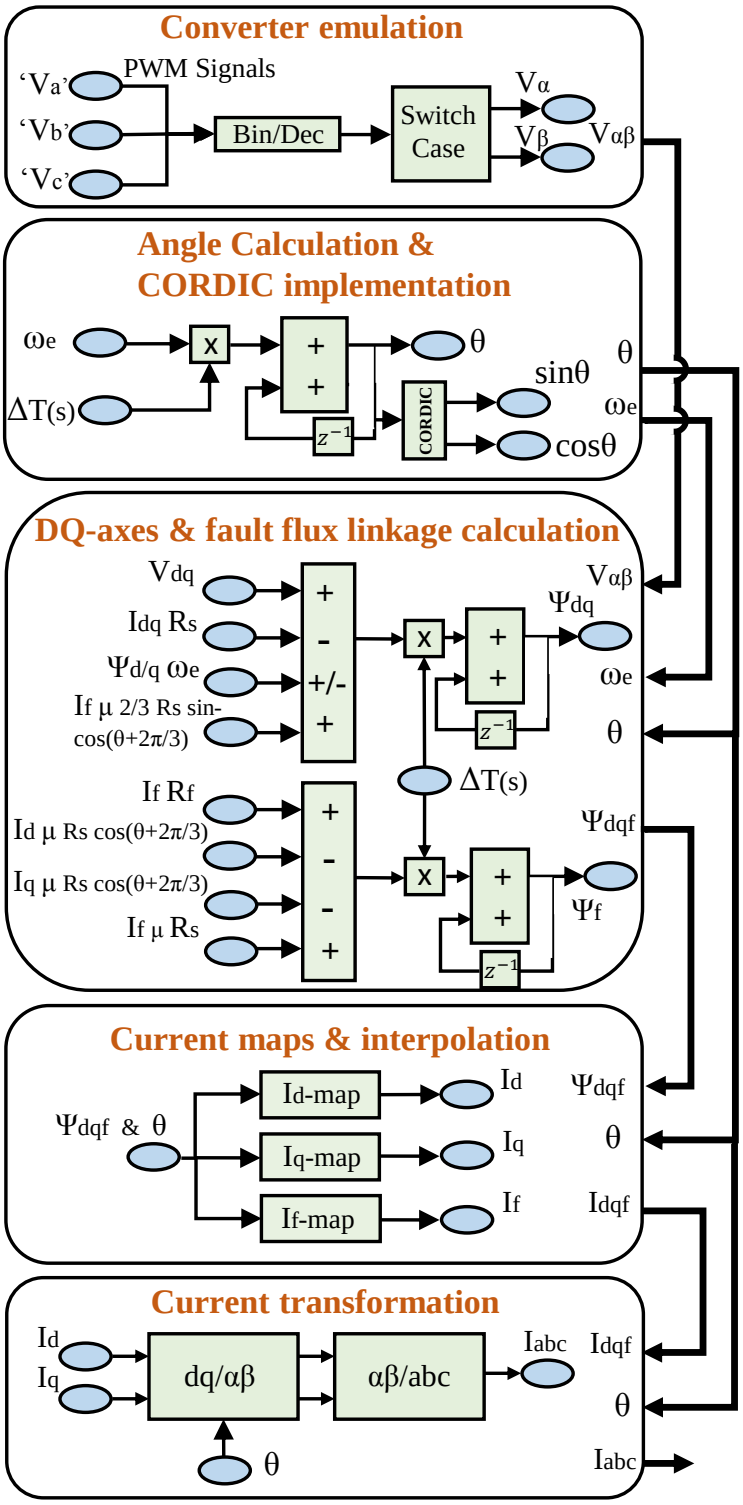

Fig. 3.20. Hardware-in-the-loop design configuration.

State variables and outputs of the model are the stator flux linkages, rotor angle and currents, respectively. Current output calculation is based on the four-dimensional current maps (63). Since FPGAs do not support multidimensional memory storage, the four-dimensional arrays containing *dq*-axes and fault currents as functions of

$\psi_d, \psi_q, \psi_f, \theta$ have been rearranged in a one-dimensional array. A computationally efficient method of memory addressing based on four-dimensional linear interpolations on one-dimensional arrays of data has been implemented as schematically illustrated in Fig. 3.21. LabVIEW FPGA presents a block capable of performing linear interpolation, however it does not allow fixed point characteristics configuration and is computationally more intensive. In principle, the interpolation problem is bilinear in nature but the proposed method is shown to work, possibly due to the relative simplicity of the current maps. The 4D look-up table is based on the application of four successive one dimensional interpolations. Appropriate offsets, depending on the spatial discretization in the $\psi_d, \psi_q, \psi_f, \theta$ space and the resulting number of elements in the tables, are required to access the correct position in the unidimensional memory array. For the case under study there are 12 steps in d-axis flux, q-axis flux, and faulted coil flux and 61 steps in rotor position θ, resulting in 105,408 elements per current map. Given the relative complexity of such system, pipelining must be employed for parallel data processing.

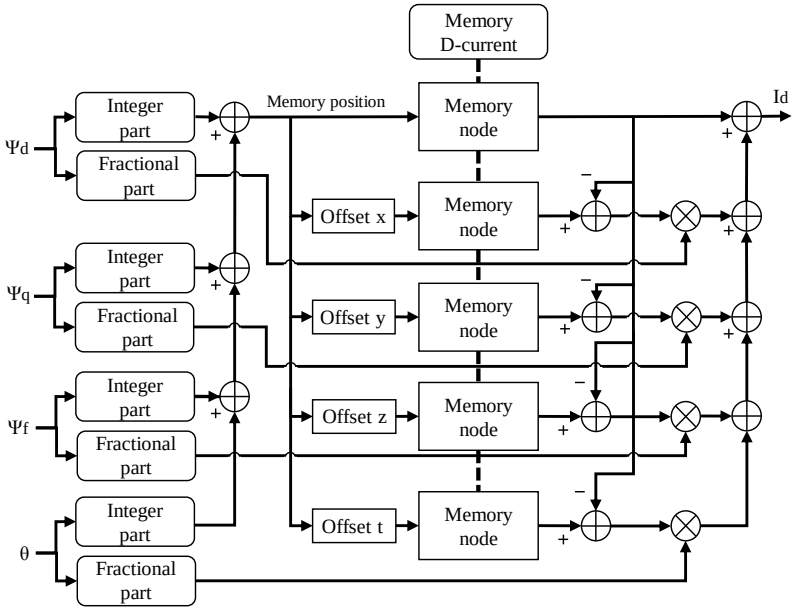

Fig. 3.21. Interpolation system block diagram consisting in four concatenated linear interpolations for *dqf*-flux and angle.

For computational efficiency and speed of execution only FPGA's internal block RAM is used for data storage of the look-up tables. The use of incremental inductances proposed e.g. in [52] might have increased storage requirements resulting in the need for additional external memory with additional overhead in terms of access time.

Three phase converter emulation has been carried out considering only 8 switching states including two zero states as seen in Table III. Dead times are not considered for this application but can be easily included.

TABLE III

THREE PHASE CONVERTER SWITCHING STATES

Switching State	Switches ON	Space vector	Va	Vb	Vc
0	Q_2,Q_4,Q_6	$V_1(0,0,0)$	0	0	0
1	Q_1,Q_4,Q_6	$V_2(1,0,0)$	$\frac{2}{3}$ Vdc	$-\frac{1}{3}$ Vdc	$-\frac{1}{3}$ Vdc
2	Q_1,Q_3,Q_6	$V_3(1,1,0)$	$\frac{1}{3}$ Vdc	$\frac{1}{3}$ Vdc	$-\frac{2}{3}$ Vdc
3	Q_2,Q_3,Q_5	$V_4(0,1,0)$	$-\frac{1}{3}$ Vdc	$\frac{2}{3}$ Vdc	$-\frac{1}{3}$ Vdc
4	Q_2,Q_4,Q_5	$V_5(0,1,1)$	$-\frac{2}{3}$ Vdc	$\frac{1}{3}$ Vdc	$\frac{1}{3}$ Vdc
5	Q_1,Q_4,Q_5	$V_6(0,0,1)$	$-\frac{1}{3}$ Vdc	$-\frac{1}{3}$ Vdc	$\frac{2}{3}$ Vdc
6	Q_1,Q_4,Q_5	$V_7(1,0,1)$	$\frac{1}{3}$ Vdc	$-\frac{2}{3}$ Vdc	$\frac{1}{3}$ Vdc
7	Q_1,Q_3,Q_5	$V_8(1,1,1)$	0	0	0

TABLE IV.

HARDWARE RESOURCES EMPLOYED IN REAL-TIME SIMULATION

Resources	Slice Registers	Slice LUTs	Block RAMs	DSP48 Blocks
Total Emulator	7235/184304 3.9%	14622/9215 15.9%	265/26 98.9%	166/18 92.2%
***dq* to ABC transformation**	1039/184304 0.6%	794/92152 0.9%	0/268 0%	4/180 2.2%
Current Maps & Interpolation	1218/184304 0.7%	1646/92152 1.8%	265/268 98.9%	0/180 0%
Flux Equations	1668/184304 0.9%	1487/92152 1.6%	0/268 0%	16/180 8.9%
Angle Calculation	1675/184304 0.9%	2074/92152 2.3%	0/268 0%	30/180 16.7%
Output & Measure	1617/184304 0.9%	1617/92152 1.8%	0/268 0%	1/180 0.6%

Table IV lists the FPGA resource usage for the proposed model. The most demanding subsystem in terms of resources is the look-up table allocation which results in 99% usage of the available block RAM. Most of the arithmetic calculations based on adders/multiplier and accumulator is implemented using the available DSP48 blocks.

Higher resolution in the current/flux maps, and hence bigger look-up tables, can easily be obtained with bigger and more expensive FPGAs or using external RAM.

Table V lists the rate of execution of each sub-system of the real-time simulation. In particular the table shows the number of cycles of the 40MHz clock required for the calculation of each subsystem. The most demanding is the current maps interpolation. Since all parts are executed in parallel, the total rate of execution is determined by the slowest, i.e. the current interpolation which requires 1.25μs. Digital to analog conversion for outputting current waveforms is executed in parallel at 115kS/s as limited by the available Digital-to-Analog Converter (DAC). Faster DACs can in principle be used.

TABLE V.

NUMBER OF CYCLES AND RATE OF EXECUTION OF REAL-TIME SIMULATION

Cycles & Execution	**Number of Cycles**	**Rate of Execution**
***dq* to ABC transformation**	10	250*ns*
Current Maps & Interpolation	50	1.25μs
Flux Equations	8	200*ns*
Angle Calculation	43	1.075μs
Output & Measure	349	8.725μs

The proposed method based on interpolation over 4-D LUTs results in significantly shorter execution time compared with iterative methods required for solving the nonlinearities resulting from iron saturation effects. As an example, several hundreds μs with a 100MHz clock are required in [38] for solving the nonlinear permeance network with an iterative Newton-Raphson algorithm. Similar latencies to those shown in Table V are reported in other publications that use analytical models or look-up tables e.g. [41], [47].

B. Healthy Parallel Implementation

In addition to the implementation of a fault model running on an FPGA, and thus capable of emulating the fast dynamics of an electric machine, a healthy only model is implemented in a different platform, in parallel with a real machine, with the aim of carrying model-based fault detection based on residuals obtained through comparison of their current outputs. Model-based fault detection is described in detail in Chapter 4.

Prior to comparison with a real machine, the healthy only parallel model is implemented in an extended version of the arrangement presented in Fig. 3.19 on section A. The new arrangement, shown in Fig. 3.23 and Fig. 3.22, contains an OP5600 OPAL-RT platform running a 3.46GHz, Virtex-6 FPGA and 6-core CPU, where the parallel model is implemented.

While in reality only two phase currents are needed as control feedback, the current residual is generated for the three phases in the same device than the parallel model is run. Synchronization between models is obtained through machine position, which can be provided to the parallel model either by means of a virtual encoder, as it is done for the controller, or by estimation.

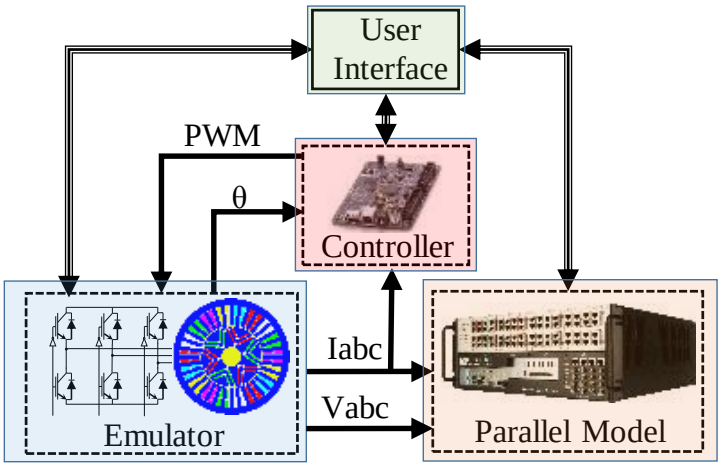

Fig. 3.23. Model-based fault detection HIL arrangement.

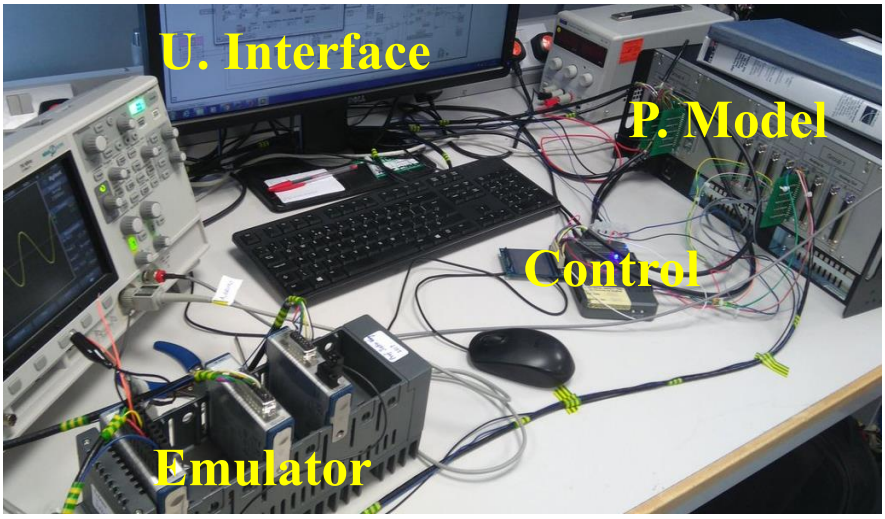

Fig. 3.22. Model-based fault detection HIL experiment showing user interface, machine emulator, control and parallel model platform.

Given the parallel model operates only under healthy conditions, the fault extension provided in equations (64)-(66) is not required, resulting in

$$\psi_d(k+1) = \psi_d(k) + \Delta t\left[v_d(k) - R_s i_d(k) + \omega_e(k)\psi_q(k)\right] \quad (67)$$

$$\psi_q(k+1) = \psi_q(k) + \Delta t\left[v_q(k) - R_s i_q(k) - \omega_e(k)\psi_d(k)\right] \quad (68)$$

3.6. Real-Time Validation Results

Extensive experimental validations against an already available prototype machine have been performed using the dynamometer test rig shown in Fig. 3.24. The prototype IPM machine used for validation is based on the design described in Section III. The machine stator windings shown in Fig. 3.24 allow for the short-circuiting of two turns in phase C through external contactors for emulation of the inter-turn fault. In particular, a three-phase contactor connected to the faulted turns was triggered using a timer circuit tor turn for a relatively short time in the range of hundreds of milliseconds to prevent any machine damage due to overheating. The extra resistance added by the contactor and cabling has been included in the model and add up to approximately 5.5mΩ.

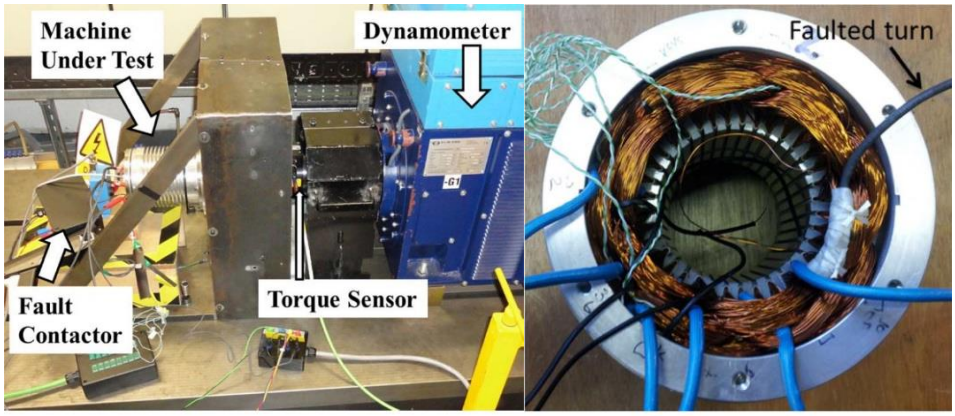

Fig. 3.24. Experimental setup and stator winding with inter turn short circuit fault in phase C.

Validation of the proposed model is performed with the machine driven at constant speed by the dynamometer and operating as generator supplying a three-phase resistive load. Fault transient tests have been performed in a wide range of operating conditions. By way of example, shows the fault current at 3500 r/min on a 2.2Ω. The comparison between FE simulation and the results from the real-time HIL implementation is presented both in time and frequency domain as shown in Fig. 3.25, respectively, showing an excellent agreement.

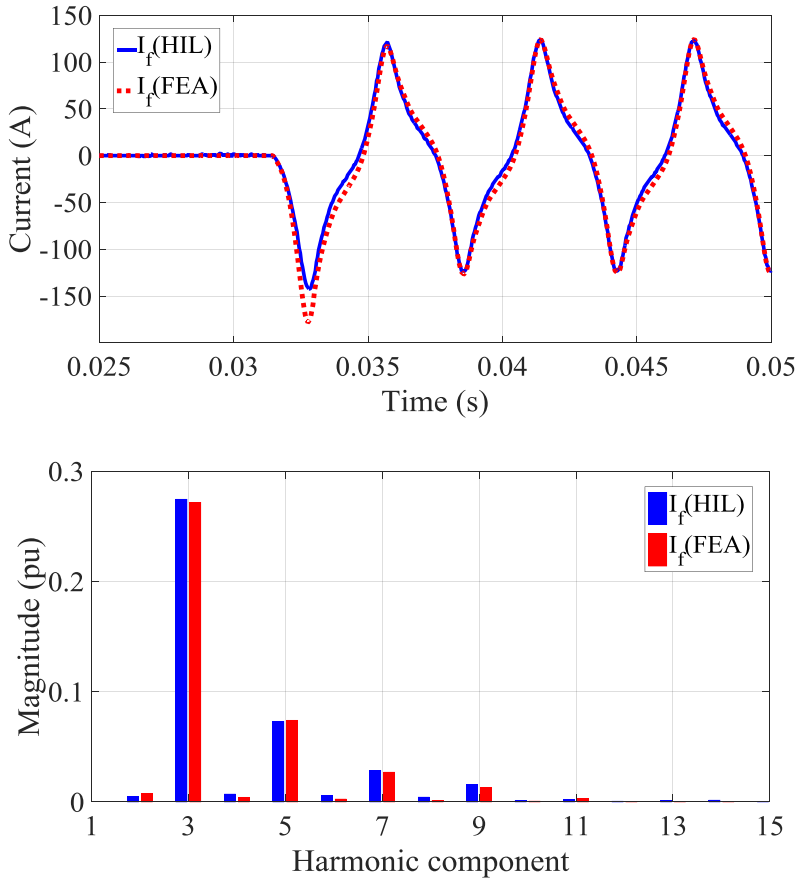

Fig. 3.25. Transient time domain comparison (top) of FEA and HIL fault currents, and FFT comparison (bottom) at 3500 r/min and 2.2Ω load.

Peak and rms fault current results are compared for different speeds ranging from 500 to 6500 r/min and four different load conditions (no load, 2.2Ω, 1Ω and 069Ω) as shown in Fig. 3.26. FEA results are shown in a dotted blue line, HIL results in red and finally, experimental results are shown in green.

In general, a good match between FEA, HIL and experimental results is shown, with a maximum error below 15% occurring at lower rotor speeds and lower load resistance. The main cause of error is the poor repeatability of the contactor resistance which varies from 2 to 2.5mΩ (25% variation) at different contactor closures during the experiments. At lower speeds, the resistive component dominates the overall fault impedance compared with higher speeds, where the dominating contributor is inductance.

Fig. 3.27 show measured and simulated fault current waveforms in four different conditions at rotor speeds of 1500 and 5500 r/min under no load and at 0.69-Ω load, respectively. Fig. 3.28-Fig. 3.30 show comparisons in *d*- and *q*-axis current ripples in three different operating conditions at 5500 and 3500 r/min, respectively, confirming the

good agreement between the proposed real-time modelling and the experimental measurements.

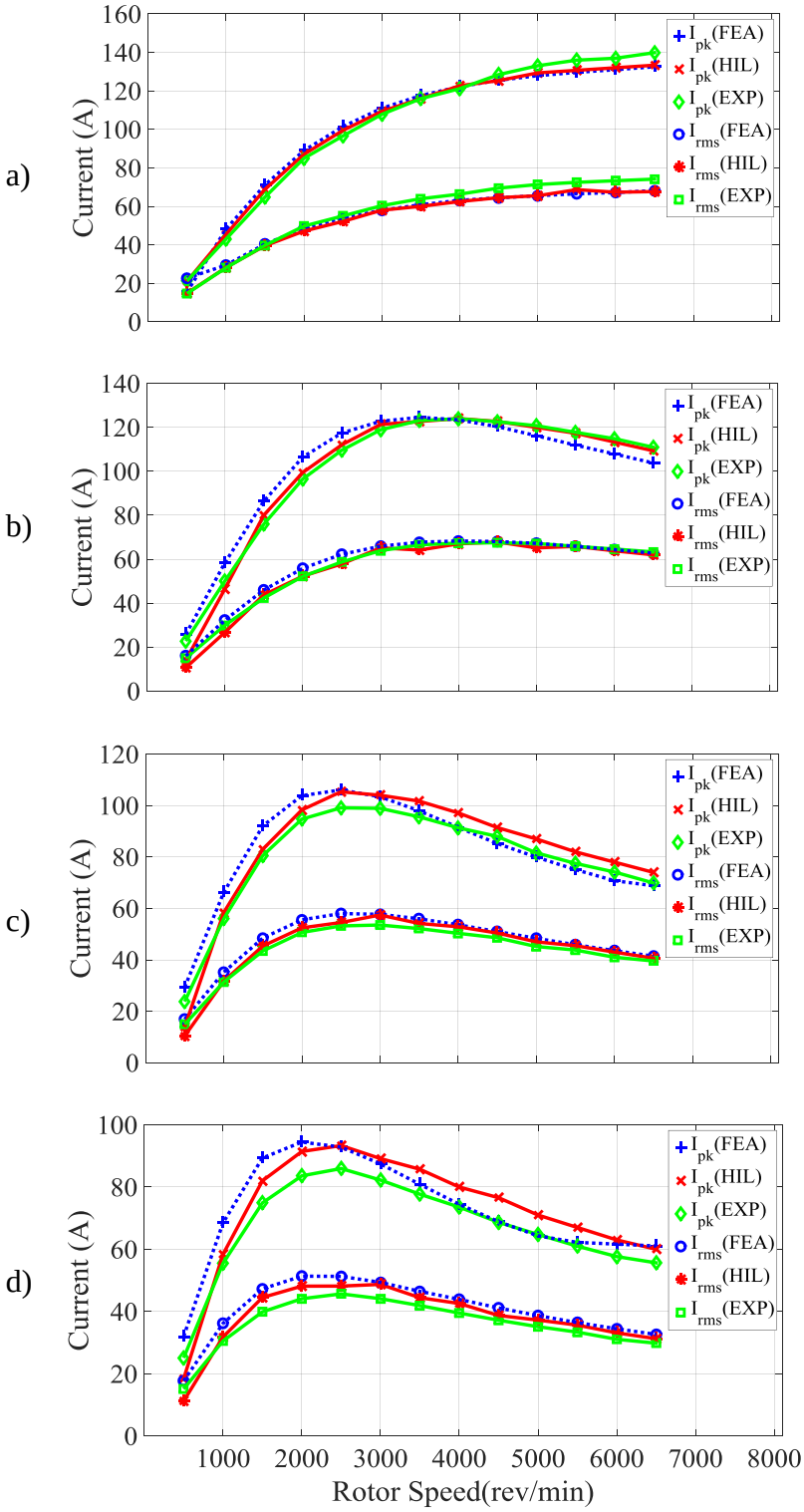

Fig. 3.26. Comparison of FE based simulation, hardware-in-the-loop (HIL) and experimental (EXP) rms and peak fault current values at various speeds and loads. (a) No load (b) 2.2Ω, (c) 1Ω and (d) 0.69Ω.

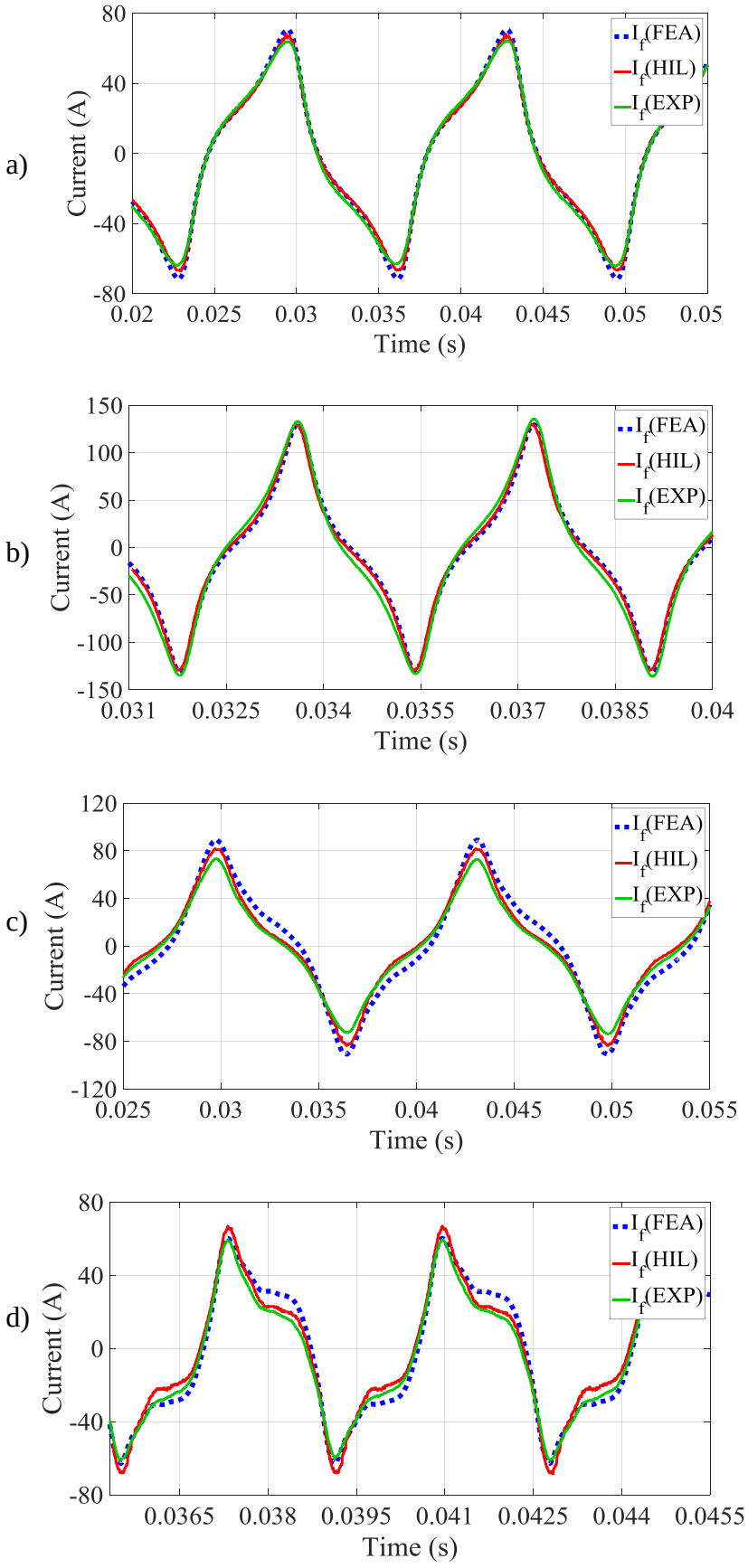

Fig. 3.27. Comparison of FE based simulation, hardware-in-the-loop (HIL) and experimental (EXP) fault currents at (a) 1500 r/min and no load, (b) 5500 r/min and no load, (c) 1500 r/min and 0.69Ω load, and (d) 5500 r/min and 0.69Ω load.

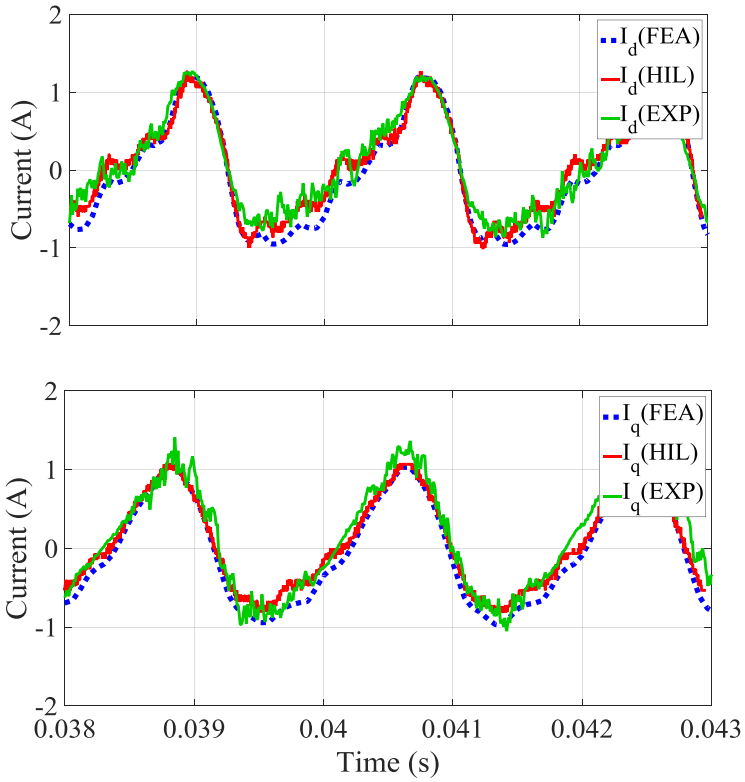

Fig. 3.28. Comparison of FE based simulation, hardware-in-the-loop (HIL) and experimental (EXP) *d*-axis current (top) and *q*-axis current (bottom) at 5500 r/min and 2.2Ω load.

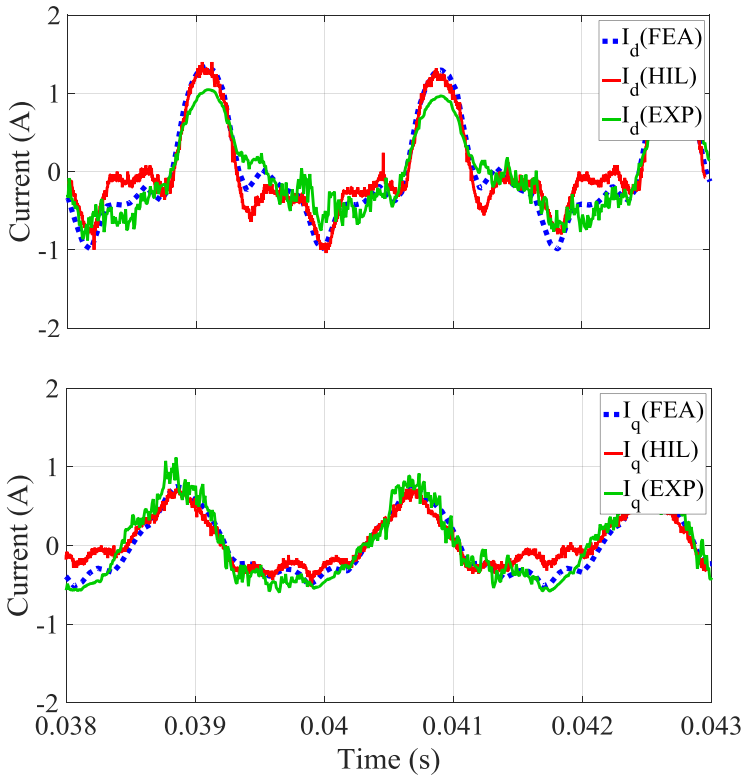

Fig. 3.29. Comparison of FE based simulation, hardware-in-the-loop (HIL) and experimental (EXP) *d*-axis current (top) and *q*-axis current (bottom) at 5500 r/min and 0.69Ω load.

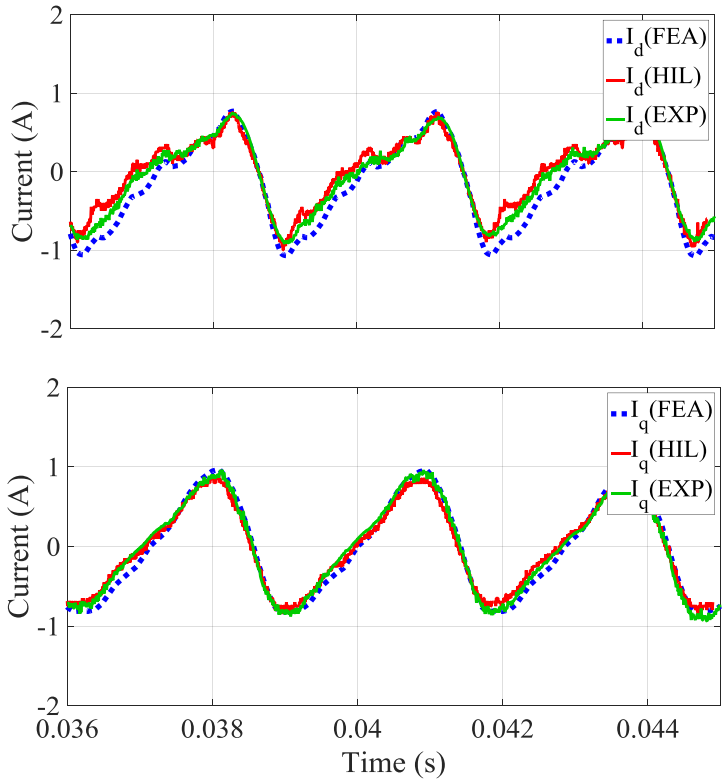

Fig. 3.30. Comparison of FE based simulation, hardware-in-the-loop (HIL) and experimental (EXP) *d*-axis current (top) and *q*-axis current (bottom) at 3500 r/min and 2.2Ω load.

3.7. Example of Application

In order to demonstrate the application of the proposed real-time emulation to the development and test of fault detection strategies, two fault transients cases are presented here. Fig. 3.31 shows the output currents following the inter-turn short-circuit fault when the machine is operated in both generator mode supplying a 2.2Ω resistive load, on the left, and motoring mode, on the right. The motoring mode is driven by a virtual inverter operating at 10kHz switching frequency and controlled with standard FOC using the platform of Fig. 3.19. In this case, the current control partially compensates for the distortion following the fault, making current signature-based fault detection more difficult. A frequency domain analysis of current in phase C shown in Fig. 3.32, demonstrates the potential application of a fault detection indicator based on tracking of the third harmonic in phase currents [55]. Although many different fault detection techniques exist in literature [25], simple strategies as the previously mentioned may be used as a proof of application. The purpose here is not to propose a novel fault detection method, but to provide a practical application example of the proposed emulation tool for the development of fault detection and classification strategies.

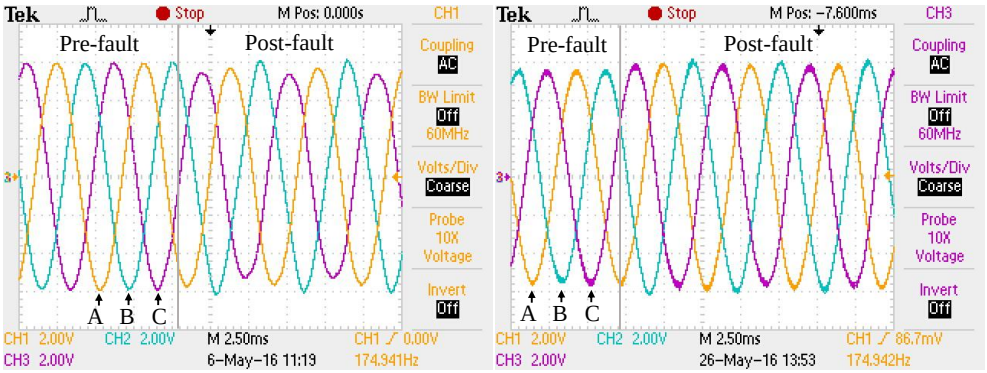

Fig. 3.31. Three phase currents before and after the fault for generating mode (left) and motoring mode (right). Scale: 5 A/div.

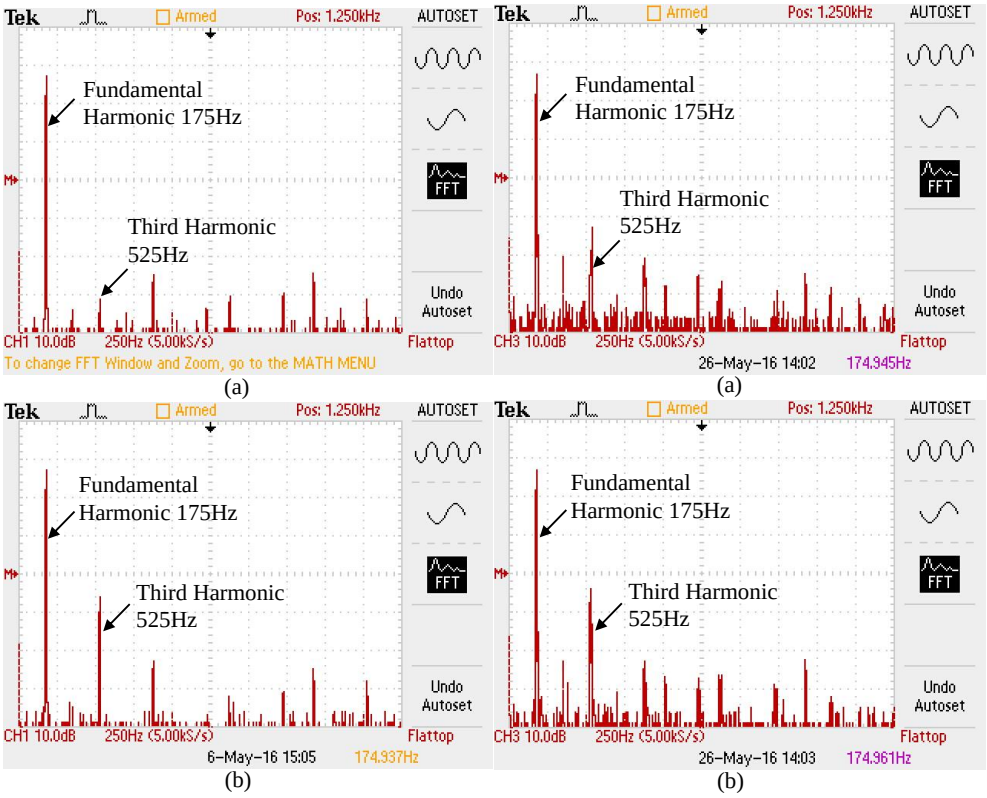

Fig. 3.32. FFT of the faulted phase current I_c (a) before and (b) after the fault for generating mode (left) and motoring mode (right).

The post-fault increase of third harmonics in phase currents results in an increase in the second harmonics in the synchronous *dq*- reference frame currents.

A potentially more robust fault detection method based on the extraction of the second harmonic in the *q*-axis current [64], has also been implemented using a single-frequency Fourier series tracking algorithm schematically illustrated in Fig. 3.33. The resulting fault indicator is shown in Fig. 3.34.

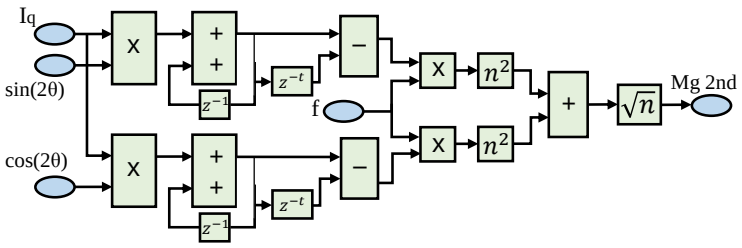

Fig. 3.33. Single-frequency Fourier series second harmonic component magnitude monitoring algorithm.

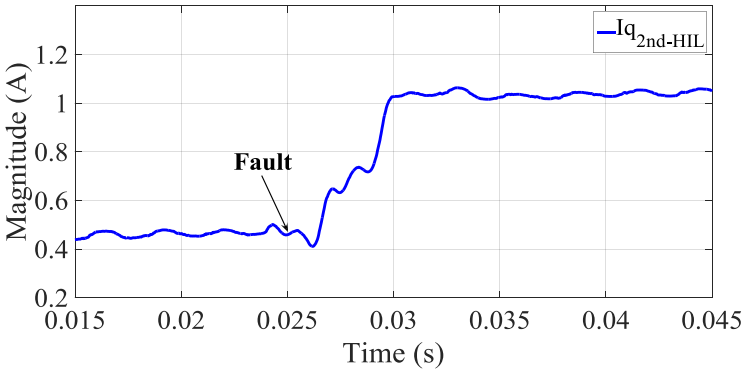

Fig. 3.34. *q*-axis current second harmonic component magnitude before and after the fault.

3.8. Summary

This chapter has presented the selection of a high-fidelity model based on offline FE simulations, suitable for real-time modelling of PMSMs under both healthy and faulty conditions. Additionally, an insight into the behaviour of a machine under inter-turn fault has been provided through transient FEA. The modelling framework of the selected model is in particular suitable for HIL development and tests of motor controllers and is capable of accurately representing machines with stator winding inter-turn faults. Detailed description of the modelling, hardware requirements as well as experimental results for different operating conditions have been presented. The proposed modelling framework is validated through extensive simulation and experimental tests. Potential applications to the development of fault detection strategies are highlighted.

Exploiting the computational efficiency of the model, its real-time implementation on a FPGA platform is discussed, including implications on FPGA resources and execution time.

The validated HIL modelling framework represents a valuable platform for the development of drive control, fault detection and diagnostic algorithms in a safe and

relatively inexpensive environment. The model could also be further refined to account for thermal effects as well as additional fault conditions such as partial demagnetization.

The developed modelling will be used in the rest of this thesis. It accounts for the model used in model-based fault detection presented in Chapter 4 and it has been extensively employed for all simulations of nonlinear conditions in this thesis, particularly in signal-based fault detection described in Chapter 5.

CHAPTER 4

RESIDUAL MODEL BASED FAULT DETECTION

4.1. Overview

Model-based fault detection has a potential benefit of being less sensitive to transient conditions compared to frequency-domain based methods for fault detection, provided accurate machine models are available, allowing for an accurate fault detection whilst avoiding false alarms. This chapter describes a model-based fault detection method that builds on the work published in [116]. The method is based on the analysis of the residual between measured currents and those predicted by the accurate real-time nonlinear model of the machine presented in Chapter 3. The use of the residual provides an effective way to isolate frequency components caused by a fault. The method is implemented and tested in computer simulation and experimentally. Experimental validation is presented at two different sampling frequencies. First, it is sampled at 10 kHz aiming at an implementation running inside the controller. Later it is sampled at a much higher sampling rate of 1 and 2MS/s, depending on the case, independent from the drive system. Whilst its implementation in real-time has not been successfully achieved due to hardware constrains, details about implementation are provided as well, including the testing rig from which the experimental data has been extracted.

A third machine is employed in this chapter, both in terms of model reference as well as experimental validation. The machine was extensively studied in [117]–[119]. It consist on a triple redundant, 9-phase 45kVA Permanent Magnet Assisted Synchronous Reluctance Machine (PMA SynRM) prototype. This machine differs from those used in previous chapters in that it contains nine phases. However, since only one of the 3-phase sets is analysed, and as long as the machine is under balanced conditions, it behaves identically to a 3-phase machine. Its topology is shown in Fig. 4.1, and its characteristics are summarized in Table I. The same experiment rig and thus the same machine is employed as well in chapters 5 and 6.

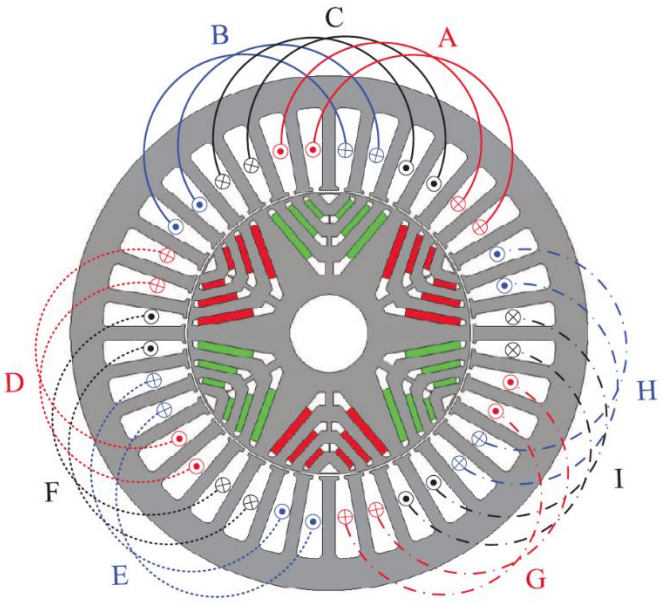

Fig. 4.1. 36 slot-6pole nine phase machine diagram including winding arrangement [118].

TABLE I

NINE PHASE MACHINE CARACTHERISTICS

Characteristic	Value	Unit
Peak Torque	119.4	Nm
Rated Torque	95.5	Nm
Base Speed	4000	rpm
Max Speed	19200	rpm
Peak Power	50	kW
Rated Power	40	kW
DC link Voltage	270	V
Rated Current	120	A
Number of pole-pairs	3	-
Number of Slots	36	-
Turns per coil	8	-
Shaft Diameter	27	mm
Back iron Thickness	10.15	mm
Active Stack Length	110	mm
Stator Diameter	180	mm
Rotor Outer Diameter	103.5	mm
Number Of Phases	9	-

4.2. Fault Detection Method

The residuals are computed by calculating the difference between measured machine's phase currents and the output currents of the FE based nonlinear high-fidelity and computationally efficient model operating under healthy conditions. As it was discussed in Chapter 3, the model is based on precompiled current lookup tables extracted from magnetostatic analysis for all combinations of *dq*-axes currents and rotor position for one electrical revolution. Current maps are obtained as the inverse solution of generated flux linkage maps.

The block diagram in Fig. 4.2 illustrates the proposed methodology. The nonlinear model inputs are the phase voltages measured at the converter output. Residuals $R_{a,b,c}$ are computed by subtracting measured machine's currents from model output currents. These residuals are, in principle, independent from the transient effects caused by speed or load variations, eliminating the probability of false alarms, and improving in general the behaviour of MCSA methods which would otherwise be constrained to stationary conditions.

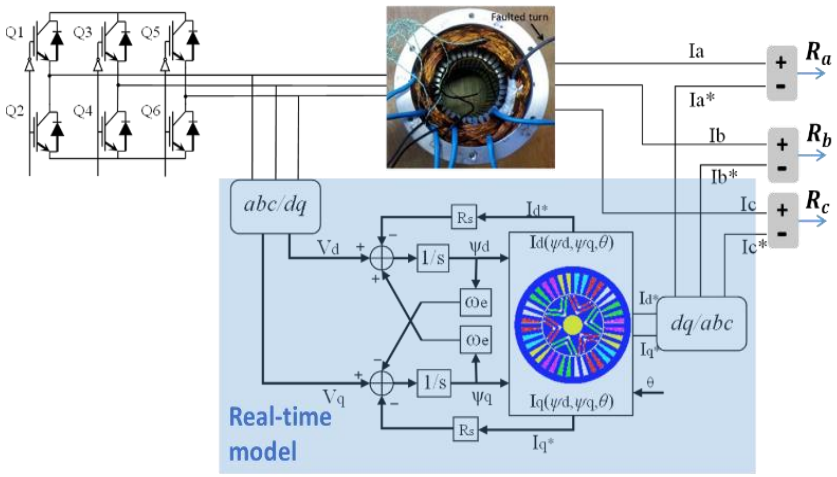

Fig. 4.2. Residual generation diagram.

Theoretically, current residuals should be close to zero during healthy operation and suffer a drastic change right after the fault, as it is shown in section 4.3. In reality however, model inaccuracies due discrepancies between model and actual machine due to manufacturing, the effect of temperature, measurement inaccuracies and switching harmonics created by the inverter, will cause non-zero residuals even in healthy conditions as will be extensively shown in sections 4.6 and 4.7.

4.3. Simulation Results

The method is tested first in an offline computer simulation environment. For this purpose, the nonlinear high-fidelity PMSM model described in Chapter 3, is placed twice in the same simulation environment, as shown in Fig. 4.3. However, at least one of the models, the one on the left in this case, is required to be able to work under faulty conditions, requiring an extension to account for the fault. The fault is created by changing the same value of a fault resistor R_{f1} which short circuits two turns. The model on the right labelled "Healthy only model" is identical to the one on the left but its fault resistor value R_f is kept constant at a value above fault inception. In a real-time implementation such as inside and FPGA, the healthy only model would be simplified to save resources.

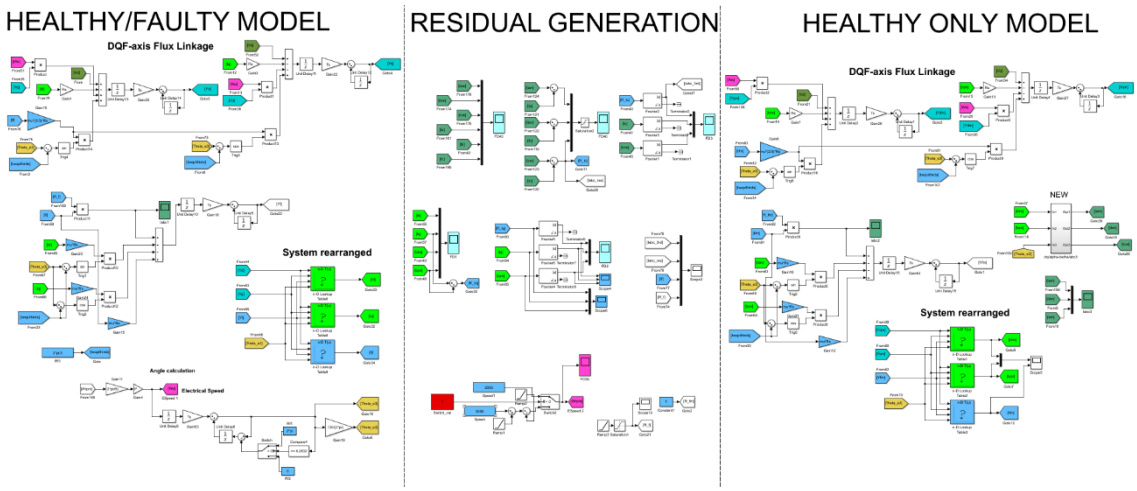

Fig. 4.3. Simulink simulation environment including both models and residual generation.

The simulation shows the effects of the fault process as demonstrated in Fig. 4.4 and Fig. 4.5. Initially, both models operate in healthy conditions and the fault resistor value R_f, as shown in Fig. 4.4 a) and Fig. 4.5 a), is equal to 1Ω. As the value of R_f is gradually reduced towards 5.5mΩ, the third harmonic of the phase current residual and the second harmonic of q-axis current residual, are shown to increase. Similarly, the residuals themselves, obtained from phase current I_c which contains the fault, and q-axis current, as well as the fault current I_f, begin to deviate from the initial zero conditions.

Fig. 4.6 allows a dq-axes current comparison between the extended model, emulating the machine, and the healthy only model. As the models are identical and share the controller, there is virtually no difference in results, until the fault is significant enough.

Once the machine is under fault, the ripple observed in the healthy model is much greater. This is a result of the closed loop current control applied to the fault model which tries to maintain current constant in the *dq*-frame reducing harmonics and ripple at the expense of harmonics in the control voltages. These, in turn, applied to the healthy model result in the expected currents distortion.

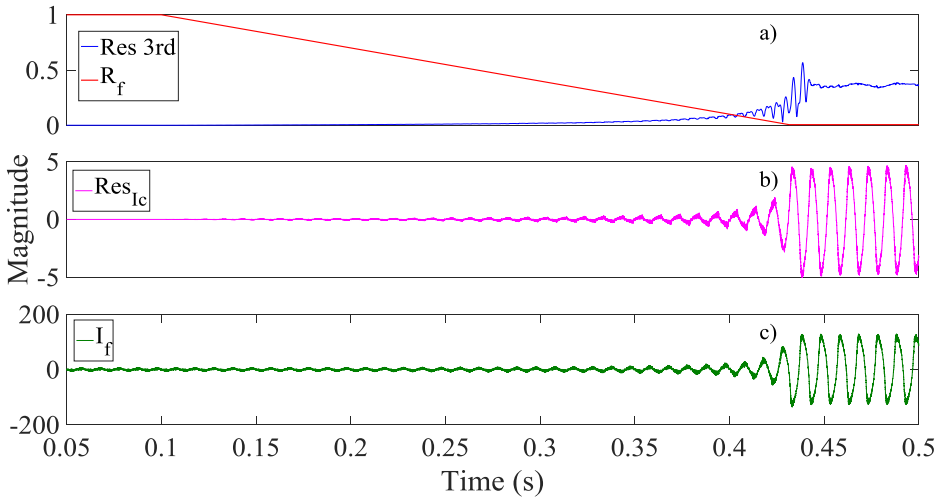

Fig. 4.4. a) R_f versus I_c residual 3rd harmonic, b) I_c residual and c) I_f before and after the fault (caused gradually).

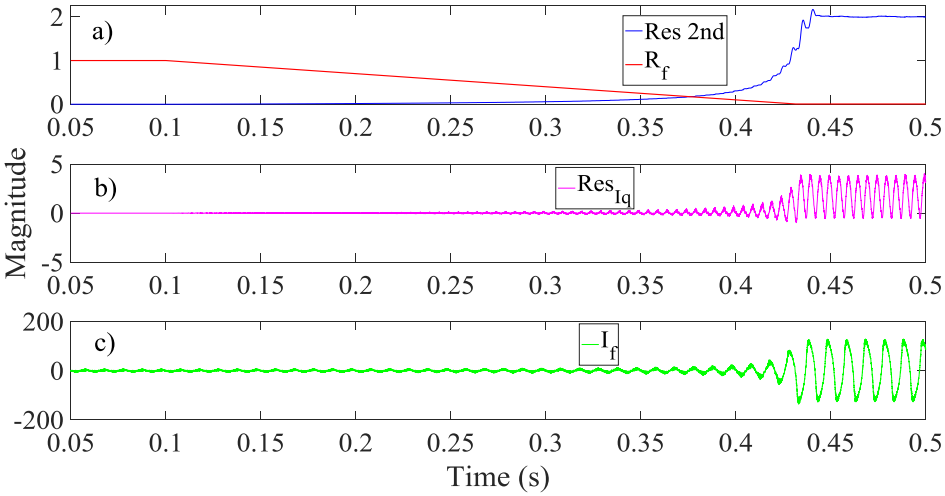

Fig. 4.5. a) R_f versus I_q residual 2nd harmonic, b) I_q residual and c) I_f before and after the fault (caused gradually).

The usefulness of the proposed residuals is clearly depicted in Fig. 4.7 and Fig. 4.8. While the analysed third harmonic for both models does not provide a clear fault indicator in transient conditions, the third harmonic of the residual clearly follows the increased intensity of the fault level, i.e. the decrease in the short-circuit resistance Rf.

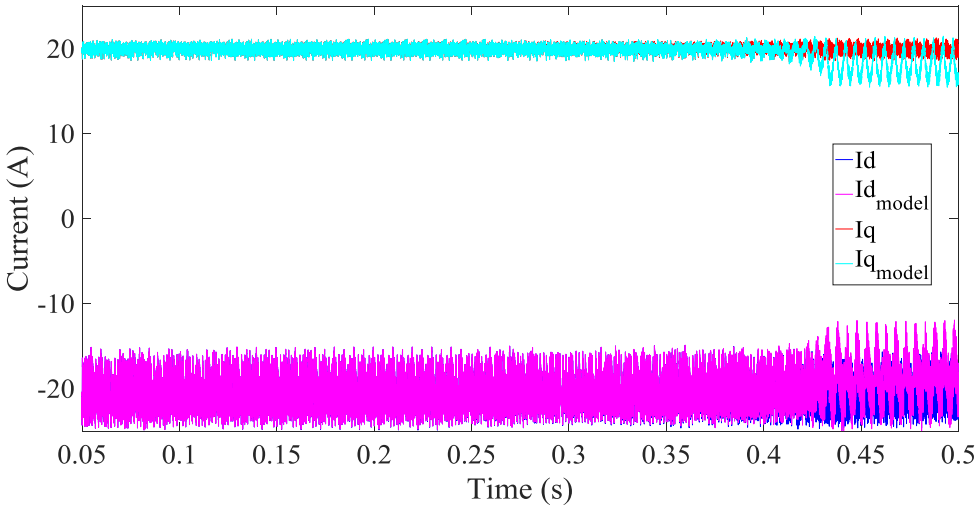

Fig. 4.6. *dq*-axes currents comparison of extended model (blue and red), versus healthy online model (magenta and cyan), before and after the fault.

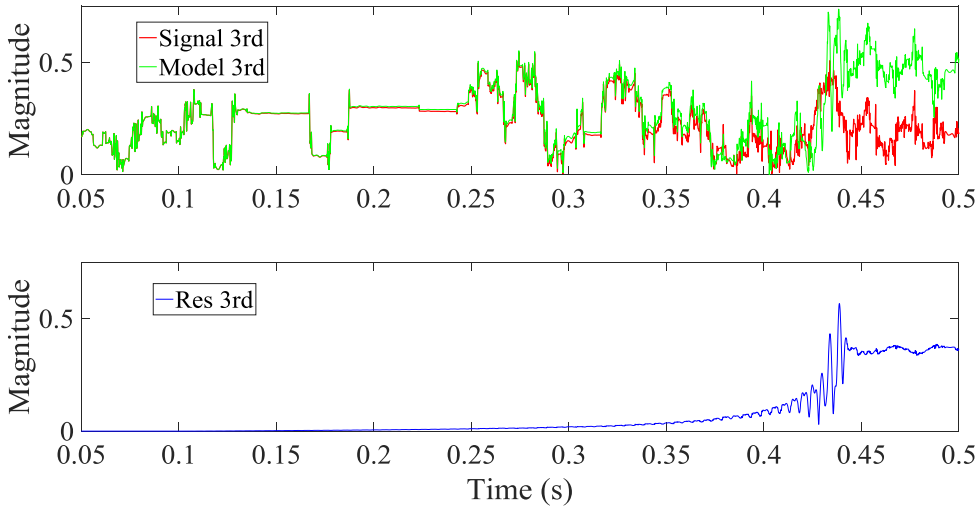

Fig. 4.7. 3rd harmonic of phase current residual (bottom) in blue, versus extended model (red, top) and healthy only model in (green, top), before and after the fault (caused gradually).

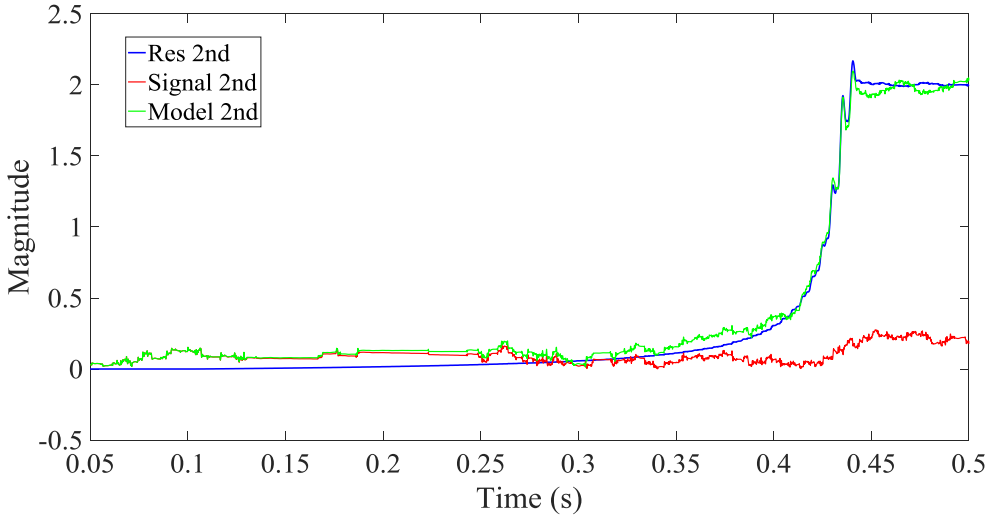

Fig. 4.8. 2nd harmonic of q-axis residual (blue), versus extended model (red) and healthy only model (green), before and after the fault (caused gradually).

On the other hand, both model's and residual's second harmonic of *q*-axis current show the ability to track the fault process. However, the residual is employed since it is in principle, not affected by transient conditions due to load or speed changes. Detailed discussion on calculation of harmonics will be presented in Chapter 5.

Further simulations after a step change in R_f simulating an instantaneous inter-turn fault are shown here. *dq*-axes currents are displayed, together with I_{abc} residuals, and third harmonic response, as shown in Fig. 4.9, Fig. 4.10 and Fig. 4.11.

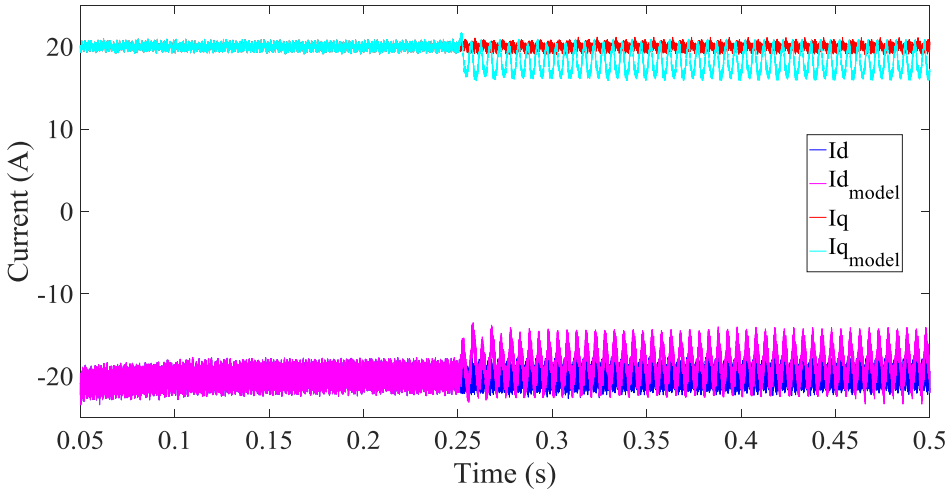

Fig. 4.9. *dq*-axes currents comparison of extended model versus healthy online model under fault conditions (caused instantaneously, by step in R_f).

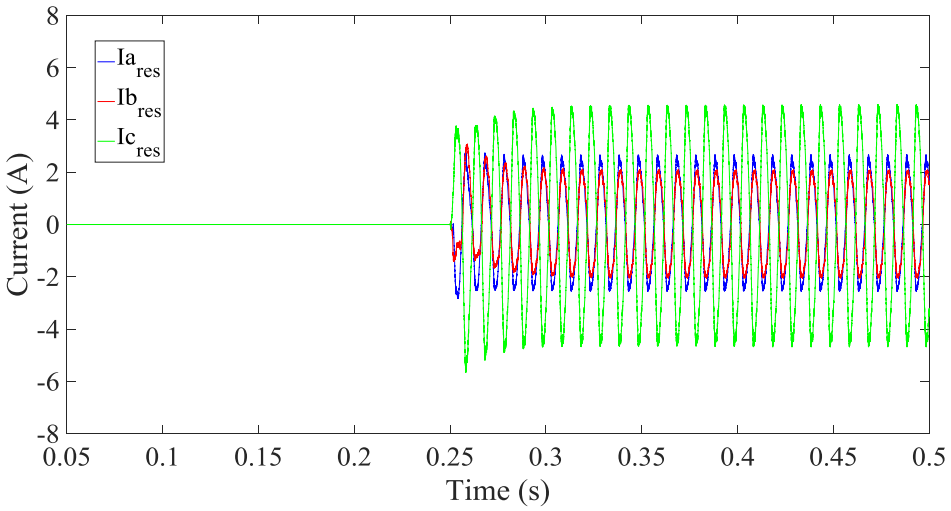

Fig. 4.10. I_{abc} residuals under fault conditions (caused instantaneously, by step in R_f).

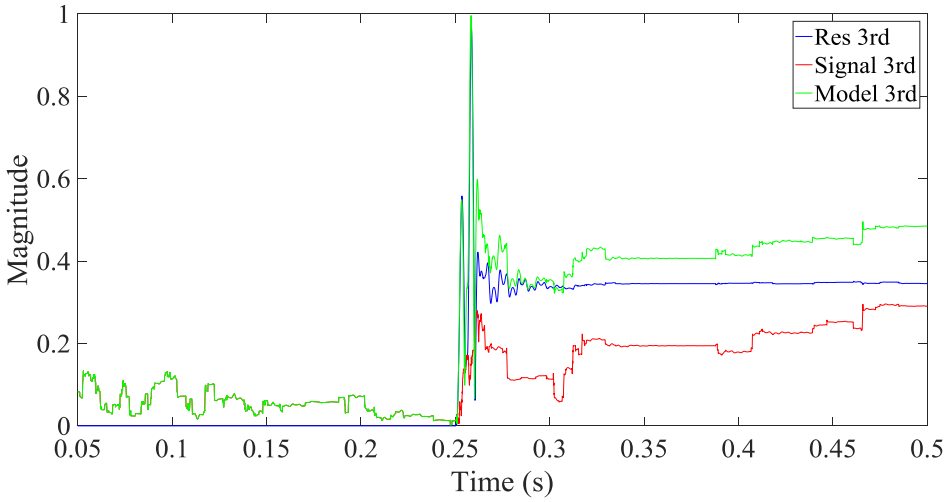

Fig. 4.11. 3rd harmonic of residual, extended and healthy model under fault conditions.

During transient conditions due to a change in loading conditions, *dq*-axes currents, the residual and its third harmonic do not deviate at all as shown by Fig. 4.12-Fig. 4.18. These results provide a proof of concept, which is experimentally validated in sections 1.6 and 1.7. Fig. 4.12-Fig. 4.15 show the response to a current step. As expected, a significant increase of the phase current third harmonic and *q*-axis current second harmonic of both machine and healthy model is generated due to a sudden change of loading conditions.

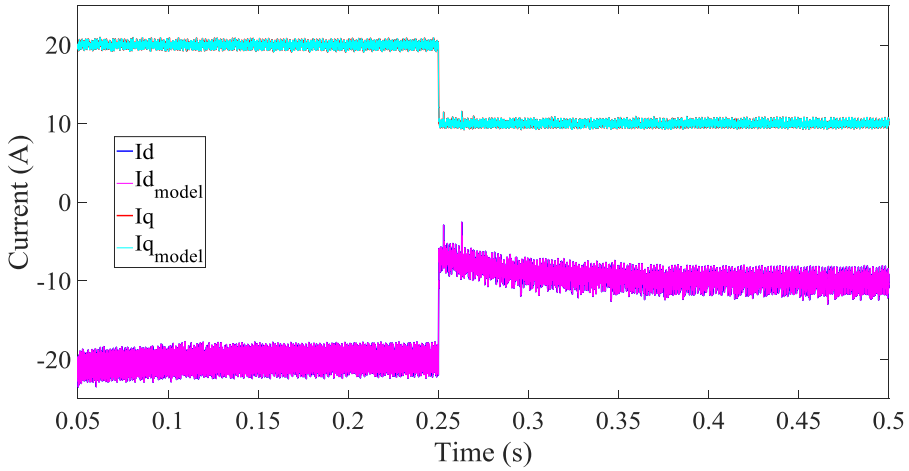

Fig. 4.12. *dq*-axes currents comparison of extended model versus healthy online model under current transient conditions.

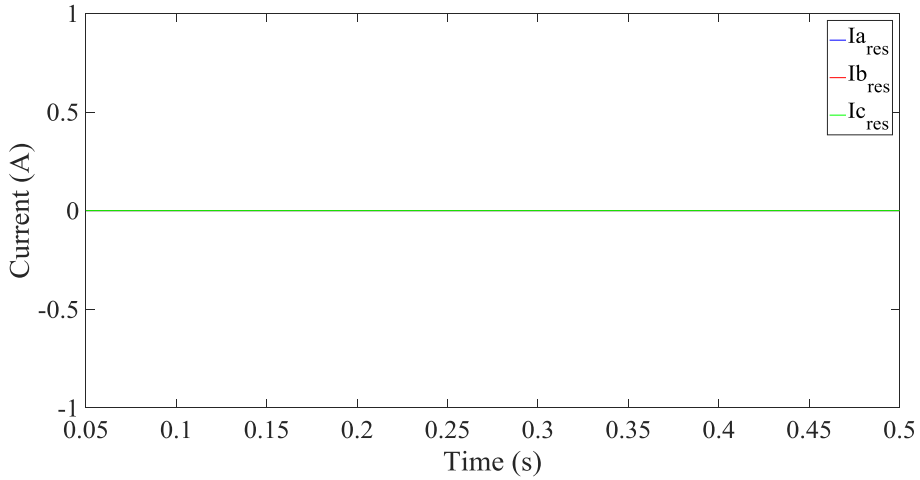

Fig. 4.13. Iabc residuals under current step transient conditions.

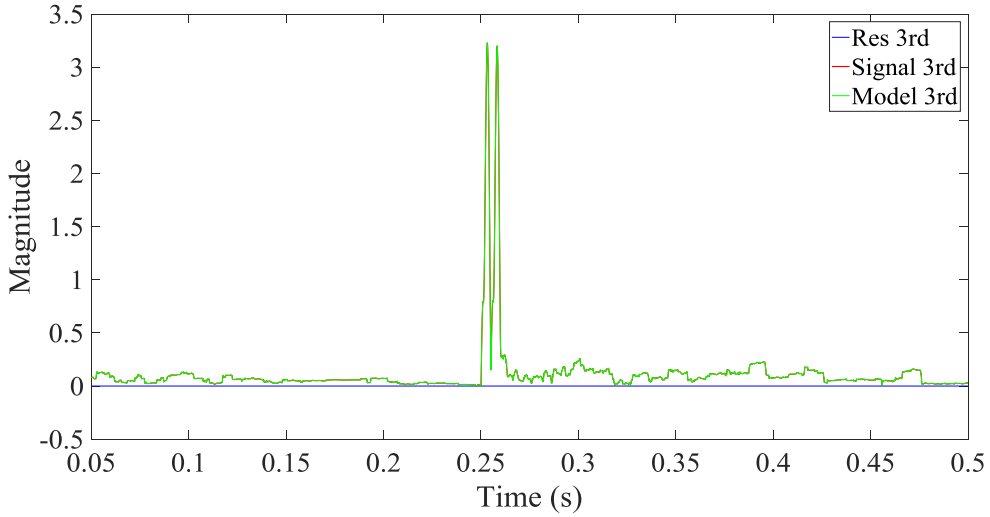

Fig. 4.14. 3rd harmonic of phase current residual, extended and healthy model under current transient conditions.

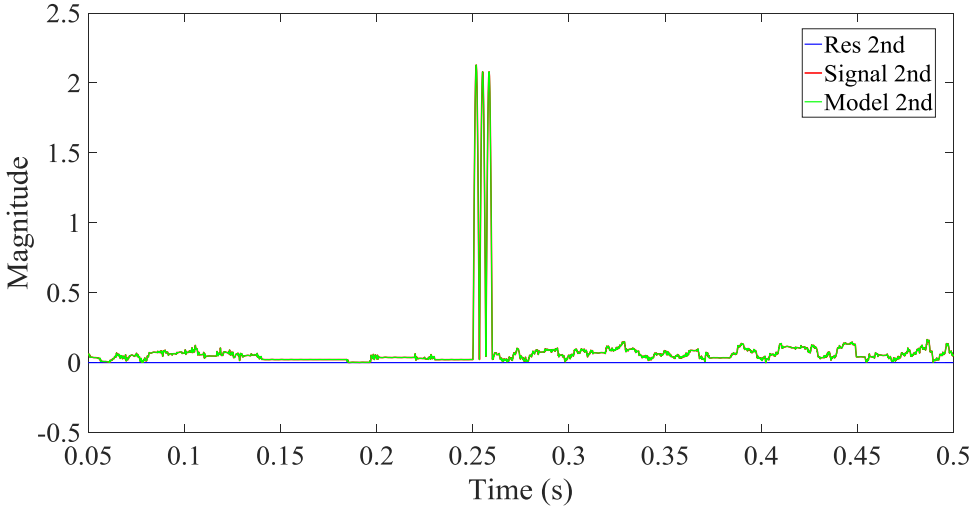

Fig. 4.15. 2nd harmonic of *q*-axis current residual, extended and healthy model under current transient conditions.

On the other hand, a speed ramp, shown in Fig. 4.16-Fig. 4.18, should not have a significant effect on the third harmonic. However, given the inability of the single Fourier series analysis employed to track the change of fundamental frequency, the third harmonic of both machine and model seem greatly affected by this transient, while the residual's is again equal to zero. Whilst the second harmonic of *q*-axis current for both machine and model does not ramp up as seen for phase current third harmonics, there is still a visible effect, even under ideal conditions. Under speed ramp conditions, residuals themselves are equal to zero similarly to what was shown in Fig. 4.13 for load transient conditions.

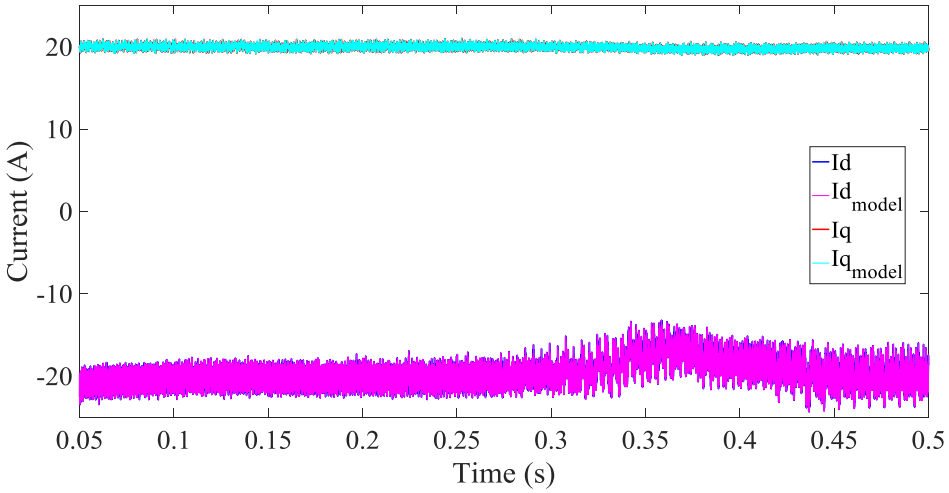

Fig. 4.16. *dq*-axes currents comparison of extended model versus healthy online model under speed transient conditions.

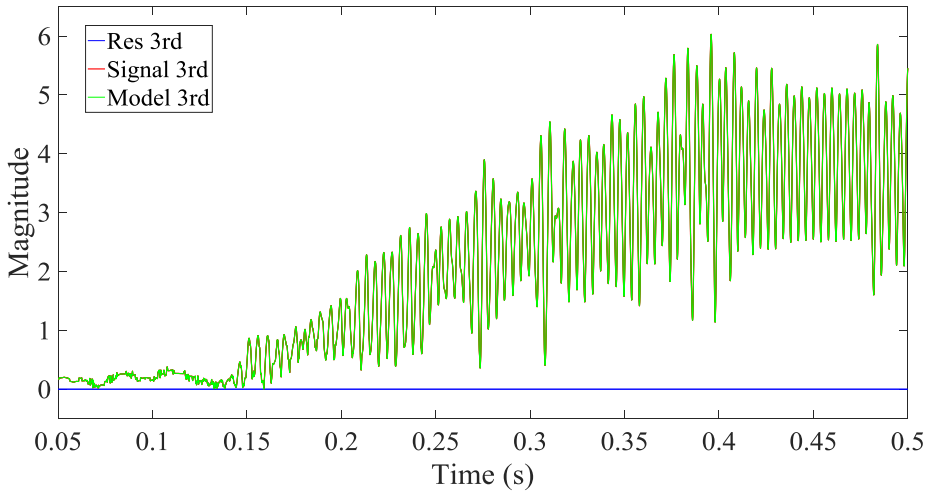

Fig. 4.17. 3rd harmonic of phase current residual, extended and healthy model under speed transient conditions.

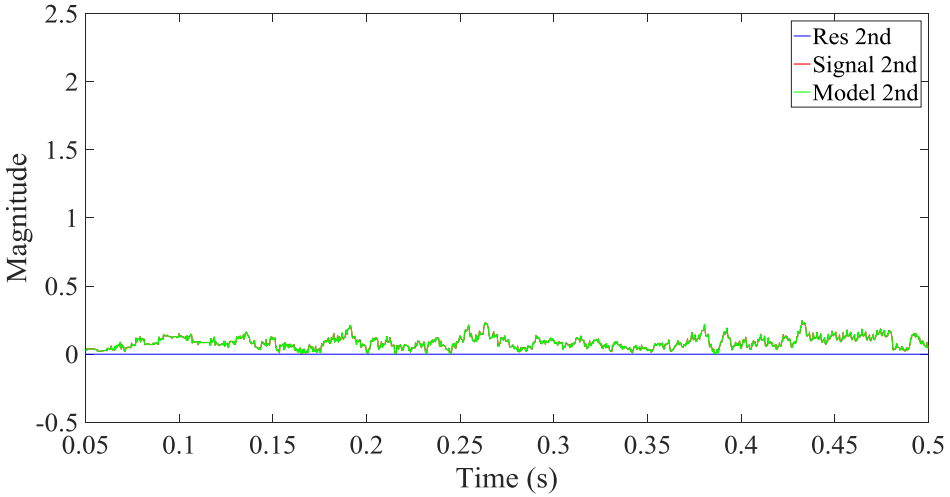

Fig. 4.18. 2nd harmonic of *q*-axis current residual, extended and healthy model under speed transient conditions.

4.4. Implementation of the proposed methods

As a preliminary step, the method has been tested in a real-time HIL implementation, then using data sampled at 10kS/s and 1MS/s on an experimental test rig.

For the HIL arrangement, the same model is implemented in two different platforms as it was showed in Chapter 3, section 1.5 B. One of them emulates the machine with fault capability while the other emulates the reference healthy machine. The model accounting for the fault was originally presented in [18] and adapted for real-time Hardware-in-the-loop (HIL) in [120].

Experimental validation has been performed using data collected from a 9-phase 45kVA aerospace starter-generator drive prototype [118] mounted on an electrical dynamometer rig to allow for operation at different conditions. The machine is composed of three sets of three phases. During healthy operation, the machine behaves as a three phase machine simplifying the modelling task. Details on modelling and construction of the machine are presented in [118], [121].

The use of converter output voltages as inputs to the model is relatively straight forward, the only exception been the need to compensate for nonlinear behaviour of employed semiconductor devices not accounted for in the model, as shown in [117]. Device forward voltage drop and deadtime distortion are taken into account and computed based on available data from the manufacturer. Forward voltage drop can be adjusted by adding an R_{Vce} coefficient to the stator resistance in (1). Deadtime distortion however, requires compensation in the three phase voltages described by

$$V_{td} = -sgn(i_L)t_d f_s V_{dc} \quad (4)$$

where the load current $\boldsymbol{i_L}$ determines the polarity of the error voltage, $\boldsymbol{t_d}$ is the deadtime, $\boldsymbol{f_s}$ the sampling frequency and $\boldsymbol{V_{dc}}$ the DC link voltage value [122]. Additionally, compensation to account for the voltage input common mode is necessary to improve the behaviour of model outputs and computed residuals.

Finally, an attempt to validate the method online was carried out employing the same experiment rig used to gather data for offline simulation. The machine consists on a triple-redundant Permanent Magnet Assisted Synchronous Reluctance Machine (PMA SynRM) prototype, designed as an aerospace starter-generator. The model is implemented on an OP5600 OPAL-RT platform running a 3.46GHz, 6 core CPU and Virtex-6 FPGA.

The experimental setup is shown in Fig. 4.19. A high precision in-line torque transducer is employed to mount the machine on a dynamometer. The machine is oil cooled and driven by three independent 3-phase inverters controlled through digital signal processor (DSP) based current feedback loop which are water cooled as seen in Fig. 4.20. Three phase voltages are acquired by differential voltage probes measuring from three phase connections with the inverter to machine neutral, employing the turn fault relay as shown on the right bottom corner of Fig. 4.19.

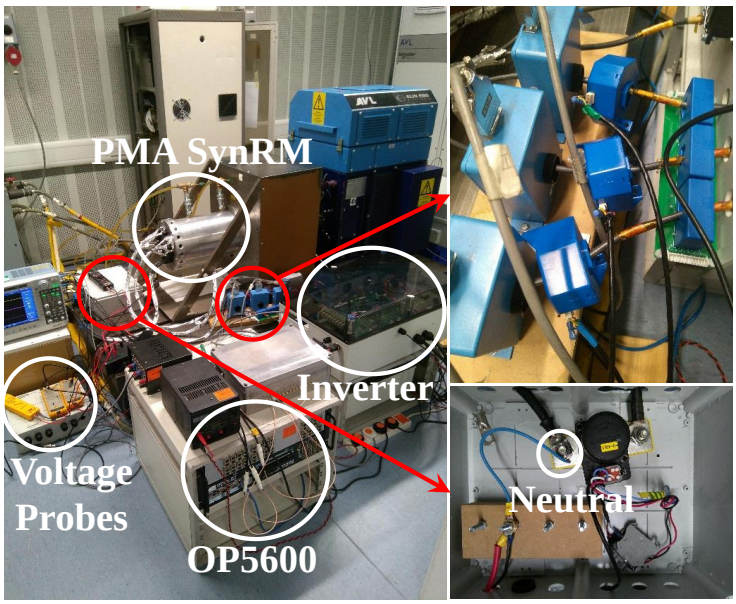

Fig. 4.19. Experimental Test Rig including phase current sensors and turn fault relay.

Only one current sensor is required by phase, however, three are shown in Fig. 4.19. One was employed for the validation under analysis, one was already in place as part of

the rig to provide feedback to the current controllers, and an additional was in place connected to a power analyser to extract additional information and to provide a means to visualise the effects of commands to the dynamometer.

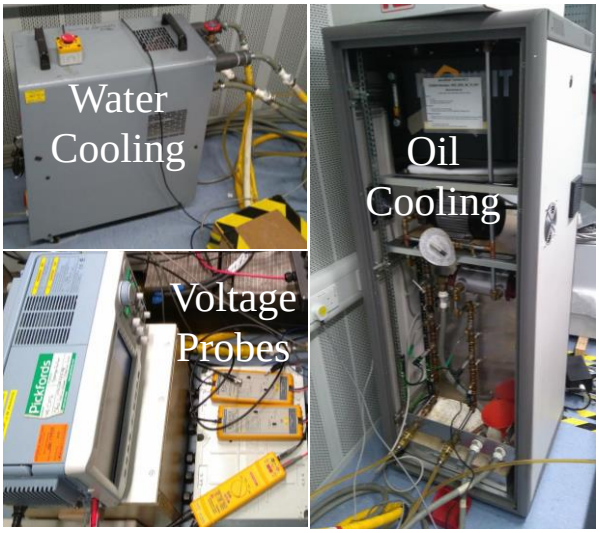

Fig. 4.20. Experimental Test Rig water and oil cooling, and differential voltage probes.

4.5. Hardware-in-the-Loop Results

Results from the real-time HIL emulation are reported in this section. A single case containing both fault and load variation is under study in this section. The fault is generated at around 1.49s and the load variation at around 4.9s. One of the phase currents for both faulty machine emulator (blue) and healthy model (red), the residual obtained from subtracting them (black) and the fault current (green) are shown in Fig. 4.21, and zoomed in at the fault instant in Fig. 4.22. A residual is generated for both phase current C (which contains the fault) and *q*-axis current. Once the residual is computed, the third harmonic of phase current and second harmonic of q-axis currents are plotted for healthy model, machine emulator and residual, and compared.

In Fig. 4.23 it is possible to see that both phase currents and residual show an increase in the third harmonic's magnitude. After the load variation, done in the form of a current, step has been included, both models show a sudden peak in phase current third harmonic but there is no visible effect on the residual one. This proves the ability of the residual to avoid false alarms when aiming at fault detection. The third harmonic increase is introduced into the healthy model as well through the voltage inputs but its magnitude is much smaller compared to the machine emulator one. Given the HIL rate of execution is

in the range of microseconds, fault detection time is not greatly affected by computation time, achieving reliable detection in a few milliseconds.

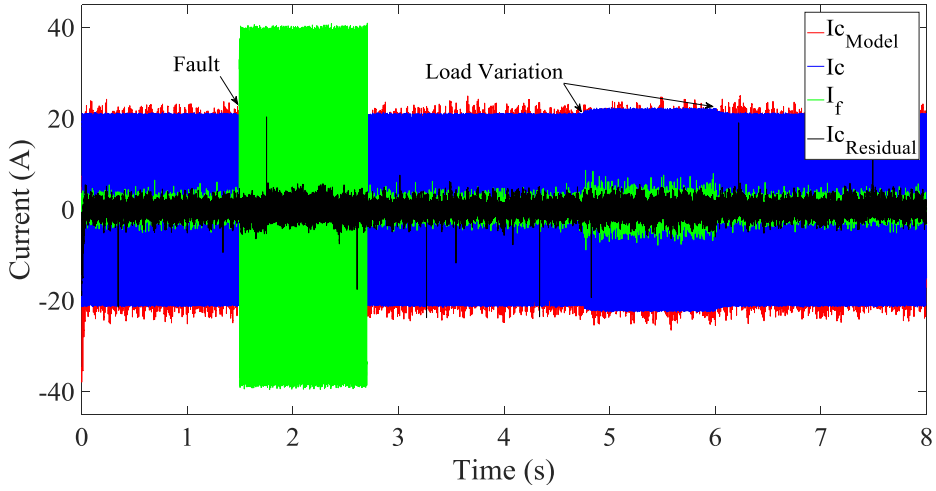

Fig. 4.21. HIL emulation test case including phase c current for model, HIL and residual, and fault current.

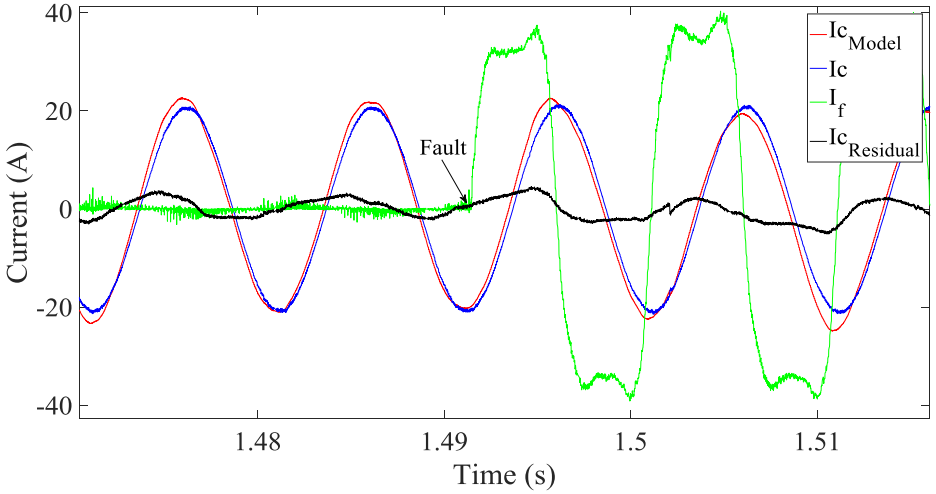

Fig. 4.22. HIL emulation case fault transient including phase c current for model, HIL and residual, and fault current.

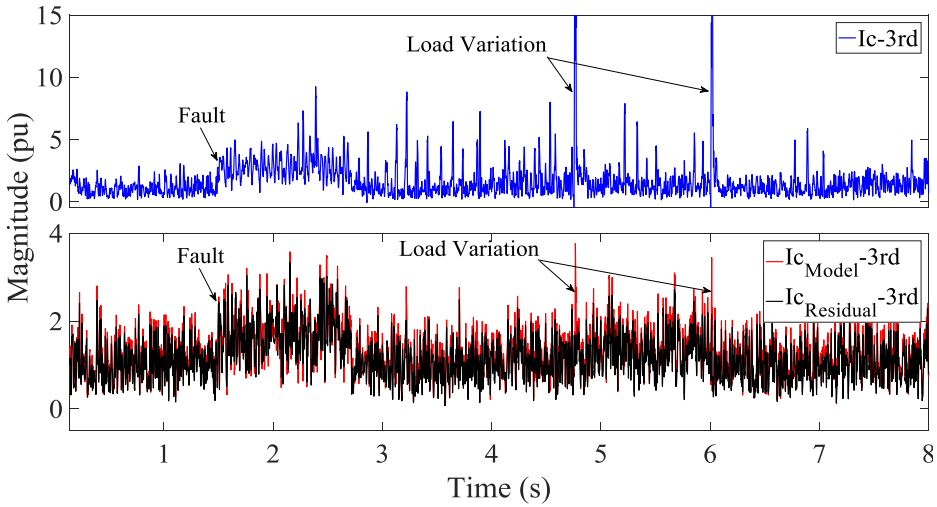

Fig. 4.23. Normalized third harmonic components of phase current of machine emulator, healthy model and residual.

An analysis of the second harmonic of *q*-axis currents seen in Fig. 4.24, has also been provided for the same test case, as presented in Fig. 4.25, showing a more reliable detection of the fault than that of the third harmonic. As it was shown for the third harmonic case, the residual's second harmonic is the only one not affected by the transient conditions caused by current steps.

The difference between machine emulator and model *q*-axis currents causes a non-zero residual due to the use of voltage inputs generated in close loop for the machine emulator acting as open loop on the model side.

The ripple seen in signals from the healthy model may be explained in part due to the effect of using in open loop the input voltages which were generated for the fault model in closed loop, and transmitted through PWM modulation. Additionally, there are some differences between rates of execution and sampling frequency of different real-time devices.

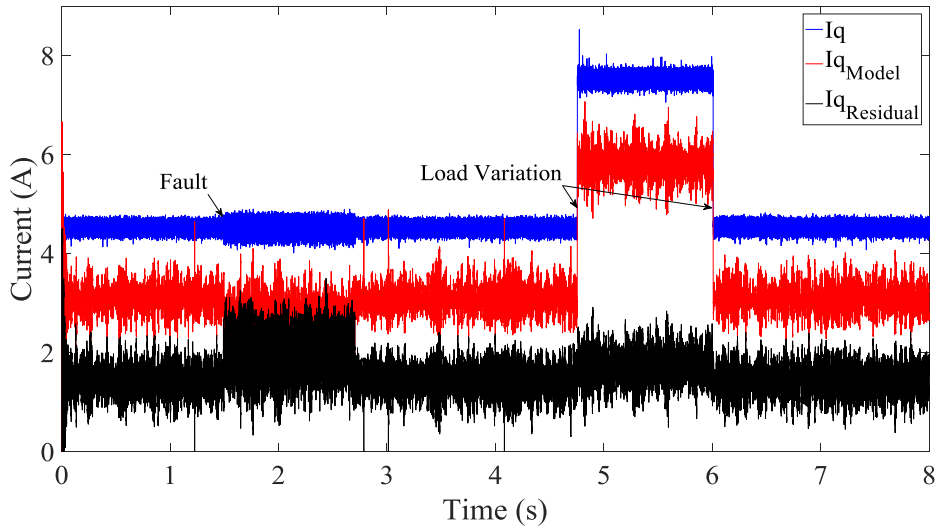

Fig. 4.24. Machine emulator, healthy model and negative residual *q*-axis currents.

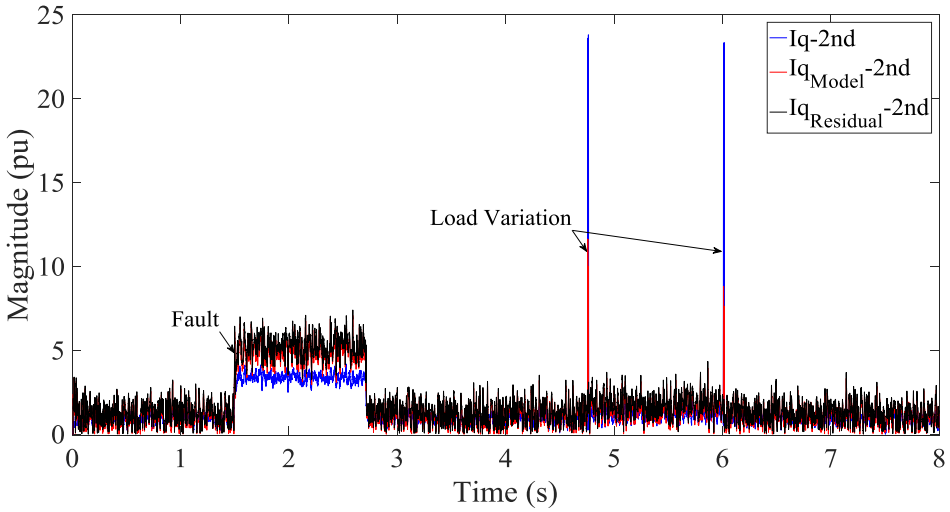

Fig. 4.25. Normalized second harmonic components *q-axis* current of machine emulator, healthy model and residual.

4.6. Experimental Validation Low Sampling Frequency

The method is experimentally validated using two alternative implementations with different sampling frequencies. The first implementation, discussed in this section, uses experimental data sampled at 10kHz by the controller. The inverter illustrated in Fig. 4.19, is controlled by a TI TMS320F28377 dual-core DSP sampling currents at 10kHz synchronously with the PWM update. The control output *dq*-axes voltages are also saved at 10kHz together with the abc-currents and transferred to a PC over CAN-bus.

Whilst the proposed model-based fault detection has not been implemented directly in the DSP, dq-voltages, abc-currents and rotor angle, sampled at 10kHz and streamed to

the PC, have been used as input to the proposed fault detection, emulating operation in the DSP controlling the inverter. A fault case is shown in Fig. 4.26, Fig. 4.28 and Fig. 4.30, while a load variation caused by a 20A current step is shown in Fig. 4.27, Fig. 4.29 and Fig. 4.31. Both cases comprise roughly 0.4 seconds of operation. In the first test, the fault is turned on at approximately 0.16 seconds and off again at 0.33 seconds. Fig. 4.26 and Fig. 4.27 present a comparison between the prototype machine output currents and the model based generated ones.

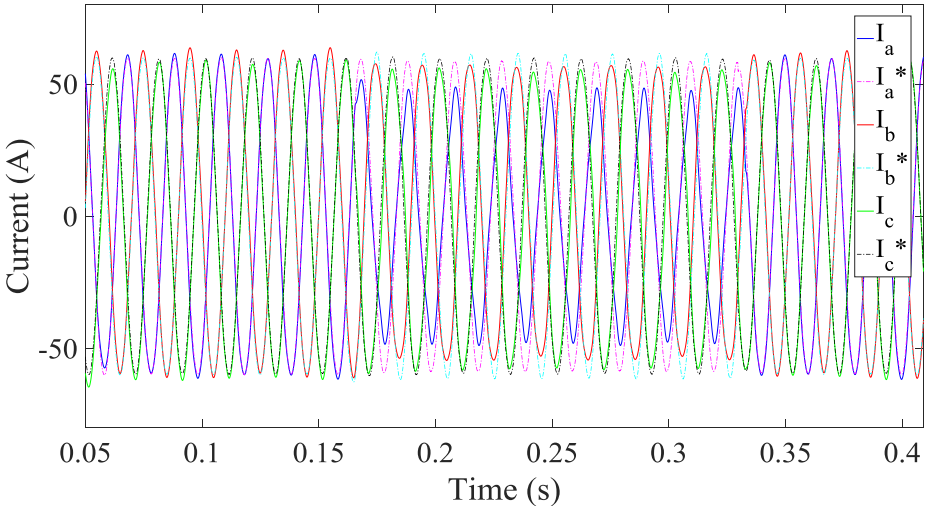

Fig. 4.26. Three phase currents comparison under fault.

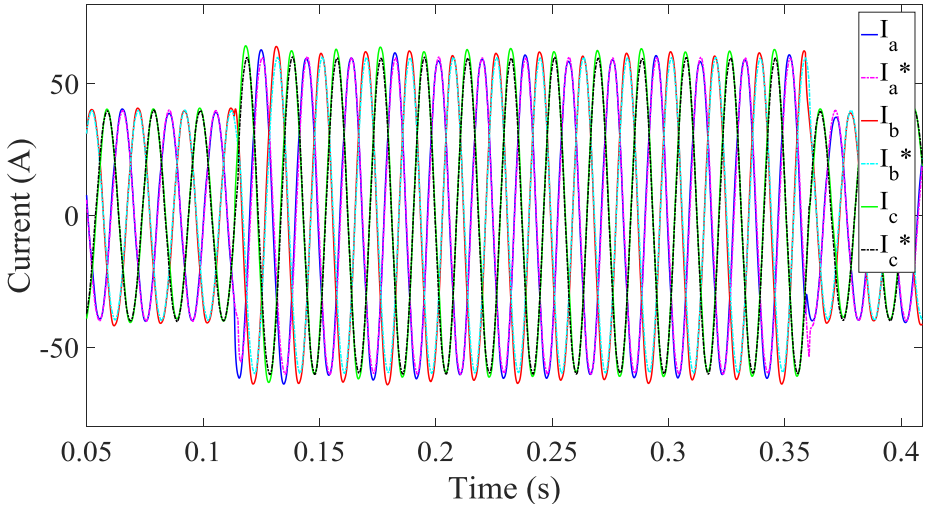

Fig. 4.27. Three phase currents comparison under load variation.

In healthy conditions the model predicted currents closely match the machine measured three phase currents, although a relatively small difference is present, causing the residual to be non-zero. Computed residuals are shown in Fig. 4.28 and Fig. 4.29. This

difference in healthy conditions is in part due to model inaccuracies mainly created by the effect of temperature or others such as manufacturing tolerances or iron losses, which are not accounted for in the model.

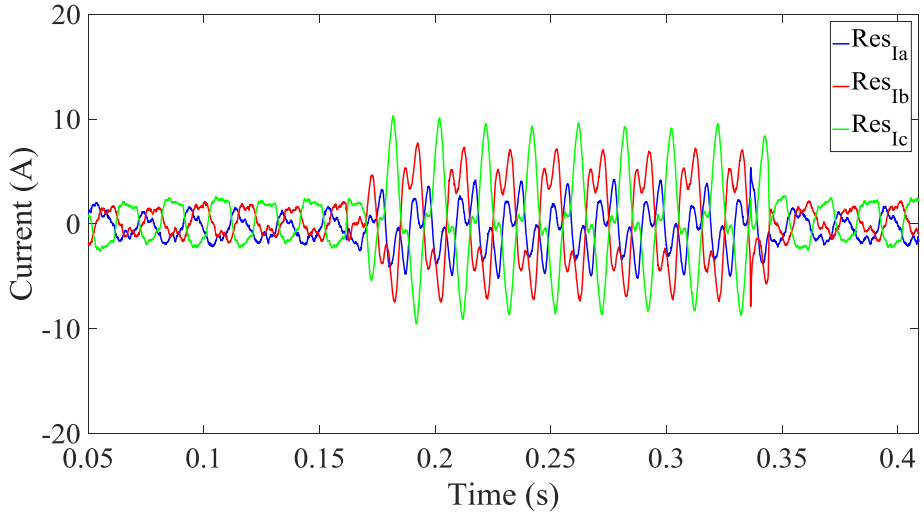

Fig. 4.28. Three phase current residuals under fault.

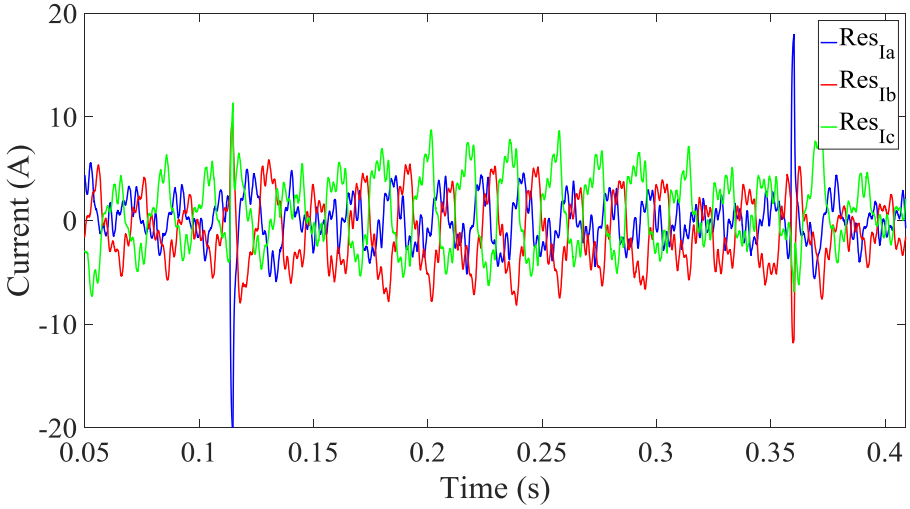

Fig. 4.29. Three phase current residuals under load variation.

Given the ability of the proposed method in decoupling the residual from transient conditions, a simple threshold value could in principle suffice as a fault indicator. However, it is also possible to perform an analysis of the residual, improving drastically its reliability. By mean of example, single Fourier series analysis of phase current third harmonic is shown in Fig. 4.30 and Fig. 4.31. In the residual, the third harmonic increase is much more easily observed for fault conditions relative to the magnitude of the residual itself, while the third harmonic appearing in the phase current of the machine prototype is relatively small with respect to the magnitude of the fundamental component.

On Fig. 4.31 it is possible to notice how the third harmonic of the residual, relative to the magnitude of the residual itself, for transient conditions due to load variation is not affected significantly, except for brief peaks at the points corresponding to the positive and negative current steps. Comparison of Fig. 4.30 and Fig. 4.31 suggests that a threshold indicator >0.2p.u. could be useful for discriminating faults from transient load variations.

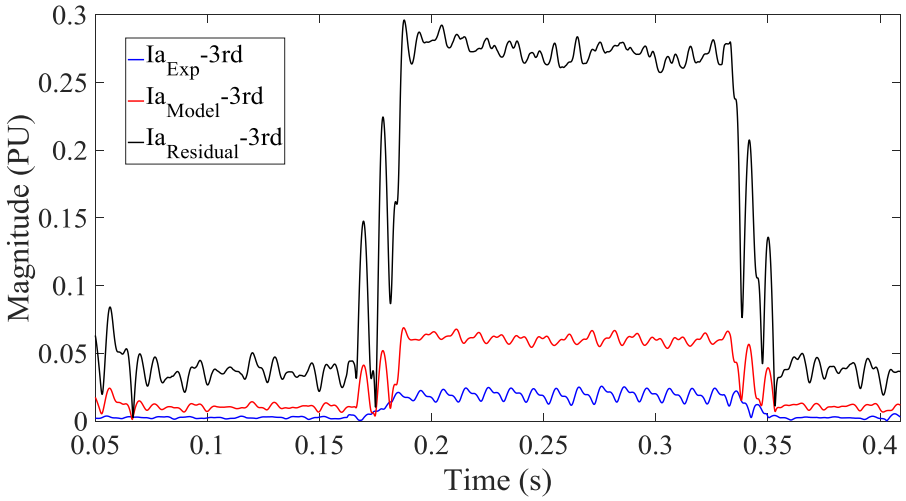

Fig. 4.30. Single series Fourier analysis of phase current a under fault.

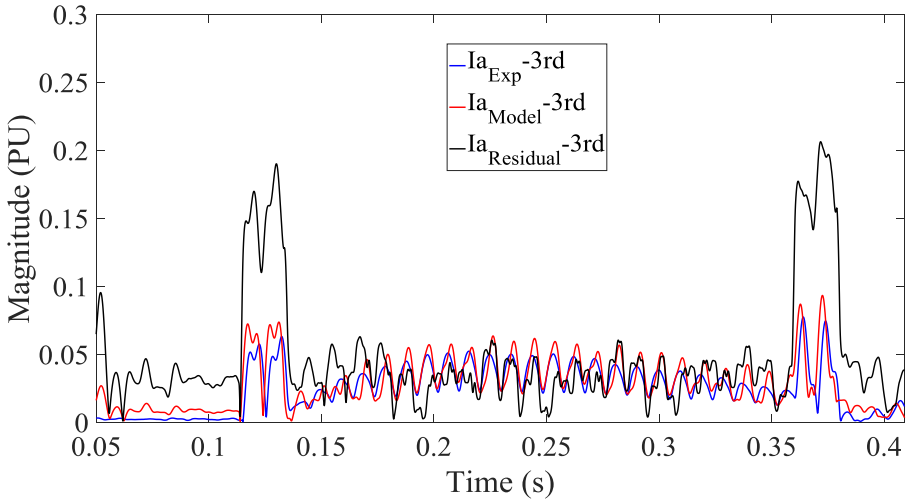

Fig. 4.31. Single series Fourier analysis of phase current a under load variation.

It is noticeable how experimental and model results show a transient in the middle of Fig. 4.31, while the residual maintains a fixed average. However, peaks at the beginning and end of the current step can be found, showing perhaps a more significant than expected effect of the peaks shown in Fig. 4.29, due to model inaccuracies. The same

analysis is carried out for *q*-axis current in Fig. 4.32-Fig. 4.35. Residual generation under fault and current step is shown in Fig. 4.32 and Fig. 4.33 respectively.

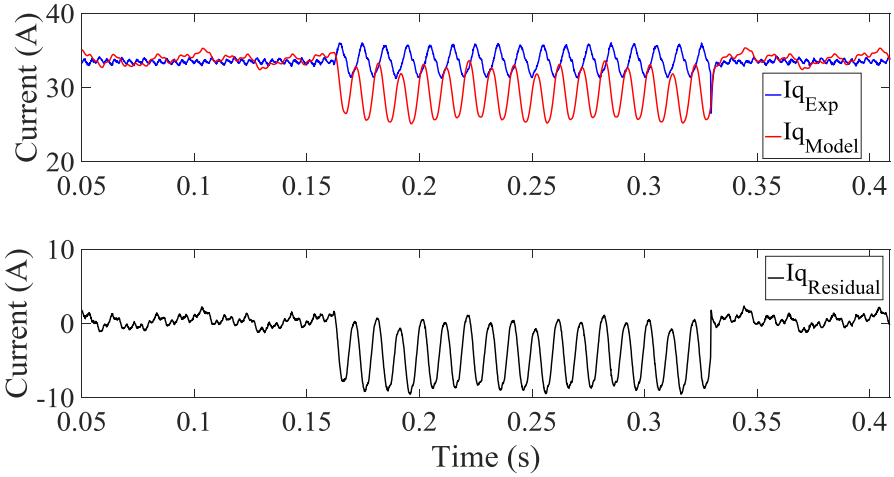

Fig. 4.32. *q*-axis current comparison and residual under fault.

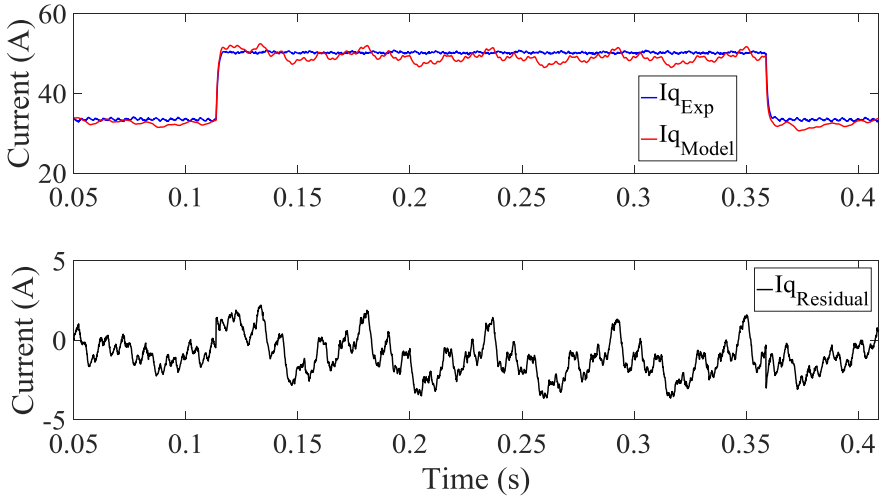

Fig. 4.33. *q*-axis current comparison and residual under load variation.

Similarly to what was shown for phase current third harmonic analysis, for *q*-axis current second harmonic the effect of the fault is much more easily observed relative to the size of the signal on the residual, as shown in Fig. 4.34 (bottom). Furthermore, the second harmonic of the residual under load variation is not affected at all by transient conditions, allowing to use again a threshold indicator at least greater than 0.25p.u.

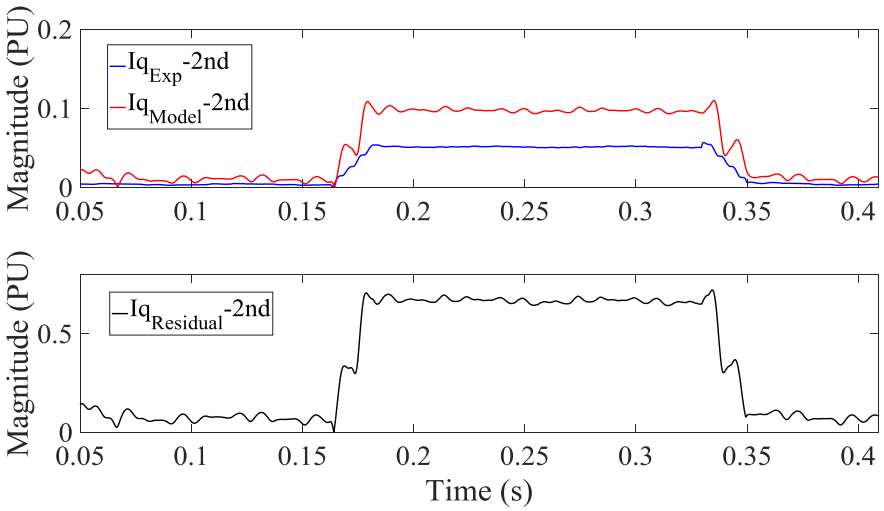

Fig. 4.34. Single series Fourier analysis of *q*-axis current second harmonic under fault.

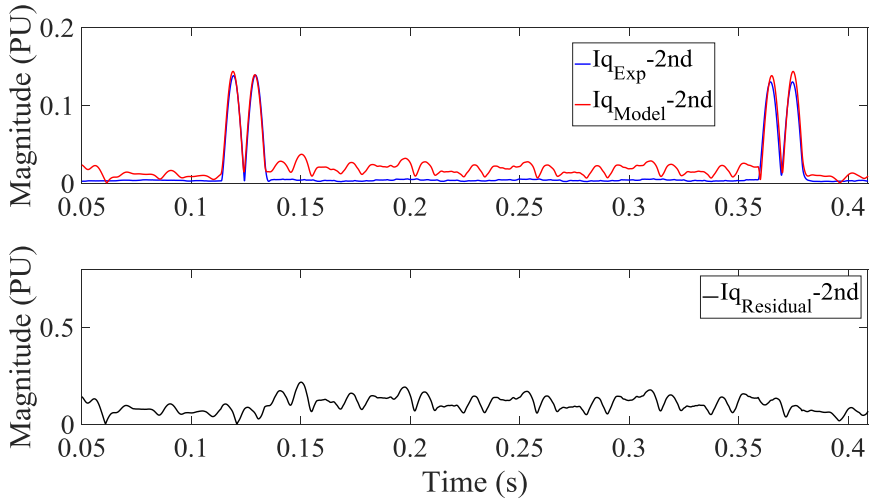

Fig. 4.35. Single series Fourier analysis of *q*-axis current second harmonic under load variation.

4.7. Experimental Validation High Sampling Frequency

If the proposed method is not implemented in the inverter drive controller, then higher sampling frequency might be possible. Experimental tests at 1 and 2MS/s are presented here. Phase voltages are acquired using differential voltage probes with 50MHz bandwidth.

Similarly to section 1.6, results are presented as a comparison between machine and model three phase currents, current residuals, and single series Fourier analysis of phase current third harmonic in healthy and faulty conditions as well as following load and speed change. Three different cases are compared at similar current magnitude (defined as the square root of I_d squares plus I_q squared) and speed conditions, 50-30A and 1000rpm. Cases include single turn fault, a 20A current step and a 500rpm speed ramp.

These cases are graphically presented by oscilloscope screenshots, containing three phase currents, voltages and fault current, as shown in Fig. 4.36.

a)

b)

c)

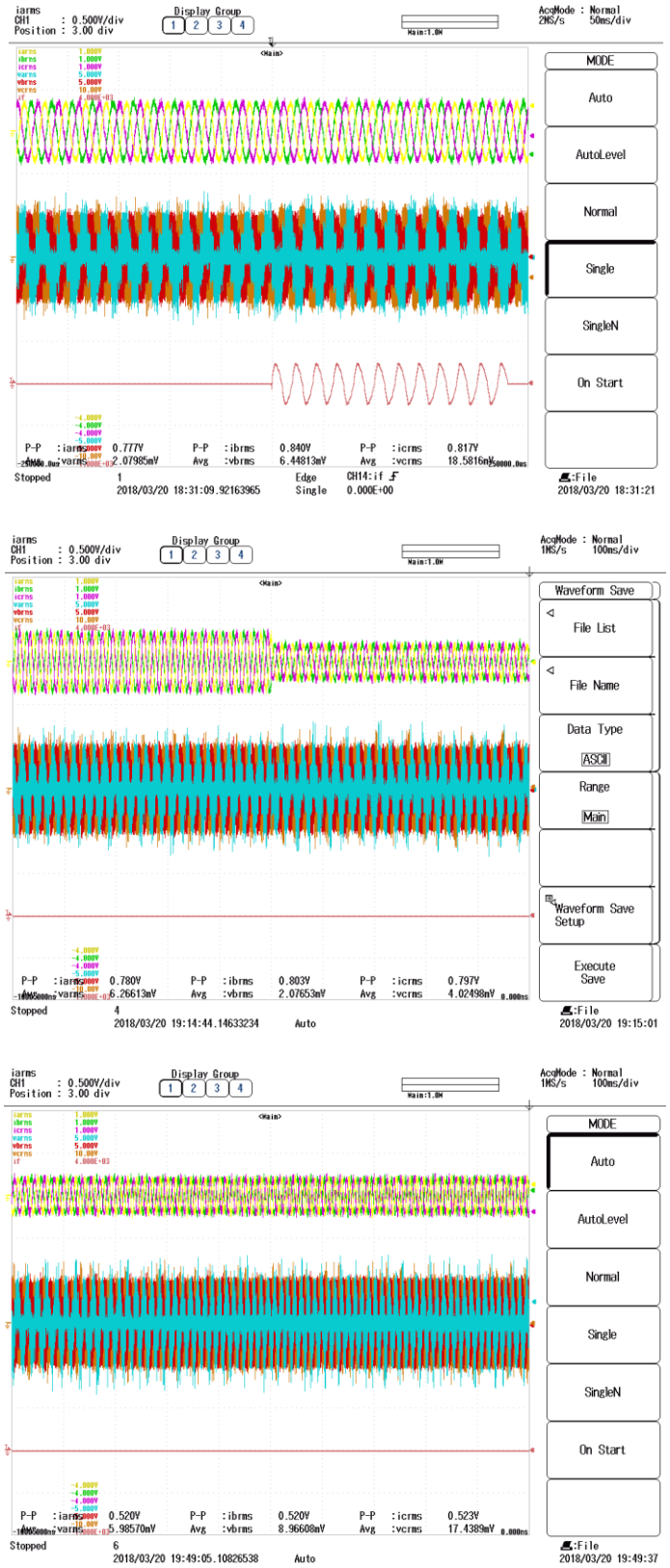

Fig. 4.36. Three phase currents, voltages and fault current for a) fault, b) current step, and c) speed ramp, captured by oscilloscope.

a)

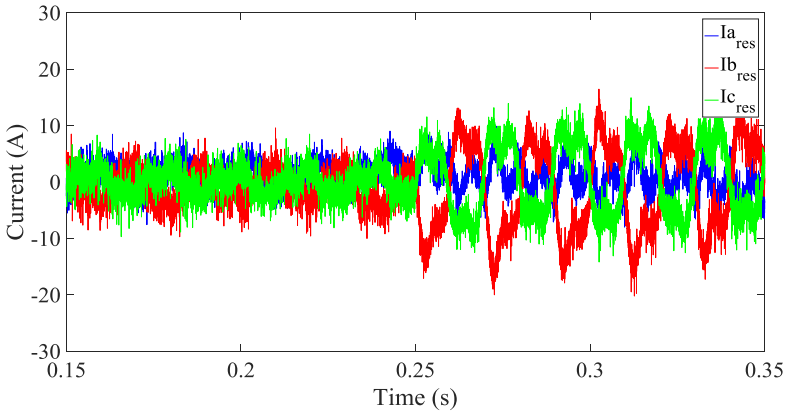

b)

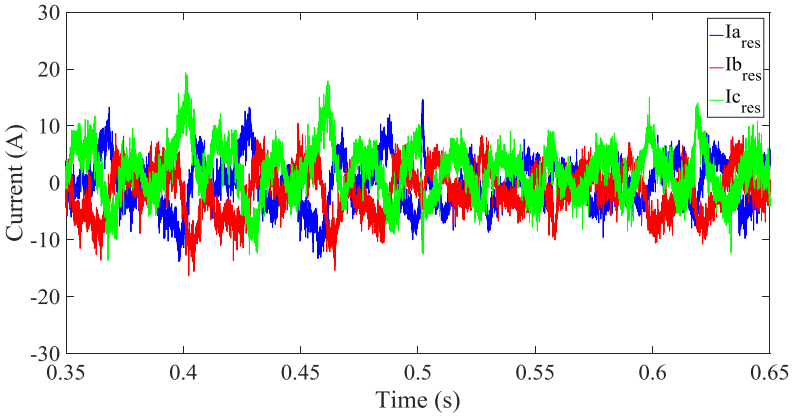

c)

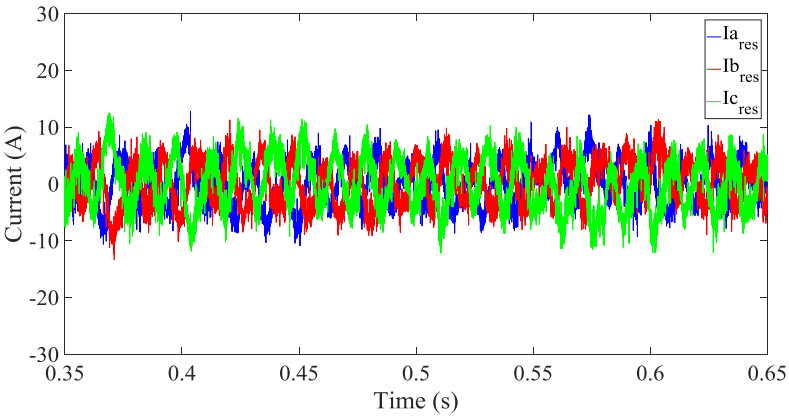

Fig. 4.37. Three phase current residuals for a) fault, b) current step, and c) speed ramp.

Residuals obtained from the subtraction of three phase currents can be found in Fig. 4.37. While the residual under fault conditions changes significantly, those under transient in healthy conditions are not disturbed in the same manner. Particularly, little change is shown for the speed ramp. The apparent improvement shown for current step is most likely due to closer to rated conditions after the step and decreased ripple in input signals. As shown in Fig. 4.37, the residual itself clearly indicates the presence of a fault,

however, it is desirable to use a fault indicator able to discriminate between healthy and faulty operation by a simple threshold. For that reason, single Fourier series analysis of the third harmonic is employed on the residual. Furthermore, the same analysis is performed on both machine and model phase current A. The fault is located in phase B but can be detected from any of the three. The comparison is shown in Fig. 4.38 for all three cases.

a)

b)

c)

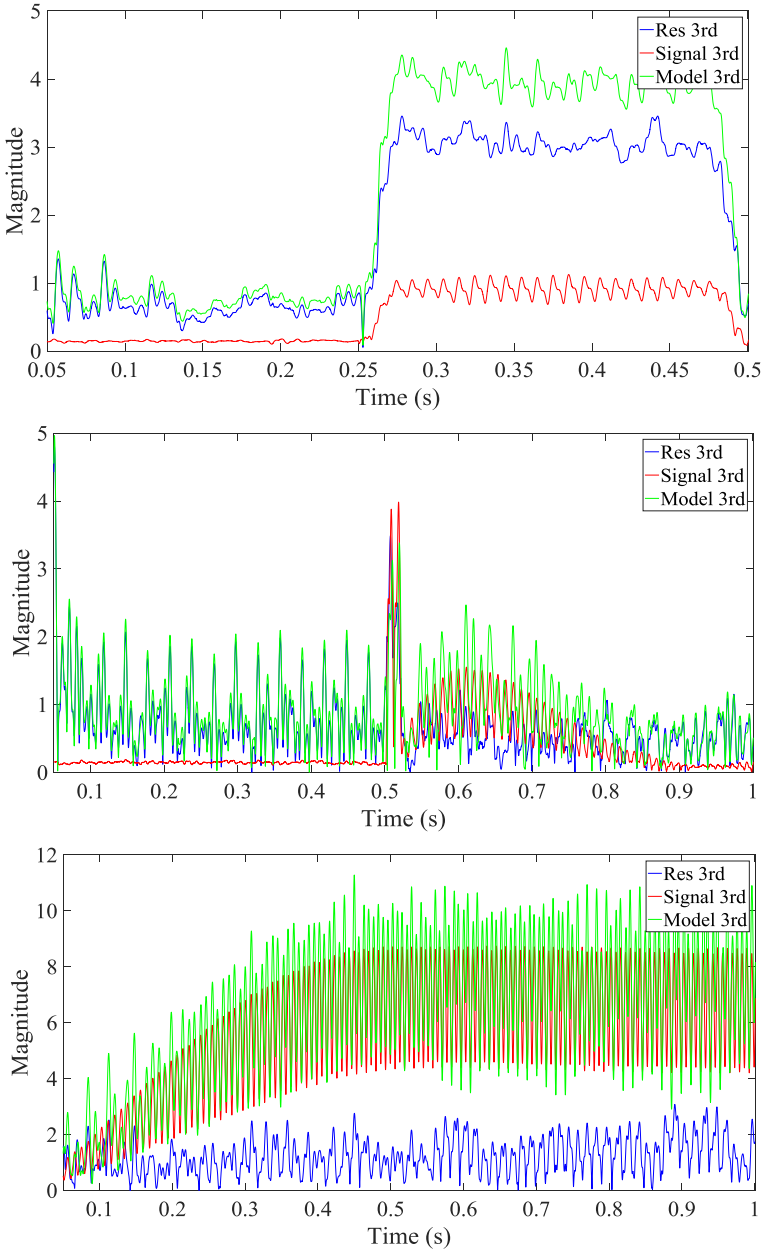

Fig. 4.38. Single Series Fourier analysis of residual, machine and model for fault a), current step b), and speed ramp c).

A comparison between machine and model generated *dq*-axes currents is shown in Fig. 4.39, where the better match of higher sampled data is easily observed, displaying a significantly smaller ripple for healthy conditions.

a)

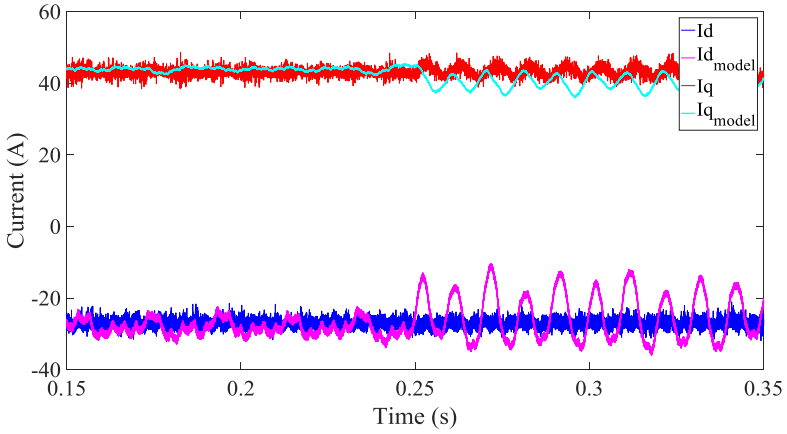

b)

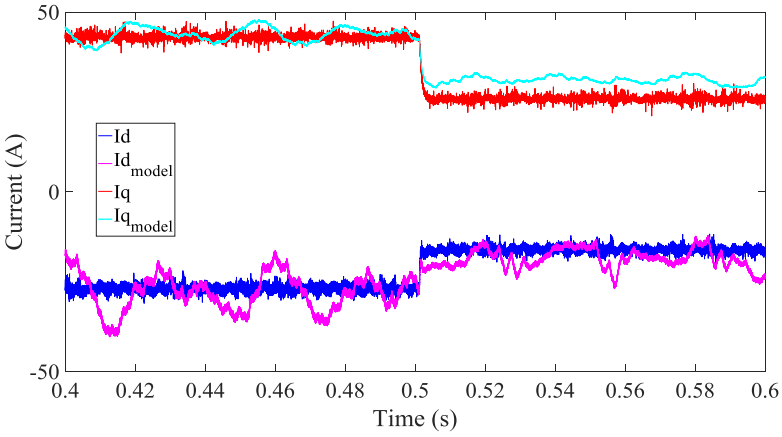

c)

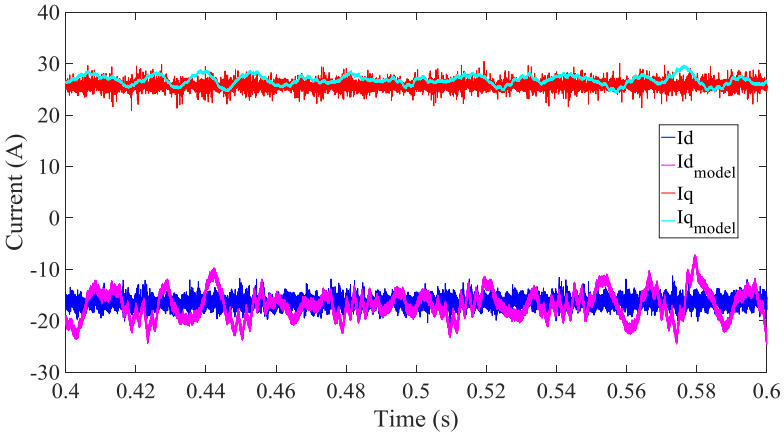

Fig. 4.39. Machine versus model *dq*-axes currents for fault a), current step b), and speed ramp c).

Once again, differences between machine and model results are caused by using as model inputs the voltages calculated in closed loop for machine control.

A direct analysis of the third harmonic on machine or model currents yields poor results, making a discrimination between faulty and healthy transitory conditions difficult. However, a second harmonic analysis of the residuals, seen in Fig. 4.40, shows

a significant increase for fault conditions and little change for a speed ramp. There is however a brief increase of the indicator at the exact moment of the current step, but still drastically smaller than for phase currents analysis (third harmonic). In addition, if the indicator response is considered relative to the magnitude of the signal from which it is extracted, the third harmonic is much greater for the case of the residual.

a)

b)

c)

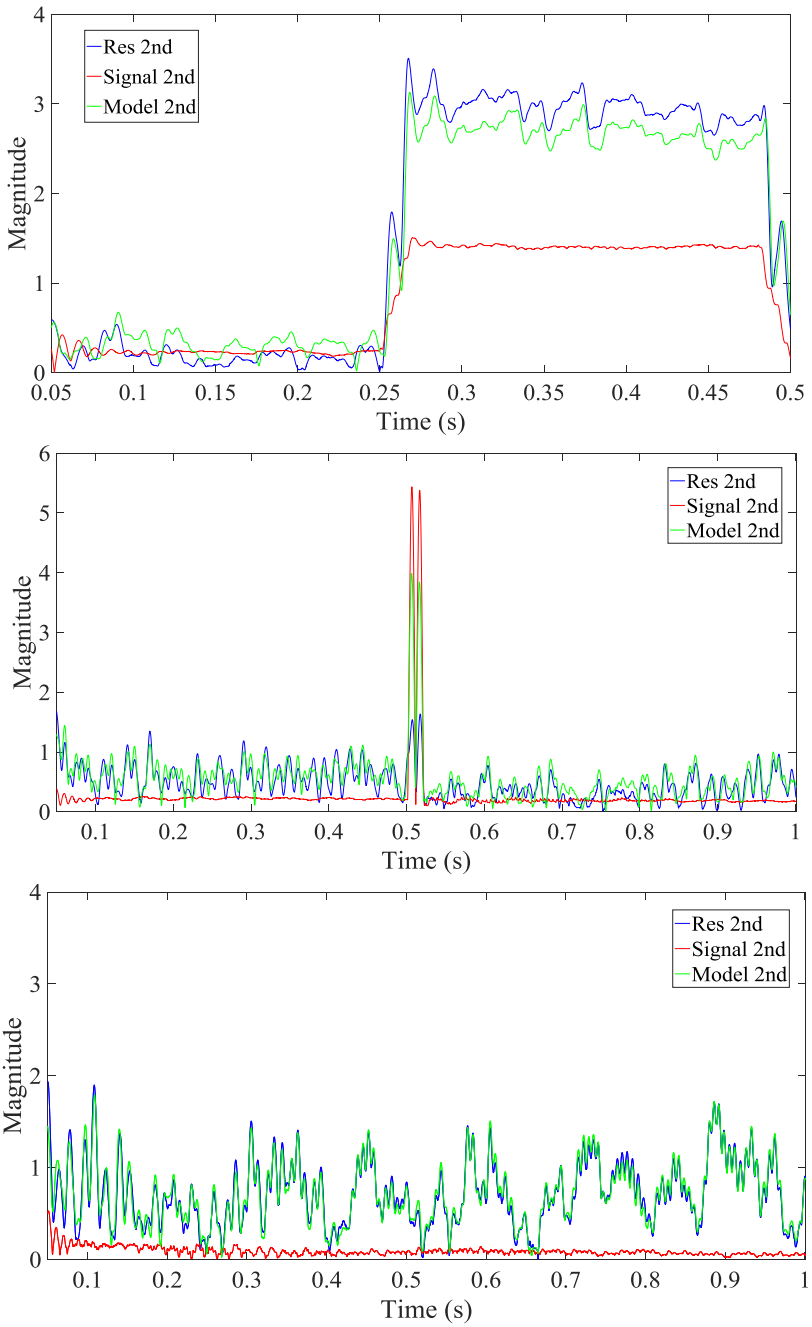

Fig. 4.40. Second harmonic Single Series Fourier analysis of residual, machine and model for fault a), current step b), and speed ramp c).

Whilst it is clear at this point that the residual behaviour under fault and speed ramp is consistent with what was theorized and simulated, the behaviour under current step

displays an unexpected response, making it close to the response of the signals from which the residual is computed. Possible reasons for this response where briefly commented after Fig. 4.31. A worsened effect is shown in Fig. 4.38 resulting in a step response identical to those found in the original signals. This effect is even noticeable for second harmonic analysis in Fig. 4.40, while previously not present as per Fig. 4.33. Indicator's decreased performance may be explained by a number of testing limitations, some of which constituted the root cause for which real-time implementation has not been experimentally validated. The modelling approach described requires the use of rotor angle for transformation of acquired signals from *abc* to *dq0* reference frame. The machine's rotor position feedback is normally obtained from encoder or resolver. While the testing rig incorporated a resolver, access to it was not available. Instead, angle is generated by use of a Phase Lock Loop (PLL), without achieving ideal conditions. The most likely reason for the effects observed is that a current step generates a sudden transient in the angle that the PLL is unable to track. This didn't constitute an issue for results shown previously, such as those seen in Fig. 4.33 and Fig. 4.35, since model input data was captured with the controller, and thus included *dq0* variables as well as rotor angle.

Non-related with results shown but with regards to attempted real-time implementation, an issue not present at high sampling frequencies can be found at lower ones. For example, a maximum of 125kS/s was available during real-time conditions. Given low speed was imposed due to testing conditions designed to limit fault current, a reduced duty cycle (low modulation index) was observed, and thus increased difficulty when capturing PWM modulated voltage signals.

Once the angle issue is fixed, improvements on discrimination between fault and transient conditions may be possible employing a more advanced signal-analysis method. Examples of this in the form of time-frequency signal processing are Wavelet Transforms (WT) or the Hilbert Huang Transform (HHT), discussed in Chapter 5.

4.8. Summary

This chapter has presented a model-based, current residual indicator for PMSM interturn fault detection. A description of the technique based on the models discussed in Chapter 3 has been provided. Its implementation in simulation environment, as well as in real-time HIL emulation and experimental validation have been discussed in detail.

Finally, results have been presented including offline comparisons with experimental data. Two potential implementations are suggested: namely implementing the method in the drive controller and using reference dq-voltages as input sampled by the controller at PWM frequency, or implementing the method on an external data acquisition system. In the latter case, control reference V_{dq} voltages are not available, and phase voltages need to be sampled directly. However, due to fast PWM switching, a high sampling rate is required.

This method has been implemented in the available real-time processing platform (OPAL-RT 5700). Unfortunately, it was found that the maximum rate of execution was limited to 125kS/s which was found insufficient for accurate voltage measurement with the 10kHz switching frequency. Tests have shown that for 10kHz switching frequency, and the low duty cycle imposed by testing conditions, approximately 1MS/s sampling rate for phase voltages is required for accurate capture of voltages and their use in the proposed model-based method. A reduction in the required sampling rate could be achieved in principle, by adding a stage of filtering resulting in sinusoidal voltage inputs.

From the point of view of theory and simulation, the method is proven to work effectively without falling into false alarms due to transient conditions unrelated to the fault. With regards to experimental validation, two implementations have been carried out. One at the switching frequency (10kS/s) with data being acquired by the controller, and one at much higher sampling rate (1 and 2MS/s). Particularly for the higher sampling frequency test, limitations in the availability of rotor angle from the testing rig resulted in an inability to discriminate effectively between stator winding faults and sudden load variations (e.g. current steps).

If the last results are ignored on the basis of the limitations found during testing, it is possible to affirm that residual signals, on their own, allow discriminating between a fault and transient conditions unrelated to it, as shown in Fig. 4.32 and Fig. 4.33. Furthermore, the use of signal analysis (e.g. single Fourier series) on the residuals further increases the reliability of the proposed method, as seen in Fig. 4.34 and Fig. 4.35.

In any case, it appears this limitation has a lesser influence when analysing the second harmonic component of q-axis current, rather than phase current third harmonics. More accurate models to include the effect of iron losses and changes with temperature would in theory, improve the reliability of the current residual.

CHAPTER 5

TIME-FREQUENCY SIGNAL ANALYSIS BASED FAULT DETECTION

5.1. Overview

A large number of methods based on Motor Current Signature Analysis (MCSA) have been proposed and reviewed in Chapter 1. The simplest of MCSA methods are based on monitoring phase current third harmonics or *dq*-axes currents second harmonic components. These are used for illustration throughout this chapter. A novel method of stator winding fault detection based on instantaneous features extracted by Hilbert-Huang transform (HHT) is also introduced here and comparatively assessed.

HHT is a time-frequency signal analysis method based on the empirical mode decomposition (EMD) and the Hilbert transform. It is suited for reliable fault detection since it promises better performance under transient conditions which might otherwise cause false alarms. The use of HHT has been demonstrated in recent years for bearing fault detection of induction machines [75]–[78] and demagnetization fault of Permanent Magnet Synchronous Machines (PMSM) [79], [80]. This Chapter explores the possibility of applying the technique to the detection of stator short-circuit faults in PMSMs, particularly those of low severity such as single or interturn fault, identified as critical to avoid further damage to the machine. Since these involve only a single or a few turns in the windings, the effect on terminal currents is often very small and therefore their detection is in general difficult due to the small fault 'signature' signal embedded in a very noisy signal. Therefore, the detection of single turn short provides the worst-case scenario from the point of view of fault detection.

A method based on online statistical analysis of the instantaneous frequency (IF) and instantaneous magnitude (IM) of the intrinsic mode function (IMF) containing the fundamental frequency, calculated by the HHT, is proposed and demonstrated through real-time Hardware-in-the-Loop (HIL) simulation and experimental validation employing an aerospace starter-generator. Its conceptual basis is also presented and its effectiveness demonstrated.

5.2. Fourier-Based Fault Detection

As illustrated in Chapter 2, stator windings faults result in phase currents unbalances that present specific and identifiable "signatures" which can be detected using frequency-domain analysis tools. It has been demonstrated that third harmonics components in the phase currents when analysed in the stationary reference frame, or second harmonic components in the synchronous reference frame, provide a stator fault signature. Many signal processing methods for extracting these signatures have been proposed, the most common being those based on Fourier transforms, such as Fast Fourier Transform (FFT). This subsection provides a Fourier-based analysis in order to provide a point of reference to compare further signal-based methods.

A. Fast Fourier Transform

FFT is a well-known computationally efficient algorithm for the calculation of the Fourier transform allowing the identification of signals components in frequency domain. However, strictly speaking, the FFT can only be applied to non-transient steady-state conditions. The phase current measured following a single turn fault, obtained from the experimental rig presented in Chapter 3, is analysed in Fig. 5.1 and Fig. 5.2. Fig. 5.1 (top) shows the phase current during a transition between healthy and faulty conditions. Fig. 5.1 (bottom) shows the corresponding frequency-domain harmonics analysis obtained using three windows, one window entirely in healthy conditions (green), one entirely in faulty conditions (red) and one covering the transient between healthy and faulty (magenta) with the fault instant (around 0.34s) marked by a vertical line (top).

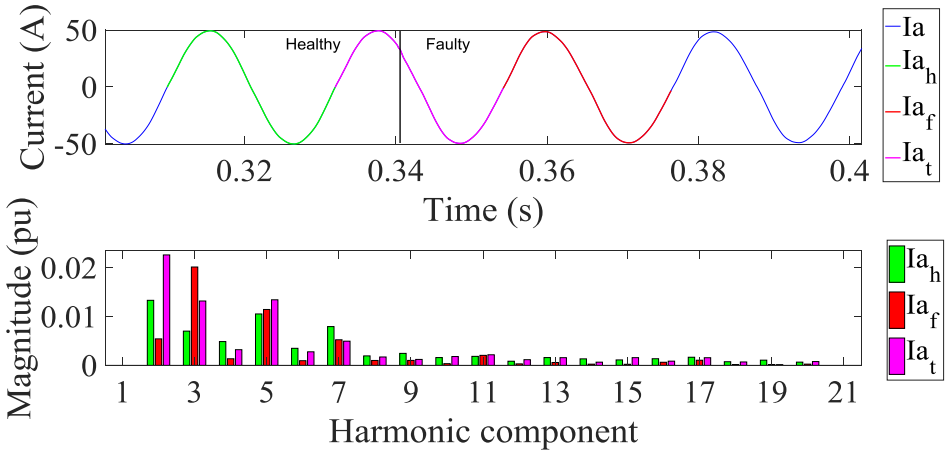

Fig. 5.1. Phase current (top) and its FFT third harmonic in frequency domain (bottom) for healthy (green), faulty (red) and transient case (magenta). Top's vertical bar shows fault.

The rise in third harmonic in faulty conditions becomes evident. Fig. 5.2 shows the evolution in time domain of the magnitude of the third harmonic, obtained by computing the FFT over a continuously running window.

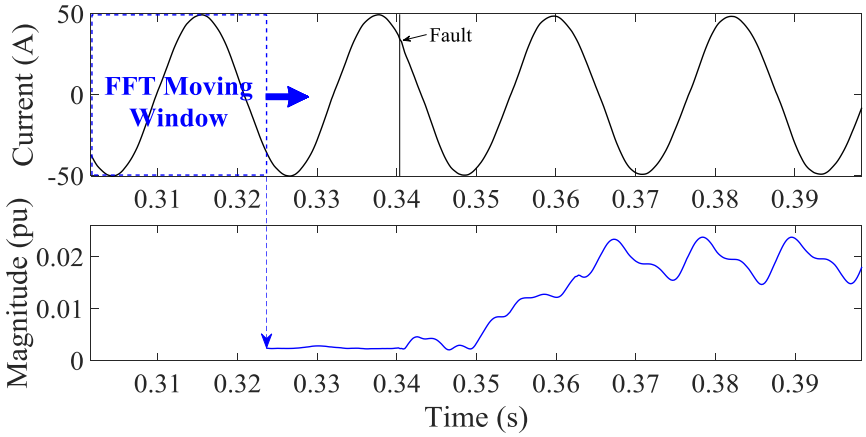

Fig. 5.2. Phase current (top) and its FFT third harmonic in time domain (bottom) before and after fault.

A similar analysis is illustrated under transient conditions in Fig. 5.3 and Fig. 5.4. In particular, Fig. 5.3 shows the phase current (top) following a step change in the load and the corresponding (bottom) magnitude of its third harmonic component. It's clear that a transient condition, a current step in this case, can have transient frequency components which can negatively affect harmonic-based fault detection with spurious transients which can result in false alarms. Similarly, Fig. 5.4, show the phase current during a transient speed/frequency variation. Again, the speed transient generates spurious frequency components in the region of interest affecting the detectability of faults.

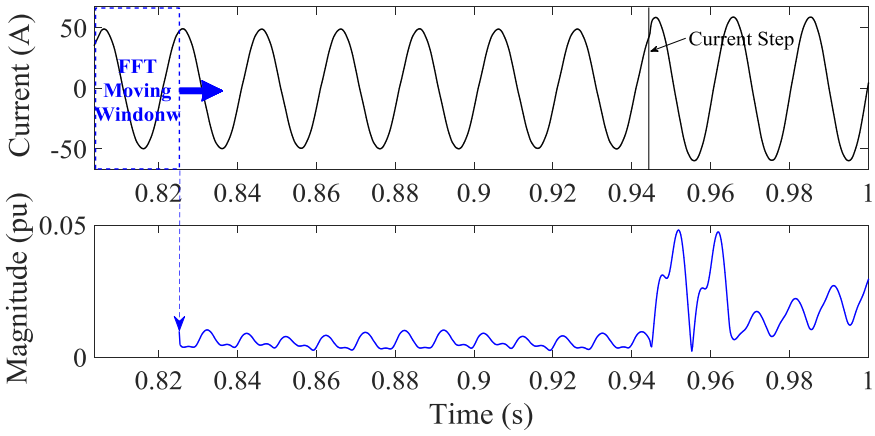

Fig. 5.3. Phase current (top) and its FFT third harmonic in time domain (bottom) for current step.

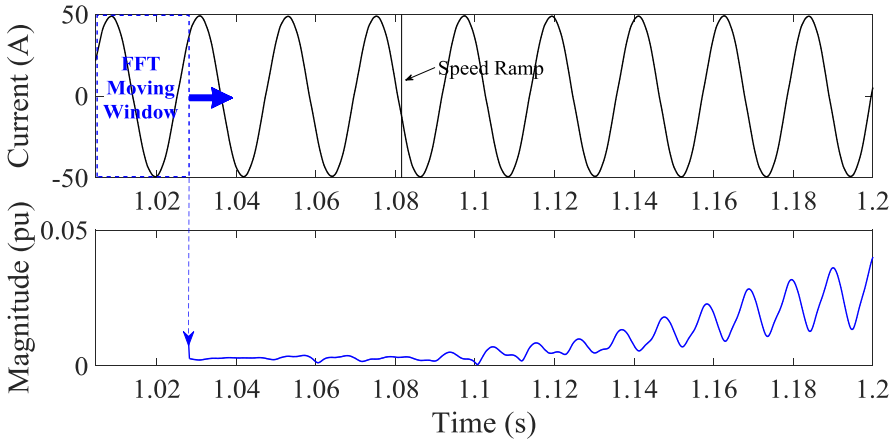

Fig. 5.4. Phase current (top) and its FFT third harmonic in time domain (bottom) for speed ramp.

A continuation in time of the computed FFT moving window results shown in Fig. 5.2-Fig. 5.4 can be seen at the end of this chapter, where they are compared with the final HHT results for the same cases.

B. Single Fourier series Analysis

The FFT calculates all the harmonics component in the signal. This is usually unnecessary for the purpose of fault detection since, as mentioned above, the fault signature is present in a limited number of harmonics. The single-component Fourier series analysis is employed here for illustration. The Fourier series of a function $f(t)$ is defined as:

$$f(t) = \frac{a_0}{2} + \sum_{n=1}^{\infty} a_n \cos(n\omega t) + b_n \sin(n\omega t) \tag{69}$$

Where:

$$a_n = \frac{2}{T}\int_{t-T}^{t} f(t)\cos(n\omega t)dt \tag{70}$$

$$b_n = \frac{2}{T}\int_{t-T}^{t} f(t)\sin(n\omega t)dt \tag{71}$$

$$T = \frac{1}{f_1} \tag{72}$$

And f_1 is the fundamental frequency. The amplitude of a single-component is

$$|H_n| = \sqrt{a_n^2 + b_n^2} \tag{73}$$

Tracking of a single component has already been presented in the past, as shown in the literature review, albeit applied to voltages by *T. Boileau* in [91], using the algorithm shown in Fig. 5.5, and applied to active and reactive power by *B. Wang* in [117], seen in Fig. 5.6. A simple block diagram, which can be easily implemented in simulation software such as MATLAB's Simulink, is shown in Fig 7. In particular, Fig. 5.7 presents a basic diagram of the method employed for tracking the third harmonic of the input signal. It is obtained by computing the module of the integrated products of input signal multiplied by sin and cosine of 3θ. A variable transport delay is used to account for variable frequency operation, as per definition of the components a_n, b_n, the integration is obtained over a fundamental period whose duration varies with frequency. The transport delay, together with a product by the known signal's frequency, allows it to operate even under transient speed conditions, unlike a similar version of the same method employed at the end of Chapter 3.

Implementation of described single Fourier series analysis is not trivial in real-time and was made possible by availability of built-in Simulink blocks, particularly a variable transport delay block, which when fed by a frequency or speed feedback signal allows adjusting to changes in speed, and thus, fundamental frequency in the case of synchronous machines. By default, available "Fourier" blocks do not have the ability to change its input frequency. Given this method is capable of adapting to changing conditions, it already performs better than a FFT moving window.

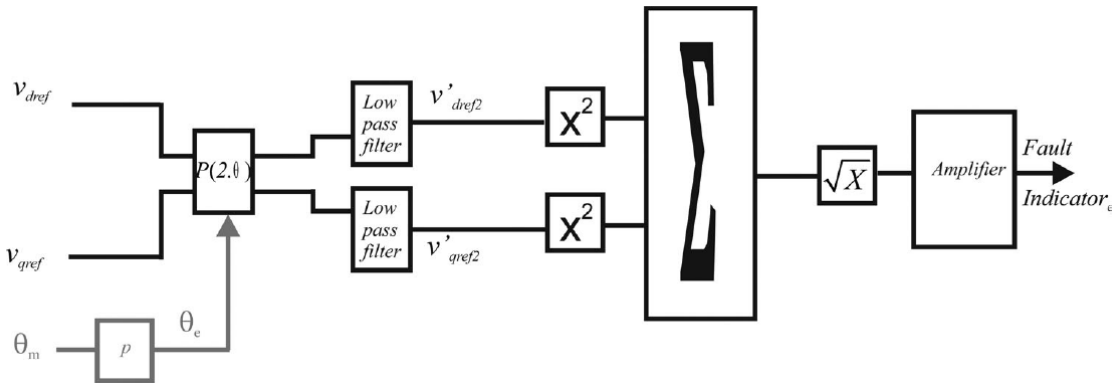

Fig. 5.5. 2nd harmonic monitoring by *T. Boileau* [91].

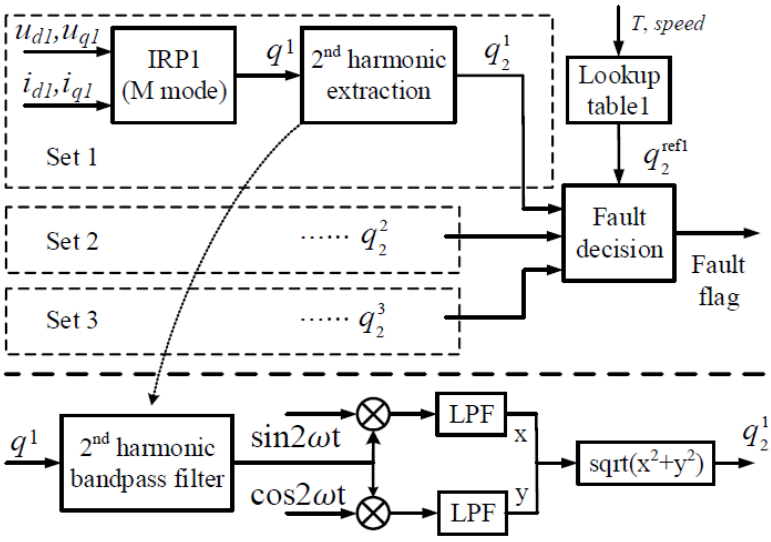

Fig. 5.6. 2nd harmonic monitoring by *B. Wang* [117].

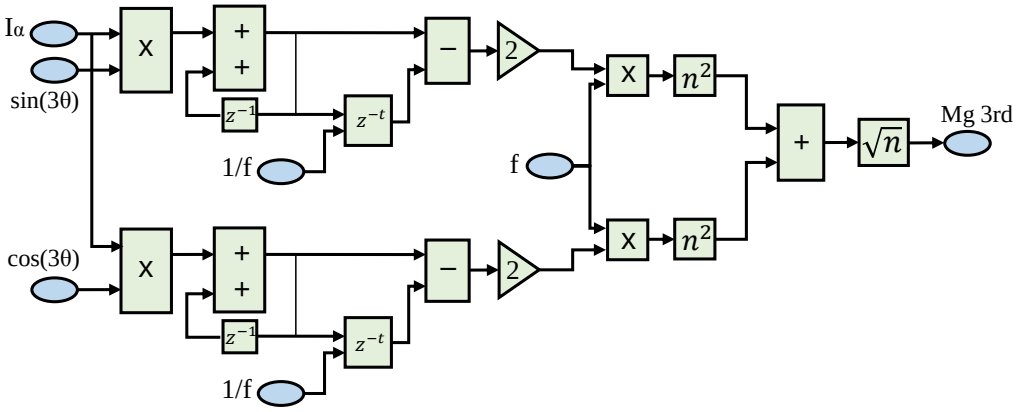

Fig. 5.7. Improved single Fourier series analysis diagram.

An analysis of the same fault presented in Fig. 5.2 is shown in Fig. 5.8 employing this method for both phase current third harmonic (top), and q-axis second harmonic (centre). Furthermore, it is compared with one of the methods found in literature plotted in red (bottom), and found to be a stronger indicator when applied to current signals. The same analysis is provided for a current step transient in Fig. 5.9 and for a speed ramp in Fig. 5.10. Looking at the three figures, it can be seen that a threshold value may not suffice to discriminate between transient conditions under healthy operation and faulty conditions. Whilst the speed ramp response remains within the same magnitude levels, the indicator increases significantly for a current step. When tracking phase current's third harmonic, the indicator under step current surpasses the level reached under faulty conditions. The improved second harmonic of q-axis current seen in blue in the centre of the three figures, provides a stronger indicator, facilitating perhaps the use of a simple discriminator.

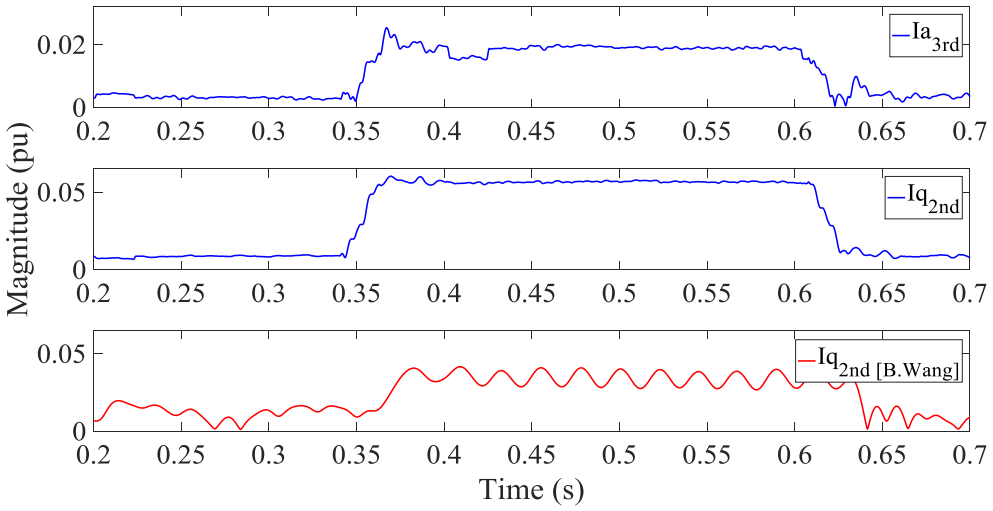

Fig. 5.8. Improved Fourier harmonic tracking versus literature *q*-axis current second harmonic monitoring of fault.

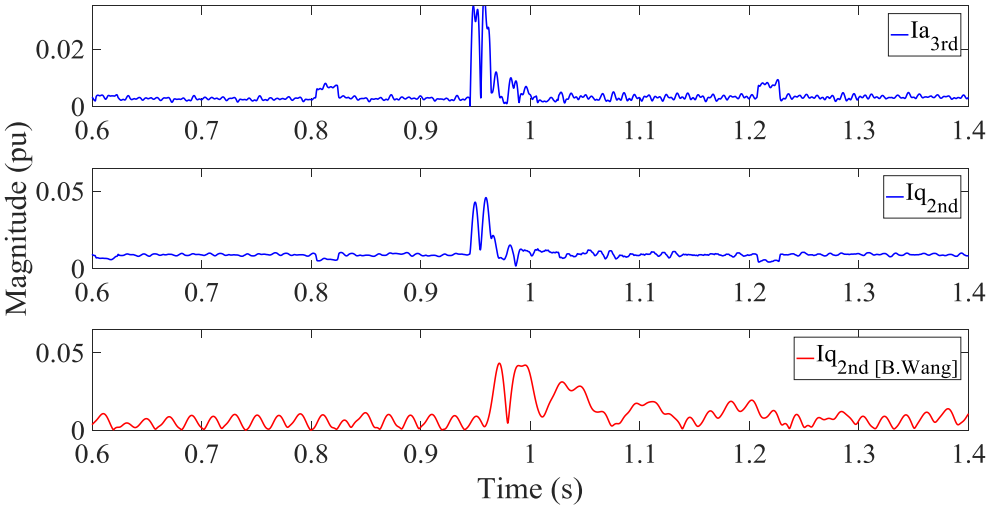

Fig. 5.9. Improved Fourier harmonic tracking versus literature *q*-axis current second harmonic monitoring of current step.

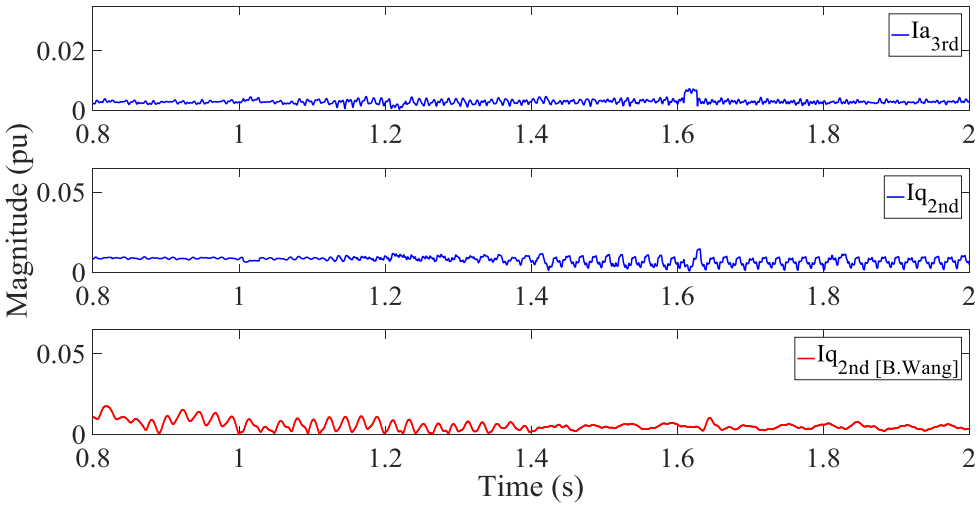

Fig. 5.10. Improved Fourier harmonic tracking versus literature *q*-axis current second harmonic monitoring of speed ramp.

Small disturbances in the form of bumps seen in the top and middle part of Fig. 5.9 (0.8s and 1.2s) and Fig. 5.10 (1.6s) are caused by loss of data of the acquisition system. The data shown was collected employing the real-time simulator OP5600 from OPAL-RT which occasionally encounters "overrun" when working at the limit of its capabilities. In this particular case it was running with a very demanding time step (8μs) for the CPU. Use of the FPGA instead of the CPU should in principle solve this limitation, however this possibility was not available at the time of testing due to software license constrains.

5.3. Hilbert-Huang Transform: Analytical Description

HHT is based on obtaining and analysing IMFs by means of EMD and Hilbert spectral analysis, respectively. Once the Hilbert transform is performed on each IMF, it is possible to obtain the instantaneous frequency and represent the spectrum of frequencies corresponding to each relevant harmonic component in the signal. An IMF is defined as a function for which the number of local extrema (local maxima and minima) and the number of zero crossings differ at most by 1. Furthermore, the mean value at any point of the envelopes defined by local maxima and minima is zero. The EMD extracts the IMF following a sifting process [80]:

1) the upper $u(t)$ and lower $l(t)$ envelopes of the input signal $x(t)$, (e.g. phase currents), are obtained with a suitable interpolation (e.g. with cubic splines) of its local maxima and minima, respectively.
2) the mean $m(t) = 1/2\big(u(t) + l(t)\big)$, of those envelopes is computed.
3) the residual $h(t) = x(t) - m(t)$ is calculated
4) The process terminates if the sifting residual $h(t)$ is an IMF, i.e. if the difference between the number of local maxima and minima in the window of interest and the number of zero crossings is zero or 1. Otherwise, a new sifting process is executed and $h(t)$ becomes the input signal for the next iteration through steps 1-4.

The sifting process is applied as many times as needed until an IMF is obtained. There are several possibilities for the stopping criterion of the sifting process based on standard deviation, number of iterations, threshold method, etc. For the case under study, a stopping criterion based on the standard deviation is applied as:

$$\sum_{t} \frac{[h_{k-1}(t) - h_k(t)]^2}{h_{k-1}^2(t)} < SD \tag{74}$$

were $h_k(t)$ is the sifting result in the k-th iteration, and *SD* is the standard deviation threshold, typically set between 0.2 and 0.3. The next IMF is extracted applying the EMD to the residue, obtained from subtracting the obtained IMF from the original signal

$$r_1(t) = x(t) - c_1(t) \tag{75}$$

were $c_1(t)$ denotes the first IMF. This process is repeated until the last residue $r_n(t)$ has at most one local extremum. The first IMF component contains the highest oscillation frequencies found in the original signal $x(t)$, as seen in Fig. 5.12.

The IMF generation process is graphically illustrated in Fig. 5.11 and Fig. 5.12. A signal containing significant 3rd and 5th harmonic components shown in Fig. 5.11 (top), is decomposed into its IMFs, shown in Fig. 5.12. First, the upper envelope shown in cyan and the lower envelope shown in magenta are computed. Then, the average of the envelopes is computed and subtracted from the original signal, if the resulting signal complies with the stopping criterion shown in (74), this becomes the first IMF seen top of Fig. 5.12 for this case. Then, the original signal minus the first IMF becomes the starting point for steps 1-4, as shown in the centre of Fig. 5.11. Three IMFs are obtained corresponding to the 5th and 3rd and fundamental components. The sifting process is often applied several times per IMF. The more symmetric and less polluted by noise a signal is, the less sifting iterations it requires. An example of the residue resulting from the extraction of all IMFs is shown in section 5.6.

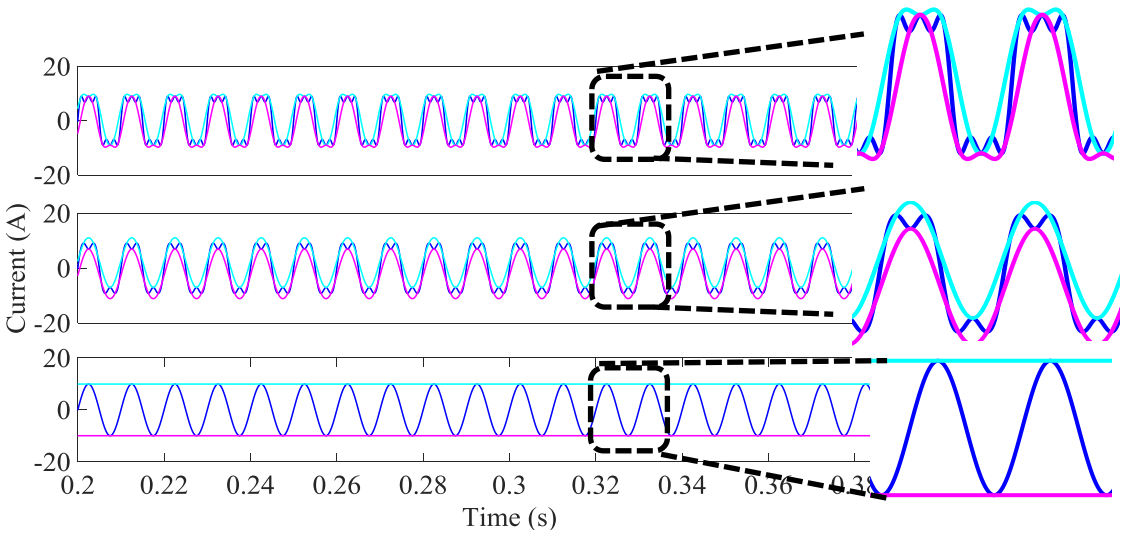

Fig. 5.11. EMD decomposition of signal containing significant 3rd and 5th harmonics.

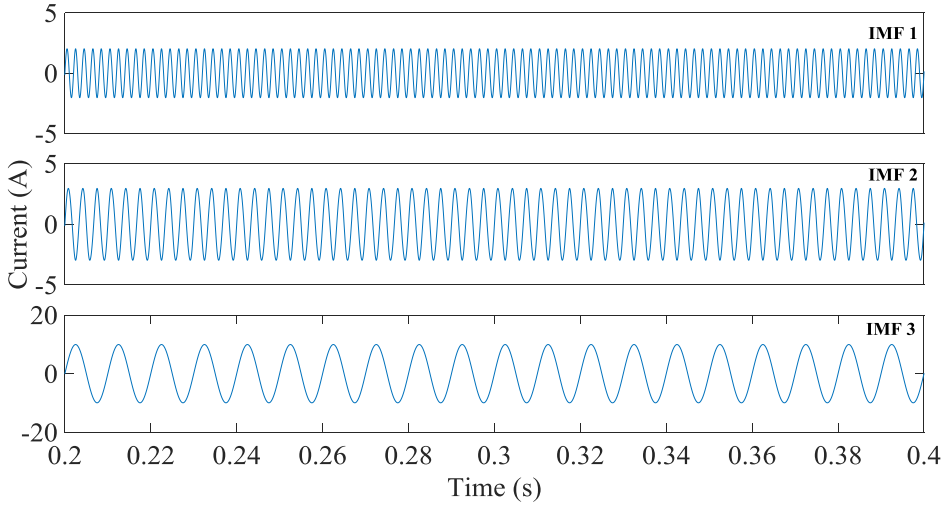

Fig. 5.12. IMFs of signal containing significant 3rd and 5th harmonics.

The Hilbert transform $H[c_i(t)]$ converts the local energy and IF derived from the IMFs to a full-energy-frequency-time distribution of the data by (76)

$$H[c_i(t)] = \frac{1}{\pi}\int_{-\infty}^{+\infty}\frac{c_i(\tau)}{t-\tau}d\tau \tag{76}$$

For a discrete signal x(n), the discrete formulation of the Hilbert transform is given by (77) as presented in [80]

$$x^h(n) = x(n) * h(n) \tag{77}$$

where * denotes the convolution product, the superscript h corresponds to the Hilbert transform of the stator current x(n), and:

$$h(n) = \begin{cases} 0 & \text{for n even,} \\ \dfrac{2}{\pi n} & \text{for n odd} \end{cases} \tag{78}$$

The analytical signal $z^h(n)$ of x(n), without negative frequency components, is obtained as

$$z^h(n) = x(n) + jx^h(n) = a(n)e^{j\phi(n)} \tag{79}$$

Once the analytical signal is generated, the Instantaneous Magnitude (IM) and Instantaneous Frequency (IF) can be computed as:

$$IM(n) = |z^h(n)| \tag{80}$$

$$IF(n) = \frac{1}{2\pi}(\angle(z^h(n+1)) - \angle(z^h(n)))F_s \tag{81}$$

where F_s is the sampling rate, $|.|$ and $\angle(.)$ are the modulus and the argument of complex-valued signal $z^h(n)$, respectively. It is possible then to combine the analysis shown in (79)-(81) in an energy-frequency-time distribution of the data. The representation of such a distribution is commonly known as the Hilbert spectrum, and can be expressed as

$$X(n) = \sum_{j=1}^{n} IM(t) \exp\left(j \int IF(t)dt\right) \tag{82}$$

Once the Hilbert spectrum is defined, it is also possible to derive the marginal spectrum of it, known as marginal Hilbert spectrum (MHS) from it, which offers a measure of the total amplitude contribution from each frequency value [74]. The MHS may be defined as

$$MHS(IF) = \int_0^T H(IF, t)dt \tag{83}$$

5.4. HHT-Based Fault Detection

Whilst the HHT does not identify the harmonic components specifically, the fault is detected through an increase in the third harmonic, which is a well-known indicator of short circuit fault [55]. The effects of this increased third harmonic in one of the phase currents due to short circuit can be visually illustrated in the alpha-beta current representation seen in Fig. 5.13 a).

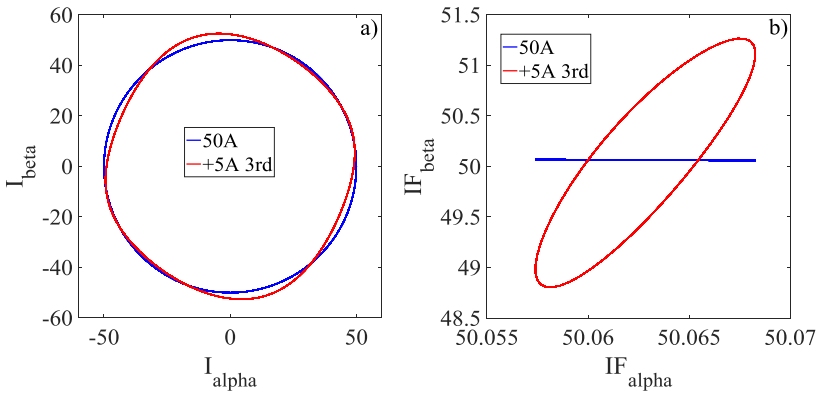

Fig. 5.13. Third harmonic effect on $I_{\alpha\beta}$ and $IF_{\alpha\beta}$.

Here a large enough 3rd harmonic is introduced on top of a 50A fundamental to visually showcase the effect. In this case, the third harmonic, located in phase B, presents a magnitude equal to 10% of the fundamental.

Given that the increment on the third harmonic is in phase B, I_β is greatly affected by the change, and its fundamental IF, shown in Fig. 5.13 b), begins oscillating significantly, in contrast with the behaviour of I_α. In a real case however even I_α would see itself affected by the fault due to the imbalance created by such a fault. This oscillation, and especially the transient conditions between healthy and faulty state, point to the difficulty of detecting the fault by conventional means. On the other hand, the HHT allows for a visualization of instantaneous variations of frequency and magnitude since it decomposes the signal in time domain. Together with simple statistical analysis such as the standard deviation, it allows taking advantage of the behaviour of instantaneous features that contain information of the fault, even for a single IMF containing the fundamental frequency, generating a clear fault indicator. This can be seen in Fig. 5.14 and Fig. 5.15, where the addition of a third harmonic on top of a pure sine wave of magnitude 50 increases the oscillation of IF, shown in a), and IM, shown in b), around the value of the fundamental.

Additionally, it is possible to combine both features in a single MHS. The spectrum, shown in Fig. 5.14 c), allows to visually represent the harmonic content of the signal which can be associated with the severity of a short circuit fault. As the severity increases, so does the harmonic content of the currents, resulting in a different distribution of frequencies, usually across a bigger range. For the case shown in Fig. 5.14, fault severity has been simulated by increasing the magnitude of a third harmonic on top of the fundamental component. The third harmonic magnitudes are 0A (blue), 0.02A (red), 0.05A (green) and 0.2A (magenta), while fundamental (50Hz) has a magnitude of 50A. This very low severity represents what a single turn fault might look like. The time axis is employed only to show the variation as the third harmonic magnitude increases. The typical application of HHT has an additional limitation due to edge effect seen in Fig. 5.14 and Fig. 5.15, a) and b) at the transitions between one sampling period and the next. This effect can be avoided in real-time implementation as seen in section 5.7 of this Chapter.

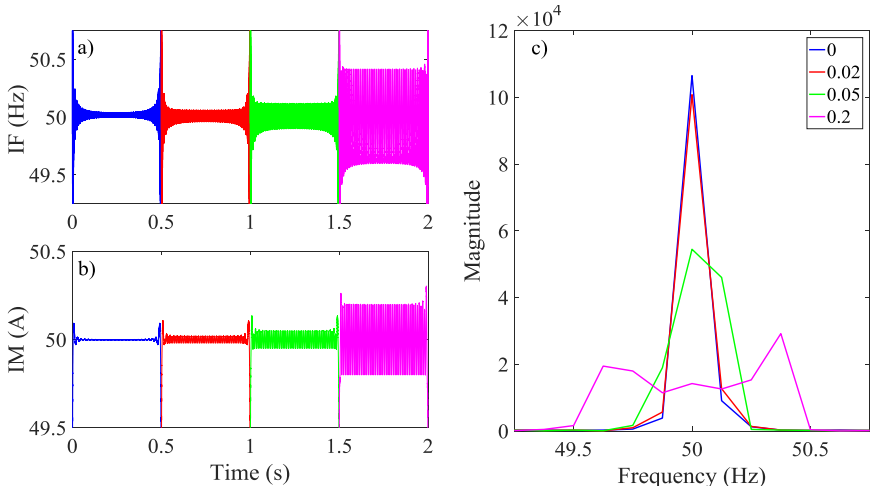

Fig. 5.14. IF a), IM b) and MHS c) with different magnitude third harmonics.

Due to the nature of the EMD method employed by the HHT, there is a possible limitation in the severity of the fault that can be detected by analysis of phase currents. The reason for this limitation lies on the way the expected third harmonic component modifies the shape of the original signal, modifying in turn the computed envelopes. Due to the very low amplitude of fault-generated harmonics, the EMD process might be unable to find an extra IMF which would generally suffice as a fault indicator. However, if the magnitude of the third harmonic is greater or equal than approximately 11.5% of the fundamental (5.75A for the case under study), a new IMF (shown in red) corresponding to the third harmonic (150Hz in this case) will be computed by the HHT as shown in Fig. 5.15.

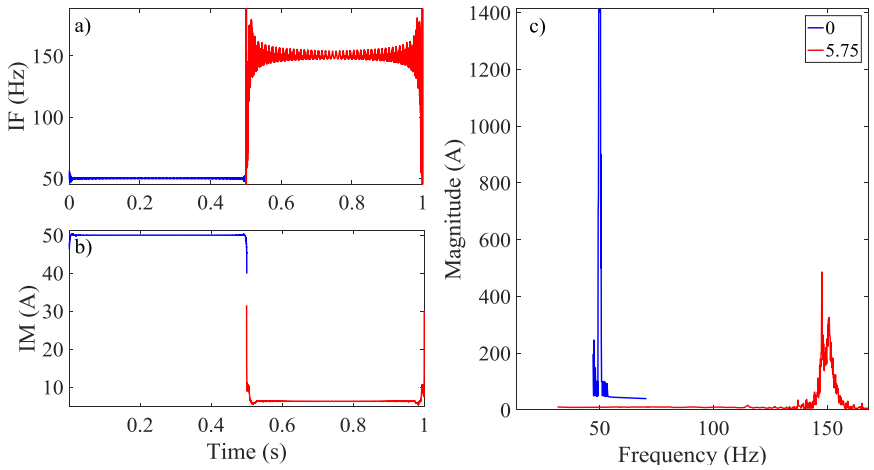

Fig. 5.15. IF a), IM b) and MHS c) with significant third harmonic.

Whilst the HHT was initially applied to one or all three phase currents, the same analysis can be performed in similar manner by studying alpha-beta variables. Even more, combining these two, allows in fact to reduce the analysis to a single frequency and magnitude variable. For that purpose, alpha and beta IF and IM must be first obtained independently and combined as shown in (11), (12).

$$IF = \sqrt{\frac{IF\alpha^2 + IF\beta^2}{2}} \tag{84}$$

$$IM = \sqrt{\frac{IM\alpha^2 + IM\beta^2}{2}} \tag{85}$$

To separate the indicators from the effects of transient conditions not related to the fault, combined IF and IM are subtracted from the real frequency and magnitude to create two residual signals. Frequency may be obtained by encoder or resolver, or estimated by use of phase-locked loop. On the other hand, magnitude, can be just computed as the module of alpha and beta currents as seen in (13).

$$I = \sqrt{I\alpha^2 + I\beta^2} \tag{86}$$

The standard deviation is then applied to the residual or error signals resulting from subtracting HHT IF and IM from the real frequency and magnitude. The standard deviation is calculated as:

$$s = \sqrt{\frac{\sum_{i=1}^{N}(x_i - \overline{x})^2}{N-1}} \tag{87}$$

where x_i are the observed values of the sample items, $\overline{x}$ is the mean value of these observations, and N is the number of observations in the sample.

In summary, this Chapter proposes analysing in detail the IMF containing the fundamental frequency, which is distorted by an inter-turn stator fault. However, it is expected that the low amplitude of the fault-generated harmonics is not sufficient to generate a new IMFs specific to the fault. The HHT is still necessary to arrive to the fundamental IMF and to improve the behaviour of the Hilbert transform.

5.5. Real-Time Implementation and Test Rig

The proposed HHT-based technique is first verified on a Hardware-in-the-loop (HIL) platform that allows modelling and testing of different fault conditions in real-time. The real-time modelling and the HIL platform has been extensively described and validated in [18], [117], [120]. Later, an experimental validation is carried out employing a 9-phase 45kVA PMSM aerospace starter-generator prototype running in a dynamometer test rig at different conditions.

Real-Time implementation has been realized in a similar manner to what was required for the model-based fault detection method presented in Chapter 4. The HHT is implemented on a commercially available real-time simulation platform OP5600 from OPAL-RT. This platform employs MATLAB's Simulink as user interface, simplifying the coding process. A simple Simulink function block is employed to place the HHT into the device's CPU which is then automatically converted to *C* code. The arrangement is graphically represented in Fig. 5.16. It differs from that presented in section 3.5-B (Chapter 3) in that it no longer requires voltage inputs.

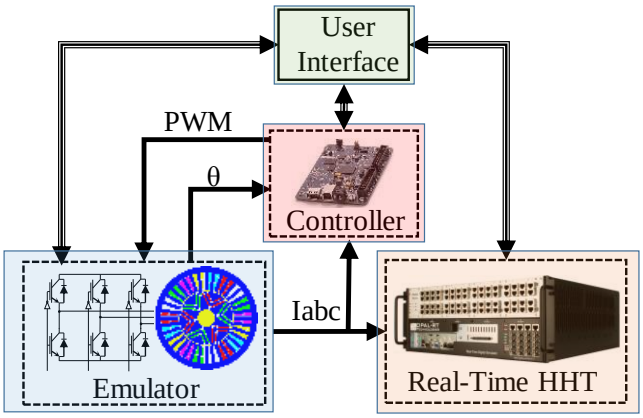

Fig. 5.16. HIL arrangement for signal-based fault detection based on HHT.

5.6. Simulation Results

First, the PMSM is simulated offline under different operating conditions. The machine model is subjected to constant transient conditions in the form of a speed ramp during the entire simulation. First the IMF is computed from the phase current as shown in Fig. 5.17 (middle) for the fault instant (0.4s). A step up load variation is generated at 0.2s and an interturn fault is generated at 0.4s. As a result, the unfiltered IF and IM seen in Fig. 5.18 of the computed IMF are affected accordingly. The result of the interturn fault

is evident, beginning an oscillation around the fundamental value of the frequency due to the addition of a third harmonic, typically produced due to short circuiting of the stator winding as explained in section 5.4.

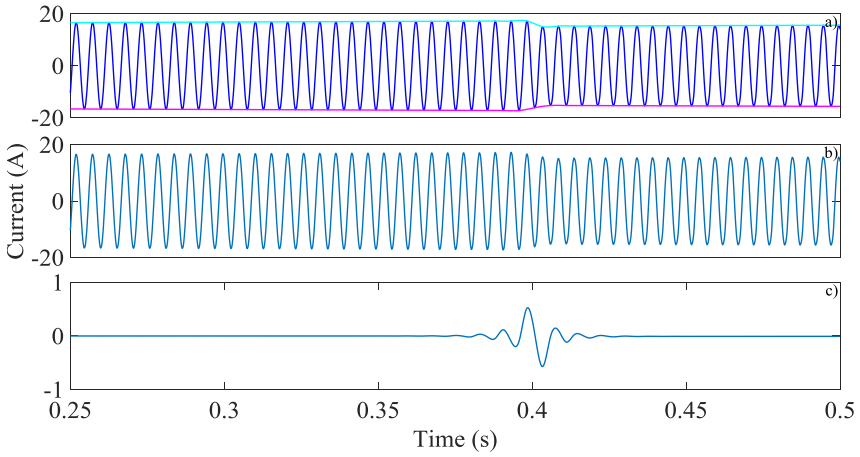

Fig. 5.17. Original signal plus envelopes a), computed IMF b) and residue c).

For a single-turn or interturn short circuit, the severity of the fault is not big enough to generate a new IMF as presented before by Fig. 5.14, Fig. 5.15. Nevertheless, the spectral analysis based on the MHS shown in Fig. 5.19, demonstrates a tendency to produce peaks and distortion around the fundamental frequency component, almost 200Hz when the fault is created. This could be identified by more advanced methods based on machine learning techniques for image or pattern recognition [82].

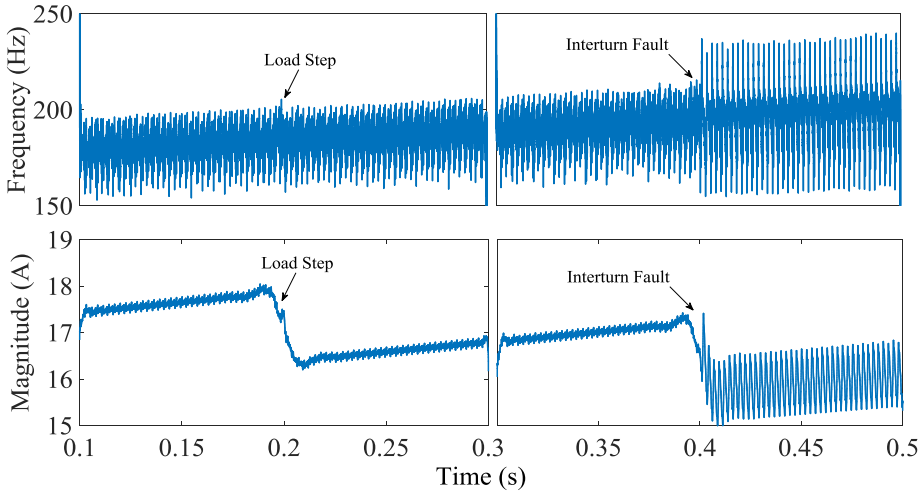

Fig. 5.18. Phase current IF and IM transient behaviour under load step (left) and fault (right).

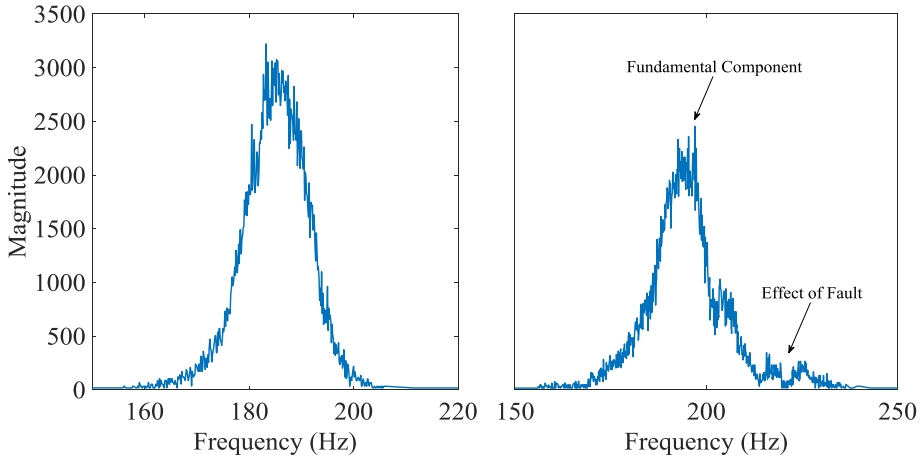

Fig. 5.19. Phase current MHS under load step (left) and fault (right).

Fig. 5.20 presents an implementation of this technique. The model is subjected to a series of transient conditions with load steps, speed ramps and a speed step. A fault is applied at t=0.4s, off at t=0.7s and on again at t=1s. The phase current signal is shown in dark blue (top). The measured frequency of the fundamental component (*freq*) is shown in black versus the IF of the single IMF calculated in green (middle). The standard deviation of the IF (sdIF) and IM (sdIM), in blue and red respectively, and finally the fault indicator in magenta which is activated when the standard deviation of the IF surpasses a threshold value of 10 for the time instant 0.4s. The magnitude of the indicator is fixed to 0 for healthy conditions and 30 for faulty conditions so its activation is visually noticed.

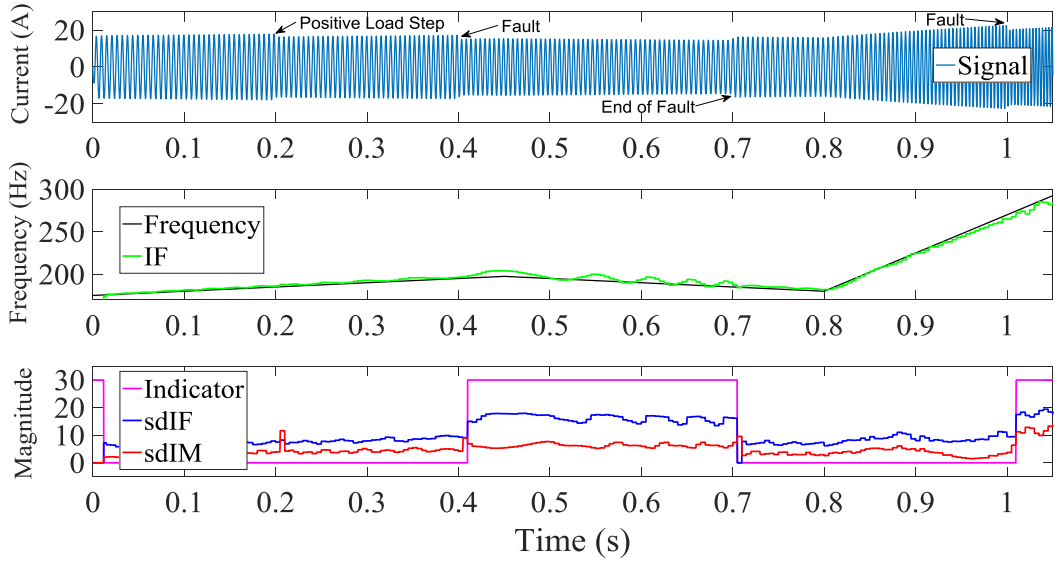

Fig. 5.20. In-Simulation implementation of HHT.

The threshold value is changed dynamically depending on IF and IM to further avoid false alarms. As can be seen, the IF (green line) changes following the fault, however, it also changes as a function of motor speed. On the other hand, the standard deviation of the IF (middle blue) changes significantly following the fault but is not affected by speed transients, demonstrating its usefulness for fault detection.

5.7. Hardware-in-the-Loop Results

Further results are presented here to validate the proposed technique for real-time conditions. In this particular case of application, the HHT is running with a relatively slow rate of execution of 5kHz, which is imposed by limitation of the hardware platform and the relative computational complexity of the algorithm. An unintended effect of the slow rate of execution is found in filtering out every frequency component above it, including PWM ripple, which simplifies obtaining the IMF corresponding to the fundamental frequency.

A. Generating Mode

The machine is first set in generating mode feeding a resistive load with an initial speed of 2000rpm. Given the considered machine contains 3 pole pairs, the fundamental frequency is 100Hz. A fault, positive load step and a positive speed step are simulated. The behaviour of the IF for these three transient conditions is shown in Fig. 5.21.

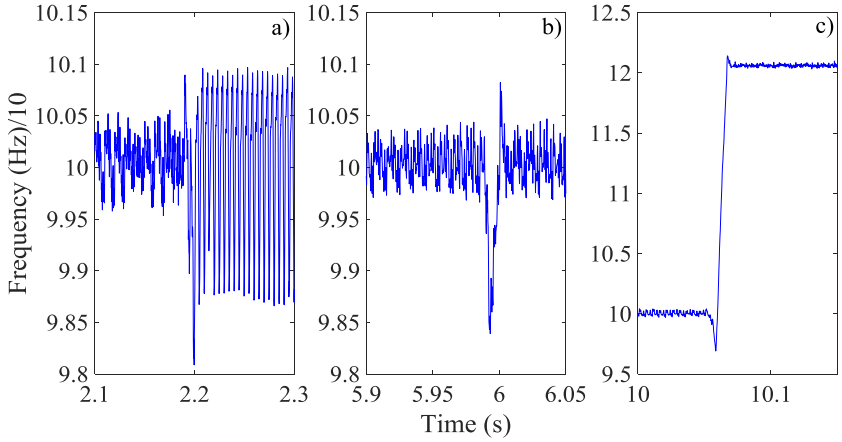

Fig. 5.21. Scaled IF during fault a), load step b), and speed step c) for generating mode.

The standard deviation of the same IF (blue), together with an indicator based on it (red), decoupled from the effects of transitory conditions to avoid false alarms, is presented in Fig. 5.22. The indicator is based on the standard deviation of the IF (sdIF), adjusted with normalized values of IF and IM to smooth its output behaviour and filtered

by a moving average filter. Under generating mode, the effect of the fault on the indicator is significant enough to allow for a simple, constant threshold (green), as shown in Fig. 5.22.

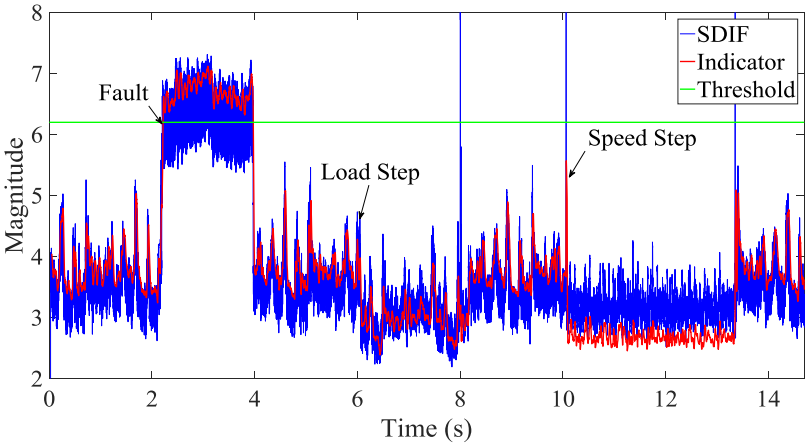

Fig. 5.22. Standard deviation of the IF, indicator and threshold during transient conditions for generating mode.

The indicator is generated applying a moving average filter on the sdIF resulting in a slower but more reliable detection of the fault. Additionally, the signal is adjusted by employing normalized values of IF and IM. The purpose of this is to further eliminate the effect of transients. This method is refined in section 5.8 of this Chapter by use of magnitude and frequency residuals. Given that the HHT was executed with a time step of 0.2ms and the average was calculated using 128 points, it would add up to 25.6ms of delay. However, since the average is calculated for every new point, the change is gradual, so in reality, it tends to lie around half of that value, 13ms which are added regardless of the fundamental frequency. Similarly, the HHT itself is applied for each two periods of the signal for every new point, losing the oldest element at the same time it acquires a new one. With a fundamental frequency of 100Hz, two periods corresponds to 20ms.

For the particular case depicted in Fig. 5.21 and Fig. 5.22, the fault is produced at t= 2.181s and it is detected by the indicator at t=2.214s requiring approximately 33ms for detection. The IF ripple increases at t= 2.193s, or 12ms after the fault, showing that slightly more than one period after the fault is needed to begin detection. Ultimately, the detection of the fault is a trade-off between reliability and speed of detection.

B. Motoring Mode

Further HIL testing has been carried out in motoring mode under field-oriented control as illustrated in Fig. 5.16. Similarly to what was done in generating mode, different transient conditions including an interturn fault, together with load and speed steps are represented. Fault detection under motoring mode becomes more challenging due to the compensating action by the current controllers in the FOC. The current controllers will try to suppress any distortion due to faults to keep sinusoidal output currents. For that reason, a dynamic threshold was considered for motoring HIL results, changing automatically in a similar manner to the adjustment done for the indicator itself, presented in section 5.7 A. This correction shown in (88), later dismissed, was intended to help avoid false alarms due to step changes in frequency and magnitude. The reason for its later avoidance was due to being considered an *ad hoc* solution, not of general application. Alternatively, the use of magnitude and frequency residuals and the alpha-beta combination of IF and IM shown in section 5.4 can should be used. The threshold was computed as:

$$Thr_i = Thr_0 \frac{IF_i}{IF_0} \frac{IM_i}{IM_0} \tag{88}$$

where Thr_0 is a constant value obtained at the initial conditions for healthy operation. In addition, for HIL results, an increase in speed was partially reflected as an increase in standard deviation of IF due to a fixed window buffer size. Considering a synchronous machine, if speed varies, the analysed window must adjust accordingly.

Fig. 5.23 and Fig. 5.24 show results obtained at 3500rpm, which correspond to 175Hz of fundamental frequency. In particular Fig. 23 shows the IF during fault a), load step b), positive speed step c) and negative speed step d). In the case fully represented in Fig. 5.24, the fault occurs at t= 1.535s and is reliably detected at t=1.694s, resulting in detection delay of t=159ms. The difference between generator and motor mode is partially explained by a double application of averaging. In the later, the averaging filter is also applied not only to the standard deviation of the IF but to the IF itself, in part to reduce the distortion caused by the PWM modulation, adding an extra delay. The remaining delay can be explained simply by how the threshold was defined, to avoid false alarms.

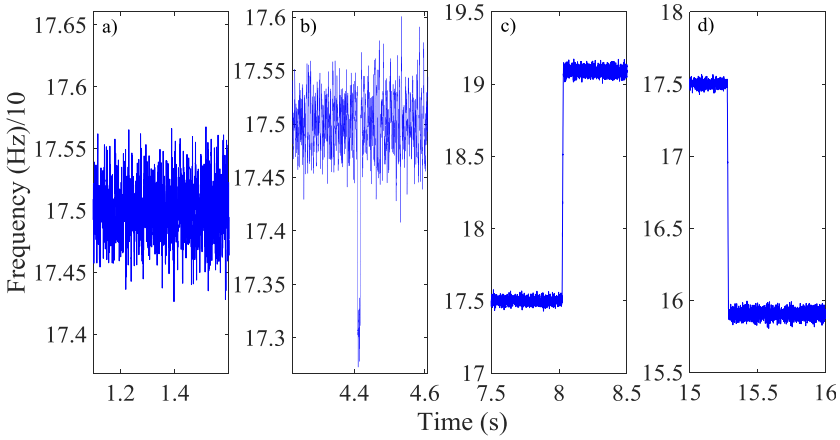

Fig. 5.23. Scaled IF during fault a), load step b), positive speed step c), and negative speed step d) for motoring mode.

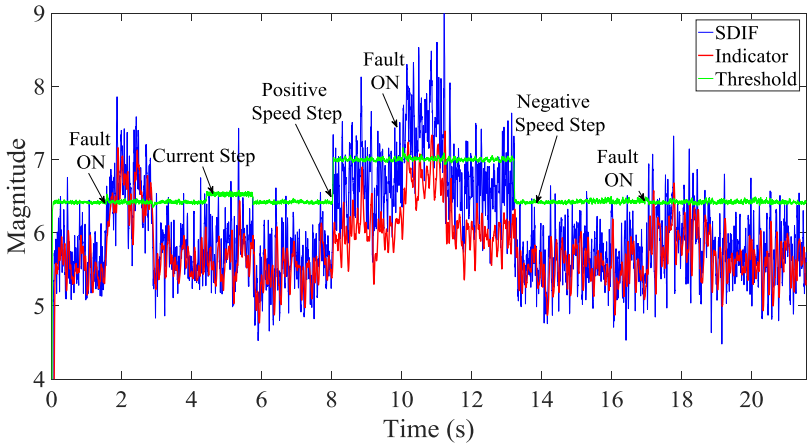

Fig. 5.24. Standard deviation of the IF, indicator and threshold during transient conditions for motoring mode.

5.8. Experimental Validation

Finally, the HHT is tested online against experimental data measured on a 45kVA aerospace starter-generator employing the same experiment setup described in Chapter 4. Different conditions are tested allowing to discriminate between a short circuit fault, and the transient conditions generated due to current steps or speed ramps under healthy operation.

Similarly to what was done on section 5.4, the IF, IM and the Marginal Hilbert Spectrum MHS of combined $\alpha\beta$ currents are presented for these three cases in Fig. 5.25-Fig. 5.27, with MHS being computed offline. Furthermore, each one is represented in three stages, including before (blue), during (green) and after (red) the transient occurs. Both IF and IM are shown to have an increased ripple for faulty conditions while the

spectral analysis visibly decreases in average and spreads over a wider range around the fundamental frequency, as shown by Fig. 5.25. On the other hand, the transient behaviour of MHS for a step current, seen in Fig. 5.26, deviates from the fundamental and towards higher frequencies. The difference in MHS peak magnitudes between faulty (1.8×10^4) and healthy (3.5×10^4) conditions can be explained by the difference in time length of the analysed window for each case and the nature of the spectrum. Given that MHS is generated as the accumulated magnitudes over the frequency range of an IMF (83), the longer the analysed window in time domain, the higher the magnitudes recorded in the spectrum. For all cases, the approximate bell curve shape obtained from computing the MHS in steady state conditions, is shown to have maximum peak magnitude and minimum frequency range.

Usually, an edge effect on both IF and IM is expected when applying HHT offline, as seen in section 5.4. However, this is not present for real-time conditions due to the moving window implementation which outputs a single point based on the average of the central part of the IF and IM waveforms, avoiding the edges. While the analysis is shown here for a combined $\alpha\beta$ signal to minimize computational requirements and cover the entire machine, it is still possible to identify the fault by analysing any of the three phase currents. The increased dispersion and average change in IF and IM under faulty conditions seen in Fig. 5.25, points once again to the feasibility of fault detection through online statistical analysis.

Finally, the resulting indicators, combined $\alpha\beta$ signal's sdIF and sdIM, corresponding to standard deviation of IF and IM respectively, are plotted versus time and compared to the improved single Fourier analysis, described in Fig. 5.7, of the combined $\alpha\beta$ third harmonic in Fig. 5.28-Fig. 5.30. The cases analysed are the same previously shown in Fig. 5.25-Fig. 5.27. Each case is represented as a direct comparison in their original magnitudes. Given the magnitudes made before the analysis are already normalized, it should not be necessary to normalize the indicators again, however given that the Fourier indicator shown in green is in a different scale, they are plotted separately. The Fourier indicator makes use of real-time frequency obtained through measured speed or estimated by PLL, to dynamically calculate the third harmonic magnitude of I$\alpha\beta$, as shown in Fig. 5.7.

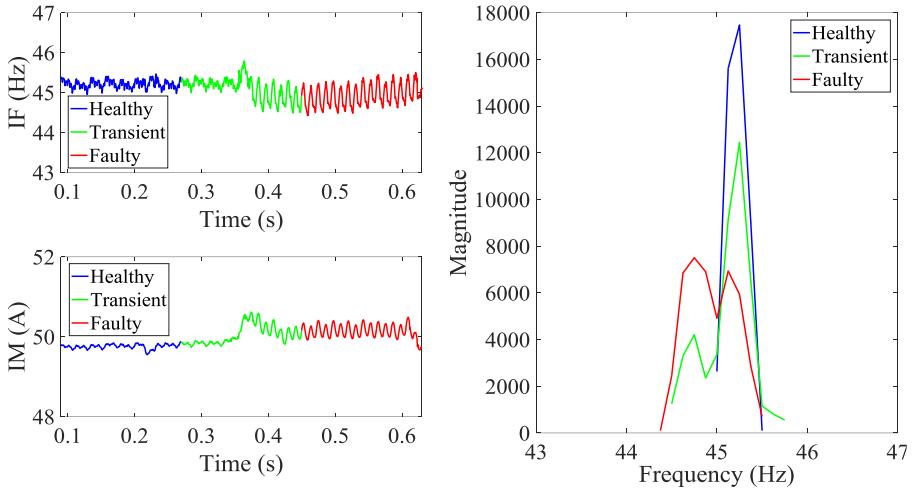

Fig. 5.25. IF, IM and MHS of fault case.

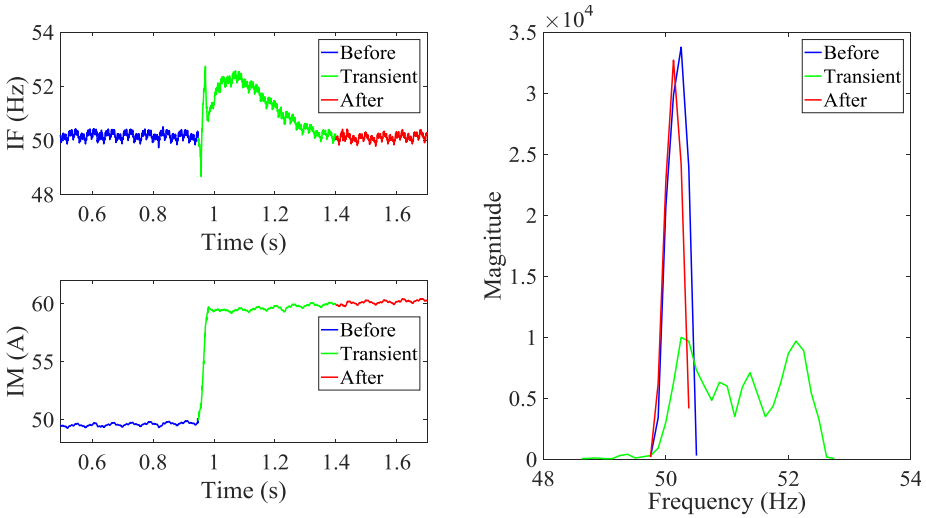

Fig. 5.26. IF, IM and MHS of 10A current step.

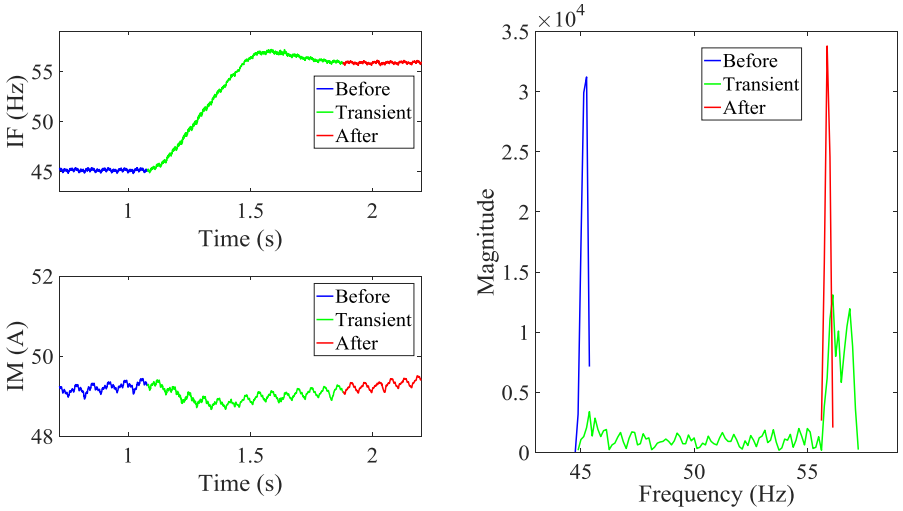

Fig. 5.27. IF, IM and MHS of 200rpm speed ramp.

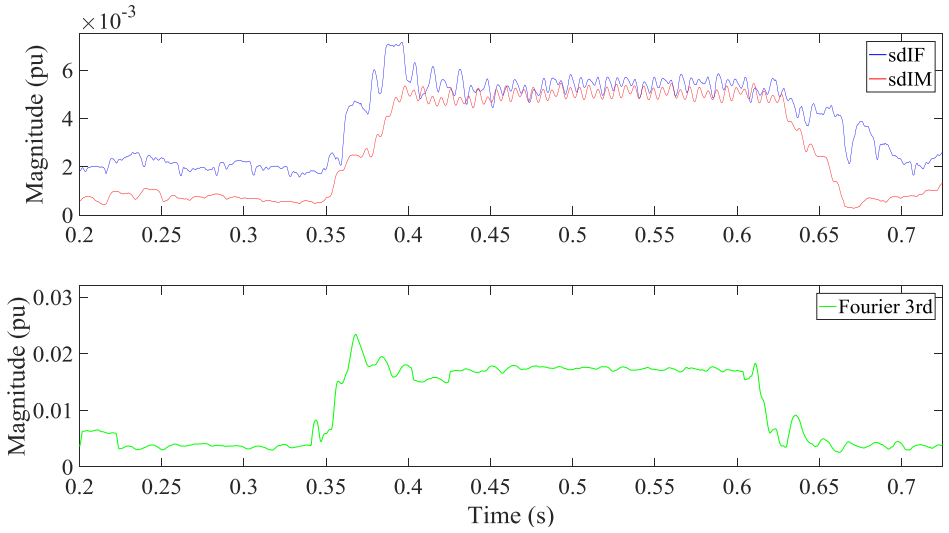

Fig. 5.28. HHT extracted indicators vs Fourier ones of fault case.

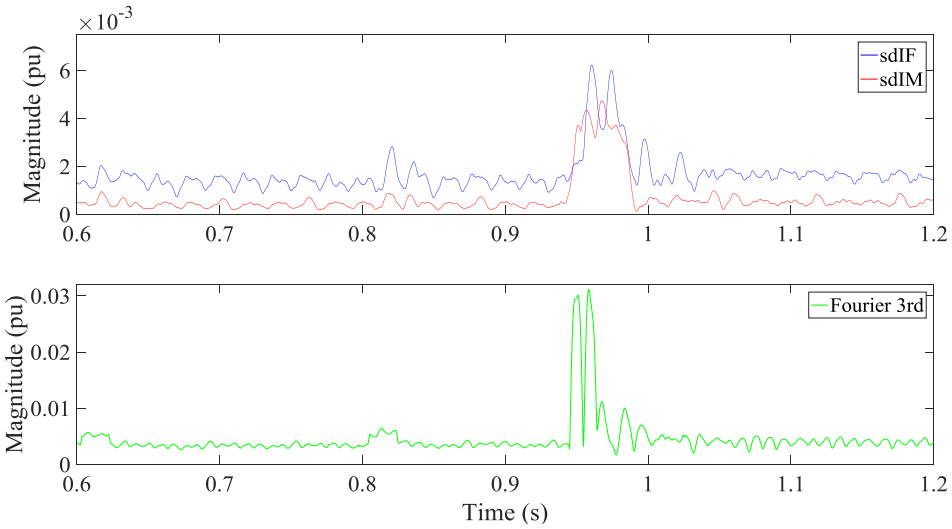

Fig. 5.29. HHT extracted indicators vs Fourier ones of 10A current step.

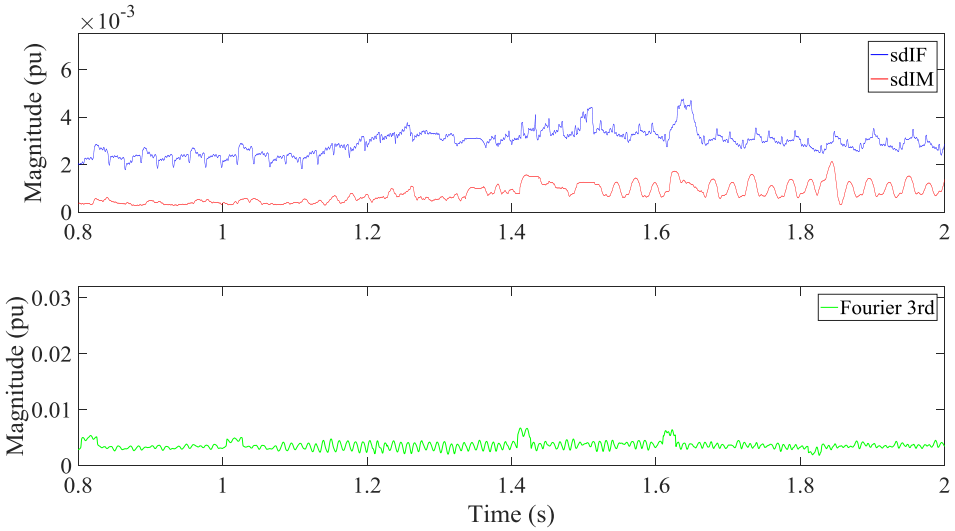

Fig. 5.30. HHT extracted indicators vs Fourier ones of 200rpm speed ramp.

Analysing the results it is possible to show that the response for the sdIF and sdIM indicators is similar although slightly slower than the improved Fourier's. Particularly for fault conditions, the sdIM indicator appears more sensitive than Fourier and sdIF. Also, while speed transient conditions, seen in Fig. 5.30, don't affect significantly the indicators, transients due to significant enough current steps present the risk of triggering a false alarm, due to the inherent behaviour of phase current third harmonics under stator winding fault. Still, under current step both the sdIF and sdIM indicators present a smaller percentage change than the improved Fourier indicator. While the HHT method response climbs to a similar magnitude than that seen under fault conditions, the improved Fourier under current step almost doubles it.

In addition, a comparison is included with results presented at the beginning of this chapter in Fig. 5.2-Fig. 5.4, which depict the same three cases shown in this section but analysing α current by means of offline computed FFT moving window. Looking at Fig. 5.31-Fig. 5.33, it is evident the use of HHT proposed in this chapter provides a much stronger indicator to discriminate between healthy or faulty conditions.

Furthermore, the ability of the HHT to detect other type of faults, such as PMSM demagnetization or bearing fault, points out to the possibility of extending this work, in the near future, to discriminate different types of faults for automated classification and diagnosis purposes.

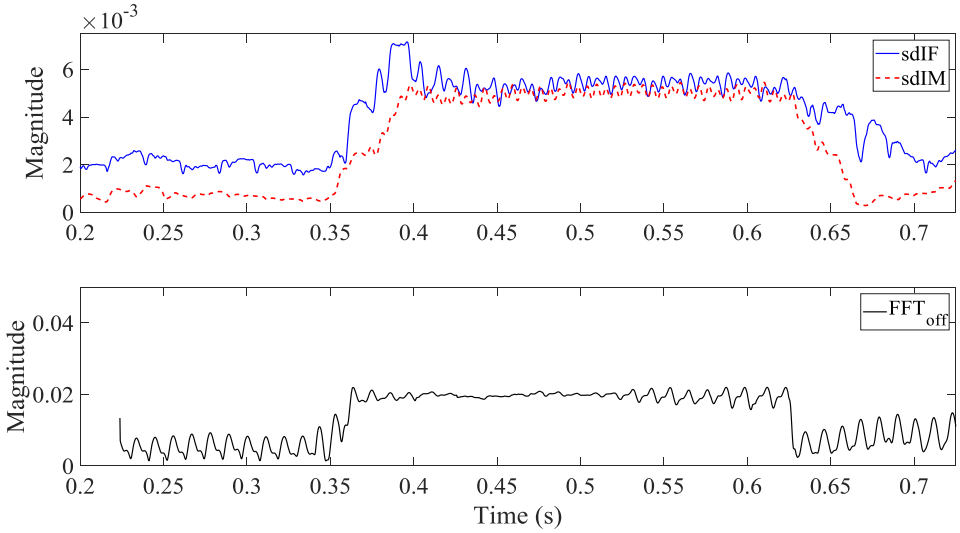

Fig. 5.31. HHT extracted indicators vs Iα FFT of fault case.

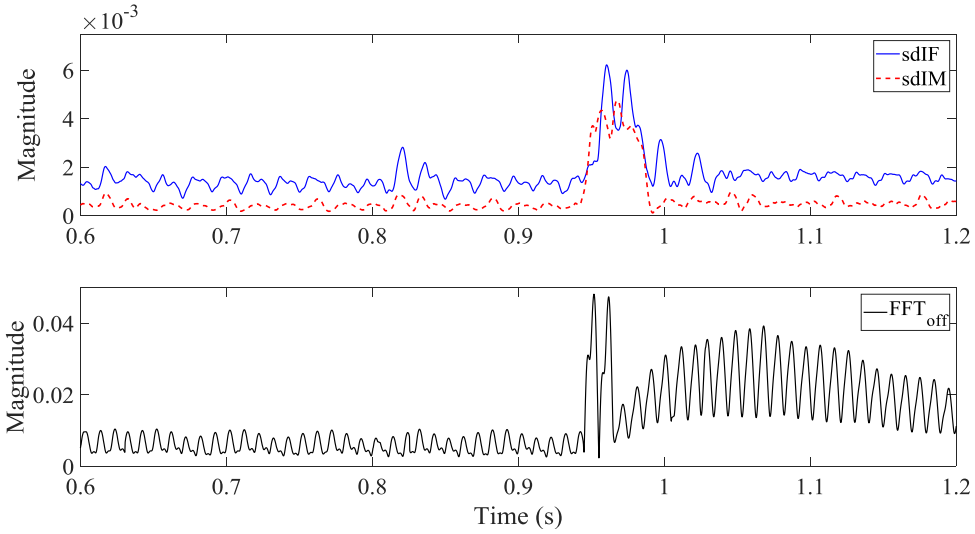

Fig. 5.32. HHT extracted indicators vs Iα FFT of 10A current step.

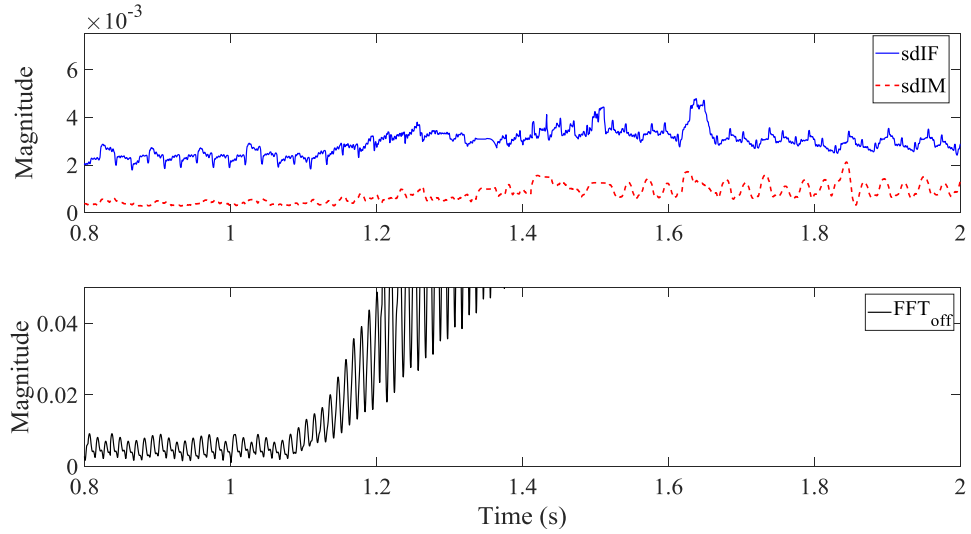

Fig. 5.33. HHT extracted indicators vs Iα FFT of 200rpm speed ramp.

5.9. Summary

This Chapter has presented a novel method for the detection of short circuit faults in PMSMs by means of HHT generated instantaneous features of the IMF corresponding to the fundamental frequency. Furthermore, it has provided a slight improvement on single Fourier series tracking implementation, which is employed to compare and validate the results. The analytical description of the HHT, the fault detection method and the basis that motivates the development of such method have been presented as well. Simulation results and real-time implementations have been provided in a number of cases to demonstrate the validity of the proposed methodology and discuss some of the

limitations. It is demonstrated that the HHT can identify the IF and IM of the signal under consideration correctly and when applied to phase current can track speed variations as well as small changes caused by interturn faults. Unfortunately the instantaneous signals variations might be too small for reliable fault detection in inverter-controlled motors. An alternative based on the standard deviation of the IF and IM is proposed which is demonstrated to be more effective in all cases considered. Whilst the standard deviation is calculated originally from three phase currents, a study of combined alpha-beta currents alleviates the computational requirements reducing the number of studied signals from three to two and the sdIF and sdIM indicators from six to two. Additionally, creating magnitude and frequency residuals, it is possible to further improve the indicators response by separating it from sudden changes due to fast transitory conditions. Further work might be still needed to improve the sensitivity of the method and the ability to avoid false alarms due to current steps. While different fault severities should be identified in a straight forward manner, additional work is being considered to include the ability to discriminate between different types of fault such as demagnetization.

CHAPTER 6

FAULT DETECTION BASED ON MACHINE LEARNING CLASSIFICATION TECHNIQUES

6.1. Overview

A significant amount of data can be available from machine operation, electrical measurements (e.g. currents or voltages in time domain or harmonics in the frequency domain) and others such as vibration or temperature measurements. In principle, it could be useful to combine all this data to provide a comprehensive condition monitoring solution which allows not only classification into healthy and faulty data, but also discriminating between different types of faults (stator faults, demagnetization, bearing faults) and their severity.

As shown in section 1.5 D. of Chapter 1, some papers in literature have investigated these aspects. Research in AI and pattern recognition has developed methods for classification in multi-dimensional spaces such as Neural Networks (NN), Particle Swarm Optimization (PSO) or Support Vector Machine (SVM).

The scope of this chapter is more limited and in particular will deal with the potential application of these mathematical techniques to the problem of fault detection, i.e. the classification of machine operation in two possible outcomes: healthy or faulty conditions. In particular the second, third and fourth standardized moments are employed as features for use as inputs to a linear discriminant analysis and then to a SVM.

It is demonstrated that most data available is linearly separable into healthy and faulty conditions, and thus a simple linear discriminant method could suffice. However a SVM is also explored with aims at a future nonlinear analysis, and results of a three dimensional implementation using standard deviation, skewness and kurtosis were also provided given its theoretical ability to discriminate even nonlinear data, something identified as of significant importance.

6.2. Feature Extraction

This chapter proposes using a time-frequency signal analysis method combined with simple statistical analysis to generate reliable features for fault classification. As it was shown in Chapter 5, a fault indicator may be found after performing Hilbert Huang Transformation (HHT) on machine currents. The standard deviation, skewness and kurtosis of instantaneous frequency (IF) and magnitude (IM) provide valuable information to discriminate between healthy and faulty conditions. While the standard deviation has been demonstrated to work on its own, skewness and kurtosis are presented here to provide additional features, given they have been proposed before [111], they can be extracted with relatively simplicity and they are shown to change under fault conditions as shown later in section 6.4, even though their contribution to classification is less significant.

Since the standard deviation is the square root of the variance, the three statistical variables employed are simply the second, third and fourth statistical moments, as shown in (89)-(91) of the analysed function.

$$\text{Variance:}\quad \widetilde{\mu_2} = \frac{\mu_2}{\sigma^2} = \frac{E\left[(X-\mu)^2\right]}{(E[(X-\mu)^2])^{2/2}} = 1 \tag{89}$$

$$\text{Skewness:}\quad \widetilde{\mu_3} = \frac{\mu_3}{\sigma^3} = \frac{E\left[(X-\mu)^3\right]}{(E[(X-\mu)^2])^{3/2}} = 1 \tag{90}$$

$$\text{Kurtosis:}\quad \widetilde{\mu_4} = \frac{\mu_4}{\sigma^4} = \frac{E\left[(X-\mu)^4\right]}{(E[(X-\mu)^2])^{4/2}} = 1 \tag{91}$$

The HHT has been used before for machine condition monitoring feature extraction purposes together with Support Vector Machine (SVM) [82]. While IF may be used for fault detection directly [123], the authors have found more reliable to go one step further, and extract information from the frequency signal itself. Additionally, the same algorithm may be employed to detect other type of faults such as demagnetization [79] or bearing faults [75]–[78]. Time-frequency analysis has been combined with SVM already to detect and classify stator faults [104], [108], [109]. Whilst this chapter proposes employing three features based on statistical analysis of IF and IM, previous work is known to have used up to twenty different features [111].

6.3. Classification

Two types of classification are considered in this chapter, one limited to linear discrimination and another capable of both linear and nonlinear discrimination. The linear classification method employed is also known as Fisher's Linear Discriminant method (FLD). FLD is relatively simple on its implementation. In this chapter FLD will be used to investigate the suitability of the extracted features for correct fault classification and, if possible, allow for fault discrimination without the need of a more complex method. This is expected to be enough for data collected in steady state conditions for both healthy and faulty conditions. On the other hand, it is expected that for cases involving transient conditions a nonlinear method might be required. A two class SVM has been developed for those cases, even though all data available can be successfully classified with linear methods. Both 2D and 3D implementations of the SVM are graphically represented.

A. Fisher's Linear Discriminant

FLD allows for a visualization of extracted features in a lower dimensional subspace [101], a process known as dimensionality reduction, by generating a linear function of the employed data as (92).

$$y = w^T x \tag{92}$$

where y is the one-dimensional projection of the N-dimensional feature input vector x, and w is the N-dimensional weight. To avoid overlapping in the one dimensional projection, the weight vector w is employed to maximise class separation.

While it is possible for FLD to solve a multiclass problem, the analysis carried out in this chapter is limited to two classes, corresponding to healthy and faulty data. Means vectors $m_{1,2}$ for $N_{1,2}$ points of each class $C_{1,2}$ are:

$$\begin{aligned} m_1 &= \frac{1}{N_1} \sum_{n \in C_1} x_n \\ m_2 &= \frac{1}{N_2} \sum_{n \in C_2} x_n \end{aligned} \tag{93}$$

A measure of the separation between classes is obtained by computing the difference between class means as shown in (94).

$$\begin{aligned} m_2 - m_1 &= w^T (m_2 - m_1) \\ m_k &= w^T m_k \end{aligned} \tag{94}$$

The within class variance of the projected data y_n of x_n is given by:

$$s_k^2 = \sum_{n \in C_k} (y_n - m_k)^2 \tag{95}$$

It is possible then to define the total within class variance by adding s_1^2 and s_2^2.The Fisher criterion may be computed as the ratio of the separation between classes defined by $m_2 - m_1$ to the variance within classes given by $s_1^2 + s_2^2$ as seen in (96), [124].

$$J(w) = \frac{(m_2 - m_1)^2}{s_1^2 + s_2^2} \tag{96}$$

Additionally, it is possible to make the dependence on the weight *w* explicit, and thus reformulate Fisher's criterion as:

$$J(w) = \frac{w^T S_B w}{w^T S_W w} \tag{97}$$

where the new terms S_B and S_W correspond to covariance matrixes between and within classes respectively, and are defined by:

$$S_B = (m_2 - m_1)(m_2 - m_1)^T \tag{98}$$

$$S_W = \sum_{n \in C_1} (x_n - m_1)(x_n - m_1)^T + \sum_{n \in C_2} (x_n - m_2)(x_n - m_2)^T \tag{99}$$

After differentiating (97), Fisher's criterion for linear discrimination $J(w)$ is maximized when

$$(w^T S_B w) S_W w = (w^T S_W w) S_B w \tag{100}$$

Considering the terms between parentheses in (100) are just scalar factors and the information sought after is in the *w* vector direction, it is possible drop the scalars and simplify by multiplying both sides by S_w^{-1} resulting in:

$$w \propto S_w^{-1}(m_2 - m_1) \tag{101}$$

B. Support Vector Machine

A SVM is a binary learning machine, capable of providing a global solution for a non-linear classification problem by means of a constructed hyperplane with a maximized decision boundary, provided significant training data is available [102]. The original input data space is transformed into a feature space where classification takes places.

The support vectors are extracted by the algorithm from the training sample itself and are what configure the hyperplane as seen in Fig. 6.1.

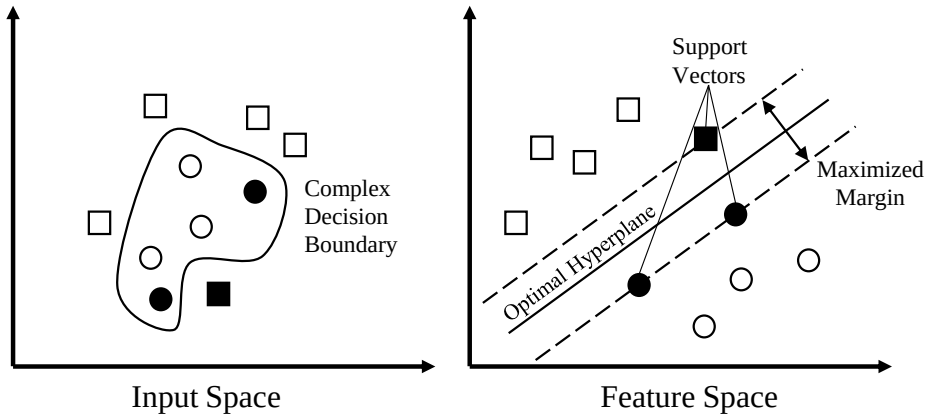

Fig. 6.1. SVM classification diagram.

The main difference between SVM and other supervised machine learning algorithms for classification, such as the well-known Neural Networks, is that SVM do not present local minima and thus find an optimal, global solution.

To simplify its mathematical definition, it is assumed that all data can be separated linearly, and in this way, the hyper-plane can be expressed by:

$$\omega^T \cdot x + b = 0 \tag{102}$$

Where ω is an n-dimensional weight vector and b is a bias vector. The following equation is used as the decision function to determine the class defined by the values +1 or -1 of an input data x:

$$f(x) = sgn(\omega^T \cdot x + b = 0) \tag{103}$$

To get the best hyper-plane with the largest margin between two classes, the parameters ω and b are determined thus by taking the support vector x_i on the boundary and solving the quadratic optimization problem

$$\left\{ \begin{matrix} Minimize & \frac{1}{2}||\omega||^2 \\ Subject\ to & y_i(\omega^T \cdot x + b) \geq 1 \end{matrix} \right\} \tag{104}$$

The SVM decision algorithm is done by solving the following optimization problem which applying Lagrange multipliers transforms into a maximization problem

$$\left\{\begin{array}{c} Maximize\ \ L(\alpha) = \sum_{i=1}^{N} \alpha_i - \frac{1}{2}\sum_{i=1}^{N}\sum_{j=1}^{N} \alpha_i \alpha_j y_i y_j K(x_i, x_j) \\ Subject\ to\ \ (p) \sum_{i=1}^{N} \alpha_i y_i = 0 \\ (2)\ 0 \le \alpha_i \le C \quad for \quad i = 1,2 \ldots N \end{array}\right\} \tag{105}$$

Where C is a positive parameter specified by the user and $K(x_i,xj)$ is a nonnegative definite matrix called the kernel matrix or *Gram*. The use of the kernel inner product $k(x,x_i)$, or in this case the kernel matrix, neglects the need to compute the weight vector w, something known as the *kernel trick*. Constraint *(p)* arises from optimization of the Lagrangian $L(\alpha)$ with respect to the bias b seen in (102) [105].

6.4. Experimental Validation Results

Validation of the proposed methods is performed employing experimental data acquired with the setup presented in Chapter 4, based on a 9-phase 45kVA Permanent Magnet Assisted Synchronous Reluctance Machine (PMA SynRM) prototype. HHT features were obtained in real time and later post processed offline to obtain standard deviation, skewness and kurtosis average values independent from time for classification purposes. Excluding transient conditions, often neglected in literature, data available is largely linearly separable. FLD would then, in principle, suffice as a classification method. However, the aim of this chapter is not limited to classification results, but rather to exploring novel tools and methods capable of fault classification under both steady state and transient conditions. For that purpose, FLD is first explored through the use of IM's standard deviation extracted as described in Chapter 5, followed by a more complete use of statistical analysis of both magnitude and frequency for SVM classification. For both cases scripts have been developed and run in MATLAB. Employed scripts can be found in Annex 3.

A. Fisher's Linear Discriminant Results

As shown in Chapter 5, alpha-beta analysis of currents and instantaneous features provides valuable indicators of stator winding fault. An alpha-beta representation of IF and IM can be computed obtaining a limited window of data from the time domain representation shown in Fig. 6.2 and Fig. 6.3. In this case, three hundred data points have been selected, representing at least three cycles of the fundamental frequency employed

(40-50Hz sampled at 5kHz). Alpha versus beta IFs under healthy (blue) and faulty (red) conditions overlap each other, but IMs are visibly separated, as shown in Fig. 6.4. Nonetheless, as shown by Fig. 6.2 and Fig. 6.3, it is clear that under faulty conditions both IF and IM spread over a wider range, displaying an increased "ripple", which motivates the use of statistical analysis, particularly standard deviation.

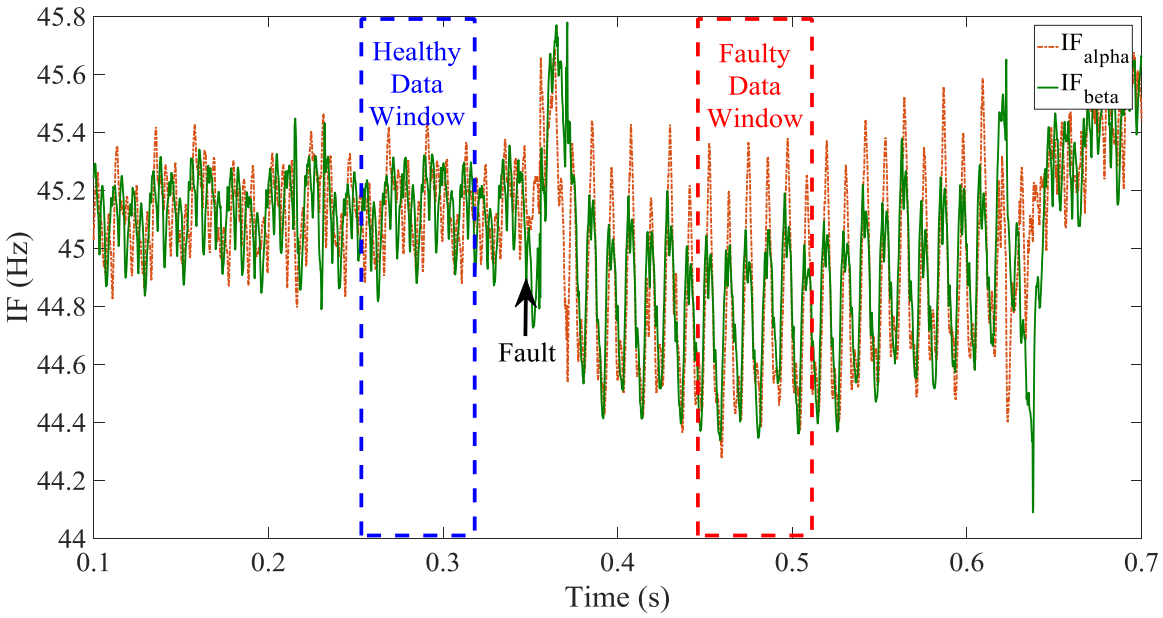

Fig. 6.2. Alpha (dotted brown) vs Beta (green) instantaneous frequencies for fault case (B08).

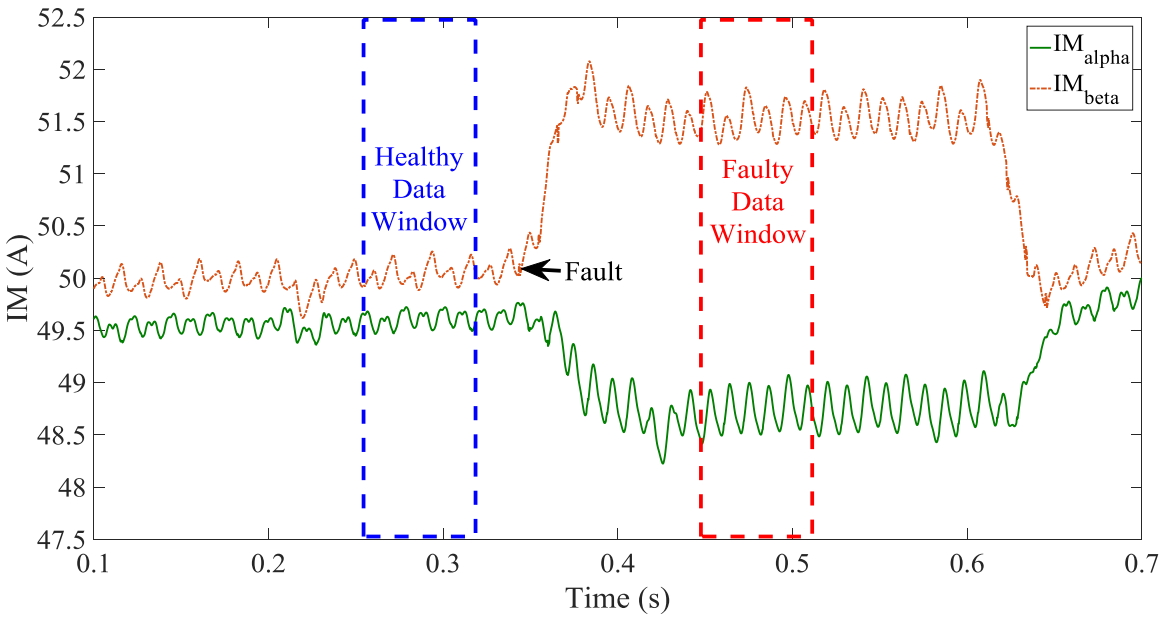

Fig. 6.3. Alpha (dotted brown) vs Beta (green) instantaneous magnitudes for fault case (B08).

An analysis of the standard deviation provides a clear separation for both, as seen in Fig. 6.5, where discrimination between healthy and faulty steady state conditions can be

easily achieved. Alpha-beta currents were normalized before obtaining standard deviation magnitudes which explains the relatively low magnitudes (in p.u.) seen in Fig. 6.5. Furthermore, the combined changes in IF and IM are directly visible on alpha-beta current, as seen in Fig. 6.6. Under faulty conditions, the current circle is slightly distorted, even for the interturn fault under study. The same fault case (B08) was employed for Fig. 6.4-Fig. 6.6, and was already extensively employed as the experimental fault case in Chapter 5.

Three examples of linear classification are provided in Fig. 6.7 and Fig. 6.8. The first two cases employ standard deviation of the IM while the third, provided mainly for comparison, employs the standard deviation of IF. The first case, seen in Fig. 6.7, accounts for 10 different cases, 6 fault cases in red and 4 healthy transient cases.

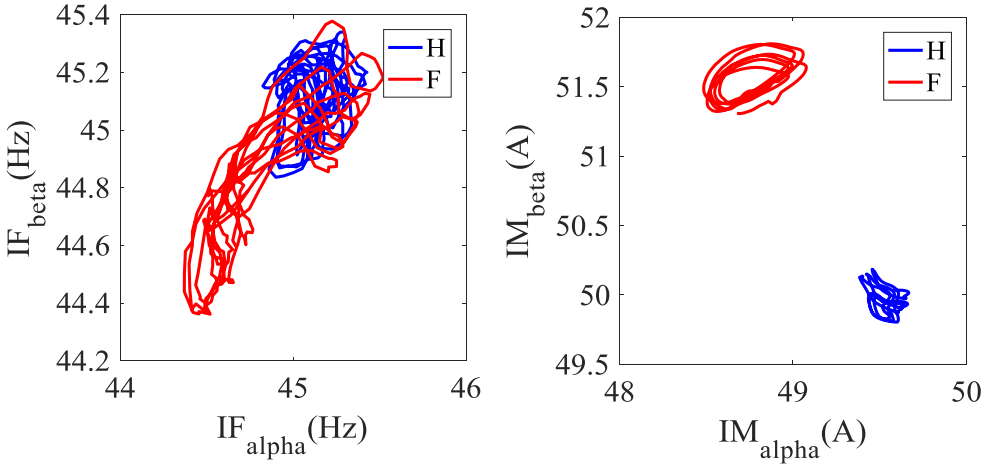

Fig. 6.4. Alpha-Beta representation of IF (left) and IM (right).

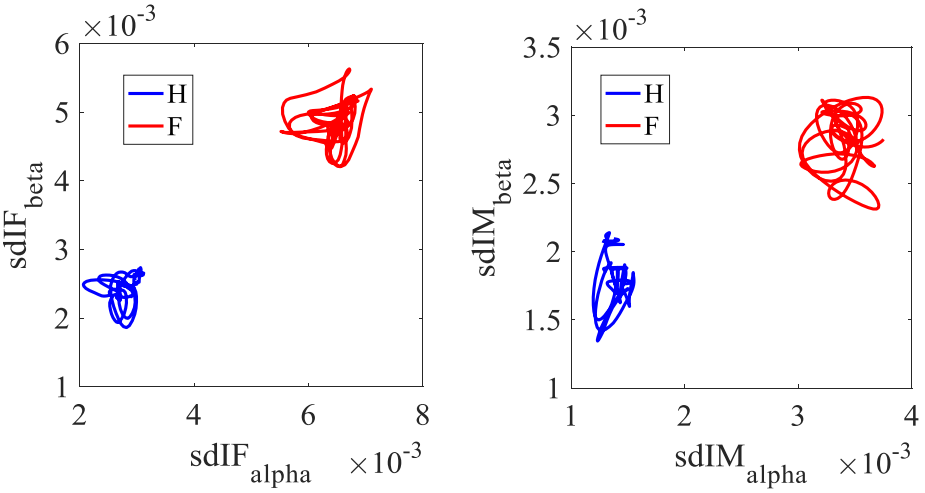

Fig. 6.5. Alpha-Beta representation of standard deviation of IF (left) and IM (right).

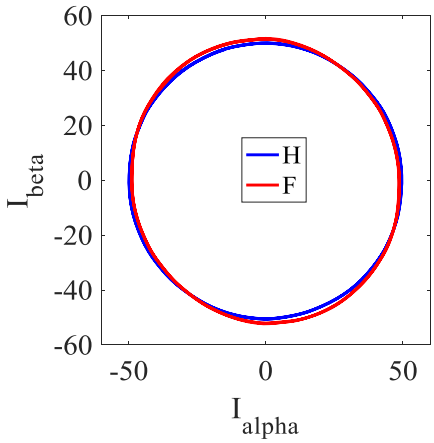

Fig. 6.6. Alpha-Beta current for healthy and faulty conditions.

Transient cases shown in blue, correspond simply to a different healthy state than initial conditions, such as after a current step or a speed ramp. For each case, only steady state conditions before and after the change are shown, while data corresponding to the transient itself is neglected, since transient data is non-linearly separable. Case $c1_2$ represents a positive current step (50-60A), c2 a negative current step (60-50A), c6 a positive speed ramp (900-1100rpm) and c7 a negative one (1100-900rpm).

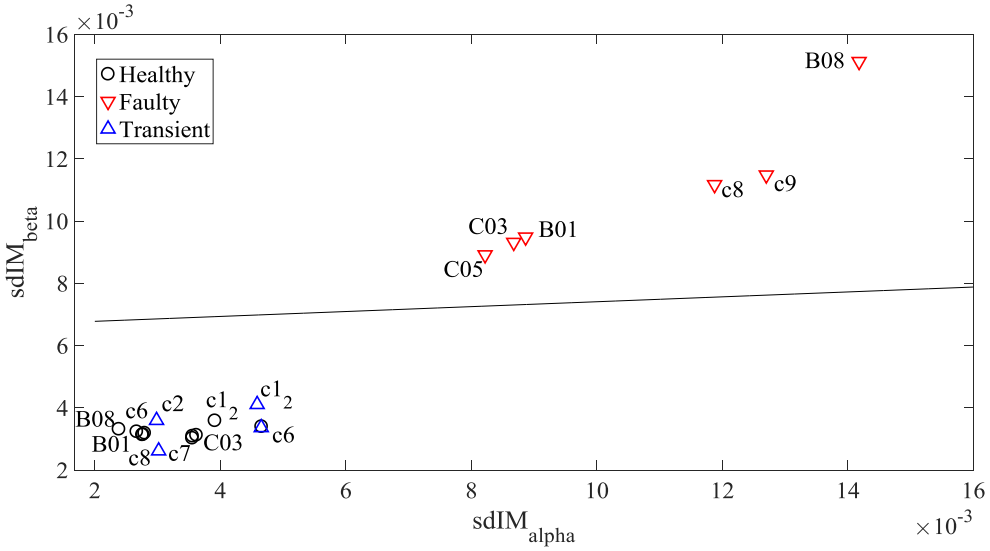

Fig. 6.7. Ten case Fisher's Linear Discriminant employing alpha-beta standard deviation of IM.

Fig. 6.8 presents another example in which 15 different cases are accounted for. All previous cases are included, with 5 additional fault cases (A06, A07, C10, B02 and A00). The linear discriminant is computed based on the average distance between healthy and faulty results, being modified accordingly when adding extra cases. In theory, speed should not have a significant effect on data under ideal conditions, however, given the number of points employed to generate HHT instantaneous features changes depending

on an estimate of the current signal's fundamental frequency, it is not unexpected to see some degree of clustering in data points for different operating speeds. This clustering is an effect of imperfections on the HHT real-time implementation and, in a lesser manner, the actual differences in sampled signals at different speeds.

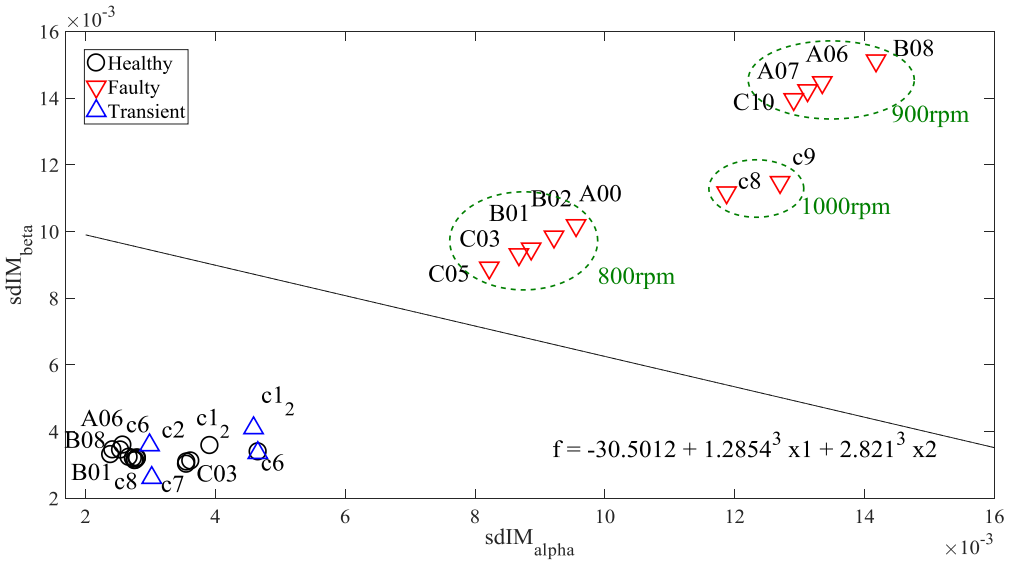

Fig. 6.8. Fifteen case Fisher's Linear Discriminant employing alpha-beta standard deviation of IM.

Finally, the third example, shown in Fig. 6.9, employs standard deviation of the IF to discriminate between 13 cases. The cases depicted are the same shown in Fig. 6.8, except two of the fault cases (C05 and c9) which presented errors in IF due to loss of data of the real-time platform employed to generate HHT features.

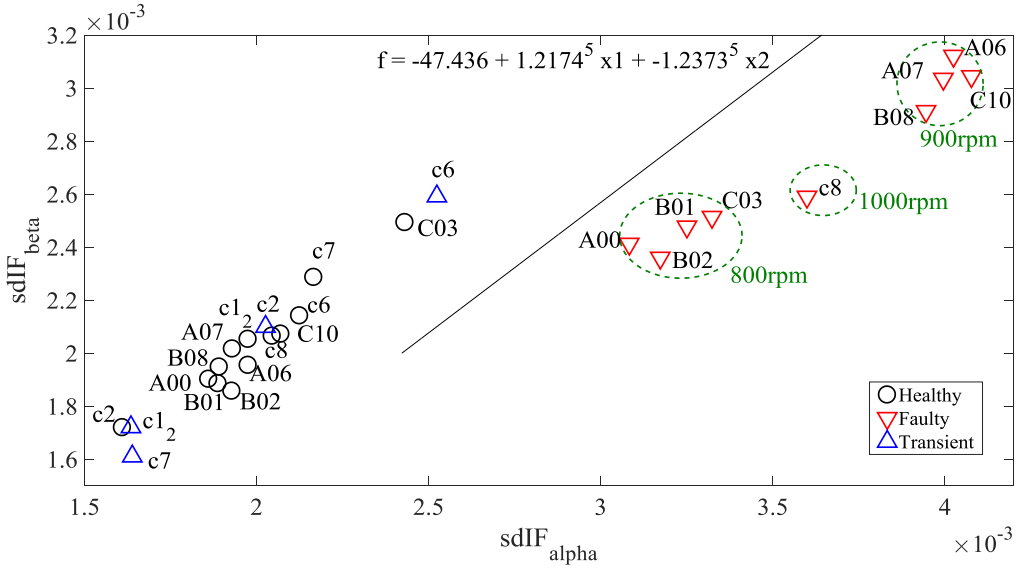

Fig. 6.9. Thirteen case Fisher's Linear Discriminant employing alpha-beta standard deviation of IF.

For standard deviation of IM both alpha and beta axes allow for clear discrimination. This is shown by an almost identical distribution of data points along each axis (between $2x10^{-3}$ and $5x10^{-3}$ for healthy conditions and between $8x10^{-3}$ and $16x10^{-3}$ for faulty conditions). On the other hand, when using standard deviation of IF, the alpha axes is arguably more significant, displaying a clear separation between healthy and faulty conditions values, in contrast to what is seen for the beta axis. Similarly to what may be seen in Fig. 6.7 and Fig. 6.8, data under faulty conditions seen in Fig. 6.9 tends to cluster depending on speed of the test.

B. Support Vector Machine Results

As explained previously, all data available is in principle linearly separable given it has been extracted from steady state conditions. However, in fault detection classification, the interest lies, in particular, in the ability to discriminate between a fault, and load or speed change, during transient conditions. For that reason, the final aim of the work presented here, still on an early stage, is to provide a mean to classify data in transient conditions which is often, from the point of view of employed features, nonlinearly separable. The reason for the lack of linearity lies in the response of employed features to a fault and e.g. a current step. The magnitude of the indicator under both cases may, at times, be the same.

With that aim and contrary to what was done in the previous subsection, data is first treated "locally" for use with SVM. Instead of classifying all cases into healthy or faulty, a limited period of a single fault case is classified. This is done as well with aims at a real-time implementation, and would provide, in principle, detailed study under transient conditions. Data is, in this case, shown in time domain, but excluding the time axis from the representation. Later, the SVM classification is performed globally (one averaged data point per case) for all available cases, similarly to what was seen in subsection A. For both local and global implementations, standard deviation, skewness and kurtosis of IF and IM have been employed as features. The response of these three indicators for combined alpha-beta currents during an interturn fault case (B08) is presented in Fig. 6.10. Standard deviation is shown on top, followed by skewness in the middle and finally kurtosis on the bottom part of Fig. 6.10 for IF (blue) and IM (red). While the use of standard deviation is clear and provides a visible fault indicator on itself, skewness and kurtosis also provide information.

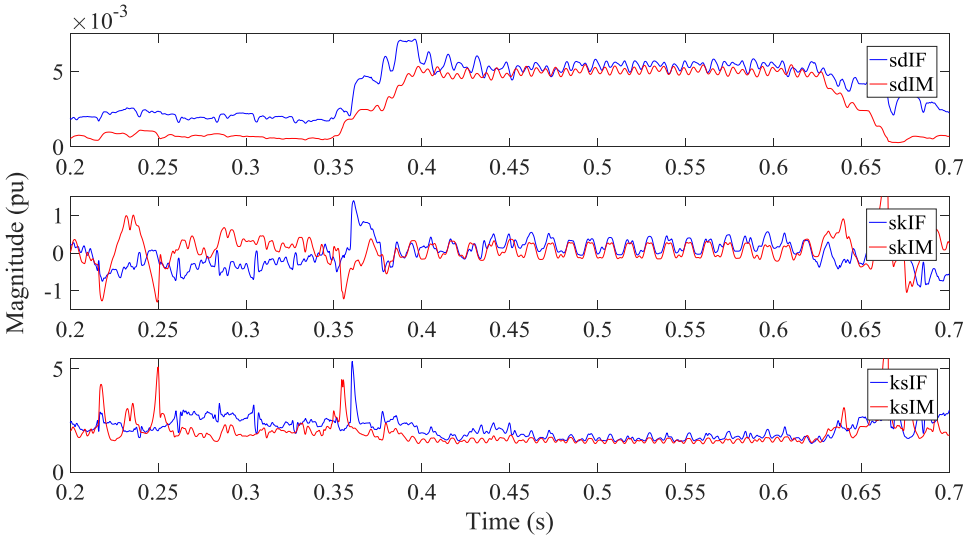

Fig. 6.10. Combined alpha-beta currents standard deviation (top), skewness (middle) and kurtosis (bottom) for fault case (B08).

In theory, the SVM is capable of extracting information from the change in trend shown in Fig. 6.10. For a global implementation the average value will be employed. By mean of example the average value of the three features analysed before under healthy and faulty conditions are shown in TABLE I. Standard deviation is shown to provide most consistent change, followed by kurtosis and finally skewness.

TABLE I
STANDARD DEVIATION, SKEWNESS AND KURTOSIS OF FAULT CASE (B08)

Feature	Healthy	Faulty
Standard Deviation IF	0.0020	0.0054
Standard Deviation IM	0.0007	0.0050
Skewness IF	-0.2667	0.2089
Skewness IM	0.1014	0.0695
Kurtosis IF	2.3998	1.6799
Kurtosis IM	2.0945	1.5255

1) Local Implementation

By mean of example, local implementation of SVM classification has been performed with data corresponding to three cycles of the studied signals, combined alpha-beta currents in this case. Data windows of combined alpha-beta standard deviation, skewness and kurtosis were computed in a similar manner to what was done for Fig. 6.2 (IF) and

Fig. 6.3 (IM) in subsection A. One fault case (B08) is employed to train the SVM and another at similar operating conditions (A06) is classified, as seen in Fig. 6.11, Fig. 6.12. Once trained, the SVM is able to discriminate between healthy and faulty conditions based on the HHT extracted features and compute a three dimensional (in this case) decision boundary. Statistical variables have been extracted from IF for Fig. 6.11 and IM for Fig. 6.12. Whilst the decision boundary plotted represents graphically the discriminant between healthy and faulty data, the SVM function employed in MATLAB evaluates internally if classification has been successfully, marking sometimes data that falls apparently in its "correct region" as misclassified (here flagged with an outer red circle). For example, one point under healthy conditions and four points under faulty conditions, in the case shown in Fig. 6.11, are flagged as misclassified. Ignoring the decision boundary, five points out of three hundred represents a very high degree of success in classification, at around 98.33% for the case depicted in Fig. 6.11. However, the case depicted in Fig. 6.12 achieves around 80% of successful classification with around sixty points of misclassified data. It is unclear at this point if this degree of error is due to an implementation of SVM with time dependency, errors in SVM scripting or, given the decision boundary computed, a false alarm flagging what may be a 100% success in classification.

It was initially thought that the error might be associated with the close to transient conditions found at the vicinity of the fault. However, on close inspection of the data employed, graphically represented in Fig. 6.2 and Fig. 6.3, it would appear that there is a different cause for these results.

A most likely cause for false alarm arouses from the use of two different MATLAB functions, "*fitcsvm*" to generate and train the SVM and "*svmtrain*" to generate the decision boundary, finding some contradiction between misclassified data found and what can be observed in the figures. Due to a recommendation by Mathworks, MATLAB's developing company, *fitcsvm* was identified as the only necessary function to develop the SVM since it is supported for all latest versions. However it was found by the author to be a significant challenge to represent a three-dimensional decision boundary (or hyperplane) by use of this function. It is for this reason that a second SVM function, *svmtrain*, was employed, to take advantage of this functionality, only for plotting purposes. It appears that, from the point of view of *svmtrain*, there are no classification errors since the three-dimensional decision boundary stablishes a successful

separation between healthy and faulty data. It is then assumed by the author that *fitcsvm* stablishes a different boundary that results in the error reported before.

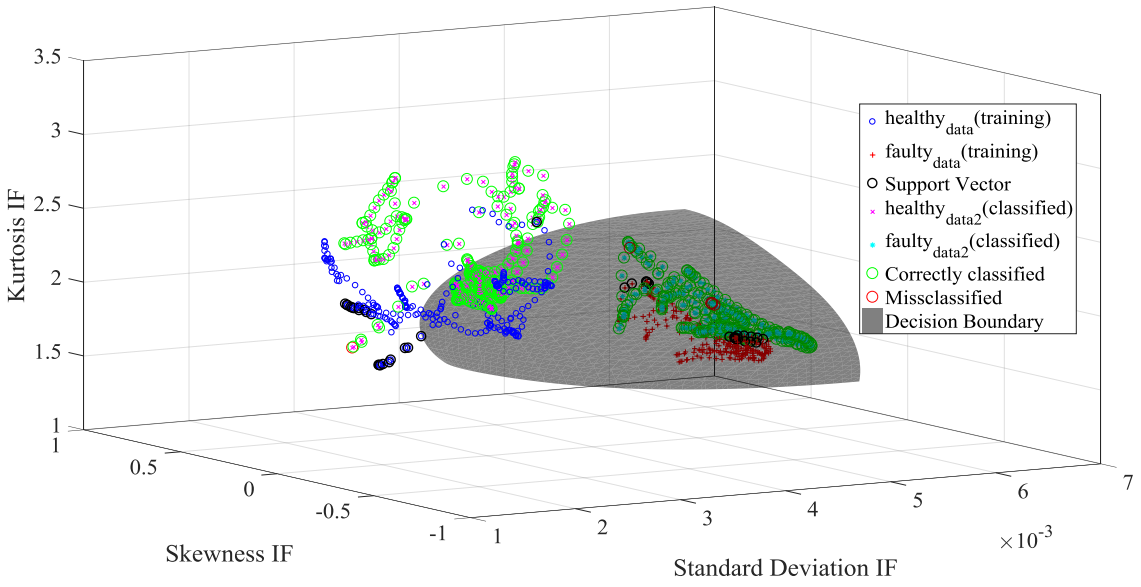

Fig. 6.11. Three dimensional analysis of fault case employing standard deviation, skewness and kurtosis of IF.

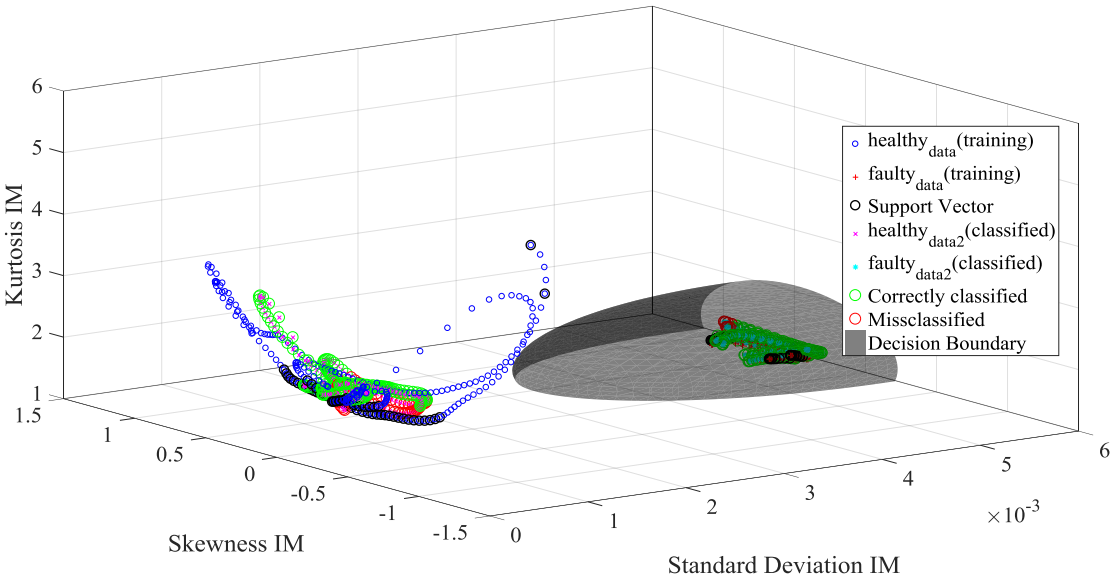

Fig. 6.12. Three dimensional analysis of fault case employing standard deviation, skewness and kurtosis of IM.

2) Global Implementation

Global implementation of SVM classification, employing only one data point per case as it was done in subsection A, is shown in Fig. 6.13 for IF and Fig. 6.14 for IM. Whilst the decision boundary observed for IF in Fig. 6.13, is close to "linear", the one generated for IM results, shown in Fig. 6.14, clearly represents the lack of linearity of the

classification problem when employing the selected combination of features. The analysis shown in three dimensions for SVM is equivalent to that shown in subsection A for two dimensions.

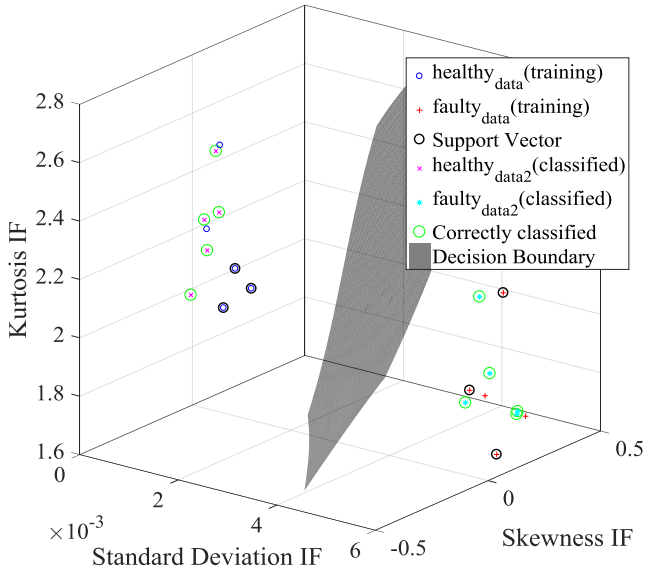

Fig. 6.13. Three dimensional classification employing standard deviation, skewness and kurtosis of IF.

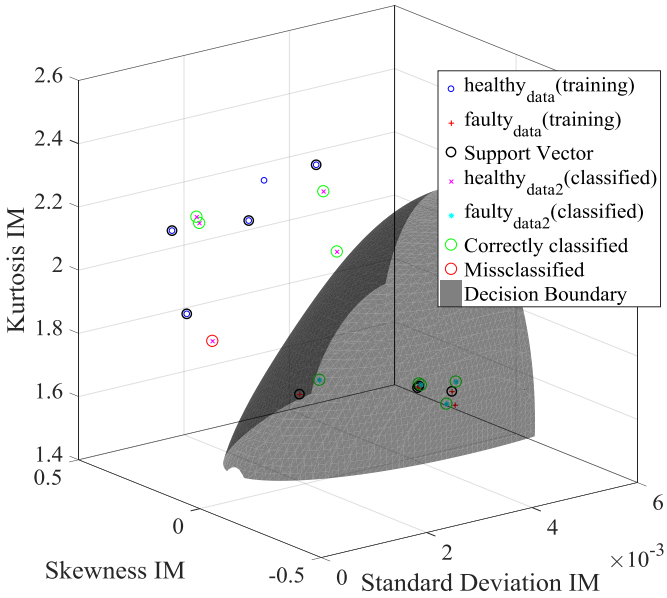

Fig. 6.14. Three dimensional classification employing standard deviation, skewness and kurtosis of IM.

Similarly to what was seen in Fig. 6.11 and Fig. 6.12, one case is flagged as misclassified in Fig. 6.14. According to the decision boundary it falls into a false alarm, however the SVM implementation done in MATLAB evaluates it as incorrectly classified. Still, this represents a very high degree of success at 100% for Fig. 6.13 and

90% for Fig. 6.14. Whilst the validity of SVM's "local" implementation is unclear, the "global" implementation employing one data point per case is well known and common practice. It is expected that an increase in the number of cases available would improve the results of classification. Furthermore, additional features of analysed signals could be employed to further extend the analysis presented.

6.5. Summary

This chapter has presented a PMSM stator fault classification method for linearly and potentially non-linearly separable data. Details on feature extraction as well as extensive descriptions of the classification methods employed have been provided. Both methods are validated through use of experimental data already available, achieving a very high degree of success in classification. Whilst work presented in this chapter displays only the first steps taken into machine learning classification, results show potential for this methodology, particularly for computed features.

Steady state data employed for fault detection classification has been demonstrated to be linearly separable which indicates that Fisher's linear discriminant should in principle suffice. However, in the eventuality of using transient data, it is expected that nonlinearity may arouse, giving way to the use of more complex methods such as the SVM presented here. Further work on this topic is planned outside this thesis, particularly the ability to, in theory, discriminate between different types of faults such as stator winding, demagnetization or bearing fault, and their severity.

CHAPTER 7

CONCLUSION AND FURTHER WORK

This thesis summarises the work carried out in an attempt to answer a series of research questions relating to Permanent Magnet Synchronous Machines (PMSM) modelling, real-time emulation and, in particular, fault detection. In order to do so it has follow a series of objectives, beginning with gaining an insight into the origins of the effects caused by a stator winding fault in PMSM currents. Whilst a specific question has not aroused with regards to real-time Hardware-in-the-Loop implementation, its value as a tool to pursue the questions proposed marks this development as a significant objective on its own right. Other objectives sought after are more directly linked to questions identified from gaps found in the literature review. Examples of this can be found in Chapters 4 and 5. In Chapter 4, a model-based method has been presented consisting on current residuals, while in Chapter 5, a signal-based one has been described relying on time-frequency analysis of machine currents. Both methods have been applied to the task of discriminating between PMSM operation under faulty conditions and healthy transitory conditions, such as load or speed variations. Finally, the fault indicators generated from Chapter 5 have been employed for classification purposes in Chapter 6 with the objective of addressing the last research question.

7.1. Work Summary

An extensive literature review on machine fault modelling and fault detection methods, presented in Chapter 1, revealed that whilst this topic has been around for decades, global solutions of general application are still far from being a reality, especially for PMSM. A trend has been observed in recent times to shift from pure Motor Current Signature Analysis (MCSA) methods based on frequency analysis, such as the study of harmonic components, to more complex ones, such as time-frequency-energy analysis (Wavelet, Hilbert Huang Transform, etc.), model-based methods, sometimes combined with signal-based one resulting in hybrid techniques, or even data-based ones. The reason for this shift is mostly due to limitations of MCSA under transitory conditions unrelated to a fault. This thesis has attempted to tackle most of these methods with modest contributions to each of them. First, a demonstration on the origin of the effects often

attributed to a stator winding fault has been presented in Chapter 2, including analytical modelling, simulation and experiments. Afterwards, contributions to electrical machines under healthy and faulty conditions have been shown in Chapter 3, particularly regarding real-time Hardware-in-the-Loop (HIL) implementation of machine models. Throughout this thesis, real-time HIL modelling has been key for validating further work. In particular, it has allowed carrying out online model-based fault detection, and has provided in general an intermediate validation step between software simulation and experimental validation on a real drive system.

Contributions to model-based fault detection have been made through the use of current residual signals in Chapter 4. Residuals have been generated online by comparison between machine and model output currents when using the same input voltages, and its usefulness further improved by single Fourier series analysis. Given the machine model accurately represents the real machine, residual signals in simulation are shown to remain unchanged without a fault, and only deviate from near zero conditions when the fault appears, as theorized. Effectively, they isolate the effect of the fault and enhance its detection, given the magnitude of the fault effects relative to signal magnitude are much greater. Third harmonic of phase current residuals and second harmonic of *q*-axis residuals have been analysed. The use of harmonic tracking has been made possible given residuals are nearly unaffected by transient conditions not related to a fault.

However, mixed results are found for the experimental validation. Whilst the residual behaviour under fault and speed ramp, for all conditions, is consistent with what was theorized and simulated, the residual under current step showcases a similar response to the signals from which it is computed. The most likely cause for the unexpected results can be found in the required rotor angle "θ". Results at 10kHz, sampled by the controller, include both *dq0* reference frame variables as well as rotor angle θ. While the model is defined in terms of *dq*-axes voltages, real inputs are three phase voltages acquired by use of differential voltage probes. These voltages require transformation from the *abc* reference frame to a direct, quadrature and zero components in a rotating reference frame. In ideal conditions the rotor angle θ would we acquired, either from and encoder or a resolver, and then used for this transformation. However, the resolver found in the testing rig was not available for the author of this thesis under risk of affecting the nominal operation of the drive controller. Instead, the angle was generated by use of a Phase Lock Loop (PLL), without achieving ideal tracking. Still, except for the last results shown in

Chapter 4 unrelated to the proposed method, model-based fault detection is found to constitute a reliable mean to avoid the effects of transient conditions. Particularly for those results in which rotor angle and *dq*-axes variables are available as shown in section 4.6 or more specifically in Fig. 4.32-Fig. 4.35.

In addition to the relatively simple single Fourier series, signal-based contributions have been made through Hilbert Huang Transform (HHT) time-frequency-energy analysis of machine currents in Chapter 5. HHT has been employed to obtain instantaneous frequency (IF) and magnitude (IM), as well as a combination of the two in a marginal Hilbert spectrum. Simple statistical analysis such as standard deviation has been employed on obtained instantaneous features to provide reliable fault indicators. Unlike what was found in literature, it has been demonstrated that HHT can be used to detect the minimum possible severity of stator winding fault. However, the fault is detected by taking a new approach and applying it on a single intrinsic mode function (IMF) of empirical mode decomposition (EMD), corresponding to the fundamental frequency, rather than obtaining a new IMF with a frequency often attributed to this type of fault, three times the fundamental for phase currents. The inability of HHT to generate a new IMF corresponding to the fault is a limitation due to the very low severity, which hardly changes the shape of the analysed current signal. Furthermore, while this method has been proven its reliability for transient conditions due to speed change, current steps of significant magnitude may cause a false alarm in detection. This may be explained by dependence of this method on harmonic components. Whilst EMD and HHT in general study oscillatory moments and not harmonics specifically, the influence caused by these type of faults on the later makes them the main disturbance picked up by the analysis.

Once results from Chapter 4 and Chapter 5 have been independently analysed, it is possible to attempt a comparison and assess which one is better suited for dealing with low severity stator winding faults under transient conditions. On one hand, a limitation of model-based fault detection has been pointed out in the risk of miss-tracking rotor angle. On the other hand HHT has an inherent limitation due to the inability to avoid the effects of harmonic components during transients unrelated to the fault. A comparison can be made between the "best" achieved results. Under faulty conditions model-based results are shown in Fig. 4.32 (signals and residual) and Fig. 4.34 (harmonic analysis) vs signal-based best ones shown in Fig. 5.28 (versus online single Fourier series) and Fig. 5.31 (versus offline FFT moving window). Under current step, results are shown in Fig. 4.33

(signals and residual) and Fig. 4.35 (harmonic analysis) for model based, while those for signal-based can be seen in Fig. 5.29 and Fig. 5.32. The most significant difference is that, while both allow detecting the fault with a reasonable degree of success, only the model based results are shown to be unaffected by the fault. To showcase this difference, Fig. 4.35 and Fig. 5.32 are included below to explicitly facilitate this comparison.

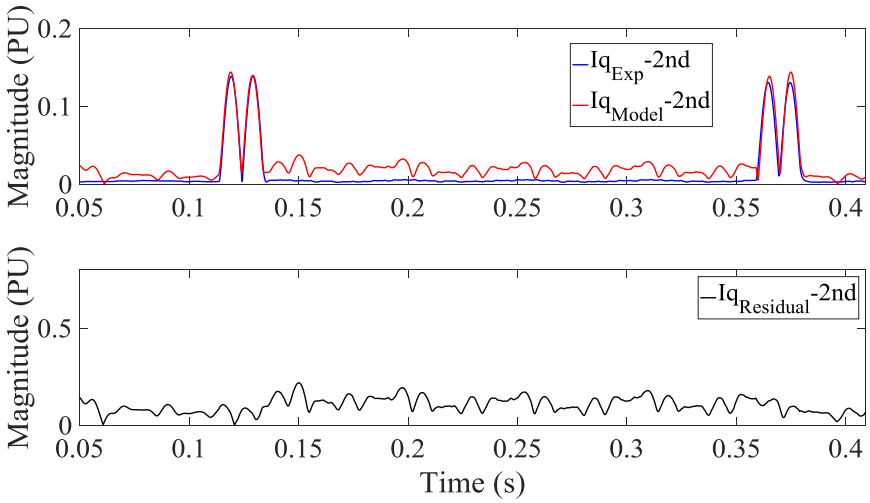

"Fig. 4.35. Single series Fourier analysis of q-axis current second harmonic under load variation."

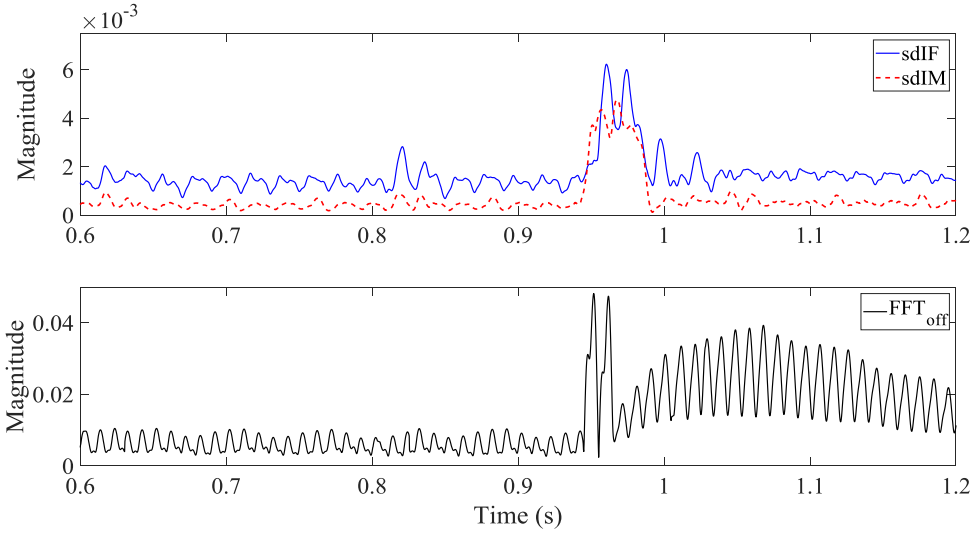

"Fig. 5.32. HHT extracted indicators vs Iα FFT of 10A current step."

Finally, data-based fault detection has been implemented by classification in Chapter 6, making use of described signal-based generated features. Although data employed was linearly separable and therefore Fisher's linear discriminant (FLD) would suffice as a classification tool, it is expected that in the event of analysing transient conditions nonlinearity may be found and thus more complex machine learning methods, such as described Support Vector Machine (SVM), would be required. Although work presented

in this chapter has shown only a first attempt by the author into machine learning fault classification, results confirm the potential of these techniques and, more interestingly, the usefulness of proposed features, particularly standard deviation of IF and IM.

7.2. Further Work

Whilst this thesis has made general contributions to the fault detection process, several aspects not included have been identified as a logical evolution of the methods and work described. A first example of a path not explored in this thesis is the analysis of the HHT generated spectrum by means of image recognition. As shown in Chapter 5, a significant difference can be stablished between fault cases and those under healthy conditions by means of MHS, seen in Fig. 5.25-Fig. 5.27. It is believed by the author, than a simple implementation of image recognition could potentially discriminate between those conditions. However, this has been finally left out of the scope of this thesis and is just mentioned here as a note, since it will be studied by the author of this thesis in the near future.

The analysis carried out in the conclusion justifies the assumption, to some degree, that model-based fault detection is better suited for the study of faults under transient conditions than signal-based fault detection, as long as model inputs are synchronized and rotor angle is available, or does not significantly affect residuals under current steps. However, it is reasonable to assume that a combination of the two would yield the best results, something partially shown by the single Fourier series analysis of proposed residuals. Then, the combination of proposed residuals with the HHT analysis is identified as the next logical step in the continuation of this thesis.

In terms of implementation, the best way to proceed with a combination of the two would be to first identify a more application-specific platform that allows running the model with a sufficiently high rate of execution, such as an FPGA, combined with a platform suited for running a signal-processing code, perhaps a DSP or even an ARM processor. There are several alternatives available ranging from less than £100, such as a MiniZed from AVNET (Xilinx Zynq 7Z007S FPGA + ARM-Cortex A9) up to a few hundreds of pounds, like the Red Pitaya from STEMlab (Xilinx Zynq 7010 FPGA + Dual Core ARM-Cortex A9). This last one is ideally suited for the task since it displays SubMiniature version A (SMA) connector inputs and outputs capable of up to 125MS/s of sampling.

Once a more appropriate devices has been selected a few changes to implementation might be required. First, it is possible to alleviate the computational requirements of real-time model running by discarding part of the points of employed current maps. This has been tested in the past and it has been shown to work. However if too many points are discarded it will have an effect on the accuracy of the dynamic machine representation. Furthermore, and most importantly, the HHT is currently employing a running windows which analyses all points (between 200 and 300 for the cases under study). Every time step, it acquires a new point at the same time it loses one. For this reason, the maximum frequency of execution achieved was 5kHz. Given HHT is applied mostly around the fundamental frequency component of phase currents (normally up to a few hundreds of Hz), it is not necessary to capture all points and thus the running window can be moved every certain amount of points, alleviating dramatically the requirements of implementation. While this didn't constitute a problem with regards to its operation, it is of significant importance with regards to a more efficient implementation of the algorithm.

Furthermore, two aspects in particular have been left out due to lack of time and available material, the analysis of different types of faults and the severity of the fault. The literature review hints at the ability of employed methods to detect other types of faults such as demagnetization and bearing fault. In addition, when combined with a more mature use of machine learning, a fault detection and diagnosis tool of general application could be developed with the ability to learn and classify a number of faults. The value of such a tool for use in academia and particularly in industry would be unquestionable.

In terms of machine learning, and particularly for a SVM as the one analysed in Chapter 6, further work is required regarding data availability. Data employed in this thesis, at less than twenty cases, constitutes a very limited sample resulting from testing similar conditions numerous times. The randomization factor is therefore constrained by the similitude of this conditions. In order to guarantee the success in classification, a much wider amount of data is required, involving at least tens of tests at different speed, and current levels. Furthermore, testing different severities of the same fault under analysis is a logical second step. Allowing characterization of the fault. Ideally, these tests would be performed on an easier to handle machine rated for lower power and current, simplifying the fault mechanisms, avoiding risk of destroying test equipment and most importantly, saving the cost in the event of permanent damage to the machine.

ANNEX 1

FPGA MODEL IMPLEMENTATION

This annex provides details on the FPGA model implementation described in Chapter 3. Coding of the FPGA is performed automatically by LabVIEW FPGA which converts its graphical interface (shown below) into VHDL code. In this annex, two "models" known as virtual instruments (VI) in the LabVIEW environment, are presented. One VI corresponds to the machine model while the other corresponds to the control. The front panels, which acts as interactive user interface, as well as the contents of each while loop (grey boxes run once per time step) employed in the two VIs are presented.

The machine model VI is divided into four different while loops: virtual inverter and PWM inputs, voltage equations (rearranged as flux linkage equations), current maps and outputs. The front panel allows selecting scaling for input and output variables as well as machine speed, DC link voltage and fault resistor R_f.

Furthermore, the controller VI divided into four while loops as well: Inputs, PI regulators, PWM generation and outputs. Similarly to what was shown for the machine model front panel, the controller front panel allows selecting: input and output variables scaling, *dq*-axes current commands, PI regulators Kp and Ki constants, DC link voltage value, switching frequency and machine speed. For correct operation, machine speed and DC link must be the same for machine model and controller, and scaling must be chosen accordingly.

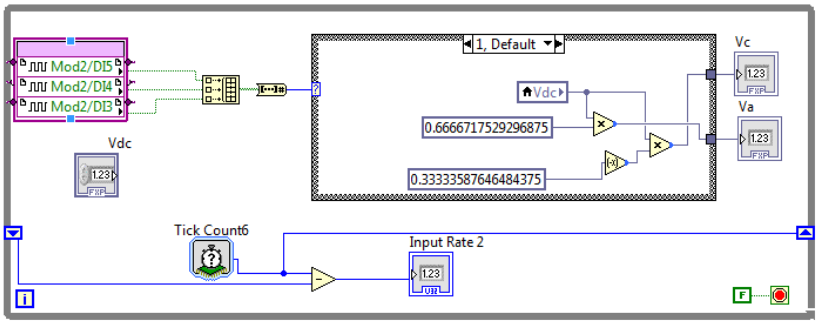

Fig. A1.1. LabVIEW FPGA virtual inverter and PWM inputs while loop.

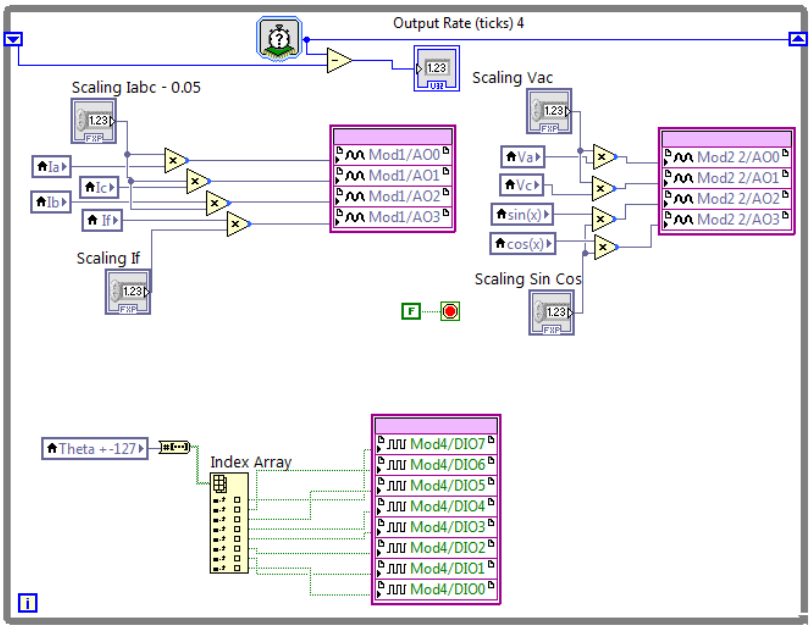

Fig. A1.2. LabVIEW FPGA machine model outputs while loop.

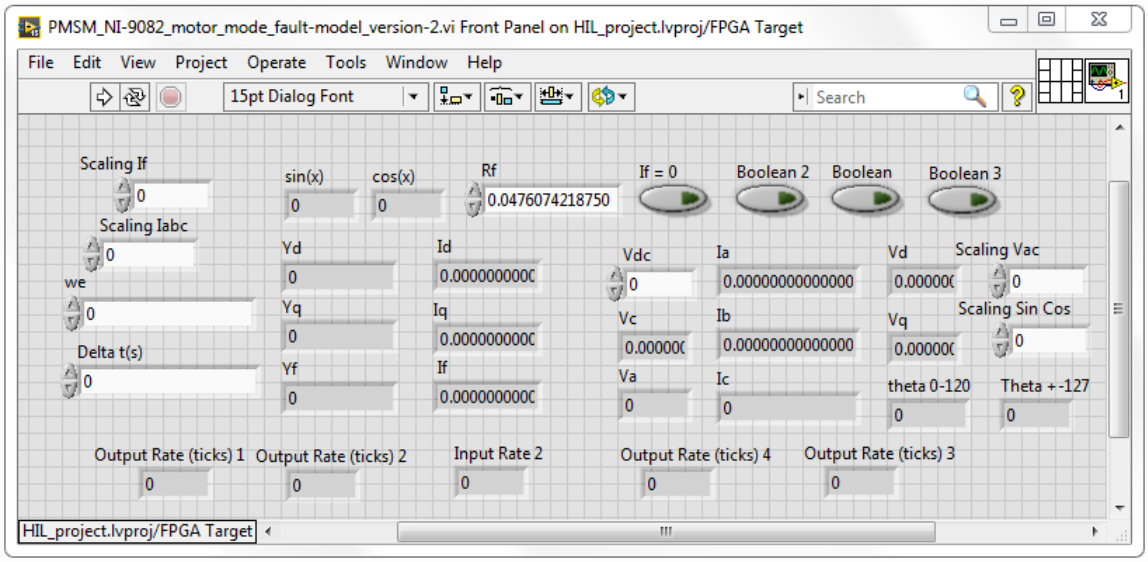

Fig. A1.3. LabVIEW FPGA machine model front panel.

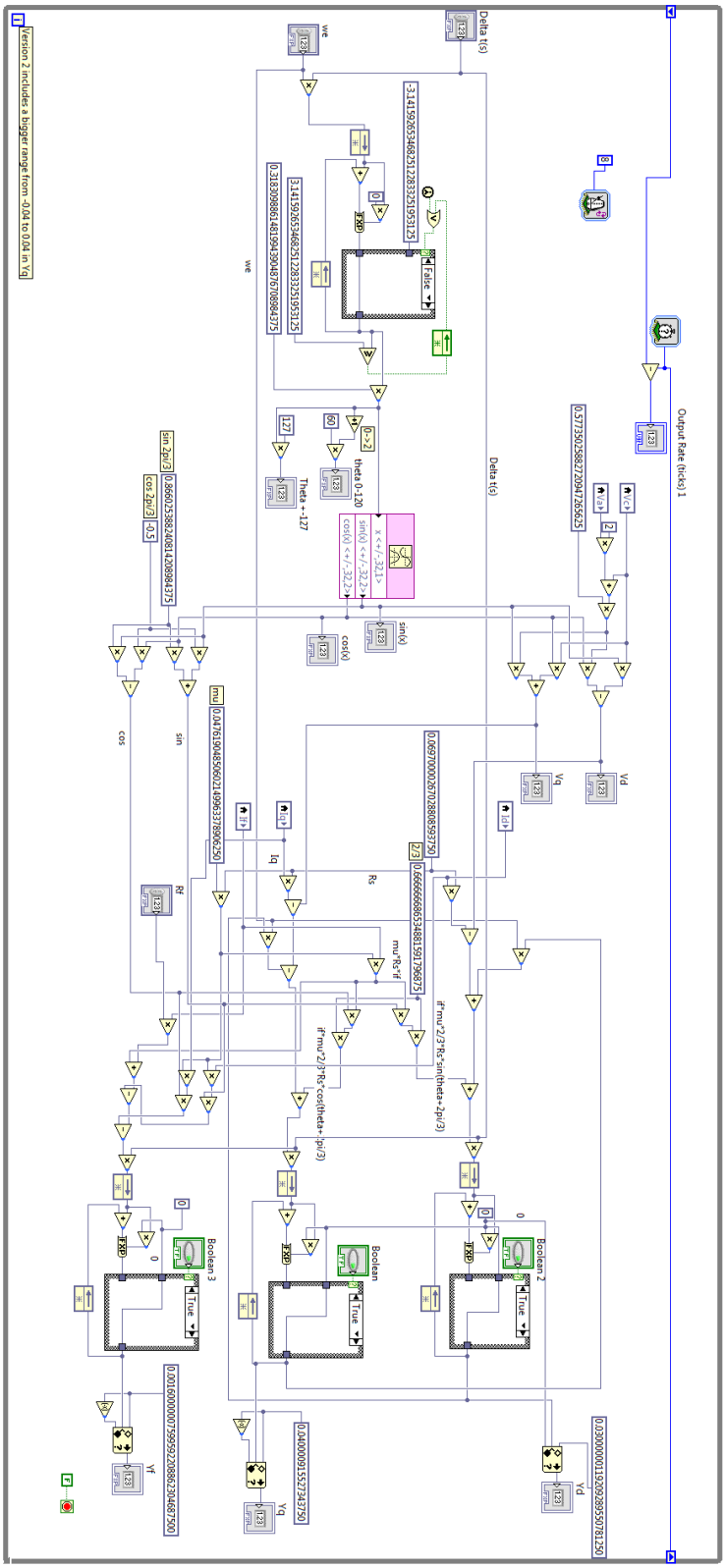

Fig. A1.4. LabVIEW FPGA voltage equations while loop.

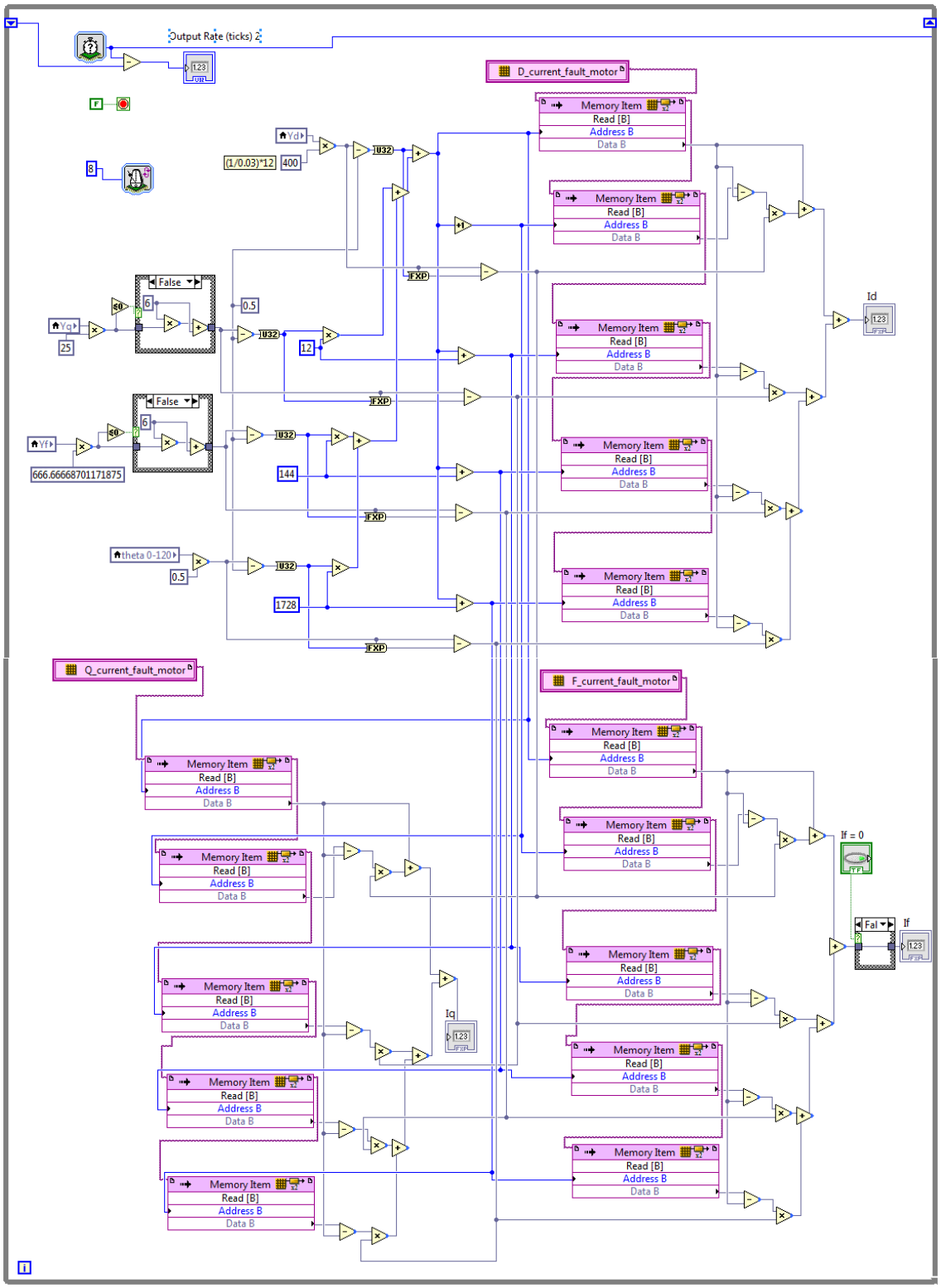

Fig. A1.5. LabVIEW FPGA current maps and triple linear interpolation while loop.

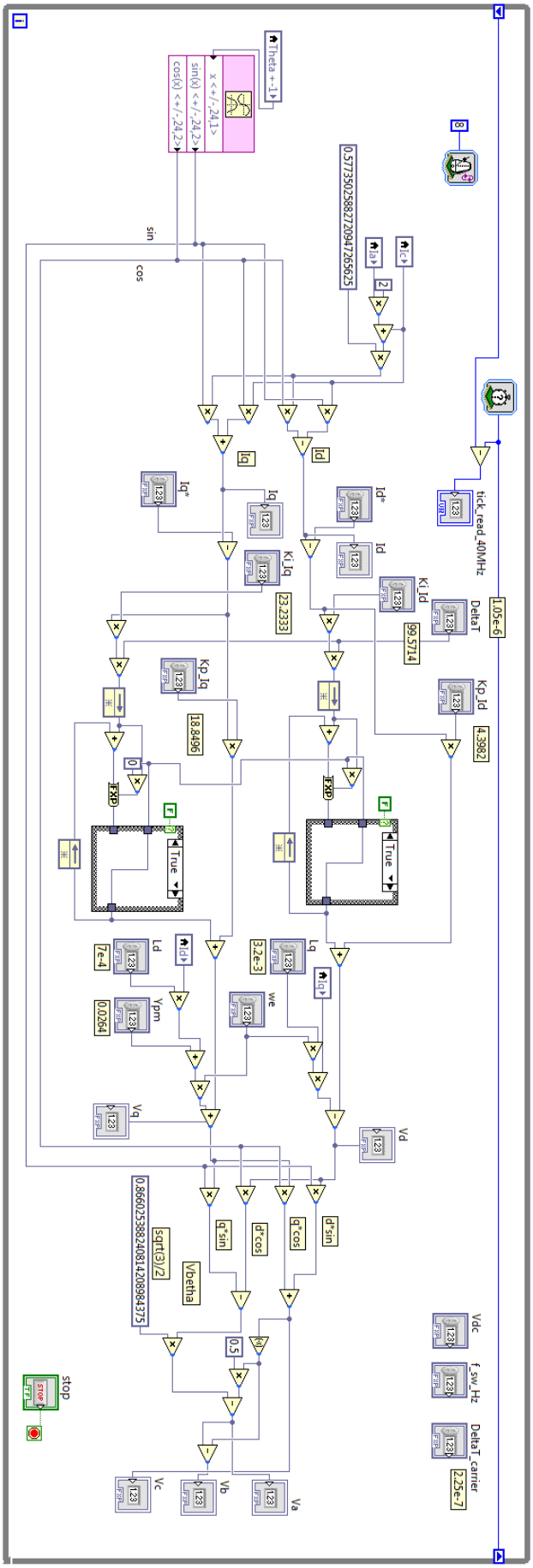

Fig. A1.6. LabVIEW FPGA controller PI regulators while loop.

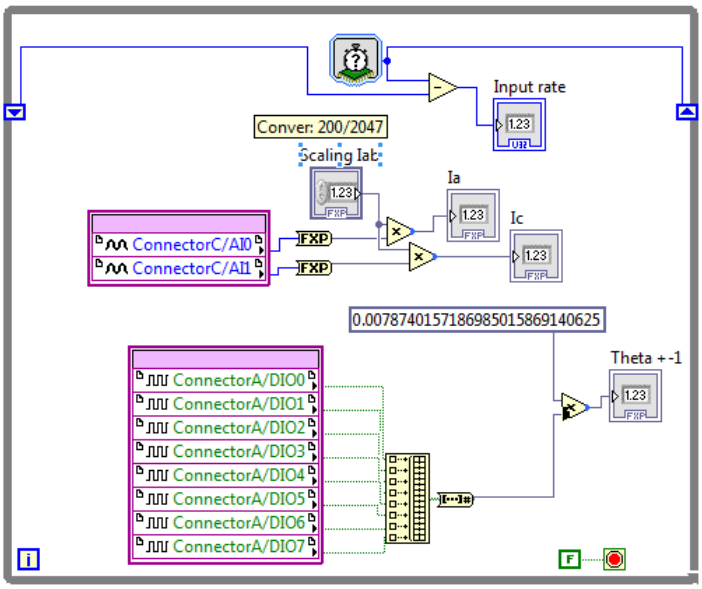

Fig. A1.7. LabVIEW FPGA controller inputs while loop.

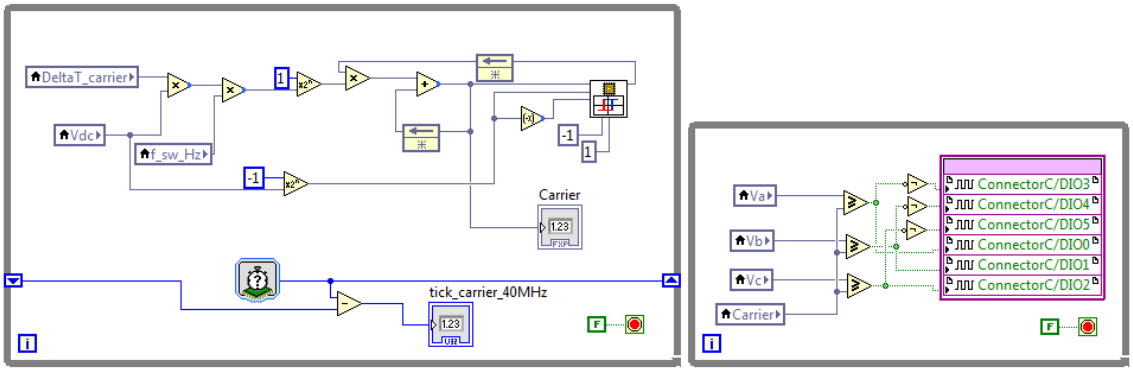

Fig. A1.8. LabVIEW FPGA controller PWM generation and outputs while loop.

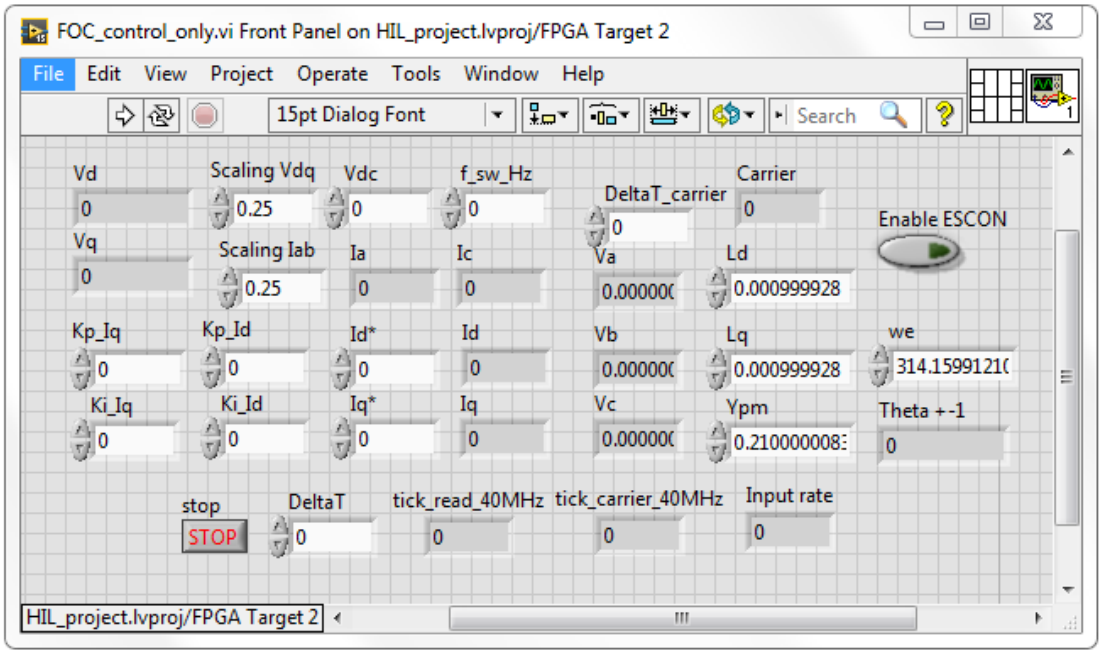

Fig. A1.9. LabVIEW FPGA controller front panel.

ANNEX 2

HHT IMPLEMENTATION SCRIPT

This annex provides the MATLAB script employed for Hilbert Huang Transform implementation. The scripts makes use of available MATLAB functions when possible. Given implementation is done for online operation, it was not always possible to employ the latest available versions of functions since the software lacks C code generation for some of them. The code is located inside a function block ready to use in the Simulink simulation environment available both in offline and real-time online simulations (MATLAB running inside OPAL's OP5600). The input to the function block is an already buffered vector of the current signal composed of a variable number of samples between 200 and 300 points obtained at the sampling frequency (5kHz) imposed by capabilities of real-time simulator. The number of points changes depending on an estimation of the fundamental frequency of phase currents. The output of the function block containing the script is a vector of four elements, instantaneous frequency (IF) and magnitude (IM) at each time step (calculated as the average of the central part as explained in the last section of Chapter 5), and the value of instantaneous frequency and magnitude at initial steady state conditions, often employed for normalization.

The scripts is divided into the following steps:

1. First, the script initializes all required variables.
2. Then, the script runs the empirical mode decomposition of the buffered vector to obtain a single intrinsic mode function (IMF) given the absence of significant noise and higher frequencies. It may be easily modified to obtain several IMFs.
3. Once an IMF is obtained, the Hilbert transform is applied and IF and IM are calculated.
4. Finally, the function block containing the script outputs the four element vector containing last and initial IF and IM values.

```
function y  = pks(u,v)
persistent kc IF0 IM0
if isempty(kc); kc = 1; end
if isempty(IF0); IF0 = 1; end
if isempty(IM0); IM0 = 1; end
uu = [u(kc+1:v),u(1:kc)];
```

```
kc = kc + 1;
if kc > v; kc = 1; end
y = [0 0 0 0]';

if u(end) ~= 0
    lu = length(uu);
    elem2 = round((lu/2)-(lu/3));
    limx = lu/(1/2e-4);
    Fs = lu/limx;
    SD = 0.3;
    h1 = zeros(lu,1)';
    stop = zeros(lu,1)';
    last_p = 0;
    last_n = 0;
    r1 = uu;
    h = r1;
    k = 1;
    SDk = 1;
    while(SDk>SD)
        n = h;
        [~,pind] = findpeaks(n); % find maxima ,'minpeakwidth',1
        [~,pindn] = findpeaks(-n); % find minima
        if isempty(pind);pind=last_p;end
        if isempty(pindn);pindn=last_n;end
        if length(pind) < 2
            sp = zeros(lu,1);
            for p = 1:lu;sp(p) = sp(p) + pind;end
        else
            sp = interp1(pind,n(pind),(1:lu),'spline')'; % maxima
spline
        end

        if length(pindn) < 2
            sn = zeros(lu,1);
            for p = 1:lu;sn(p) = sn(p) + pindn;end
        else
            sn = interp1(pindn,n(pindn),(1:lu),'spline')'; % minima
spline
        end

        for p = 1:lu
            h1(p) = n(p) -((sp(p)+sn(p))/2);
        end
        for ww = 1:lu
            stop(ww) = (h(ww)-h1(ww))^2/h(ww)^2;
        end
        SDk = sum(stop);
        h = h1;

        k = k+1;
        if k == 20;SDk = 0.1;end
        last_p = max(pind);
        last_n = max(pindn);
    end

    % Before Hilbert
    xh = h1;

    [xh,nshifts] = shiftdim(xh);
    nh = size(xh,1);
```

```
    x = fft(xh,nh,1);
    if isempty(x)
        hh = zeros(nh,0);
    else
        hh = zeros(nh,1);
    end
    if nh > 0 && 2*fix(nh/2) == nh
      hh([1 nh/2+1]) = 1;
      hh(2:nh/2) = 2;
    elseif nh>0
      hh(1) = 1;
      hh(2:(nh+1)/2) = 2;
    end
    x = ifft(x.*hh(:,ones(1,size(x,2))));
    z = shiftdim(x,-nshifts);
    instfreq1 = Fs/(2*pi)*diff(unwrap(angle(z)));
    instmag1 = abs(z);

    y1 = mean(instfreq1(round(lu/2)-elem2:round(lu/2)+elem2));
    y2 = mean(instmag1(round(lu/2)-elem2:round(lu/2)+elem2));
    if IF0 == 1;IF0 = y1;end
    if IM0 == 1;IM0 = y2;end
    y3 = IF0;
    y4 = IM0;
    y = [y1 y2 y3 y4]';
else
    y = [0 0 0 0]';
end
```

ANNEX 3

SVM IMPLEMENTATION SCRIPT

This annex provides the MATLAB script employed for support vector machine (SVM) implementation. Contrary to what is seen in Annex 2, there is not limitation to the use of functions available in MATLAB, given the offline nature of the analysis carried out with this script. This script is divided into four steps:

1. First, data for each independent case is loaded and statistic parameters of interest (standard deviation, skewness and kurtosis) are grouped and stored in vectors.
2. Data is divided into healthy, transient and faulty data by both order and assignation of group names.
3. The first classification problem (2D case) is trained, tested and results plotted.
4. The second classification problem (3D case) is trained, tested and results plotted.
5. Finally, due to its complexity, the 3D decision boundary is plotted by use of additional functions.

```
clear all
close all
clc

%  I 12 IF 34 IM 56 sdIF 78 skIF 910 ksIF 1112 sdIM 1314 skIM 1516
ksIM 1718
if exist('B08_data2','var') == 0 % training data
    load B08_data2.mat;
    load B02_data2.mat;
    load B01_data2.mat;
    load C10_data2.mat;
    load c8_data2.mat;
end
if exist('A06_data2','var') == 0 % predicting data
    load A06_data2.mat;
    load A00_data2.mat;
    load C03_data2.mat;
    load A07_data2.mat;
    load c9_data2.mat;
end

sdIF_ptT = [B08_data2_pt(1,4) B02_data2_pt(1,4) B01_data2_pt(1,4)
C10_data2_pt(1,4) c8_data2_pt(1,4)...
    B08_data2_pt(2,4) B02_data2_pt(2,4) B01_data2_pt(2,4)
C10_data2_pt(2,4) c8_data2_pt(2,4)]';
skIF_ptT = [B08_data2_pt(1,5) B02_data2_pt(1,5) B01_data2_pt(1,5)
C10_data2_pt(1,5) c8_data2_pt(1,5)...
```

```
    B08_data2_pt(2,5) B02_data2_pt(2,5) B01_data2_pt(2,5)
C10_data2_pt(2,5) c8_data2_pt(2,5)]';
ksIF_ptT = [B08_data2_pt(1,6) B02_data2_pt(1,6) B01_data2_pt(1,6)
C10_data2_pt(1,6) c8_data2_pt(1,6)...
    B08_data2_pt(2,6) B02_data2_pt(2,6) B01_data2_pt(2,6)
C10_data2_pt(2,6) c8_data2_pt(2,6)]';
sdIF_ptP = [A06_data2_pt(1,4) A00_data2_pt(1,4) C03_data2_pt(1,4)
A07_data2_pt(1,4) c9_data2_pt(1,4)...
    A06_data2_pt(2,4) A00_data2_pt(2,4) C03_data2_pt(2,4)
A07_data2_pt(2,4) c9_data2_pt(2,4)]';
skIF_ptP = [A06_data2_pt(1,5) A00_data2_pt(1,5) C03_data2_pt(1,5)
A07_data2_pt(1,5) c9_data2_pt(1,5)...
    A06_data2_pt(2,5) A00_data2_pt(2,5) C03_data2_pt(2,5)
A07_data2_pt(2,5) c9_data2_pt(2,5)]';
ksIF_ptP = [A06_data2_pt(1,6) A00_data2_pt(1,6) C03_data2_pt(1,6)
A07_data2_pt(1,6) c9_data2_pt(1,6)...
    A06_data2_pt(2,6) A00_data2_pt(2,6) C03_data2_pt(2,6)
A07_data2_pt(2,6) c9_data2_pt(2,6)]';

sdIM_ptT = [B08_data2_pt(1,7) B02_data2_pt(1,7) B01_data2_pt(1,7)
C10_data2_pt(1,7) c8_data2_pt(1,7)...
    B08_data2_pt(2,7) B02_data2_pt(2,7) B01_data2_pt(2,7)
C10_data2_pt(2,7) c8_data2_pt(2,7)]';
skIM_ptT = [B08_data2_pt(1,8) B02_data2_pt(1,8) B01_data2_pt(1,8)
C10_data2_pt(1,8) c8_data2_pt(1,8)...
    B08_data2_pt(2,8) B02_data2_pt(2,8) B01_data2_pt(2,8)
C10_data2_pt(2,8) c8_data2_pt(2,8)]';
ksIM_ptT = [B08_data2_pt(1,9) B02_data2_pt(1,9) B01_data2_pt(1,9)
C10_data2_pt(1,9) c8_data2_pt(1,9)...
    B08_data2_pt(2,9) B02_data2_pt(2,9) B01_data2_pt(2,9)
C10_data2_pt(2,9) c8_data2_pt(2,9)]';
sdIM_ptP = [A06_data2_pt(1,7) A00_data2_pt(1,7) C03_data2_pt(1,7)
A07_data2_pt(1,7) c9_data2_pt(1,7)...
    A06_data2_pt(2,7) A00_data2_pt(2,7) C03_data2_pt(2,7)
A07_data2_pt(2,7) c9_data2_pt(2,7)]';
skIM_ptP = [A06_data2_pt(1,8) A00_data2_pt(1,8) C03_data2_pt(1,8)
A07_data2_pt(1,8) c9_data2_pt(1,8)...
    A06_data2_pt(2,8) A00_data2_pt(2,8) C03_data2_pt(2,8)
A07_data2_pt(2,8) c9_data2_pt(2,8)]';
ksIM_ptP = [A06_data2_pt(1,9) A00_data2_pt(1,9) C03_data2_pt(1,9)
A07_data2_pt(1,9) c9_data2_pt(1,9)...
    A06_data2_pt(2,9) A00_data2_pt(2,9) C03_data2_pt(2,9)
A07_data2_pt(2,9) c9_data2_pt(2,9)]';

numb=5;% Half my total number of points
Y1=ones(numb,1);
Y2=-1*ones(numb,1);
Y=[Y1;Y2];
for p = 1:length(Y)
    if Y(p) == 1
        GroupNames(p) = {'H'};
    else
        GroupNames(p) = {'F'};
    end
end
GroupNames = GroupNames';

%% 2d Problem
X = [sdIM_ptT skIM_ptT];

SVMModel = fitcsvm(X,Y,'KernelFunction','rbf','ClassNames',[-1 1]);
```

```
classOrder = SVMModel.ClassNames;

sv = SVMModel.SupportVectors;
CVSVMModel = crossval(SVMModel);
classLoss = kfoldLoss(CVSVMModel);

figure(1)
gscatter(X(:,1),X(:,2),Y,'rb','+o');hold on;
plot(sv(:,1),sv(:,2),'ko','MarkerSize',10,'linewidth',1.5);hold on;

d = 0.01;
[x1Grid,x2Grid] =
meshgrid(min(X(:,1)):d:max(X(:,1)),min(X(:,2)):d:max(X(:,2)));
xGrid = [x1Grid(:),x2Grid(:)];
[~,scores] = predict(SVMModel,xGrid);

X2 = [sdIM_ptP skIM_ptP];
Yv2=ones(numb*2,1);
Yv2((numb+1):(numb*2))=-1;
Prediction = predict(SVMModel,X2);
gscatter(X2(:,1),X2(:,2),Prediction,'cm','*x');hold on;

mydiff = (Prediction == Yv2); % Classified correctly
for ii = mydiff % Plot green circles around correct points
    plot(X2(ii,1),X2(ii,2),'go','MarkerSize',12);hold on;
end
for ii = not(mydiff) % Plot red circles around incorrect points
    plot(X2(ii,1),X2(ii,2),'ro','MarkerSize',12);hold on;
end

xlabel('Standard Deviation IM');
ylabel('Skewness IM');
x = 0;
for ii = 1:length(mydiff)
    if mydiff == 0
    x = x+1;
    end
end
if x >= 1

legend('faulty_d_a_t_a(training)','healthy_d_a_t_a(training)','Support
Vector','faulty_d_a_t_a_2(classified)','healthy_d_a_t_a_2(classified)'
,'Correctly classified','Missclassified','Decision Boundary');
else

legend('faulty_d_a_t_a(training)','healthy_d_a_t_a(training)','Support
Vector','faulty_d_a_t_a_2(classified)','healthy_d_a_t_a_2(classified)'
,'Correctly classified','Decision Boundary');
end
set(gca,'FontSize',25,'FontName','Times New Roman');

%% 3d Problem
X = [sdIM_ptT skIM_ptT ksIM_ptT];

SVMModel2 = fitcsvm(X,Y,'KernelFunction','rbf','ClassNames',[-1 1]);
classOrder = SVMModel2.ClassNames;

sv = SVMModel2.SupportVectors;
CVSVMModel2 = crossval(SVMModel2);
classLoss = kfoldLoss(CVSVMModel2);
```

```
figure(2)
scatter3(X(1:numb,1),X(1:numb,2),X(1:numb,3),'b');hold on;
scatter3(X((numb+1):(numb*2),1),X((numb+1):(numb*2),2),X((numb+1):(num
b*2),3),'r+');hold on;
plot3(sv(:,1),sv(:,2),sv(:,3),'ko','MarkerSize',10,'linewidth',1.5);ho
ld on;

% Predict scores over the grid
d = 0.02;
[x1Grid,x2Grid,x3Grid] =
meshgrid(min(X(:,1)):d:max(X(:,1)),min(X(:,2)):d:max(X(:,2)),min(X(:,3
)):d:max(X(:,3)));
xGrid = [x1Grid(:),x2Grid(:),x3Grid(:)];
[~,scores] = predict(SVMModel2,xGrid);

X2 = [sdIM_ptP skIM_ptP ksIM_ptP];
Yv2=ones((numb*2),1);
Yv2((numb+1):(numb*2))=-1;
Prediction2 = predict(SVMModel2,X2);

%%%% Based on prediction %%%%
for p=1:numb*2
    if Prediction2(p)==1
        scatter3(X2(p,1),X2(p,2),X2(p,3),'mx');hold on;
    else
        scatter3(X2(p,1),X2(p,2),X2(p,3),'c*');hold on;
    end
end
%%%%%%%%%%%%%%%%%%%%%%%%%%%%%

mydiff = (Prediction2 == Yv2); % Classified correctly
for ii = mydiff % Plot green circles around correct points
    plot3(X2(ii,1),X2(ii,2),X2(ii,3),'go','MarkerSize',12);hold on;
end
for ii = not(mydiff) % Plot red circles around incorrect points
    plot3(X2(ii,1),X2(ii,2),X2(ii,3),'ro','MarkerSize',12);hold on;
end

xlabel('Standard Deviation IM');
ylabel('Skewness IM');
zlabel('Kurtosis IM');
set(gca,'FontSize',25,'FontName','Times New Roman');

%% 3D decision boundary
svmStruct =
svmtrain(X,GroupNames,'showplot','false','kernel_function','rbf',...
  'boxconstraint',1,'kktviolationlevel',0.05,'tolkkt',5e-3);
svm_3d_matlab_vis(svmStruct,X,GroupNames);

x = 0;
for ii = 1:length(mydiff)
if mydiff(ii) == 0
    x = x+1;
end
end
if x >= 1

legend('healthy_d_a_t_a(training)','faulty_d_a_t_a(training)','Support
```

```
Vector','healthy_d_a_t_a_2(classified)','faulty_d_a_t_a_2(classified)'
,'Correctly classified','Missclassified','Decision Boundary');
else

legend('healthy_d_a_t_a(training)','faulty_d_a_t_a(training)','Support
Vector','healthy_d_a_t_a_2(classified)','faulty_d_a_t_a_2(classified)'
,'Correctly classified','Decision Boundary');
end
pbaspect([1 1 1])
```

LIST OF FIGURES

REFERENCES

[1] IEEE, "Motor Reliability Working Group, Report of Large Motor Reliability Survey of Industrial and Commercial Installations, Part I," *IEEE Trans. Ind. Appl.*, vol. IA-21, Jul, no. 4, pp. 853–864, 1985.

[2] IEEE, "Motor Reliability Working Group, Report of Large Motor Reliability Survey of Industrial and Commercial Installations, Part II," *IEEE Trans. Ind. Appl.*, vol. IA-21, Jul, no. 4, pp. 865–872, 1985.

[3] T. Herold, D. Franck, E. Lange, and K. Hameyer, "Extension of a D-Q Model of a Permanent Magnet Excited Synchronous Machine by Including Saturation, Cross-Coupling and Slotting Effects," *2011 IEEE Int. Electr. Mach. Drives Conf.*, pp. 1363–1367, 2011.

[4] R. Krishnan, *Permanent Magnet Synchronous and Brushless DC Motor Drives*. 2009.

[5] O. a. Mohammed, S. Liu, Z. Liu, and a. a. Khan, "Improved physics-based permanent magnet synchronous machine model obtained from field computation," *2009 IEEE Int. Electr. Mach. Drives Conf.*, pp. 1088–1093, 2009.

[6] O. A. Mohammed, S. Liu, and Z. Liu, "Physical modeling of PM synchronous motors for integrated coupling with machine drives," *IEEE Trans. Magn.*, vol. 41, no. 5, pp. 1628–1631, 2005.

[7] T. Boileau, N. Leboeuf, B. Nahid-Mobarakeh, and F. Meibody-Tabar, "Online identification of PMSM parameters: Parameter identifiability and estimator comparative study," *IEEE Trans. Ind. Appl.*, vol. 47, no. 4, pp. 1944–1957, 2011.

[8] X. Chen, J. Wang, B. Sen, P. Lazari, and T. Sun, "A high-fidelity and computationally efficient model for interior permanent-magnet machines considering the magnetic saturation, spatial harmonics, and iron loss effect," *IEEE Trans. Ind. Electron.*, vol. 62, no. 7, pp. 4044–4055, 2015.

[9] X. Chen, J. Wang, and A. Griffo, "A High-Fidelity and Computationally Efficient Electro-thermally Coupled Model for Interior Permanent-Magnet Machines in Electric Vehicle Traction Applications," *IEEE Trans. Transp. Electrif.*, vol. 7782,

no. c, pp. 1–1, 2015.

[10] C. Gerada, K. Bradley, and M. Sumner, “Winding turn-to-turn faults in permanent magnet synchronous machine drives,” *Fourtieth IAS Annu. Meet. Conf. Rec. 2005 Ind. Appl. Conf. 2005.*, vol. 2, pp. 1029–1036, 2005.

[11] L. Romeral, J. C. Urresty, J. R. Riba Ruiz, and A. Garcia Espinosa, “Modeling of surface-mounted permanent magnet synchronous motors with stator winding interturn faults,” *IEEE Trans. Ind. Electron.*, vol. 58, no. 5, pp. 1576–1585, 2011.

[12] J. Ahmed Farooq, T. Raminosoa, A. Djerdir, and A. Miraoui, “Modelling and simulation of stator winding inter- turn faults in permanent magnet synchronous motors,” *COMPEL - Int. J. Comput. Math. Electr. Electron. Eng.*, vol. 27, no. 4, pp. 887–896, 2008.

[13] O. A. Mohammed, Z. Liu, S. Liu, and N. Y. Abed, “Internal short circuit fault diagnosis for PM machines using FE-based phase variable model and wavelets analysis,” *IEEE Trans. Magn.*, vol. 43, no. 4, pp. 1729–1732, 2007.

[14] B. Vaseghi, B. Nahid-Mobarekeh, N. Takorabet, and F. Meibody-Tabar, “Experimentally validated dynamic fault model for PMSM with stator winding inter-turn fault,” *Conf. Rec. - IAS Annu. Meet. (IEEE Ind. Appl. Soc.*, no. Umr 7037, pp. 1–5, 2008.

[15] B. Sen and J. Wang, “Analytical modelling of stator turn fault in surface mounted permanent magnet machines,” *2013 IEEE Energy Convers. Congr. Expo. ECCE 2013*, pp. 4445–4452, 2013.

[16] B. Sen, J. Wang, and P. Lazari, “A detailed transient model of Interior Permanent Magnet motor accounting for saturation under stator turn fault,” *2013 IEEE Energy Convers. Congr. Expo. ECCE 2013*, pp. 3548–3555, 2013.

[17] B. Sen and J. Wang, “A Fast Detection Technique for Stator Inter-turn Fault in Multi- Phase Permanent Magnet Machines using Model Based Approach,” *IET Int. Conf. Power Electron. Mach. Drive*, pp. 1–6, 2014.

[18] B. Sen, J. Wang, and P. Lazari, “A High-Fidelity Computationally Efficient Transient Model of Interior Permanent-Magnet Machine With Stator Turn Fault,” *IEEE Trans. Ind. Electron.*, vol. 63, no. 2, pp. 773–783, 2016.

[19] I. Jeong, B. J. Hyon, and K. Nam, "Dynamic modeling and control for SPMSMs with internal turn short fault," *IEEE Trans. Power Electron.*, vol. 28, no. 7, pp. 3495–3508, 2013.

[20] N. Leboeuf, T. Boileau, B. Nahid-Mobarakeh, G. Clerc, and F. Meibody-Tabar, "Real-time detection of interturn faults in PM drives using back-EMF estimation and residual analysis," *IEEE Trans. Ind. Appl.*, vol. 47, no. 6, pp. 2402–2412, 2011.

[21] N. Leboeuf, T. Boileau, B. Nahid-Mobarakeh, N. Takorabet, F. Meibody-Tabar, and G. Clerc, "Estimating permanent-magnet motor parameters under inter-turn fault conditions," *IEEE Trans. Magn.*, vol. 48, no. 2, pp. 963–966, 2012.

[22] N. Leboeuf, T. Boileau, B. Nahid-Mobarakeh, N. Takorabet, F. Meibody-Tabar, and G. Clerc, "Inductance calculations in permanent-magnet motors under fault conditions," *IEEE Trans. Magn.*, vol. 48, no. 10, pp. 2605–2616, 2012.

[23] N. Leboeuf, T. Boileau, B. Nahid-Mobarakeh, N. Takorabet, F. Meibody-Tabar, and G. Clerc, "Hybrid data-based/model-based inter-turn fault detection methods for PM drives with manufacturing faults," *2013 IEEE Transp. Electrif. Conf. Expo Components, Syst. Power Electron. - From Technol. to Bus. Public Policy, ITEC 2013*, 2013.

[24] B. G. Gu, J. H. Choi, and I. S. Jung, "Development and analysis of interturn short fault model of PMSMs with series and parallel winding connections," *IEEE Trans. Power Electron.*, vol. 29, no. 4, pp. 2016–2026, 2014.

[25] A. Gandhi, T. Corrigan, and L. Parsa, "Recent Advances in Modeling and Online Detection of Stator Interturn Faults in Electrical Motors," vol. 58, no. 5, pp. 1564–1575, 2011.

[26] A. K. and T. S. D. Min, "Fault Analysis of a PM Brushless DC Motor Using Finite Element Method," *IEEE Trans. Energy Convers.*, vol. 20, no. 1, pp. 1–6, 2005.

[27] B. Vaseghi, N. Takorabet, and F. Meibody-Tabar, "Fault analysis and parameter identification of permanent-magnet motors by the finite-element method," *IEEE Trans. Magn.*, vol. 45, no. 9, pp. 3290–3295, 2009.

[28] J. F. Watson, N. C. Paterson, and D. G. Dorrell, "The use of finite element methods to improve techniques for the early detection of faults in 3-phase induction

motors," *IEEE Trans. Energy Convers.*, vol. 14, no. 3, pp. 655–660, 1999.

[29] C.-E. Kim, Y.-B. Jung, S.-B. Yoon, and D.-H. Im, "Fault diagnosis of rotor bars in squirrel cage induction motors by time-stepping finite element method," *IEEE Trans. Magn.*, vol. 33, no. 2, pp. 2131–2134, 1997.

[30] J. Faiz, B. M. Ebrahim, B. Akin, and H. A. Toliyat, "Finite-element transient analysis of induction motors under mixed eccentricity fault," *IEEE Trans. Magn.*, vol. 44, no. 1, pp. 66–74, 2008.

[31] O. A. Mohammed, N. Y. Abed, and S. Ganu, "Modeling and characterization of induction motor internal faults using finite-element and discrete wavelet transforms," *IEEE Trans. Magn.*, vol. 42, no. 10, pp. 3434–3436, 2006.

[32] T. Boileau, B. Nahid-Mobarakeh, and F. Meibody-Tabar, "Back-EMF based detection of stator winding inter-turn fault for PM synchronous motor drives," *VPPC 2007 - Proc. 2007 IEEE Veh. Power Propuls. Conf.*, pp. 95–100, 2007.

[33] Z. Sun, J. Wang, D. Howe, and G. Jewell, "Analytical prediction of the short-circuit current in fault-tolerant permanent-magnet machines," *IEEE Trans. Ind. Electron.*, vol. 55, no. 12, pp. 4210–4217, 2008.

[34] A. H. Bonnett and C. Yung, "Increased efficiency versus increased reliability," *IEEE Ind. Appl. Mag.*, vol. 14, no. 1, pp. 29–36, 2008.

[35] A. H. Bonnett and G. C. Soukup, "Cause and Analysis of Stator and Rotor Induction Motors," *IEEE Trans. Ind. Appl.*, vol. 28, no. 4, pp. 921–937, 1992.

[36] B. Asghari and V. Dinavahi, "Experimental Validation of a Geometrical Nonlinear Permeance Network Based Real-Time Induction Machine Model," *IEEE Trans. Ind. Electron.*, vol. 59, no. 11, pp. 4049–4062, 2012.

[37] K. Liu, H. Tian, and Y. Zhang, "Development of HIL simulation platform for metro vehicle Linear induction motor driving system," *2015 IEEE Int. Conf. Mechatronics Autom. ICMA 2015*, pp. 403–408, 2015.

[38] N. R. Tavana and V. Dinavahi, "Real-Time Nonlinear Magnetic Equivalent Circuit Model of Induction Machine on FPGA for," *IEEE Trans. ENERGY Convers.*, vol. 31, no. 2, pp. 520–530, 2016.

[39] B. Jandaghi and V. Dinavahi, “Hardware-in-the-Loop Emulation of Linear Induction Motor Drive for MagLev Application,” *IEEE Trans. Plasma Sci.*, vol. 44, no. 4, pp. 679–686, 2016.

[40] M. Matar and R. Iravani, “Massively parallel implementation of AC machine models for FPGA-based real-time simulation of electromagnetic transients,” *IEEE Trans. Power Deliv.*, vol. 26, no. 2, pp. 830–840, 2011.

[41] N. Roshandel Tavana and V. Dinavahi, “A General Framework for FPGA-Based Real-Time Emulation of Electrical Machines for HIL Applications,” *IEEE Trans. Ind. Electron.*, vol. 62, no. 4, pp. 2041–2053, 2015.

[42] Z. Ling, L. Zhou, S. Guo, and Y. Zhang, “Equivalent Circuit Parameters Calculation of Induction Motor,” *IEEE Trans. Magn.*, vol. 50, no. 2, pp. 4–7, 2014.

[43] N. Tavana and V. Dinavahi, “Real-Time FPGA-Based Analytical Space Harmonic Model of Permanent Magnet Machines for Hardware-in-the-Loop Simulation,” *IEEE Trans. Magn.*, vol. 51, no. 8, pp. 1–9, 2015.

[44] A. Griffo, D. Salt, R. Wrobel, and D. Drury, “Computationally efficient modelling of permanent magnet synchronous motor drives for real-time Hardware-in-the-Loop simulation,” *IECON 2013 - 39th Annu. Conf. IEEE Ind. Electron. Soc.*, pp. 5368–5373, 2013.

[45] C. Dufour, S. Abourida, J. Belanger, and V. Lapointe, “Real-time simulation of permanent magnet motor drive on FPGA chip for high-bandwidth controller tests and validation,” *IECON Proc. (Industrial Electron. Conf.*, pp. 4581–4586, 2006.

[46] C. Dufour and J. Bélanger, “FPGA-based real-time simulation of finite-element analysis permanent magnet synchronous machine drives,” *Power Electron. Spec. Conf. 2007. PESC 2007. IEEE*, pp. 909–915, 2007.

[47] C. Dufour, S. Cense, T. Yamada, R. Imamura, and J. Bélanger, “FPGA permanent magnet synchronous motor floating-point models with variable-DQ and spatial harmonic Finite-Element Analysis solvers,” *15th Int. Power Electron. Motion Control Conf. Expo. EPE-PEMC 2012 ECCE Eur.*, pp. 1–10, 2012.

[48] A. Hasanzadeh, C. S. Edrington, N. Stroupe, and T. Bevis, “Real-time emulation of a high-speed microturbine permanent-magnet synchronous generator using

multiplatform hardware-in-the-loop realization," *IEEE Trans. Ind. Electron.*, vol. 61, no. 6, pp. 3109–3118, 2014.

[49] J. A. Walker, D. G. Dorrell, and C. Cossar, "Flux-linkage calculation in permanent-magnet motors using the frozen permeabilities method," *IEEE Trans. Magn.*, vol. 41, no. 10, pp. 3946–3948, 2005.

[50] W. Q. Chu and Z. Q. Zhu, "Average torque separation in permanent magnet synchronous machines using frozen permeability," *IEEE Trans. Magn.*, vol. 49, no. 3, pp. 1202–1210, 2013.

[51] F. Alvarez-gonzalez and A. Griffo, "High-Fidelity Modelling of Permanent Magnet Synchronous Motors for Real-Time Hardware-in-the-Loop Simulation," *8th IET Int. Conf. Power Electron. Mach. Drives (PEMD 2016)*, pp. 1–6, 2016.

[52] A. Schmitt, J. Richter, U. Jurkewitz, and M. Braun, "FPGA-based real-time simulation of nonlinear permanent magnet synchronous machines for power hardware-in-the-loop emulation systems," *Proceedings, IECON 2014 - 40th Annu. Conf. IEEE Ind. Electron. Soc.*, pp. 3763–3769, 2014.

[53] P. Arumugam, C. Gerada, T. Hamiti, C. Hill, and S. Bozhko, "A Review on Turn-Turn Short Circuit Fault Management," in *2015 International Conference on Electrical Systems for Aircraft, Railway, Ship Propulsion and Road Vehicles (ESARS)*, 2015, pp. 1–5.

[54] G. M. Joksimovic and J. Penman, "The detection of inter-turn short circuits in the stator windings of operating motors," *IEEE Trans. Ind. Electron.*, vol. 47, no. 5, pp. 1078–1084, 2000.

[55] J. C. Urresty, J. R. Riba, and L. Romeral, "Diagnosis of interturn faults in pmsms operating under nonstationary conditions by applying order tracking filtering," *IEEE Trans. Power Electron.*, vol. 28, no. 1, pp. 507–515, 2013.

[56] W. Le Roux, R. G. Harley, and T. G. Habetler, "Detecting Faults in Rotors of PM Drives," *IEEE Ind. Appl. Mag.*, pp. 23–31, 2008.

[57] L. Liu, "Robust Fault Detection and Diagnosis for Permanent Magnet Synchronous Motors," Florida State University, 2006.

[58] B. M. Ebrahimi and J. Faiz, "Feature extraction for short-circuit fault detection in

permanent-magnet synchronous motors using stator-current monitoring," *IEEE Trans. Power Electron.*, vol. 25, no. 10, pp. 2673–2682, 2010.

[59] N. Obeid, T. Boileau, and B. Nahid-Mobarakeh, "Modeling and Diagnostic of Incipient Inter-turn Faults For a Three Phase Permanent Magnet Synchronous Motor," *IEEE Trans. Ind. Appl.*, pp. 1–1, 2016.

[60] Q. Wu and S. Nandi, "Fast single-turn sensitive stator interturn fault detection of induction machines based on positive- and negative-sequence third harmonic components of line currents," *IEEE Trans. Ind. Appl.*, vol. 46, no. 3, pp. 974–983, 2010.

[61] S. T. Lee and J. Hur, "Detection technique for stator inter-turn faults in BLDC motors based on third harmonic components of line currents," *2015 IEEE Energy Convers. Congr. Expo. ECCE 2015*, pp. 1899–1904, 2015.

[62] J. Hang, J. Zhang, M. Cheng, and J. Huang, "Online Inter-turn Fault Diagnosis of Permanent Magnet Synchronous Machine Using Zero Sequence Components," *IEEE Trans. Power Electron.*, vol. PP, no. 99, pp. 1–1, 2015.

[63] W. T. Thomson and M. Fenger, "Current signature analysis to detect induction motor faults," *IEEE Ind. Appl. Mag.*, vol. 7, no. 4, pp. 26–34, 2001.

[64] K. H. Kim, "Simple online fault detecting scheme for short-circuited turn in a PMSM through current harmonic monitoring," *IEEE Trans. Ind. Electron.*, vol. 58, no. 6, pp. 2565–2568, 2011.

[65] A. M. da Silva, R. J. Povinelli, and N. A. O. Demerdash, "Induction machine broken bar and stator short-circuit fault diagnostics based on three-phase stator current envelopes," *IEEE Trans. Ind. Electron.*, vol. 55, no. 3, pp. 1310–1318, 2008.

[66] P. S. Barendse, B. Herndler, M. A. Khan, and P. Pillay, "The application of wavelets for the detection of inter-turn faults in induction machines," *2009 IEEE Int. Electr. Mach. Drives Conf. IEMDC '09*, pp. 1401–1407, 2009.

[67] J. A. Rosero, L. Romeral, J. Cusido, A. Garcia, and J. A. Ortega, "On the short-circuiting fault detection in a PMSM by means of stator current transformations," *PESC Rec. - IEEE Annu. Power Electron. Spec. Conf.*, pp. 1936–1941, 2007.

[68] J. Rosero, A. G. Espinosa, J. Cusido, J. A. Ortega, and L. Romeral, “Simulation and fault detection of short circuit winding in a permanent magnet synchronous machine (PMSM) by means of fourier and wavelet transform,” *Conf. Rec. - IEEE Instrum. Meas. Technol. Conf.*, pp. 411–416, 2008.

[69] M. Wolkiewicz, G. Tarchała, T. Orłowska-Kowalska, and C. T. Kowalski, “Online stator interturn short circuits monitoring in the DFOC induction-motor drive,” *IEEE Trans. Ind. Electron.*, vol. 63, no. 4, pp. 2517–2528, 2016.

[70] S. Nandi, T. C. Ilamparithi, S. Bin Lee, and D. Hyun, “Detection of eccentricity faults in induction machines based on nameplate parameters,” *IEEE Trans. Ind. Electron.*, vol. 58, no. 5, pp. 1673–1683, 2011.

[71] E. Cabal-Yepez, A. G. Garcia-Ramirez, R. J. Romero-Troncoso, A. Garcia-Perez, and R. A. Osornio-Rios, “Reconfigurable monitoring system for time-frequency analysis on industrial equipment through STFT and DWT,” *IEEE Trans. Ind. Informatics*, vol. 9, no. 2, pp. 760–771, 2013.

[72] M. A. Awadallah, M. M. Morcos, S. Gopalakrishnan, and T. W. Nehl, “Detection of stator short circuits in VSI-Fed brushless DC motors using wavelet transform,” *IEEE Trans. Energy Convers.*, vol. 21, no. 1, pp. 1–8, 2006.

[73] J. A. Antonino-Daviu, M. Riera-Guasp, M. Pineda-Sanchez, and R. B. Pérez, “A critical comparison between DWT and Hilbert-Huang-based methods for the diagnosis of rotor bar failures in induction machines,” *IEEE Trans. Ind. Appl.*, vol. 45, no. 5, pp. 1794–1803, 2009.

[74] N. E. Huang, Z. Shen, S. R. Long, M. C. W. U, H. H. Shih, Q. Zheng, N.-C. Yen, C. C. Tung, and H. H. Liu, “The empirical mode decomposition and the Hilbert spectrum for nonlinear and non-stationary time series analysis,” *R. Soc.*, 1998.

[75] Y. Zhang, “Hilbert-Huang Transform and Marginal Spectrum for Detection of Bearing Localized Defects,” in *Proceedings of the 6th World Congress on Intelligent Control and Automation*, 2006, pp. 5457–5461.

[76] E. Elbouchikhi and V. Choqueuse, “Induction Machine Bearing Faults Detection based on Hilbert-Huang Transform,” in *2015 IEEE 24th International Symposium on Industrial Electronics (ISIE)*, 2015, pp. 843–848.

[77] S. Osman and W. Wang, “A Morphological Hilbert-Huang Transform Technique for Bearing Fault Detection,” *IEEE Trans. Instrum. Meas.*, vol. 65, no. 11, pp. 2646–2656, 2016.

[78] E. Elbouchikhi, V. Choqueuse, Y. Amirat, M. Benbouzid, and S. Turri, “An Efficient Hilbert-Huang Transform-based Bearing Faults Detection in Induction Machines,” *IEEE Trans. Energy Convers.*, vol. 8969, no. c, pp. 1–1, 2017.

[79] J. Rosero, L. Romeral, J. A. Ortega, and J. C. Urresty, “Demagnetization Fault Detection by means of Hilbert Huang Transform of the stator current Decomposition in PMSM,” in *2008 IEEE International Symposium on Industrial Electronics*, 2008, pp. 172–177.

[80] A. G. Espinosa, J. A. Rosero, J. Cusido, L. Romeral, and J. A. Ortega, “Fault detection by means of Hilbert-Huang transform of the stator current in a PMSM with demagnetization,” *IEEE Trans. Energy Convers.*, vol. 25, no. 2, pp. 312–318, 2010.

[81] D. Lu, W. Qiao, X. Gong, and L. Qu, “Current-Based Fault Detection for Wind Turbine Systems via Hilbert-Huang Transform,” *2013 IEEE Power Energy Soc. Gen. Meet.*, pp. 1–5, 2013.

[82] A. Soualhi, K. Medjaher, and N. Zerhouni, “Bearing Health Monitoring Based on Hilbert – Huang Transform , Support Vector Machine , and Regression,” *IEEE Trans. Instrum. Meas.*, vol. 64, no. 1, pp. 52–62, 2015.

[83] C. Wang, X. Liu, and Z. Chen, “Incipient Stator Insulation Fault Detection of Permanent Magnet Synchronous Wind Generators Based on Hilbert – Huang Transformation,” *IEEE Trans. Magn.*, vol. 50, no. 11, 2014.

[84] F. Alvarez-Gonzalez, A. Griffo, and B. Wang, “Permanent Magnet Synchronous Machine Stator Windings Fault Detection by Hilbert-Huang Transform,” in *Proc. 9th IET Conf. PEMD*, 2018, pp. 1–6.

[85] A. Sarikhani, B. Mirafzal, and O. Mohammed, “Inter-Turn Fault Diagnosis of PM Synchronous Generator for Variable Speed Wind Applications Using Floating-Space-Vector,” in *IECON 2010 - 36th Annual Conference on IEEE Industrial Electronics Society*, 2010, pp. 2628–2633.

[86] M. A. Mazzoletti, G. R. Bossio, C. H. De Angelo, and D. R. Espinoza-trejo, "A Model-Based Strategy for Interturn Short-Circuit Fault Diagnosis in PMSM," *IEEE Trans. Ind. Electron.*, vol. 64, no. 9, pp. 7218–7228, 2017.

[87] R. Hu, J. Wang, A. R. Mills, E. Chong, and Z. Sun, "Turn Fault Detection for Surface-Mounted Permanent Magnet Synchronous Machine Based On Current Residual," in *2017 IEEE International Electric Machines and Drives Conference (IEMDC)*, 2017, pp. 1–8.

[88] A. Kiselev, A. Kuznietsov, and R. Leidhold, "Model Based Online Detection of Inter-Turn Short Circuit Faults in PMSM Drives under Non-Stationary Conditions," in *2017 11th IEEE International Conference on Compatibility, Power Electronics and Power Engineering (CPE-POWERENG)*, 2016, pp. 370–374.

[89] A. Sarikhani and O. A. Mohammed, "Inter-turn fault detection in PM synchronous machines by physics-based back electromotive force estimation," *IEEE Trans. Ind. Electron.*, vol. 60, no. 8, pp. 3472–3484, 2013.

[90] N. Leboeuf, T. Boileau, B. Nahid-Mobarakeh, and F. Meibody-Tabar, "Fault detection in a current controlled PM drive using back-EMF estimation and residual analysis," *Conf. Rec. - IAS Annu. Meet. (IEEE Ind. Appl. Soc.*, pp. 1–6, 2010.

[91] T. Boileau, N. Leboeuf, B. Nahid-Mobarakeh, and F. Meibody-Tabar, "Synchronous demodulation of control voltages for stator interturn fault detection in PMSM," *IEEE Trans. Power Electron.*, vol. 28, no. 12, pp. 5647–5654, 2013.

[92] Y. Nyanteh, C. Edrington, S. Srivastava, and D. Cartes, "Application of artificial intelligence to real-time fault detection in permanent-magnet synchronous machines," *Ind. Appl. IEEE Trans.*, vol. 49, no. 3, pp. 1205–1214, 2013.

[93] J. Quiroga, D. A. Cartes, C. S. Edrington, and L. Liu, "Neural network based fault detection of PMSM stator winding short under load fluctuation," *2008 13th Int. Power Electron. Motion Control Conf. EPE-PEMC 2008*, pp. 793–798, 2008.

[94] L. Liu, D. a. Cartes, and W. L. W. Liu, "Particle Swarm Optimization Based Parameter Identification Applied to PMSM," *2007 Am. Control Conf.*, pp. 2955–2960, 2007.

[95] L. Liu, D. A. Cartes, and W. Liu, "Application of Particle Swarm Optimization to

PMSM Stator Fault Diagnosis," *Int. Jt. Conf. Neural Networks*, pp. 1969–1974, 2006.

[96] R. M. Tallam, T. G. Habetler, and R. G. Harley, "Continual on-line training of neural networks with applications to electric machine fault diagnostics," *PESC Rec. - IEEE Annu. Power Electron. Spec. Conf.*, vol. 4, pp. 2224–2228, 2001.

[97] S. S. Moosavi, A. Djerdir, Y. Ait-Amirat, and D. A. Kkuburi, "Artificial neural networks based fault detection in 3-Phase PMSM traction motor," *2012 XXth Int. Conf. Electr. Mach.*, pp. 1579–1585, 2012.

[98] X. Jin, M. Zhao, T. W. S. Chow, and M. Pecht, "Motor bearing fault diagnosis using trace ratio linear discriminant analysis," *IEEE Trans. Ind. Electron.*, vol. 61, no. 5, pp. 2441–2451, 2014.

[99] C. P. Mboo and K. Hameyer, "Fault diagnosis of bearing damage by means of the linear discriminant analysis of stator current features from the frequency selection," *IEEE Trans. Ind. Appl.*, vol. 52, no. 5, pp. 3861–3868, 2016.

[100] J. J. Saucedo-Dorantes, M. Delgado-Prieto, R. A. Osornio-Rios, and R. De Jesus Romero-Troncoso, "Multifault Diagnosis Method Applied to an Electric Machine Based on High-Dimensional Feature Reduction," *IEEE Trans. Ind. Appl.*, vol. 53, no. 3, pp. 3086–3097, 2017.

[101] K. Brigham, D. Zappalá, C. J. Crabtree, and C. Donaghy-spargo, "Automated Fault Detection in Wind Turbine Induction Generators with Rotor Electrical Asymmetry," in *9th IET International Conference on Power Electronics, Machines and Drives (PEMD 2018)*, 2018, pp. 1–6.

[102] S. Haykin, *Neural Networks and Learning Machines, Third Edition*. 2009.

[103] V. N. Vapnik, "An overview of statistical learning theory.," *IEEE Trans. Neural Netw.*, vol. 10, no. 5, pp. 988–99, 1999.

[104] E. Smart, D. Brown, and L. Axel-Berg, "Comparing one and two class classification methods for multiple fault detection on an induction motor," *ISIEA 2013 - 2013 IEEE Symp. Ind. Electron. Appl.*, pp. 132–137, 2013.

[105] J. Maitre, S. Gaboury, B. Bouchard, and A. Bouzouane, "A New Computational Approach for Inter-Turn Short Circuit Recognition in Induction Machines Using

currents analysis and Multi-Class Support Vector Machine," in *8th IET International Conference on Power Electronics, Machines and Drives (PEMD 2016)*, 2016, pp. 1–6.

[106] I. Aydin, M. Karakose, and E. Akin, "Artificial immune based support vector machine algorithm for fault diagnosis of induction motors," in *2007 International Aegean Conference on Electrical Machines and Power Electronics*, 2007, pp. 217–221.

[107] M. G. Armaki and R. Roshanfekr, "A New Approach for Fault Detection of Broken Rotor Bars in Induction Motor Based on Support Vector Machine," *Proc. ICEE 2010*, 2010.

[108] S. Das, C. Koley, P. Purkait, and S. Chakravorti, "Wavelet aided SVM classifier for stator inter-turn fault monitoring in induction motors," *IEEE PES Gen. Meet. PES 2010*, pp. 10–15, 2010.

[109] Y. K. Moorthy, P. S. Chandran, and S. Rishidas, "Motor current signature analysis by multi-resolution methods using Support Vector Machine," *Recent Adv. Intell. Comput. Syst. (RAICS), 2011 IEEE*, pp. 96–101, 2011.

[110] S. Das, P. Purkait, C. Koley, and S. Chakravorti, "Performance of a load-immune classifier for robust identification of minor faults in induction motor stator winding," *IEEE Trans. Dielectr. Electr. Insul.*, vol. 21, no. 1, pp. 33–44, 2014.

[111] D. R. Sawitri, D. a Asfani, M. H. Purnomo, I. K. E. Purnama, and M. Ashari, "Early Detection of Unbalance Voltage in Three Phase Induction Motor Based on SVM," *IEEE Int. Symp. Diagnostics Electr. Mach. Power Electron. Drives*, pp. 573–578, 2013.

[112] L. Romeral, J. C. Urresty, J. R. Ruiz, and A. G. Espinosa, "Modeling of Surface-Mounted Permanent Magnet Synchronous Motors With Stator Winding Interturn Faults," *IEEE Trans. Ind. Electron.*, vol. 58, no. 5, pp. 1576–1585, 2011.

[113] I. Tsyokhla, A. Griffo, and J. Wang, "On-line monitoring of winding insulation health using high frequency common mode voltage from PWM," *Proc. - 2015 IEEE Int. Electr. Mach. Drives Conf. IEMDC 2015*, pp. 1433–1439, 2016.

[114] B. M. Ebrahimi and J. Faiz, "Feature Extraction for Short-Circuit Fault Detection

in Permanent-Magnet Synchronous Motors Using," *IEEE Trans. Power Electron.*, vol. 25, no. 10, pp. 2673–2682, 2010.

[115] L. Wang, J. Jatskevich, and H. W. Dommel, "Re-examination of synchronous machine modeling techniques for electromagnetic transient simulations," *IEEE Trans. Power Syst.*, vol. 22, no. 3, pp. 1221–1230, 2007.

[116] F. Alvarez-gonzalez, A. Griffo, and B. Wang, "Permanent Magnet Synchronous Machines Inter-Turn Short Circuit Fault Detection by Means of Model- Based Residual Analysis," in *IECON 2018 - 44th Annual Conference of the IEEE Industrial Electronics Society*, 2018, pp. 647–652.

[117] B. Wang, J. Wang, A. Griffo, and B. Sen, "Stator Turn Fault Detection by 2 nd Harmonic in Instantaneous Power for a Triple Redundant Fault-tolerant PM Drive," *IEEE Trans. Ind. Electron. Stator*, vol. 65, no. 9, pp. 7279–7289, 2018.

[118] B. Wang, J. Wang, and A. Griffo, "Experimental Assessments of a Triple Redundant Nine-Phase Fault-Tolerant PMA SynRM Drive" *IEEE Trans. Ind. Electron.*, vol. 66, no. 1, pp. 772–783, 2019.

[119] B. Wang, J. Wang, A. Griffo, and B. Sen, "A General Modelling Technique for a Triple Redundant 3x3-phase PMA SynRM," *IEEE Trans. Ind. Electron.*, vol. 65, no. 11, pp. 9068–9078, 2018.

[120] F. Alvarez-gonzalez, A. Griffo, B. Sen, J. Wang , "Real - Time Hardware - in - the - Loop Simulation of Permanent Magnet Synchronous Motor Drives under Stator Faults," *IEEE Trans. Ind. Electron.*, vol. 64, no. 9, pp. 6960–6969, 2017.

[121] B. Wang, J. Wang, B. Sen, A. Griffo, Z. Sun, and E. Chong, "A Fault Tolerant Machine Drive Based on Permanent Magnet Assisted Synchronous Reluctance Machine," *IEEE Trans. Ind. Appl.*, vol. 54, no. 2, pp. 1349–1359, 2018.

[122] D. Salt, D. Drury, Holliday, D. Holliday, A. Griffo, P. Shanga and A. Dinu, "Compensation of Inverter Nonlinear Distortion Effects for Signal Injection based Sensorless Control," *IEEE Trans. Ind. Appl.*, vol. 47, no. 5, pp. 2084–2092, 2011.

[123] F. Vedreño-Santos, M. Riera-Guasp, H. Henao, M. Pineda-Sánchez, and R. Puche-Panadero, "Diagnosis of rotor and stator asymmetries in wound-rotor induction machines under nonstationary operation through the instantaneous frequency,"

IEEE Trans. Ind. Electron., vol. 61, no. 9, pp. 4947–4959, 2014.

[124] C. M. Bishop, *Pattern Recognition and Machine Learning*. 2006.